UNIVERSITÀ DEGLI STUDI DI CAGLIARI

PHD DEGREE
in Physics
Cycle XXXI

TITLE OF THE PHD THESIS

Modelling the radio spectra of spatially-resolved Supernova Remnants at high frequencies

Scientific Disciplinary Sector
FIS/05

PhD Student: Sara Loru
Coordinator of the PhD Programme: Prof. Paolo Ruggerone
Supervisor: Prof. Nicolò D'Amico

Final exam. Academic Year 2017–2018
Thesis defence: January 2019 Session

THIS THESIS HAS BEEN DONE IN THE CONTEXT OF THE SCIENTIFIC RESEARCH ACTIVITY OF THE "OSSERVATORIO ASTRONOMICO DI CAGLIARI - ISTITUTO NAZIONALE DI ASTROFISICA".

I WORKED IN DIRECT AND STRONG COLLABORATION WITH DR. ALBERTO PELLIZZONI AND DR. ELISE EGRON, WHO I CONSIDER MY CO-SUPERVISORS. THEY WERE RECOGNISED AS SUCH BY THE ACADEMIC BOARD OF THE PHD SCHOOL IN PHYSICS OF THE CAGLIARI UNIVERSITY, BUT BECAUSE OF THE BUREAUCRACY OF THE UNIVERSITY OF CAGLIARI, I COULD NOT INCLUDE THEM ON THE COVER PAGE OF MY PHD THESIS.

Abstract

Supernova remnants (SNRs) result from the interaction between the stellar mass ejected during a supernova explosion and the surrounding circumstellar (CSM) or interstellar medium (ISM). The stellar expanding ejecta carry a huge amount of energy ($\sim 10^{51}$ erg), which is transferred to the magnetic field and kinetic/thermal energy of shocked interstellar gas and relativistic particles. These electrons and heavier particles produce the non-thermal emission of SNRs both in the radio and gamma-ray bands. The nature of the high-energy emission is still debated, and the co-spatial study of the radio and gamma-ray emissions may provide crucial information in order to disentangle the two basic possible scenarios that are represented by leptonic (Inverse Compton and Bremsstrahlung emission) and hadronic models (π^0 mesons decay emission). In particular, the observed Bremsstrahlung and IC bumps in the gamma-ray band are bounded to the synchrotron spectral slope and cut-off in the radio domain.
The main characteristics of the radio continuum spectra of SNRs result from simple synchrotron emission. In addition, electron acceleration mechanisms can shape the spectra in specific ways, especially at high radio frequencies. These features are connected to the age and the peculiar conditions of the local ISM interacting with the SNR. Therefore, it is of interest to firmly establish a possible radio spectral break and features, and to identify regions or structures within the SNRs where they take place. Whereas the bulk radio emission is expected at up to 20−50 GHz, sensitive high-resolution images of SNRs above ~10 GHz are lacking and are not easily achievable, especially in the confused regions of the Galactic Plane. Indeed, interferometric observations are certainly unbeatable in terms of image resolution, but synthesis imaging becomes difficult in the context of extended sources (10−30 arcmin) at high radio frequencies (above a few GHz). On the other hand, sensitive radio continuum observations can be performed with single-dish telescopes, offering in this way a good trade-off between sensitivity and resolution in the frequency range 5−50 GHz. The Sardinia Radio Telescope (SRT) represents a great instrument in this context, thanks to its active surface that characterises the primary 64-m-diameter mirror, and which improves spatial resolution at high frequencies.
In their early phase, young SNRs typically do not show a spectral break in the radio band due to very efficient acceleration conditions, while a spectral index steepening is expected at radio frequencies in evolved SNRs wherein the particle acceleration mechanisms are less efficient. The middle-aged SNRs W44, IC443 and Cygnus Loop represent ideal targets in order to investigate synchrotron spectral indices and breaks in their spatially-resolved radio spectra and to constrain different emission processes that take place in their peculiar regions or structures. W44 and IC443 belong to the remnant "mixed morphology" class (Rho & Petre, 1998), and are characterized by a highly filamentary radio shell (synchrotron emission) and a central thermal X-ray emission. A rich region-dependent phenomenology characterises these nearby and large SNRs, which include atomic/molecular clouds interactions, Pulsar Wind Nebulae (PWN) associations, thermal X-ray emission, halos and filamentary structures. These interesting features have encouraged in

recent years the multi-wavelength studies of W44 and IC443, ranging from radio to gamma-rays (Castelletti et al. 2007, Ackermann et al. 2013, Cardillo et al. 2016, Castelletti et al. 2011). The lack of high-resolution images of these sources at frequencies >5 GHz makes it crucial to perform new spectral imaging (through accurate spectral index maps) with good angular resolution and sensitivity at high-radio frequencies in order to better constrain their multi-wavelength scenario and to characterise the actual energy distribution of the different electron populations responsible for both radio and part of gamma-ray emissions (Egron et al., 2017). Due to its strength, large size and its location at high Galactic latitude with little confusion by unrelated emission along the line of sight, the Cygnus Loop SNR was observed across the entire accessible electro-magnetic spectrum. Recent studies of the Cygnus Loop region based on radio continuum and polarization data in conjunction with optical, X-ray and infrared data, revealed that the Cygnus Loop consists of two SNRs rather than being a single SNR shaped by strong inhomogeneities in the interstellar medium (Uyanıker et al., 2004). Although Cygnus Loop has been frequently studied since the early years of radio astronomy until now, sensitive flux density measurements are available only up ~ 5 GHz. It is therefore of interest to firmly establish if there is a spectral break for the Cygnus Loop in the frequency range 1-10 GHz. Furthermore, the region-dependent variations on spectral indices and polarization properties observed between the two SNRs make Cygnus Loop an ideal target to investigate the region-dependent correlation between flux density intensity and spectral slopes in order to disentangle possible magnetic enhancement processes from spectral variation contributions due to different primary and secondary electron populations.

We observed the middle-aged SNRs W44 and IC443 with SRT at 1.55 GHz (L-band), 7.0 GHz (C-band) and 21.4 GHz (K-band). We also observed the young Tycho SNR at 21.4 GHz. These observations provided, for the first time, single-dish high-resolution images of W44 and IC443 at 7 GHz and 21.4 GHz, which demonstrated that a good mapping quality of large structures can be maintained with SRT in the single-dish configuration at up to high-radio frequencies. Our images provided integrated sensitive flux density measurements that we coupled with the radio data available in the literature in order to characterise the integrated and spatially-resolved spectra of these SNRs.

We performed spatially-resolved spectral measurements of W44 and IC443 by coupling 1.5 GHz and 7.0 GHz maps. For both W44 and IC443, the obtained spectral index maps reveal a spread in the spectral slope distribution, ranging from flat or slightly inverted spectra from brightest SNR regions near the limbs or filaments, to relatively steep spectra in fainter central regions and halos. We attributed these features to different electron populations and spectra, including secondary hadronic electrons, which result from peculiar shocks conditions and/or undergoing different cooling processes. On the other hand, the different spectral shapes could be related to a magnetic field amplification at SNR shocks, which results in an efficient CR acceleration. Our spectral studies, based on the 1.5−7.0 GHz SRT measurements, also suggested a possible slight spectral steepening above ~ 1 GHz for both sources, which could be related to a break in the distribution of primary or, more likely, secondary hadronic electrons.

We used our high-frequency/high resolution imaging data at 21.4 GHz in order to better investigate these spectral features and to disentangle different theoretical models that could describe the high-frequency spectra of these SNRs. With this aim, we coupled the SRT measurements with radio data available in the literature in order to characterise the integrated spectra of these SNRs at up to high-radio frequencies. Our studies on the integrated spectrum of Tycho provide a useful verification of the performance of SRT in the K-band multi-feed configuration and, at the same time, confirm (through the highest frequency single-dish observations performed so far) non-thermal synchrotron as the dominant emission process for Tycho at up to high radio frequen-

cies. For the first time, we provided direct evidence for spectral break in the radio spectral energy distribution of W44 at an exponential cut-off frequency of 15 ± 2 GHz. This result constrains the maximum energy of the accelerated cosmic-ray electrons in the range 6−13 GeV, in agreement with predictions indirectly derived from AGILE and Fermi-LAT gamma-ray observations. With regard to IC443, our results confirm the noticeable presence of a bump in the integrated spectrum around 20−70 GHz that could result from a spinning dust emission mechanism.
In view of the results obtained with SRT in the context of single-dish imaging of extended sources, we decided to observe the very extended and interesting SNR Cygnus Loop at 8.3 GHz with the Medicina radio telescope. From these observations, we obtained the integrated flux density measurement of Cygnus Loop at the highest frequency carried out so far with a single-dish telescope. We used this value in conjunction with the measurements available in the literature in order to study the integrated spectrum of Cygnus Loop. By modelling the spectral emission distribution through a simple synchrotron power-law, we obtained a spectral index that is consistent with the previous measurements reported in the literature, and rules out any spectral steepening at up to high-radio frequencies.
Although comparable in age, our observations show that W44, IC443 and Cygnus Loop present different spectral features at high radio frequencies. We ascribed this evidence to the environmental differences between these SNRs, which could lead to an enhancement of the secondary electron populations produced by hadronic interactions in regions where the SNR shock collides with dense molecular clouds and/or to a significant local enhancement of the magnetic field. In order to study implications of the morphological and evolutionary SNR characteristics on the peculiar emission processes, radio continuum observations of a large population sample of SNRs at up to high radio frequencies would be required.

TABLE OF CONTENTS

INTRODUCTION

My PhD work was developed in the context of a broad project devoted to the radio-continuum observation of Supernova Remnants (SNRs) with the Italian radio telescopes. The project to observe SNRs started in 2012, during the scientific commissioning of the Sardinia Radio Telescope (SRT). The goal was to test the radio-continuum imaging capabilities of this innovative telescope, which represents a challenging scientific project of the Italian National Institute for Astrophysics (INAF). Since SRT early results, we realized the great scientific prospects for SRT in the context of both integrated and spatially-resolved spectral studies performed on SNRs.

Due to the availability of a relatively wide amount of multi-wavelength data, their complex and challenging morphology, and their complementary visibility at the SRT site, the two evolved SNRs W44 and IC443 were selected as ideal targets to test the SRT single-dish imaging performances during the Astronomical Validation (AV[1]) activities. The observations were performed from 2014 May 27 to December 10 at the central frequency of 7.24 GHz. Thanks to the SRT active surface that characterizes the primary 64-m-diameter mirror and improves spatial resolution at high frequencies (Prandoni et al., 2017), the obtained images showed details in the morphology of W44 and IC443 that were comparable with those obtained from interferometric observations carried out at lower frequencies (up to ~1.4 GHz). The good mapping quality of large structures obtained at 7.24 GHz (Egron et al., 2016) and the possibility to maintain it even at high frequencies (K-band, 18−26.5 GHz; Loru et al. 2019) make the single dish observations with SRT a key instrument in order to investigate SNR spectra. Indeed, performing sensitive radio continuum observations of large sources like SNRs up to high radio frequencies (> 1−10 GHz) is crucial to characterizing the radio spectra and to identifying regions or structures within the SNR where the spectral break takes place. Radio interferometric observations provide a lot of information about the morphology of SNRs, but an accurate flux estimate is difficult to obtain, and the synthesis imaging of large structure like SNRs is typically feasible only at low radio frequencies (up to ~ 10 GHz).

From these promising results, a large program dedicated to the observation of SNRs with SRT (PI: A. Pellizzoni) was proposed in the framework of SRT Early Science Program (ESP[2]). I participated in this project and in the observations that were performed between 2016 February 14 and March

[1] http://www.srt.inaf.it/astronomers/astrophysical-validation-team/

[2] www.srt.inaf.it/astronomers/early-science-program-FEB-2016/

24, on the SNR W44 and IC443 at 1.55 GHz, 7.0 GHz and at 21.4 GHz. We also observed the Tycho SNR at 21.4 GHz. We carried out SNR mapping by using the On-the-Fly (OTF) scan technique, which implies that the data acquisition is continuously ongoing while the antenna performs constant-speed scans across the sky alternately in two directions.
The analysis of the OTF maps required the implementation of the SRT Single Dish Imager (SDI; Egron et al. 2017, Egron et al. (2017); user manual, Pellizzoni et al. in prep), which is a tool designed to perform continuum (and in the future, spectro-polarimetric) imaging starting from OTF scans, and which is suitable for all SRT receivers and back-ends. I contributed to the development of the SDI pipeline that was dedicated to the analysis of the acquired data and to the calibration of single dish continuum maps. I have therefore taken part in the analysis of the data and in the production of the final calibrated images.
These data allowed us to obtain, for the first time, single-dish deep imaging at 7 GHz of the W44 and IC443 complex SNRs coupled with spatially-resolved spectra in the 1.5−7 GHz frequency range. The integrated and spatially-resolved spectral index studies performed from these radio images and related results are described in Egron et al. (2017).
Subsequently, I took care of the analysis of the data acquired at 21.4 GHz as principal investigator. These data were the first obtained by using the SRT multi-feed receiver in the Best Space Coverage configuration, and for this reason they required the study of the gain curve and the beam shape in order to test the receiver performances that characterized our observations. Furthermore, the data analysis required the development of specific SDI tools in order to obtain the final calibrated maps of the targets from each individual feed map and fully verify imaging performances of the SRT multi-feed system. In the paper Loru et al. (2019), we showed the high-resolution images of SNRs W44, IC443 and Tycho at 21.4 GHz that provided accurate integrated flux density measurements. We used these high-frequency measurements in order to characterize both the integrated and spatially-resolved spectra of these SNRs, and to find significant frequency- and region-dependent spectral slope variations.
Finally, I participated in 2017 in the call for observations with the Medicina radio telescope as Principal Investigator of the proposal entitled "Modelling spatially-resolved spectra of the Cygnus Loop Supernova Remnant". Cygnus Loop is one of the most well-studied middle-aged SNRs. Thanks to its large size ($\sim 4^\circ \times 3^\circ$), this SNR is particularly well suited for morphological studies across the entire accessible electro-magnetic spectrum. The goal of the proposal was to perform accurate OTF maps of Cygnus Loop at 5 GHz and 8.3 GHz in order to study the complex morphology of the Cygnus Loop SNR with detailed maps at frequencies above those available so far. The project was approved with 80 hours of observations performed between June and August 2017, and the obtained preliminary results are described in this PhD thesis.
Chapter 1 is dedicated to the description of SNRs and in particular of their spectra. I briefly describe the main phases of SNR evolution and the classification of these objects following their radio emission morphology. I discuss particle acceleration and emission mechanisms that

take place in SNRs. I then focused on the theoretical fundamentals of the continuum radio spectra of young and evolved SNRs and their implication for multi-frequency studies. In Chapter 2, I describe in detail the project of the single-dish observations of SNRs with Italian radio telescopes. I introduce our observational project with SRT, starting with a brief description of the multi-frequency characteristics of our targets: W44, IC443, Tycho and Cygnus Loop. A detailed description of the observations performed with SRT at 1.55 GHz, 7.0 GHz and 21.4 GHz and the main steps of the data reduction is also provided. I present the resulting calibrated images of W44, IC443 and Tycho at the three observational radio frequencies, and related flux density measurements. Finally, I introduce the project associated with the observation of the SNR Cygnus Loop with the Medicina radio telescope and the related preliminary results. Chapter 3 is dedicated to the discussion of the different emission models that could explain the observed spectral features of W44, IC443, Tycho and Cygnus Loop. In the final Chapter, I summarize the main conclusions of our study and the future perspectives from the work presented in this thesis. In particular I introduce the our last observing project entitled "Challenging electron populations and acceleration models in Supernova Remnants shocks through high-frequency continuum and polarization observations" (PI: Alberto Pellizzoni) started in 2018 December with the aim to carry out high-frequency polarimetric observations on a wider population sample of middle-aged and young SNRs.

CHAPTER 1

EVOLUTION, ACCELERATION AND EMISSION MECHANISMS IN SUPERNOVA REMNANTS

During a Supernova (SN) explosion the mass of a star in the last phase of its life is ejected into the surrounding interstellar medium (ISM) at very high speed (from 5000 to 10000 km s^{-1}). Mainly two explosive mechanisms can lead a SN. Type Ia SNe result from the thermonuclear explosion of a degenerate carbon-oxygen stellar core, and they typically leave no stellar remnant. The other group consists of Types Ib, Ic and II SNe, which are the results of the gravitational collapse of very massive stars (initial mass $M \geq 8 M_{\odot}$) that have exhausted their nuclear fuel. In this case the SN can leave a neutron star or black hole stellar remnant (or possibly none). All type of SN explosions release, almost instantaneously, a huge amount of energy ($\sim 10^{51}$ erg). The nebula formed by the expelled envelope, its interaction with the ISM under the action of the shock waves, and the compact stellar remnant (in the cases where it survives) constitute the Supernova Remnant (SNR). The nebula of the SNRs is observable thousands of years after the SN explosion, although the velocity of the ejected material falls to $\sim$ 100 or even 10 km s^{-1} due the interaction with the surrounding interstellar gas, within which it appears to be almost completely dispersed.

The SNRs are observable across the whole electromagnetic spectrum. However, the hallmark of these objects is the emission in the radio band where the bulk of the 295 or so Galactic SNRs discovered so far is identified (Green, 2017). Indeed, before the advent of radio astronomy, the only known SNRs were the historical Crab Nebula and Kepler's SNRs, thanks to their optical nebulosities. However, when in the early 1950s the development of radio observation techniques opened the era of radio astronomy, it was soon realized that a substantial population of extended objects with non-thermal radio spectra (power-law, flux $S_\nu = \nu^{-\alpha}$ with $\alpha \sim 0.5$) is present in the Galaxy. The non-thermal nature of the radio emission was debated and the answer was proposed

by Shklovskii (1960), which introduced the hypothesis of a synchrotron radiation produced by the remnants of unseen SNe. Later, in 1957, the detection of polarization in the Crab Nebula by Mayer et al. (1957) confirmed the synchrotron nature of the radio SNRs emission, produced by ultra-relativistic electrons gyrating in a magnetic field. At present a catalogue of the SNRs discovered in our Galaxy is compiled and constantly updated by Green (2017), wherein the ~95% of these are detected as radio sources. In order to explain the radio spectrum of SNRs through the synchrotron emission mechanism it is necessary to assume the presence in these sources of a population of relativistic electrons, well represented by a power-law function $N(E) = KE^{-s}$ [particles cm^{-3} erg^{-1}] (Reynolds, 2008). The power law of the SNRs radio spectrum reflects the trend of the energy spectrum of the relativistic particles responsible for the observed synchrotron radio emission, and the corresponding spectral indexes are related according to the function: $\alpha = (s-1)/2$. An integrated radio spectral index with a mean value close to $\alpha \sim 0.5$ has been observed in the majority of known SNRs, implying a primary particles index of $s \sim 2$.

The synchrotron emission process is efficient if the particles have energies in the GeV range, at least six orders of magnitude higher than the energies expected from thermalization behind a shock of speed 10^3 km s^{-1}, as inferred in historical remnants. These high energies are typical of those charged particles historically referred to as the Cosmic Rays (CRs). These are mostly protons, but ions of several elements in the periodic table are represented, as well as electrons and a few positrons and antiprotons (Reynolds, 2008). It has been shown that electrons with these energies cannot result from the simple compression of the ISM due to the remnant shock. Indeed the emission spectrum obtained on the basis of an adiabatic shock compression ratios of order four is not consistent with those observed for the diffuse Galactic synchrotron background. Furthermore, many SNR shells, in particular in the young remnants, have a radio brightness far too high to be explainable simply by compression of interstellar electrons and magnetic field. For these reasons the electrons that produce the synchrotron emission in the SNRs must be subjected to a different, and most efficiently, acceleration mechanism. The most accredited theory to explain the particle acceleration to ultra-relativistic energies is the so called *diffuse shock acceleration* (DSA) proposed by Bell (1978a), Bell (1978b) and Blandford & Eichler (1987). This acceleration mechanism (also known as Fermi I mechanism) is based on the possibility for particles to gain energy as result of the multiple crossing through a shock wave.

Different astrophysical objects are characterized by strong shock waves (SNRs, active galactic nuclei, pulsars and pulsar wind nebulae), which can accelerate the particle of the surrounding medium up to $\sim 10^{15}$ eV in the case of heavier particle and $\sim 10^{12}$ eV for electrons. Indeed, in this latter case the maximum energy achievable is limited by the the energy losses induced by the synchrotron emission from the electrons captured by the ISM magnetic field. These electrons and heavier particles are responsible for the non-thermal emissions of SNRs, both in the radio and gamma-ray bands. The gamma-ray emission results from both the hadronic process of π^0 mesons decay, which is a direct signature of Cosmic Rays accelerated in SNR, and leptonic

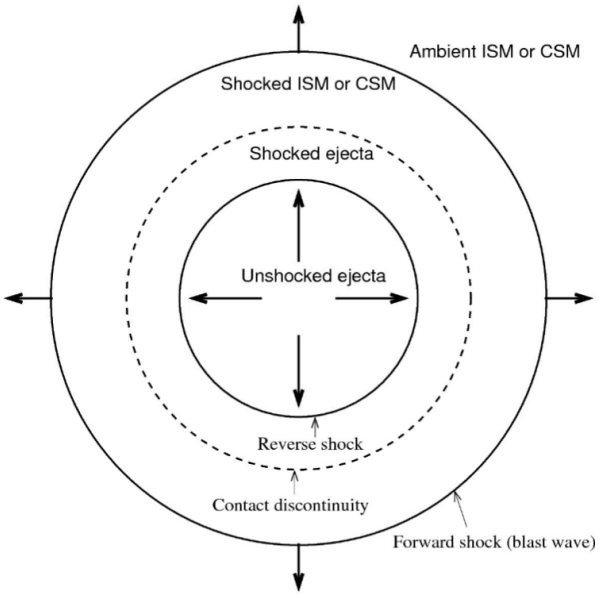

Figure 1.1: Schematic representation of the two-shock structure of a SNR in the free-expansion phase (Reynolds, 2008).

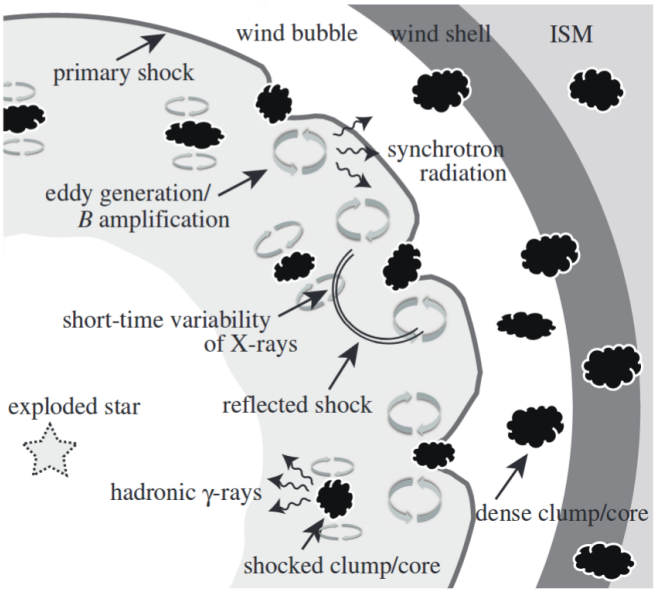

Figure 1.2: Schematic picture of the shock–cloud interaction model (Inoue et al., 2012).

processes such as Bremsstrahlung and Inverse Compton (IC). The latter are produced by the radio-electrons interacting with ambient photons, and for this reason the observed bumps in the related gamma-ray spectra are bound to the synchrotron spectral slope and to the cut-off in the radio domain. In addition to the synchrotron emission, electron acceleration mechanisms can shape the radio spectra in specific ways, especially at high radio frequencies. These features are closely linked to the specific SNR evolutionary stage and the peculiar conditions of the local ISM interacting with the SNR, which will be discussed in the following paragraph.

1.1 SNR evolution

The evolution of a SNR starts from the initial interaction of the SN ejecta with the circumstellar material (CSM) and ends with the final dispersion of the remnant into the ISM. A simplified scheme of the SNR evolution was proposed by Woltjer (1972) and consists of four phases:

- **Free expansion phase**
  In Fig.1.1 we report a schematic representation of the structure of a SNR in this early phase of its evolution. A strong shock wave, resulting from the SN explosion, accelerates the stellar ejecta at highly supersonic speed into the CSM, namely the material modified by

the progenitor star typically characterized by some anisotropies. This interaction leads to a deceleration of the shock wave, also called *forward shock* in this phase, and at the same time the shocked CSM is heated to X-ray emitting temperatures. Between the shocked CSM and the shocked ejecta there is the so called *contact discontinuity*, which is characterized by a roughly constant pressure. In this early phase of the SNR evolution the expansion is very rapid and causes the adiabatic cooling of the ejected material. In these conditions, also a small deceleration results in a velocity difference that is greater than the sound speed in the unshocked ejecta, leading to the formation of a *reverse shock*, which propagates inward, causing the shock and the heating of the internal ejecta (Reynolds, 2017). When both forward and reverse shock are present, the SNR is in its *free expansion phase*, whose duration goes from hundreds to thousands of years (Dubner & Giacani, 2015). When the accumulated mass of the CSM compressed between the forward shock and the contact discontinuity equals the ejected mass of stellar material, the pressure of the compressed CSM is not negligible and affects the expansion of the SNR, and the free expansion phase ends.

- **Adiabatic expansion or Sedov-Taylor phase**
  In this phase the SNR expansion is driven by the thermal pressure of the hot gas. The reverse shock heats the interior of the SNR so much that the gas results completely ionized. Since there is no recombination, the losses of energy by radiation are very small and the cooling of the gas is only due to the expansion. Under these conditions the SNR expands and cools adiabatically until it reaches a critical temperature of about 10^6 K, at which the recombination of the interior gas starts and the electrons can lose their excitation energy by radiation. When the radiative losses of energy become significant, an efficient radiative cooling of the gas starts with the consequent decrease of the thermal pressure in the post-shock region. Then the expansion slow-down and the SNR leaves this phase.

- **Radiative phase**
  In this phase the gas behind the shock radiates away a significant amount of energy and becomes much more compressible. However a further compression could be limited by other mechanisms, perhaps due to the action of the magnetic field, which lead to the rise of the overall shock compression ratio. This phase is also called "snow plough" since more and more interstellar gas is accumulated beyond the swept-up mass and it is much larger than the ejected stellar material (Dubner & Giacani, 2015). In this phase of the evolution the SNRs are generally so large that their expansion continues in the ISM, which is generally not uniform. Indeed it can be characterized by dense molecular clouds or "blowouts" located into much less dense regions. The cosmic-ray ions that escape from the acceleration region can produce gamma-rays through π^0 decay when they cross the dense material, due to the inelastic collisions with the thermal gas. For this reason the ISM inhomogeneities, which in this phase are included in the SNR structure, typically result in gamma-ray emitting

regions. As shown in Fig.1.2, the SNRs appear in this phase as large and complex objects that are typically characterized by large variations in conditions across the different SNR regions (Reynolds, 2017).

- **Dispersion**
  In the last phase of SNRs evolution the shock speed drops below the local ISM sound speed and the SNR disperses into the ISM.

The characteristic SNRs radiation is highly dependent on the evolutionary stage. In the very early phase (free expansion) "prompt" X-ray and radio emissions are related to the original SN event and the interaction of the SNR with the CSM. Immediately after, the interstellar gas that is accumulated behind the strong shock front is compressed and heated to X-ray-emitting temperatures. In addition to the thermal electrons that constitutes the peak of the electron energy distribution, a small fraction of electrons are accelerated at the shock to relativistic energies on the basis of the DSA, which will be discussed in Section 2.3. This power-law non-thermal electron population emits synchrotron radiation at radio wavelengths, and the emission can be detected also in the X-ray band. The optical emission is instead faint and it is observable only in few strong lines of hydrogen and possibly helium. At this early stage infrared radiation is also observable. It is produced by dust grains heated by collisions with hot gas. Then, in the free-expansion phase SNRs primarily emit radio synchrotron and thermal X-ray radiation from the gas behind both the blast wave and the reverse shock. When the SNRs reach the Sedov-Taylor phase, the emission is dominated by non-thermal radio and X-ray radiation from the shocked CSM/ISM, even if X-ray emission from the interior may still be present from enhanced abundances of heavy elements, which were previously formed at the reverse shock. Also infrared continuum from heated grains can still be produced. The spectral energy distribution (SED) of a SNR changes with the beginning of the radiative cooling. In this phase the SNRs present an optically bright spectra, but the main observational signature is represented by non-thermal synchrotron emission from electrons with GeV energies. It is important to note that the cooling times are a strong function of density. This implies that, as shown in Fig.1.2, in the case of an evolved SNR expanding in inhomogeneous ISM, some regions like "clumps" or "cloud" become radiative sooner than others making the emission from the SNRs inhomogeneous. Furthermore, the synchrotron radiation is enhanced in this phase due to the high compression ratios that characterize the radiative shock waves. Apart from the synchrotron emission, the relativistic electrons can emit up to GeV and even TeV energies as a result of upscattering of photon fields (Inverse Compton emission) or interaction with thermal ions (Bremsstrahlung emission). In addition to these leptonic contributions, hadronic process characterize the GeV-TeV spectra of SNRs in the radiative phase of their evolution. This emission is related to the relativistic protons accelerated at the shock, which do not directly radiate, but trigger the gamma-ray emission produced by neutral pions (π^0) decay. Indeed, the π^0 may be produced by inelastic scattering between relativistic protons and thermal ions. The π^0 typically decays into pairs of gamma photons, which are a direct signature of CR protons accelerated in

SNRs. The question about the leptonic or hadronic origin of the gamma-ray emission from SNRs is still debated, also in relation to the origin of different CR populations in SNRs. Further details about both leptonic and hadronic emission processes will be provided in the Section 1.4.

1.2 Morphological classification of SNRs

The radio emission is the most common identifier of SNRs and for this reason they are often classified accordingly to their radio morphology (Dubner & Giacani, 2015). The study of the radio morphology provides crucial indications about the nature and the evolution of the SNRs in the ISM. In the following, I will be briefly described the four main categories with the help of a radio SNR image associated with each of them.

- **Shell-type SNRs**
  The morphology of these SNRs is characterized by a well distinguishable limb brightened shell corresponding to the material ejected during the SN, which is subsequently swept up by surrounding ISM/CSM material. The dimension of the shell is related to the expanding shock wave produced in the SN explosion. The bright radio emission is due to synchrotron radiation from electrons accelerated at the shock front (Fig.1.3).

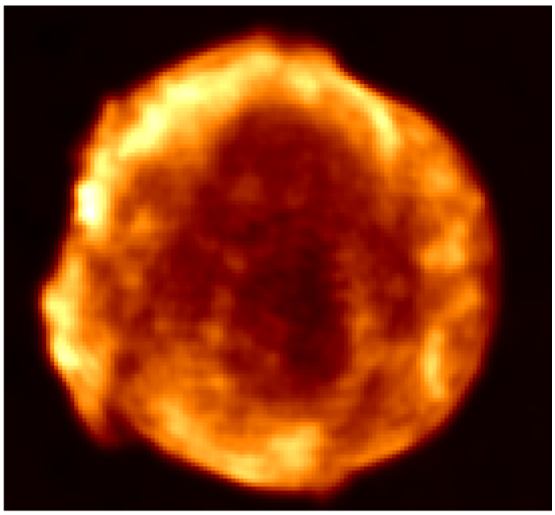

Figure 1.3: Radio image of the Tycho's remnant at 1.5 GHz in linear color scale as extracted from Morlino & Caprioli (2012).

- **Filled-center or plerions**
  Plerions are bubbles of relativistic particles inflated by the pulsar's relativistic wind. The bright radio emission arises from the so-called Pulsar wind Nebula (PWN), which is produced by the interaction between the wind of relativistic particles accelerated by the pulsar and the surrounding medium. The presence of high-energy particles and strong magnetic fields make these SNRs efficient engines for cosmic-ray acceleration up to TeV energies. For this reason the non-thermal emission produced in the PWN can be observed from radio to the highest energy gamma-rays currently detectable. An X-ray emission is also detected with a size generally shorter than their radio and optical size, due to the smaller synchrotron lifetimes of the higher-energy photons (Safi-Harb, 2012). It is interesting to note that the evidence of the PWN does not always imply the detection of the related pulsar (Fig.1.4).

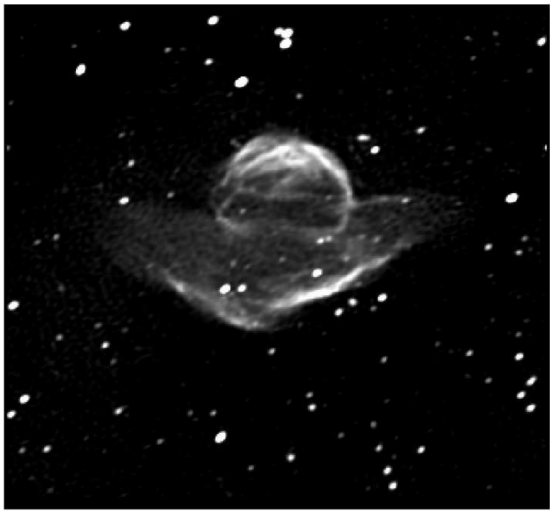

Figure 1.4: The filled-center SNR VRO 42.05.01 as observed in the radio band at 1.4 GHz (Dubner & Giacani, 2015).

- **Composite**
  The composite SNRs are characterized by synchrotron emission from a bright shell and a PWN, which is produced by the wind of relativistic particles that spiral in the magnetic field, and emits synchrotron radiation (Fig.1.5). The interaction of the PWN with its host SNR significantly modifies the relativistic particle population that eventually escapes into the ISM, and it may also give rise to the low-energy particle excess that produces gamma-ray emission through inverse-Compton scattering (Temim et al., 2015).

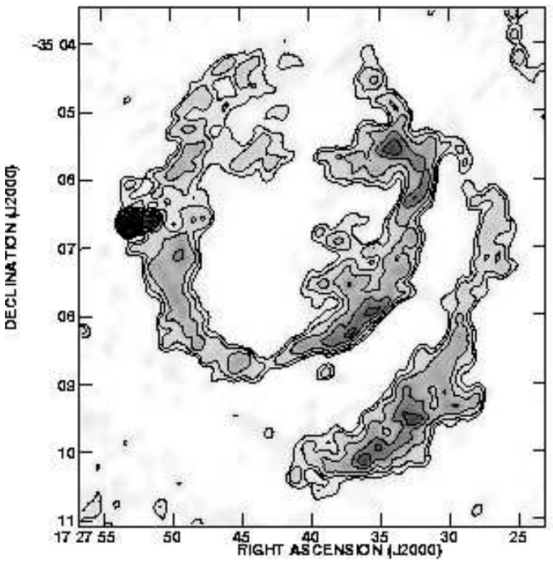

Figure 1.5: The radio image of the composite SNR G352.7-0.1 resulting from VLA observations at 4.8 GHz (Giacani et al., 2009).

- **Mixed-morphology**
  These SNRs are characterized by a highly filamentary radio shell (synchrotron emission) and a central thermal X-ray emission. The morphology of these SNRs suggests a strong interaction between the remnant with both atomic and molecular clouds. This aspect, combined with the observed gamma-ray emission of hadronic emission, made these object very interesting within the framework of the controversy leptonic/hadronic origin of the gamma-ray emission from SNRs (Fig.1.6).

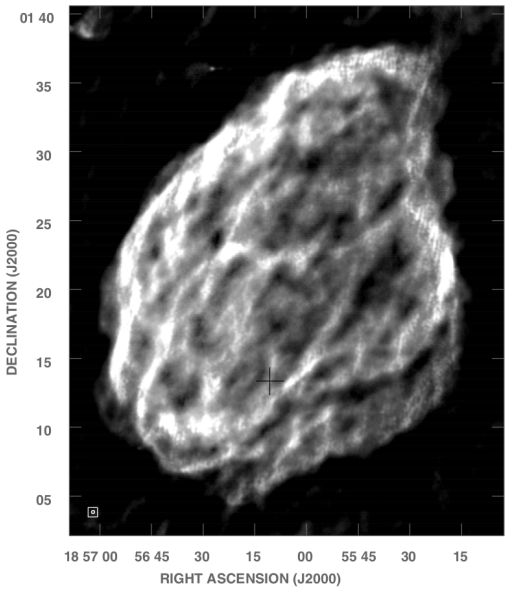

Figure 1.6: VLA radio image of the mixed-morphology SNR W44 at 324 MHz. The black plus sign indicates the position of the related pulsar (Castelletti et al., 2007).

1.3 Diffusive shock acceleration mechanism

For many years it was thought that the high energy of cosmic-ray electrons derived from SNe. These electrons could in principle simply be borrowed from the interstellar medium and compressed in the remnant shock wave. However, cosmic ray physicists realized quickly that the radiation produced by these particles in young SNRs could not be explained by simply borrowing and compressing of relativistic electrons from the cosmic-ray population in the ISM, but newly accelerated electrons are required (Reynolds, 2008).

From 1978, the particular scheme called DSA process has become increasingly attractive to explain, through the first order Fermi acceleration mechanism, the presence of high energy particles as the product of the passage of strong collisionless shock wave in the ISM. Indeed, according to this theory, the particles are accelerated systematically by scattering of the converging flow on either side of the shock front and, in the case of a SNR, they can absorb the kinetic energy of the surrounding blast wave with quite high efficiency (Blandford & Eichler, 1987). The model used to explain the DSA mechanism is that of a strong shock propagating through a diffuse medium, which is well represented by the shock waves propagating through the ISM ahead of the supersonic SNR shells. The shock wave occurs when a perturbation in a gas is propagated away from its source at a velocity greater than the speed of sound in the propagation medium. From this point of view a shock wave is no more than a discontinuity between the regions behind and ahead of the disturbance, the latter region having no prior knowledge of its imminent arrival

(Longair, 2011). This is what happens typically in the shell-like SNRs that are constituted by the envelope of the progenitor star which is heated to a very high temperature and ejected with supersonic velocity as a result of a SN explosion. The high velocity reached by the envelope leads to the formation of a shock front ahead of the expanding sphere. An abrupt discontinuity between the sphere of expanding gas and the swept-up material is associated with the shock wave. The discontinuity is represented by "the piston" in Fig.1.7.
In order to understand the physical proprieties of the shock wave we consider a system similar to that of SNRs, illustrated in Fig.1.8, which is constituted by two regions of fluid flow between which an abrupt discontinuity is present. As shown in Fig.1.8a, ahead of the shock wave the gas is stationary and it is characterized by a pressure P_1, density ρ_1 and temperature T_1; while the gas moves supersonically (with speed $U > c_1$, where c_1 is the speed of sound in the stationary medium) behind the shock with pressure P_2, density ρ_2 and temperature T_2. In order to describe the passage of the gas through the shock wave is convenient to refer to a reference frame in which the shock wave is stationary. How Fig.1.8b shows, in this representation the shock wave is at rest and is going through the undisturbed gas, which instead propagates at velocity $v_1 = |U|$. When the gas flows towards the discontinuity its velocity became $v_2 = 2|U|$. The strength of the shock is defined by the ratio $M = U/c$ also known as *Mach number*. Taking into account that: 1) the mass is conserved on passing through the discontinuity, 2) the energy passing per unit time through unit area parallel to v_1 is continuous, and 3) the momentum flux through the shock wave should be continuous, we have, respectively:

$$\rho_1 v_1 = \rho_2 v_2 \tag{1.1}$$

$$\rho_1 v_1 \left(\frac{1}{2}v_1^2 + w_1\right) = \rho_2 v_2 \left(\frac{1}{2}v_2^2 + w_2\right) \tag{1.2}$$

$$p_1 + \rho_1 v_1^2 = p_2 + \rho_2 v_2^2 \tag{1.3}$$

In Eq.1.2 we considered the energy flux through the surface normal to $\mathbf{v}$ and $w = \epsilon_m + pV$ is the enthalpy per unit mass (ϵ_m is the internal energy per unit mass and V is the volume per unit mass). We consider the medium through which the shock wave propagates as a perfect gas with a ratio of specific heat capacities Γ and with specific volume V. If the shock is very strong ($M \gg 1$), from the equations 1.1, 1.2 and 1.3 we have:

$$\frac{p_2}{p_1} = \frac{2\Gamma M_1^2}{(\Gamma + 1)} \tag{1.4}$$

$$\frac{\rho_2}{\rho_1} = \frac{(\Gamma + 1)}{(\Gamma - 1)} \tag{1.5}$$

$$\frac{T_2}{T_1} = \frac{2\Gamma(\Gamma - 1)M_1^2}{(\Gamma + 1)^2} \tag{1.6}$$

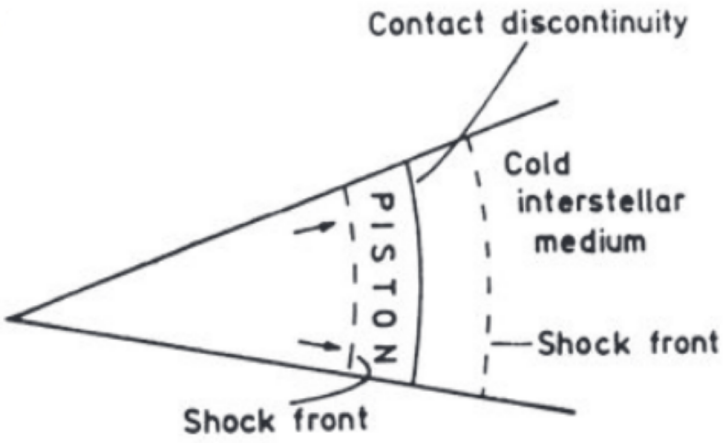

Figure 1.7: Schematic illustration of a supersonically expanding sphere of hot gas. We can imagine the sphere of ejected gas as a piston that heats and compresses the cold interstellar gas. A shock front occurs between the piston and the cold ISM with which it is associated a contact discontinuity. As the sphere expands into the interstellar gas, it is decelerated and matter inside the hot sphere begins to pile up at the contact discontinuity between the shocked interstellar gas and the interior of the sphere. An internal shock front forms as matter piles up at the interface and the temperature of the gas inside the sphere cools (Longair, 2011).

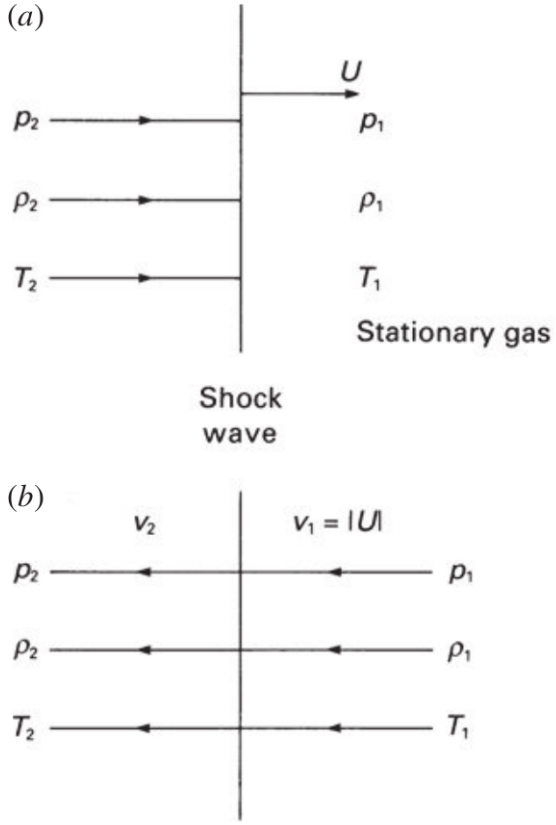

Figure 1.8: (a) A shock wave propagating through a stationary gas at a supersonic velocity U with respect to the sound velocity in the stationary medium c_1. (b) The flow of gas through the shock front in the frame of reference in which the shock front is stationary (Longair, 2011).

These important relations show us that, under the conditions of a very strong shock, the gas that passes through the shock front may be heated and accelerated up to arbitrarily large values of temperature and pressure, while the density presents an upper limit defined by the *compression ratio* $r = \frac{\rho_2}{\rho_1} = \frac{(\Gamma+1)}{(\Gamma-1)}$. This process of heating and acceleration occurs over a physical scale of the order of a few mean free paths of the atoms, and for this reason the shock front is thought to be very narrow.

Let us now have a look at how this process applies to the SNR shocks. In the case of SNRs the material ejected reaches velocities of order of 10^4 km s^{-1} and the shock wave propagates through the ISM at a highly supersonic velocity $U \gg c_s$ (where c_s is the sound speed in the ambient medium). This ensures that the aforementioned condition on the Mach number ($M \gg 1$) is satisfied for these objects. Furthermore, if we assume that the gas is mono-atomic or fully ionised ($\gamma = \frac{5}{3}$) the maximum value of the compression ratio is $\frac{\rho_2}{\rho_1} = 4$, which implies the relation $v_2 = \frac{1}{4}v_1$ between the velocity of the gas respectively in front of and behind the shock. Furthermore, two important conditions of this system must be considered to understand the particle acceleration process: there is a flux of high energy particles both in front of the shock and behind it; the particles upstream and downstream of the shock have a speed close to that of light. A schematic representation of this system is shown in Fig.1.9. In order to understand how the particles gain energy after multiple crossing through a shock wave, we will separately consider the two cases in which the particles upstream and downstream are respectively at rest. As shown in Fig.1.9c and Fig.1.9d, when crossing the shock from either side, the particle sees plasma moving toward it at a velocity of $V = \frac{3}{4}U$. We consider the system in the reference frame in which the upstream gas is stationary and related high energy particles have an isotropic velocity distribution, while the downstream gas flows through the shock wave at a velocity of $V = \frac{3}{4}U$ relative to the upstream gas (Fig.1.9c). Each downstream particle gains a little amount of energy when cross the shock wave and collides the upstream gas. The energy acquired by the particles is defined by *first-order Fermi acceleration mechanism*. We indicate with E the energy of a particle ahead the shock in the upstream reference frame. When the particle goes through the shock front and passes into the downstream region, its energy in the in the reference frame in which the downstream gas is at rest is:

$$E' = \gamma(E + V p_x) \tag{1.7}$$

Assuming the particles propagate at speeds close to that of light, while the velocity of the shock is non-relativistic, we have that:

$$\gamma = \left(1 - \frac{V^2}{c^2}\right)^{-\frac{1}{2}} \sim 1 \tag{1.8}$$

and

$$p_x = \gamma(p\cos\theta + \frac{VE}{c^2}) \sim p\cos\theta = \frac{E}{c}\cos\theta \tag{1.9}$$

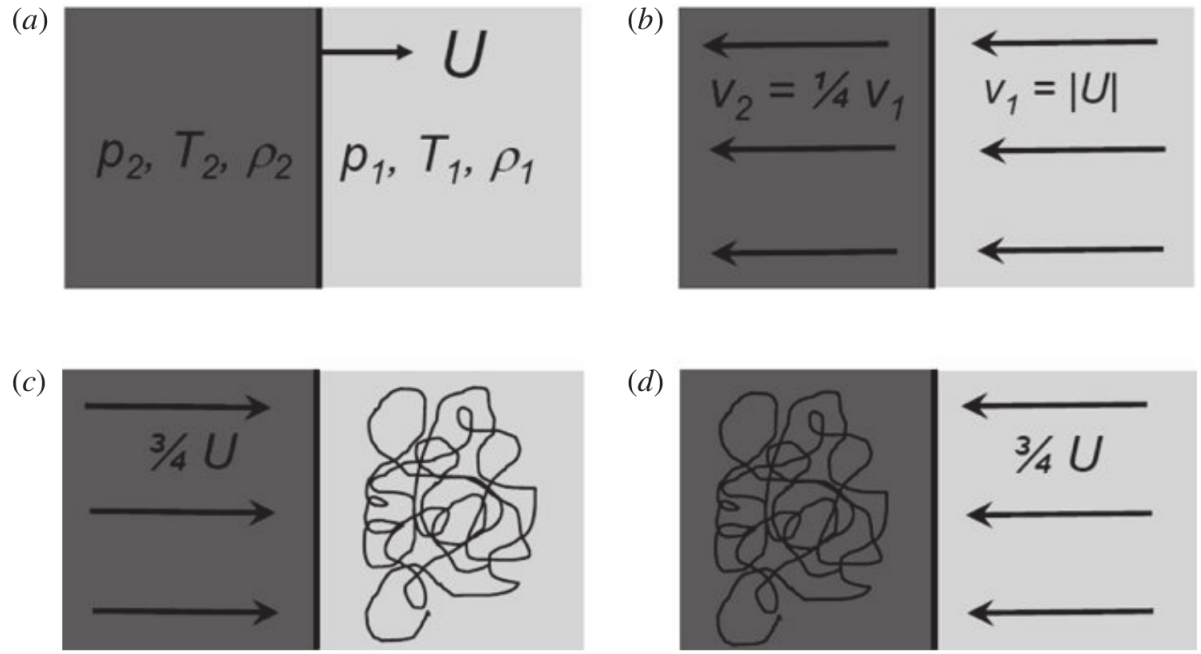

Figure 1.9: Schematic representation of the dynamics of high energy particles in the vicinity of a strong shock wave as reported by Longair (2011) for different reference frame. (a) A strong shock wave propagating at a supersonic velocity U through stationary interstellar gas. (b) The flow of interstellar gas in the vicinity of the shock front in the reference frame in which the shock front is at rest. (c) The flow of gas as observed in the frame of reference in which the upstream gas is stationary and the velocity distribution of the high energy particles is isotropic. (d) The flow of gas as observed in the frame of reference in which the downstream gas is stationary and the velocity distribution of high energy particles is isotropic.

hence:

$$\Delta E = E' - E = \frac{VE}{c}\cos\theta \tag{1.10}$$

$$\frac{\Delta E}{E} = \frac{V}{c}\cos\theta \tag{1.11}$$

Where θ is the pitch angle, namely the angle between the initial direction of the particle and the normal to the surface of the shock front. The probability that a particle will cross the shock with an angle of incidence between θ and $\theta + \delta\theta$ is $p(\theta) = 2\cos\theta\sin\theta\delta\theta$ (by considering $\theta \in [0, \frac{\pi}{2}]$). Therefore, we can obtain the energy increase for one shock crossing:

$$\langle\frac{\delta E}{E}\rangle = \frac{V}{c}\int_0^{\frac{\pi}{2}} 2\cos\theta\sin\theta\delta\theta = \frac{2}{3}\frac{V}{c} \tag{1.12}$$

We would achieve the same result if we consider the opposite process in which the upstream reference frame is a rest and the particles diffusing from behind the shock (Fig.1.9d), because the

gas appears to be moving towards particles that cross the shock front at equal velocities from each side. Taking into account this symmetry, the energy gain of each particle that completes a round trip is given by:

$$\langle \frac{\delta E}{E} \rangle = \frac{4}{3}\frac{V}{c} \tag{1.13}$$

and the energy change is given by:

$$\beta = \frac{E}{E_0} = 1 + \frac{4}{3}\frac{V}{c} \tag{1.14}$$

Furthermore, it should be noted that there are no crossings in which the particles lose energy, since the collisions are always head-on at the shock front. In order to describe the energy spectrum of the particles accelerated in SN shock fronts on the basis of the first-order Fermi acceleration mechanism, we define the probability P for a particle to remain within the accelerating region after one collision and the average energy of the particle after one collision is $E = \beta E_0$. Under these assumptions, if we looked the system after a number k of collisions we would see that there are $N = N_0 P^k$ particles with energy $E = E_0 \beta^k$, and by eliminating k we obtain:

$$\frac{\ln(N/N_0)}{\ln(E/E_0)} = \frac{\ln P}{\ln \beta} \tag{1.15}$$

from which:

$$\frac{N}{N_0} = \left(\frac{E}{E_0}\right)^{\frac{\ln P}{\ln \beta}} \tag{1.16}$$

From this relation we obtain the following power spectrum:

$$N(E)dE = constant \times E^{-1+\frac{\ln P}{\ln \beta}} dE \tag{1.17}$$

The rate of particles crossing the shock from either direction is $\frac{1}{4}nc$ (where n is the number density of energetic particles averaged over velocities and angles), while the rate of particles removed from downstream region is $nV = \frac{1}{4}nU$. It is then possible to define the fraction of particles lost per unit time as $\frac{\frac{1}{4}NU}{\frac{1}{4}Nc} = \frac{U}{c}$ and, consequently, the fraction of particles remaining after one cycle is $P = 1 - \frac{U}{c}$. Bearing in mind that we assumed a non-relativistic motion ($U \ll c$), we obtained:

$$\ln P = \ln\left(1 - \frac{U}{c}\right) = -\frac{U}{c} \tag{1.18}$$

$$\ln \beta = \ln\left(1 + \frac{4V}{3c}\right) = \frac{4V}{3c} = \frac{U}{c} \tag{1.19}$$

Then we can rewrite the energy spectrum as:

$$N(E)dE \propto E^{-2}dE \tag{1.20}$$

In condition of strong shocks with a compression ratio of $r = 4$ the DSA mechanism provides a synchrotron spectral index of $\alpha = \frac{s-1}{2} = 0.5$, which is consistent with the mean spectral index observed for Galactic SNRs. The characteristics that make the DSA the dominant acceleration mechanism within the astrophysical thinking are essentially two:

- the DSA theory provides an increase of energy of $\frac{\Delta E}{E} \propto \frac{V}{c}$ associated with one particle passage through the shock front. If we consider a single particle interaction with the shock wave, the DSA is a more efficient acceleration mechanism than the second order Fermi process, which provides an energy gain $\propto \left(\frac{V}{c}\right)^2$. Furthermore, the DSA theory provides a multiple transition of one charge particle through the shock discontinuity from upstream and downstream regions and vice versa, each of which is associated with a gain of energy (Urošević, 2014). Instead, the second order Fermi mechanism provides both head-on and following collisions, by means of which the particles lose energy.

- The DSA theory predicted a power-law energy distribution of accelerated particles in the form $N(E) \propto E^{-s}$, with an energy index of $s = 2$. This value was confirmed by the observations, which demonstrated that approximately 20% of all observed SNRs show a radio spectra with $\alpha = 0.5$ (Green, 2014).

However the DSA mechanism alone cannot explain the curved SNR radio spectra and the linear spectra (in the log−log representation) for which $\alpha \neq 0.5$. Indeed, as shown in Fig.1.10, the more and more studies of these extended sources demonstrate that only about one fourth of the 294 SNRs catalogued in Green (2014) have a spectral index in the range 0.5−0.6 (Dubner & Giacani, 2015). The spread of order 0.2 observed in the spectral index distribution of the SNRs could represent a problem for the DSA theory. The observational data show that young SNRs are characterized by steeper spectral indexes, like Cas A and Tycho SNR that have $\alpha = 0.77$ and $\alpha = 0.58$ respectively, while the DSA theory provide flatter spectra ($\alpha \leq 0.5$) for the SNRs in the free-expansion and early Sedov phases of evolution. In order to explain the steeper spectra observed, it was assumed the presence of shocks with low Mach number, but only few old SNRs would be expected to have such weak shocks (Reynolds, 2011). On the other hand, second-order Fermi mechanism and non-linear shock acceleration could explain the steeper spectra observed. Furthermore, it was noted that SNRs often show more complicated spectra than a simple power law. For instance, some historical remnants (like IC443, 3C391 and 3C396, Onić et al. 2012) show radio spectra possibly indicating a concave-up curvature (Reynolds and Ellison 1992), which could be explained by efficient shock acceleration mechanism or by other concurring emission mechanisms like thermal bremsstrahlung in case of expansion in high density environment (Onić, 2013), or spinning dust emission (Onić et al., 2017). The steepening could be also associated

with the contribute of the secondary electrons produced in inelastic proton-proton collisions, whose synchrotron emission could be dominant in the case of SNRs interacting with dense clouds (Cardillo et al., 2016). Another explanation could arise from the synchrotron emission contribute from relativistic particles generated by the pulsar that interacts with the SNR shell. Other SNRs show a low-frequency radio steepening that could be due to the contribute of different precesses like thermal absorption or synchrotron self-absorption.

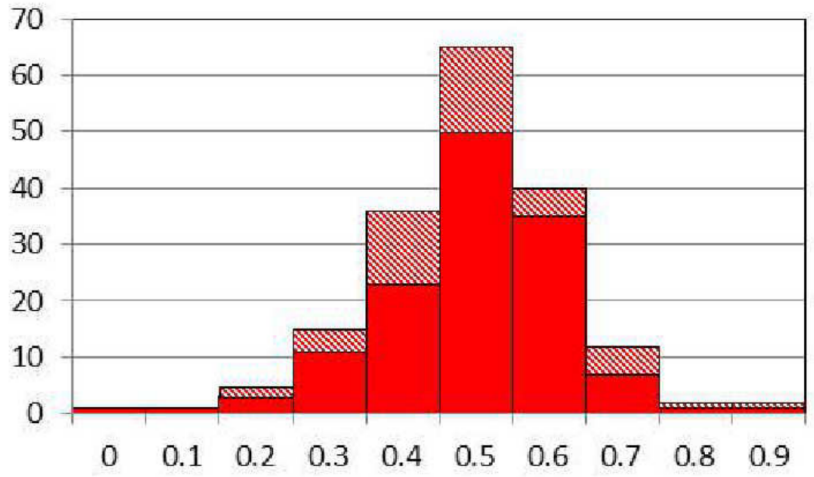

Figure 1.10: Spectral-index distribution of the SNRs reported in the Green's catalogue , in bins of 0.1 in α. The solid bars correspond to adequately measured radio spectra, while the shadowed ones to SNRs with uncertain spectral index measurements (Dubner & Giacani, 2015).

1.4 Radiative processes in SNRs

The strong shock waves associated with SNRs and the huge amount of energy that is transferred to shocked gas, provide populations of relativistic ions and electrons that produce the continuum observed radiation in these extended sources both in the radio and gamma-ray bands. As shown in Fig.1.11, the characteristic emission of SNRs from keV to TeV photon energies is produced by both leptonic (synchrotron radiation, non-thermal Bremsstrahlung and IC scattering) and hadronic processes (π^0 decay).

In the radio band, the SED of SNRs is characterized by synchrotron emission from relativistic electrons accelerated into the magnetic field by a diffusive shock mechanism. Assuming a magnetic field of the order of 10 μG, which typically arises by compression of the ISM in SNR shocks (Wielebinski & Beck, 2005), it is expected that 0.5−50 GeV electrons emit the observed synchrotron radiation in the 0.01−100 GHz frequency range. The gamma-ray emission results from both hadronic (π^0 mesons decay) and leptonic (Bremsstrahlung and Inverse Compton, IC) processes.

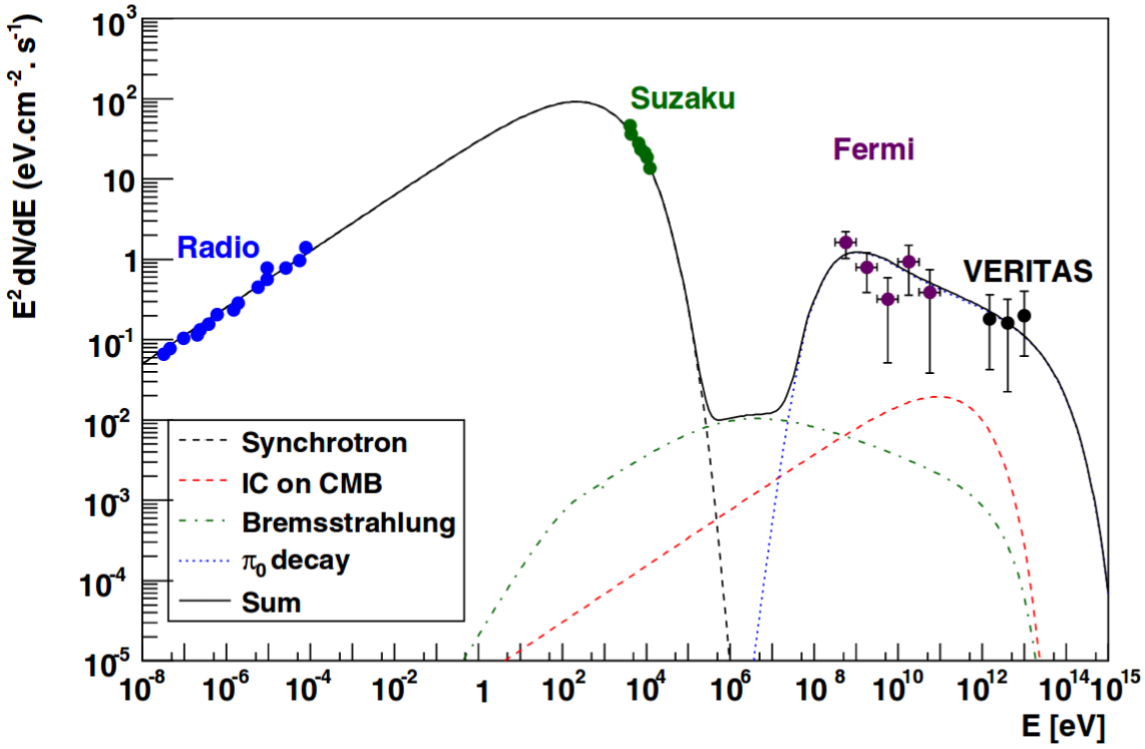

Figure 1.11: Broadband spectral energy distribution model of Tycho SNR from radio to γ-ray band, including the spectral contribution of the four basic radiative processes taking place in SNRs (Giordano et al., 2012). The dotted line indicate the emission associate with: synchrotron (black), Inverse Compton (red), Bremsstrahlung (green) and π^0 decay (blue).

- **Synchrotron radiation**

  Among all emission mechanisms, the synchrotron is the only one firmly identified in SNRs, producing photons only up to a few tens of keV. In a uniform magnetic field, an high energy electron with velocity v moves in a spiral path at a constant pitch angle θ. If we consider a particle in the ultra-relativistic limit ($v \rightarrow c$) the total loss rate is:

  $$-\left(\frac{dE}{dt}\right)_{Synch} = 2\sigma_T c U_{mag} \gamma^2 \sin(\theta)^2 \tag{1.21}$$

  Where $U_{mag} = \frac{B^2}{2\mu_0}$ is the energy density of the magnetic field, σ_T is Thomson cross-section and $\gamma = (1 - \frac{v^2}{c^2})^{-\frac{1}{2}}$ is the Lorentz factor of the electron. The irregularities in the magnetic field distribution or the streaming instabilities imply that the pitch angle distribution is likely to be randomized. On these bases, the distribution of pitch angles for a population of high energy electrons is expected to be isotropic. We note also that each high energy electron is randomly scattered in pitch angle several times during its lifetime. The average energy loss rate is obtained by averaging over an isotropic distribution of pitch angles

$P(\theta)d\theta = \frac{1}{2}\sin\theta d\theta$:

$$-\left(\frac{dE}{dt}\right)_{Synch} = 2\sigma_T c U_{mag}\gamma^2 \frac{1}{2}\int_0^\pi \sin\theta^3 d\theta = \frac{1}{4}\sigma_T c U_{mag}\gamma^2 \tag{1.22}$$

It can also be demonstrated that the spectrum of synchrotron radiation is quite sharply peaked near the critical frequency ν_c

$$\nu_c = \frac{3e}{4\pi mc} B\left(\frac{E}{mc^2}\right)^2 \tag{1.23}$$

Consider the case of a power-law electron distribution $N(E)dE = kE^{-s}dE$ (where $N(E)dE$ is the number density of electrons in the energy interval from E to $E+dE$). Since the breadth of the power-law electron energy spectrum is certainly less narrow than the spectrum of synchrotron radiation, it can be assumed that an electron of energy E radiates away its energy at the critical frequency ν_c. We can therefore express the energy radiated in the frequency range ν to $\nu+d\nu$ by electrons with energies in the range E to $E+dE$ as:

$$J(\nu)d\nu = \left(-\frac{dE}{dt}\right)N(E)dE \tag{1.24}$$

Where the energy may be express as $E = \gamma m_e c^2$. By considering the Eq.1.21, the emissivity may be expressed in terms of B and ν as:

$$J(\nu) = constants \quad \left(\frac{p+1}{2}\right)\nu^{-\frac{s-1}{2}} \Longrightarrow J(\nu) \propto \nu^{-\alpha} \tag{1.25}$$

where α is the spectral index of the synchrotron spectrum, which is determined by the slope of the electron energy spectrum s, rather than by the shape of the emission spectrum of a single electron. The quadratic nature of the relation between the emitted frequency and the energy of the electron (Eq. 1.23) accounts for the difference in slopes of the emission spectrum and the electron energy spectrum $\alpha = \frac{(s-1)}{2}$ (Longair, 2011).

- **Inverse-Compton Scattering**

  The inverse Compton process occurs when ultra-relativistic electrons scatter on low energy photons (the initial energy of the photon should be less than the electron energy in the electron's rest frame) that gain energy at the expense of the kinetic energy of the electrons. If a relativistic electron is characterized by a Lorentz factor γ, the photon will be redirected along the electron's direction of motion and its energy will increase by a factor γ^2. In the Thomson regime, in which the photons have low energy ($\epsilon_{ph} < \frac{m_e c^2}{\gamma}$), the cross section of the process is $\sigma_T = \frac{8\pi r_e^2}{3} = 6.65 \times 10^{25}\text{cm}^2$ (where r_e is the classical electron radius). The loss rate associated with the IC scattering is:

$$\left(\frac{dE}{dt}\right)_{IC} = \frac{4}{3}\sigma_T c u_{rad}\gamma^2 \tag{1.26}$$

where u_{rad} is the energy density. We can note that the form of the loss rate expression is the same in the case of IC and synchrotron processes (Eq.1.21). In particular, the synchrotron and IC losses have the same electron-energy dependence ($\frac{dE}{dt} \propto \gamma^2$), and this implies that the IC spectrum produced by a power-law distribution of electron energies is described by a power-law function with spectral index $\alpha = \frac{(s-1)}{2}$ (were s is the spectral index of the electron energy spectrum).

- **Non-thermal Bremsstrahlung**
  The non-thermal Bremsstrahlung process involves radiation emission from the acceleration of high-relativistic electrons by Coulomb interaction with ions. Electrons with energies above the shock thermal energies of at most a few tens of keV will contribute a power-law spectrum with the same photon index as their energy distribution index (Reynolds, 2008). This is the case of the particles that are accelerated in shock waves, so non-thermal bremsstrahlung radiation could be observed in objects such as SNRs. When the electron energy exceeded ~100 MeV, Bremsstrahlung photons are emitted by the same electrons that produce radio emission, so one expects a gamma-ray spectrum with $s \sim 2$ (Reynolds, 2008). The energy loss rate of ultra-relativistic electrons by Bremsstrahlung is:

$$\left(-\frac{dE}{dt}\right)_{Brems} = 4nZ^2 r_e^2 \alpha c g \tag{1.27}$$

  where r_e is the classical electron radius, α is the fine structure constant and g is a Gaunt factor (Longair, 2011).

- **π^0 decay**
  Among the four basic radiative processes that characterize the SNRs spectra, the π^0 decay is the only one of hadronic origin. The DSA theory generally predicts that a substantial fraction of the shock energy is transferred to relativistic protons. A direct signature of these high energy protons is provided by gamma rays generated in the decay of neutral pions (π^0). The π^0 are produced by the proton-proton interactions between the protons accelerated in the SNR shocks and those found in the interstellar medium, by the following reaction:

$$p + p \rightarrow p + p + \pi^0 + other \quad products$$

$$\pi^0 \rightarrow \gamma\gamma$$

  In the rest frame of the neutral pion each γ photon has an energy of $\frac{m_{\pi^0} c^2}{2} = 67.5$ MeV, where m_{π^0} is the rest mass of the neutral pion. This characteristic of the π^0 decay leads a gamma-ray number spectrum $F(E)$ peaking at the energy of 67.5 MeV and dropping symmetrically on either side (in a log-log representation). The emission spectrum in the $E^2F(E)$ representation rises then steeply below ~200 MeV and approximately traces the energy distribution of parent protons at energies greater than a few GeV. This characteristic of the spectrum, also referred to as the "pion-decay bump", is a direct signature of the π^0

decay (Ackermann et al., 2013). The efficiency of the π^0 decay process is related to the density of target protons. Indeed, the energy loss time of the CRs due to proton-proton interactions is determined by $\tau_{pp} = \frac{1}{n_{gas} c k \sigma_{pp}}$, which represent the time scale for the p-p collision. The parameters σ_{pp} and k are, respectively, the cross section and the inelasticity of the p-p interactions and both do not significantly change in the energy range from GeV to hundreds of TeV. This means that the time scale of a collision depends on the gas density only: $\tau_{pp} \approx 6 \times \frac{10^7}{n_{gas}}$ yr. In the typical ISM regions with density $n_{gas} \leq 1$ cm^{-1} the time scale of p-p interactions significantly exceeds the time scale of activity of potential CR accelerators, like SNRs (Aharonian & Atoyan, 1996). On the other hand, the proton interaction become significant in the dense molecular clouds with $n_{gas} \sim 10^2 - 10^4$cm^{-2}, which are therefore crucial for the π^0 decay emission.

1.5 The radio spectra of SNRs

As we have seen in the previous paragraphs, the spectral energy distribution of SNRs from the radio to the γ-ray band can be explained on the basis of the DSA mechanism (which accelerates high-relativistic particles at the SNR shock front) and the emission processes by which these particles produce photons with energy from keV to TeV energies (Fig.1.11).
In the framework of a multi-frequency study of SNRs, the investigation of the spectral features in the radio domain is crucial to testing theoretical models to the γ-ray emission. Indeed the same electrons responsible for the synchrotron radio emission emit in the γ-ray band through IC and Bremsstrahlung processes. For this reason, the bumps that characterize the γ-ray spectra of leptonic origin are bound to the synchrotron spectral slope and to the cutoff in the radio domain. From the gamma-ray observations of middle-aged SNRs like W44 and IC443, which showed a steepening of the primary particle spectrum at energies of 10−100 GeV, a synchrotron cutoff is expected above 10 GHz (Ackermann et al., 2013).
The main characteristics in the radio continuum spectra of SNRs result from simple synchrotron emission. In addition, electron acceleration mechanisms can shape the spectra in specific ways, especially at high radio frequencies. These features are connected to the age and the peculiar conditions of the local ISM interacting with the SNR.

1.5.1 Young SNRs

In their free expansion and early Sedov phase the SNRs are considered "young" and are characterized by very fast shock waves, with velocities typically between $\sim 10^3$ and $\sim 10^5$ km/s. On the basis of the DSA mechanism, the theory proposed by Bell (Bell 1978a, Bell 1978b) predicts that when the magnetic field direction is parallel to the shock normal (parallel shock configuration, see Fig.1.13) the DSA mechanism is very efficient. As a result of this, steep spectra are expected to be associated with evolved SNRs, according to the progressive energy loss from the shock

wave, while harder spectra are associated with young SNRs, where the particle acceleration mechanisms are very efficient (Urošević, 2014). However, this prediction is inconsistent with the observational evidence that revealed spectral indexes around 0.7 for young SNRs (see Green 2014). This inconsistence between the theoretical expectation and the observations was resolved by Bell in 2011 by assuming that the steepening or flattening of the spectra depend on the angle between the shock normal and the large scale upstream magnetic field. On these basis the quasi-perpendicular shocks lead a strong steepening of their related radio spectrum. It has been demonstrated that the magnetic field takes a quasi-perpendicular configuration when a magnetic field amplification occurs in the precursor driven by CR streaming (Bell 2004, Bell 2005). The magnetic field amplification is due to the so called *non-resonant Bell instability* driven by the CRs. As schematically shown in Fig.1.12, upstream CRs move along the magnetic field lines generating an electric current $\mathbf{j}_{CR}$ directed away from the shock. This instability results from the force $\mathbf{F}=\mathbf{j}_{CR}\times\mathbf{B}_0$ (where $\mathbf{B}_0$ is the local magnetic field) produced onto the plasma, which stretch the component of the magnetic field perpendicular to the shock normal. The stretch of the magnetic field leads the growing of the resonant instability very rapidly for high Mach number shocks, which acts more efficiently on the magnetic field. This process leads to an amplification of the magnetic field, which sweeps CRs through the shock and prevents them to return to the shock for further acceleration. Under these conditions the DSA mechanism becomes less efficient and a steepening in the radio spectrum is expected. Therefore, strong field amplification can be expected to lead preferentially quasi-perpendicular shock geometry (Fig.1.13) with the consequent steepening of the spectral index. The presence of cosmic ray current-driven instabilities is not contradicted by polarimetric observations of young SNRs which suggest a predominantly radial magnetic fields (Bell et al., 2011). This is located mainly in downstream regions of SNR shocks where the synchrotron emission is strongest, as show in Fig.1.14 for the case of SN1006.

The Bell's theory provide an explanation for the steep spectral indexes observed in young SNRs, but it is also useful to discuss spectral index variation across the SNRs. Indeed, if we consider a SNR expanding at high velocity into an uniform magnetic field, we could observe different spectral index variation:

- a weak magnetic field amplification leads an orientation of the magnetic field at the shock that is the same of the pre-existing interstellar field. In the regions in which this occurs the electron spectrum should be flatter and a strong X-ray synchrotron emission is observed at the poles.

- in the regions of the SNR where the angle between the shock normal and the magnetic field is higher, the magnetic field amplification is more efficient and the X-ray and radio emissions are expected to be fainter, with a related steepening of the spectral indexes.

This is exactly the picture that the resolved spectral index studies revealed for the SNR SN1006. As we can see in Fig.1.14(a) a bipolar symmetry of this remnant is clearly detected and is thought

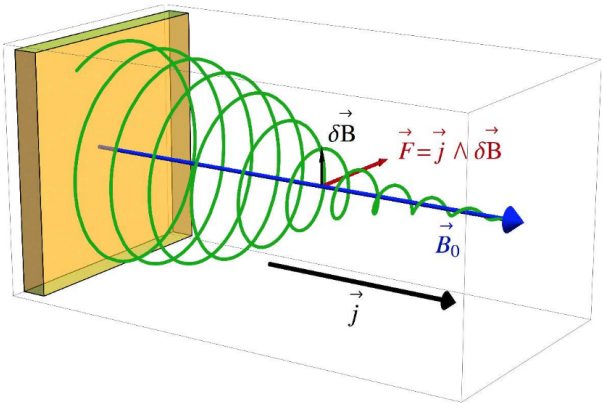

Figure 1.12: Schematic representation of the non-resonant instability mechanism: the current of CRs escaping from the shock region exerts a force $\mathbf{F}=\mathbf{j}_{CR}\times\mathbf{B}_0$ onto the plasma, thereby stretching and amplifying the initial magnetic perturbations (Morlino, 2017).

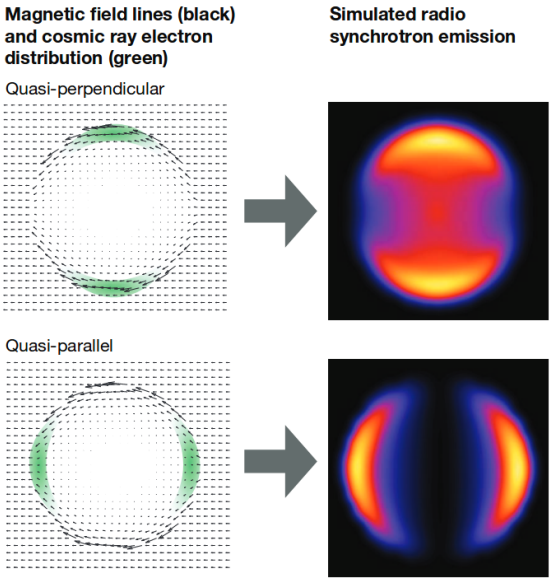

Figure 1.13: Geometry of the cosmic-ray electron distribution with respect to the magnetic field geometry in the two cases of quasi-perpendicular shocks (top) and quasi-parallel shocks (bottom). The related simulations of the synchrotron emission are also shown in the right panel (West et al., 2016).

to reflect the directionality of the ambient magnetic field Bell et al. (2011). On the basis of the cosmic ray acceleration at oblique shock, the bright caps are associated with the regions where the shock velocity is parallel to the background magnetic field. This is confirmed by the radio and X-ray observations that show a flat spectrum related to these regions, while a spectral steepening is observed towards the fainter parts (Allen et al., 2008), where the magnetic field result quasi-perpendicular with respect to the shock normal. The radio spectra of young SNRs could present a curved concave-up shape due to the dynamical reaction of accelerated particles at the shock. This is due to the pressure exerted by the CRs ahead the shock during the acceleration process, which slows down the plasma in the rest frame of the shock resulting in the so called *precursor*. The CR pressure could modify the shock structure that is reflected in changes in the spectrum of the accelerated electrons. The CR acceleration is most efficient during the early phases of SNR evolution, when the shock waves are very fast, and for this reason the effect of the CR pressure is observable in the young SNRs. As shown in Fig.1.15, the CR pressure leads to the deceleration of the upstream plasma, which is also heated by the plasma located at the CR precursor region. Therefore, in the modified shock configuration the shock discontinuity results to be degenerate into the weak subshock discontinuity and a wide transition region, which represent the CR

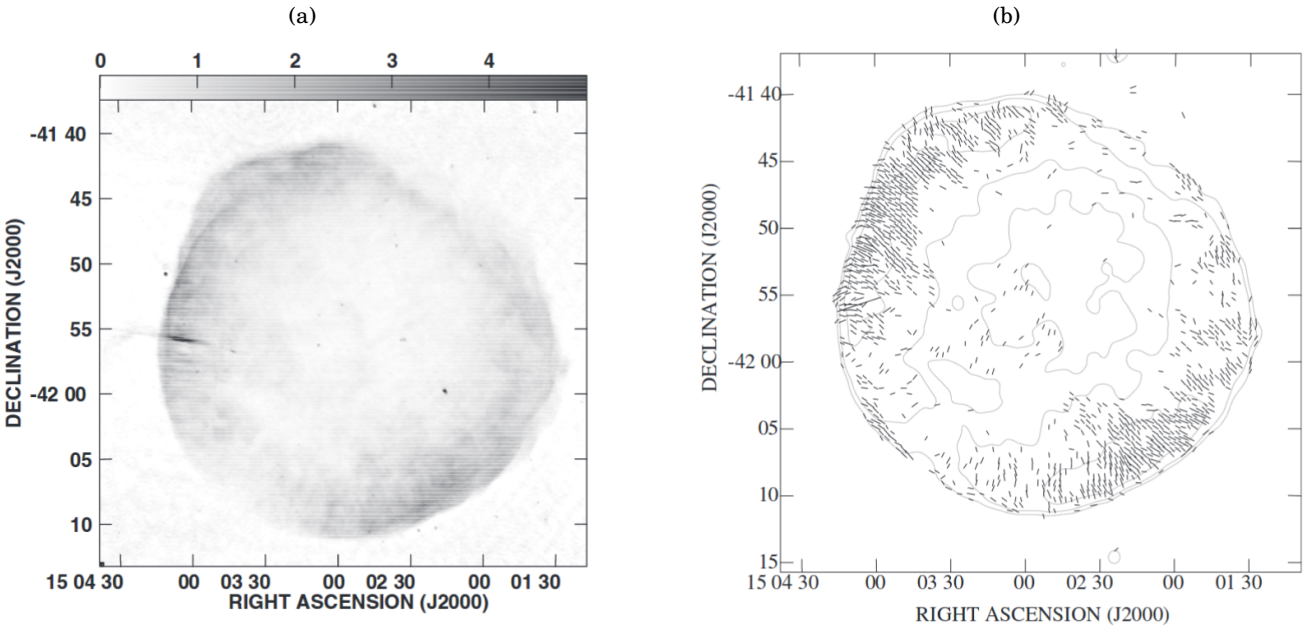

Figure 1.14: (a) Total intensity image of SN 1006 carried out at 1.4 GHz combining VLA and Australia Telescope Compact Array. The angular resolution of 10″ (Reynoso et al., 2013). (b) Distribution of magnetic field vectors on SN 1006 at 1.4 GHz. The contours are related to the total intensity radio emission (Reynoso et al., 2013).

precursor region (see velocity profile of the modified shock in Fig.1.15). In this configuration, particles with different energies are subjected to different compression factor which increases for larger energies. Indeed the Mach number becomes smaller at the jump of the subshock and in this region the compression ratio becomes $r = \frac{\Gamma+1}{\Gamma-1} < 4$. On the other hand, the total compression ratio referred to the modified shock from the upstream to the downstream becomes $r > 4$, due the presence in this region of CR with adiabatic index of $\Gamma_{ad} = \frac{4}{3}$. Under the modified shock configuration the low energy electrons, which are characterized by a small Larmor radii, are confined in the subshock region where they undergo a compression factor $r < 4$. This results in a steepening of the radio spectra at low energies, how that expected by the linear DSA. On the contrary, the high-energy electrons with bigger Larmor radius, can escape from the subshock to the precursor region (where $r > 4$) and the related energy spectrum results harder (flat radio spectrum). The overall effect is therefore a concave-up radio spectrum, with spectral index steeper than 2 for lower energies and harder than 2 for the highest energies, due to a significant CR production (Urošević 2014, Morlino 2017). In contrast with the shock discontinuities provided by the DSA theory, those related to the modified shocks have finite thickness and could be observed closer to the strong shocks. An important example is represented by the detection of H_α emission from both the shock wave and the CR precursor region observed in the knot of Tycho's SNR (Lee et al., 2007). The H_α emission is related to charge exchange interactions between the neutral

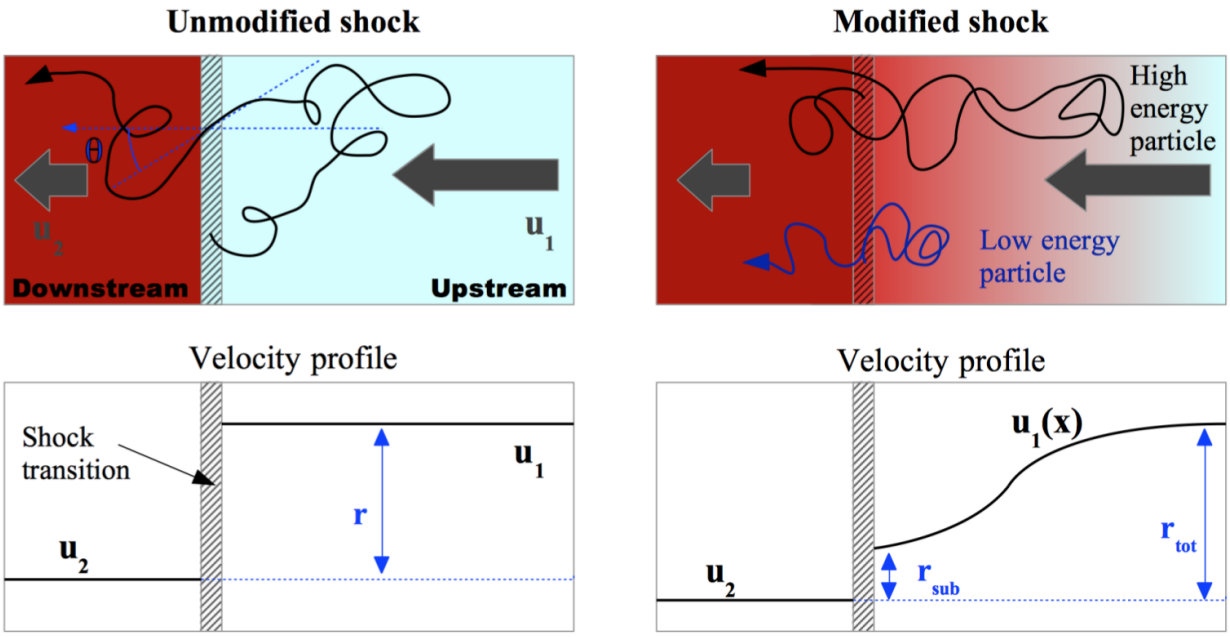

Figure 1.15: Schematic representation of the high-energy particles dynamics in a strong SNR shock wave. *Left*: According to the DSA theory the particles are diffused form upstream towards downstream with a compression factor r that is the same at all energies. *Right*: the influence of the diffusion of the high energy particles back upstream upon the structure of the shock. The CR diffusing in the upstream region exercise a pressure on the plasma in the precursor upstream region resulting in a change of the compression ratio through the shock: the low-energy particles in the subshock feel a smaller compression ratio, while the high-energy particles are diffused toward upstream infinity and are subjected to a larger compression factor (Morlino, 2017).

interstellar gas and the hot plasma in either side of the shock transition. Thanks to the atomic physics information arising from this process it is possible to derive information about physical conditions in the shock front and on the modified shock configuration. As shown in Fig.1.16, in the case of Tycho the narrow synchrotron X-ray emission allows us to detect the location of the shock front and the H_α emission, which is located to the left of the narrow X-ray feature and falls off in intensity with distance from the shock front, provides a picture of the shock and of the precursor regions. This may be observed in the profile of the H_α intensity in the vicinity of the knot (Fig.1.16), which confirms the configuration provided by the modified shock theory.

1.5.2 Evolved SNRs

The SNRs are generally defined "evolved" when they are in the Sedov or in the radiative phases of their evolution. These phases are characterized by not very efficient particle acceleration mechanisms, which less affect the SNR dynamics compared to what happens for young SNRs. Under these conditions, the DSA theory provides spectral indexes around 0.5 or higher in the

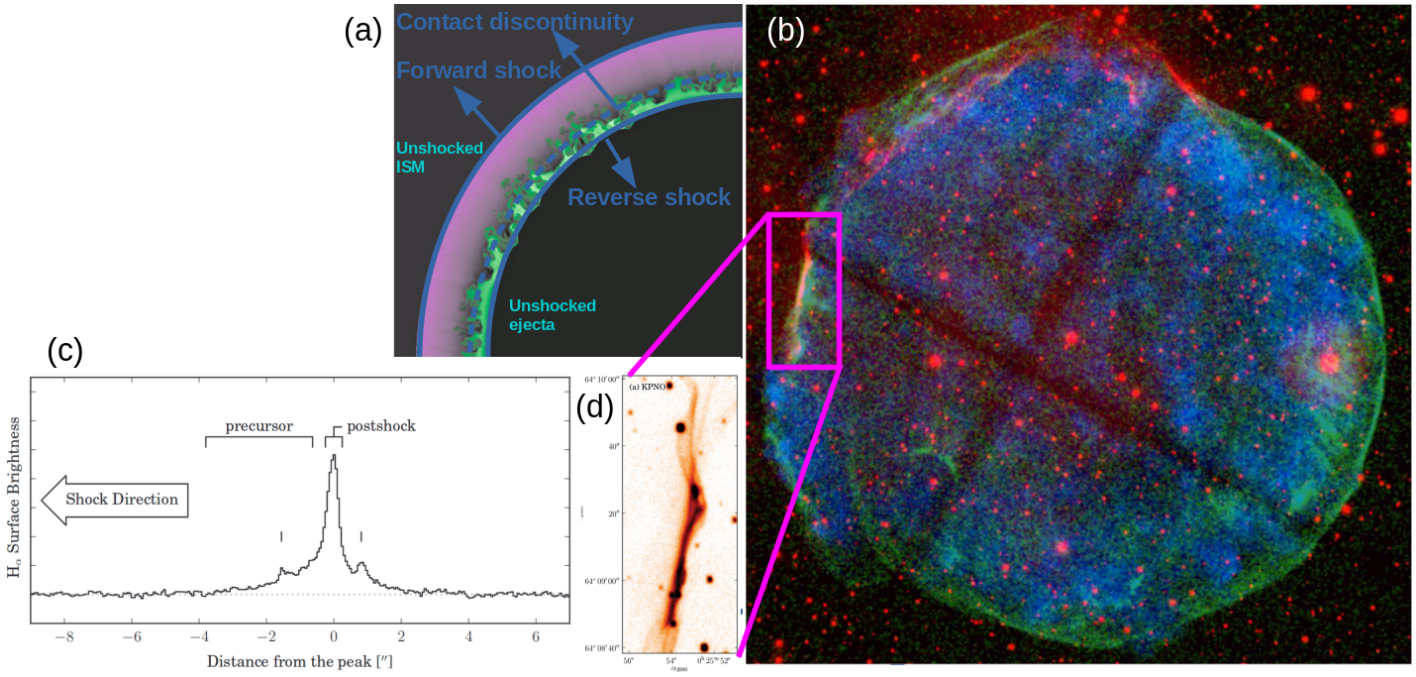

Figure 1.16: Structure of the shock discontinuity in the modified shock configuration as observed in Tycho SNR: (a) Schematic representation of the SNRs dynamics on the basis of the 3D simulated density map obtained by Ferrand et al. (2010). Eejecta are in green and ambient medium is in purple. The shock moves supersonically into ISM/CSM, while the reverse shock propagates into ejecta, starting from outside. (b) Multi-frequency image of Tycho's SNR. The H_α emission is indicated in red, while the green and blue features are related to the X-ray emission as observed by Chandra at 3−8 keV and 0.5−3 keV, respectively (Ghavamian et al., 2013). (c) H_α brightness profile across the shock normal related to the brightest filaments in Tycho . The bright narrow peak is believed to correspond to the emission from the narrow region of the immediate postshock area. The emission extends up to $4''$ toward upstream, which is interpreted as emission from the shock precursor (Lee et al., 2010)). (d) H_α image of one of the brightest Balmer-dominated filaments in Tycho (Lee et al., 2010).

case of more evolved SNRs. The observational data seem to confirm this theoretical expectation with the majority of the measured spectral indexes in the range $0.5 < \alpha < 0.6$. We can easily explain this result on the basis of the DSA mechanism by considering that the evolved SNRs are characterized by weaker shock waves wherein the particles are accelerated less efficiently and the related compression factor is lower, which determines a steep radio spectrum. However, the DSA theory cannot explain (in their linear and non-linear configuration) the flat spectra ($\alpha < 0.5$) observed in some evolved SNRs, especially in those with shell-like morphology. The question about the nature of the flat spectral indexes in some Galactic SNRs is still open and different models were proposed in order to explain them. One of this is based on the combination of the DSA theory and the second-order Fermi acceleration mechanism. As proposed by Schlickeiser & Fuerst (1989), the electrons in the vicinity of a plane-parallel shock wave could gain simultaneously

energy from shock crossing and second-order Fermi acceleration in low β-plasma, where β is defined as $\beta = \frac{P}{P_{mag}} = \frac{8\pi nk(T_e+T_i)}{B^2}$ (P is the gas pressure, P_{mag} the magnetic pressure, B the magnetic field, n the number density, k the Boltzmann constant, T_e and T_i the electron and ion temperatures respectively) (Onić, 2013). They concluded that the observed dispersion in spectral index values below α = 0.5 is attributed to a distribution of low upstream plasma β values for different SNRs (Schlickeiser & Fuerst, 1989). If we consider a typical Galactic magnetic field of 5 μG, a temperature of the medium (electron and proton temperature is the same) of 10^4 K and a number density of ~ 0.1 cm^{-3}, the plasma β is 0.16, which can reach lower values for higher magnetic field. In particular for $\beta \approx$0.05, and in conditions of high compression ratios (~2.5), a spectral index of $\alpha \approx 0.2$ can be achieved. However this model does not take into account that in some older SNRs a compression ratio higher than 4 is expected, and in this case the spectral index becomes 0.5 independently of plasma β.

An alternative explanation for the observed flat spectra of evolved SNRs in molecular clouds was proposed by Ostrowski (1999) on the basis of the second-order Fermi acceleration process in the turbulent medium near the shock wave. He found that even very weak shocks may produce very flat CR spectra in the presence of momentum diffusion (Onić, 2013).

Finally, another model involves high compression ratios. Indeed, in the case of fully radiative (isothermal) shocks, which are typical for SNRs in the post Sedov-Taylor phases of the evolution, the compression ratio become greater than 4 leading to a flattening in the related radio spectra. In particular, for parallel isothermal shock the compression ratio is $\chi = M_T^2$, where M_T^2 is the isothermal Mach number, and the DSA theory provides a spectral index $\alpha = \frac{3}{2(\chi-1)}$. The trend of this relation is shown in Fig.1.17, and we can see that flat spectral indexes ($0.2<\alpha<0.5$) are related to very weak fully radiative shocks, namely for isothermal Mach values between 2 and 3. On the other hand, only few old SNRs would be expected to have such weak shocks (Reynolds, 2011).

Furthermore, it was observed that different emission processes can shape the spectra of evolved SNRs, especially at high radio frequencies. When the spectral index change as a function of the frequency, it is likely that two different emission mechanisms compete to produce the radio continuum emission.

A radio spectral steepening is expected for evolved SNRs on the basis of the DSA theory. This is due to the effect of the synchrotron energy losses of electrons, which are diffuse away from the acceleration region. A higher energy of the electrons correlates with more significant energy losses, for this reason the spectral steepening is expected at high radio frequencies (> 1 GHz). A steepening in the spectrum is an important feature that is closely linked to the age and the evolution of the SNR in the ISM. Furthermore, the determination of the frequency at which the spectral break take place allow us to constrains the maximum energy of the accelerated electrons and then to assess the high-energy tail of the distribution of CRs accelerated in the SNRs. However, the lack of accurate flux density measurements up to 5−10 GHz, even for bright

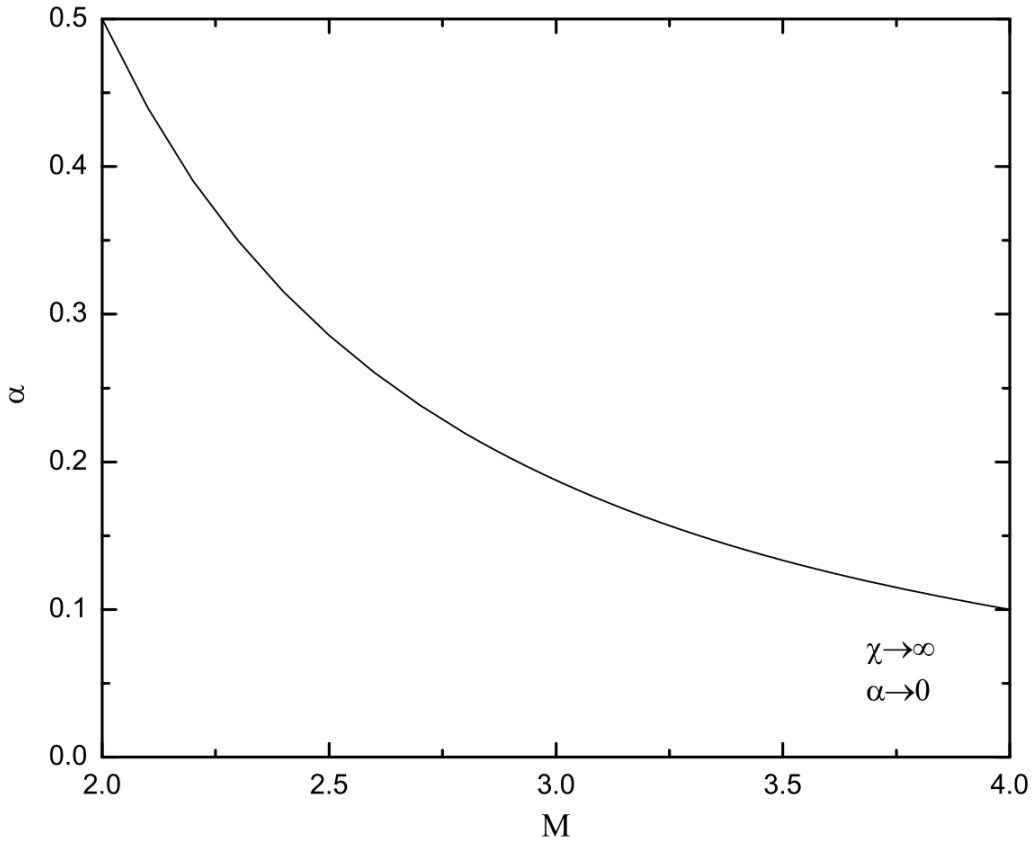

Figure 1.17: Change of integrated radio spectral index with isothermal Mach numbers of fully radiative (isothermal) SNR shock wave (Onić, 2013).

and well-known SNRs, makes the determination of a possible high-frequency spectral break difficult.

An example from literature is provided by Xiao et al. (2008), who performed a spectral study on the Galactic SNR S147 that provides an example of steepening in the radio spectra of evolved SNRs. In Fig.1.5.2 the radio spectrum of S147 between 80 MHz and 4.8 GHz is shown, which reveals a spectral steepening at the frequency of about 1.5 GHz. The authors attribute the spectral break to high synchrotron losses that occurred during the early phase of the SNR, which would cause a spectral bend at a rather high frequency, but subsequent expansion of S147 would shift the frequency toward about 1.5 GHz as well. In this work I also provide, for the first time, a direct evidence of a spectral break in the radio spectral energy distribution of the SNR W44 at an exponential cutoff frequency of 15 ± 2 GHz, which will be discussed in detail in the Section 3.1

The radio observations revealed a curvature in the spectra of some old Galactic SNRs expanding in high density environment, which results in spectral hardening at higher frequencies. The possibility of a significant production of thermal Bremsstrahlung radiation at radio continuum frequencies was proposed to describe this characteristic spectrum (Urošević 2014, Onić et al.

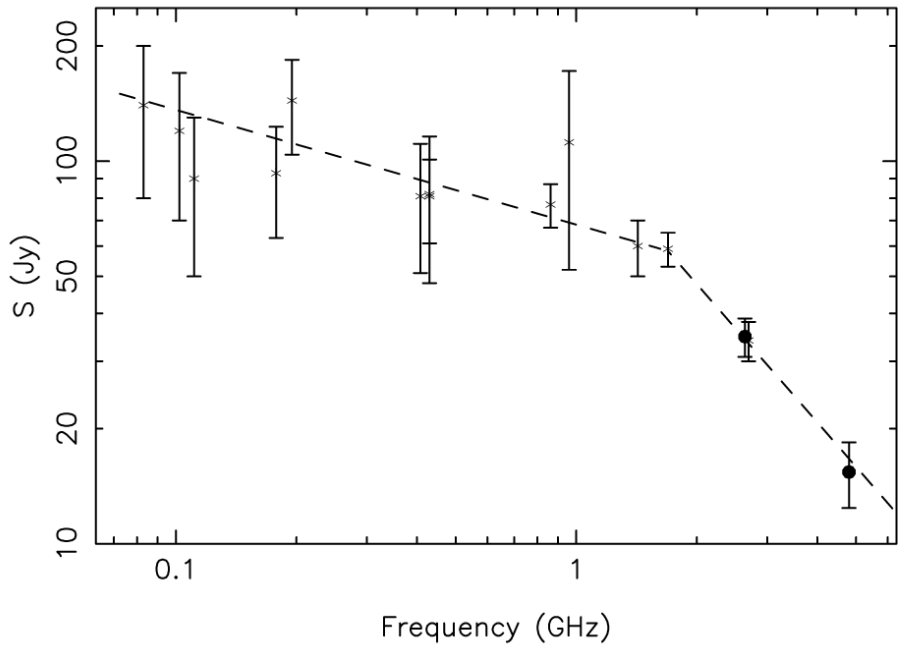

Figure 1.18: Spectral energy distribution of the SNR S147 reported by Xiao et al. (2008). The authors estimate a spectral index at low-frequency of $\alpha \sim -0.30 \pm 0.15$ and of $\alpha \sim -1.20 \pm 0.30$ above the break.

2012). Indeed, at high radio frequencies a significant component of the thermal Bremsstrahlung radiation (S$\propto \nu^{-0.1}$) can contribute to the total radio emission, in addition to the synchrotron emission (S$\propto \nu^{-\alpha}$), leading to a bend in the spectrum in the "concave up" form. The volume emissivity ϵ_ν^T of Bremsstrahlung radiation from a thermal plasma at temperature T at radio frequencies is:

$$\epsilon_\nu^T = 6.8 \times 10^{-38} g_{ff}(\nu, T) \nu^2 T^{-0.5} \quad (erg \quad cm^{-3} s^{-1} Hz^{-1}) \tag{1.28}$$

where n indicates the number density of both electrons and protons (in cm^{-3}), T is the temperature of the emitting region (in K), and $g_{ff}(\nu, T)$ is the thermally averaged Gaunt factor. We can notice from the Eq.1.28 that the thermal volume emissivity increases with the square of the number density, while it decreases with the temperature ($T^{-0.5}$). This implies that the thermal Bremsstrahlung contribution is significant in condition of high densities (1−10 cm^{-3}) and low temperatures (1000−10000 K), occurring in evolved SNRs and especially in the mixed-morphology SNRs, embedded in molecular cloud environment. These SNRs are typically in the radiative phases of their evolution, and are characterized by shock velocities less than 200 km/s (Vink, 2012) with an ensemble of cooled thermal X-ray electrons. An argument used to support this "thermally active" model is related to the detection of a low-frequency turn-over, in the integrated radio spectrum, due to a thermal absorption linked to the SNR (Brogan et al. 2005; Castelletti et al. 2011). Indeed the free-free thermal absorption leads to a "concave-down"

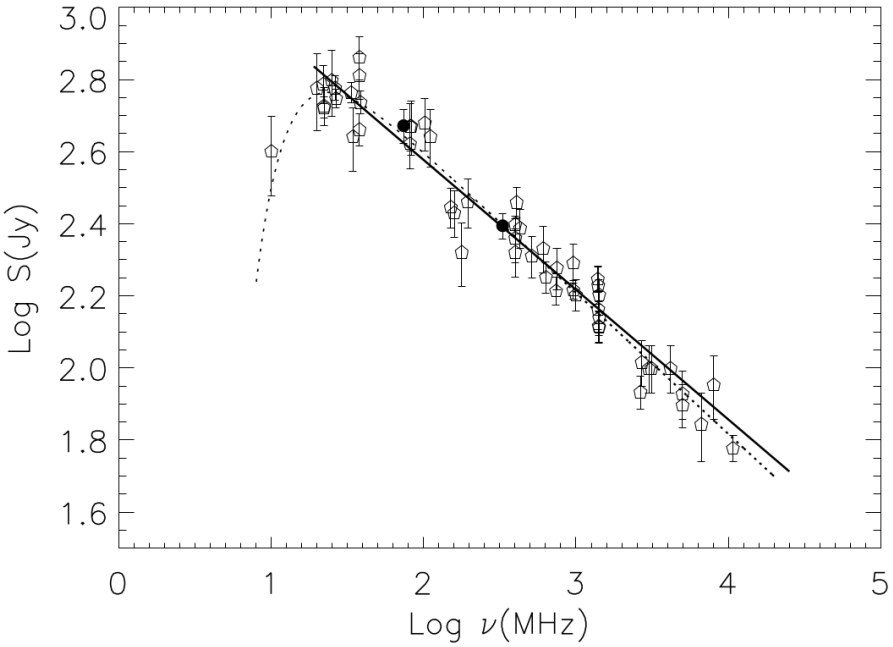

Figure 1.19: Radio continuum spectrum for SNR IC 443 obtained by Castelletti et al. (2011). The dotted line represent the fit to all of the plotted values by using the function described in Eq. 1.30, which take into account the thermal absorption component.

spectral curvature at low radio frequencies and provides an important complementary tracer of fast ionizing SNR/molecular cloud shock as well as of thermal bremsstrahlung emission at high radio frequencies (Onić et al., 2012). A low-frequency absorption related to the ISM along the line-of-sight between the SNR and the observer was observed in the Galactic SNR IC443 at ~10 MHz, as shown in Fig.1.5.2. By considering this low-frequency turn-over, Castelletti et al. (2007) modeled the spectral energy distribution of IC443 with a power law plus an exponential turnover:

$$S_\nu = S_{330}\left(\frac{\nu}{330MHz}\right)^{\alpha} \exp\left[-\tau_{330}\left(\frac{\nu}{330MHz}\right)^{-2.1}\right] \tag{1.29}$$

where 330 MHz was considered as the reference frequency at which an integrated flux density S_{330} and an optical depth τ_{330} are measured. The authors derived a free-free continuum optical depth at 10 MHz of $\tau_{10} = \tau_{330}[\frac{10}{330}]^{-2.1} = 1.07$. It is also important to note that the hot gas in the interior of the mixed-morphology SNRs is subject to a cooling rate, which directly affects the necessary conditions for a significant thermal emission. This is therefore expected for the same shock regions from which the synchrotron emission is produced, and it is favored by the interaction with dense environment ($n > 1$ cm^{-3} for ionized, atomic and molecular gas). If we consider the thermal absorption and emission as originated from the same volume of space that is placed ahead of the synchrotron emitting region, their contribution to the integrated radio

continuum spectrum can be described as (Onić et al., 2017):

$$S_\nu^{th} = S_\nu^{syn} \exp[-\tau_\nu] + S^{ff} \nu^2 (1 - \exp[-\tau_\nu]) \tag{1.30}$$

where τ_ν is the optical depth ($\tau_\nu \propto \nu^{-2.1}$), S_ν^{syn} is the synchrotron flux density given by Eq. 1.21, and S^{ff} correspond to the thermal free-free flux density at 1 GHz. However new observations are necessary to create a clear picture about the high frequency range (1−100 GHz) of the radio continuum, as well as about the question of the significant contribution of intrinsic thermal bremsstrahlung radiation and its correlation with the "concave up" radio spectra of some Galactic SNRs (Onić, 2013).

Another important process that could shape the integrated radio continuum at higher frequencies (between 10−100 GHz) is the *spinning dust emission*, which is thought to be the mechanism accountable for the Anomalous Microwave Emission (AME) from the Milky Way. This emission contribution is due to a complex mechanism whereby the dust asymmetric grains with a non-zero electric dipole moment may be spinning due to the interaction with the ISM and radiation field, and thus radiate electromagnetic waves as a result of the rotation of their electric dipole moment. The spinning-dust mechanism depends on the size, shape and charge of the emitting dust grains, as well as on the environmental conditions like the gas temperature, molecular fraction, ionization state and the intensity of the radiation field (Ali-Haïmoud et al., 2009). The contribution of the spinning dust emission results in a characteristic bump that characterizes the the continuum radio spectra in the frequency range 10−100 GHz, and the related flux density contribution can be written as (Onić et al., 2017):

$$S_\nu^{Spd} \propto \left(\frac{\nu}{\nu_0}\right)^2 \exp\left[1 - \left(\frac{\nu}{\nu_0}\right)^2\right] \tag{1.31}$$

where ν_0 is the peak frequency that usually falls in the range 10−70 GHz.

Finally, the very high-frequency (above 140 GHz) radio spectrum is likely dominated by the thermal emission associated with dust grains that survive the shock. The related flux density can be described by a simple model, which results in a modified black-body relation:

$$S_\nu^{Td} \propto nu^{\beta_d} B_\nu(T_d) \tag{1.32}$$

where $B_\nu(T_d)$ is the standard Planck black-body function for dust at temperature T_d and β_d is the dust emissivity index that usually assumes values in the range 0−2 (Onić et al., 2017).

1.6 Radio and Gamma-ray emission connections

At present, SNRs are considered the most probable sites of acceleration of galactic CRs. However, the evidence for the acceleration of electrons and protons in these objects is almost completely based on indirect arguments. This raised the problem of the CRs origin and acceleration mechanisms as one of the most discussed in the framework of the high-energy astrophysics and, more

specifically, of the study of the SNRs.

The direct evidences of the presence of ultra-high energy particles in SNRs may be obtained only through the characterization of the related radio and gamma-ray spectra. Indeed the detection of the characteristic pion-decay feature in the gamma-ray spectra uniquely identifies π^0-decay gamma rays and thereby high-energy protons, allowing a measurement of the source spectrum of CRs (Ackermann et al., 2013). On the other hand, the direct measure of the high-frequency spectral breaks in in the radio spectra of SNRs provides a direct estimate for the maximum energy of accelerated CR electrons. Furthermore, the accurate study of the radio spectral features, such as synchrotron spectral indexes and breaks is necessary to constrain the high-energy spectra in the frame of IC/Bremsstrahlung models. Indeed, in the spectral models studied to explain the gamma-ray emission from SNRs it must be considered that the gamma-ray fluxes and spectra are strongly dependent on the radio-observed parameters. For example, the global contribution to the gamma-ray spectra is related to the IC photons and target parameters and spectral break in the electron distribution, and in most cases there are no unambiguous model solutions without detailed measurements of the latter, since the former is intrinsically uncertain (Pellizzoni et al., 2017). Furthermore, the coordinated investigation of the radio high-frequency and gamma-ray emissions related to specific interesting regions of the SNRs, could provide a crucial test in order to disentangle the hadronic or leptonic origin of the CR emission. Indeed, up to now the study on the CR emission from SNRs, and related models, have never been based on spatially resolved radio spectra, implicitly assuming the existence of a single electron population for the whole SNR extent.

Thanks to gamma-ray instruments like AGILE, *Fermi*-LAT and Cherenkov telescopes over the last 10 years a significant progress has also been made on the characterization of the gamma-ray spectrum of interesting mixed-morphology SNRs, like W44 and IC443. On the basis of these data, the characteristic "pion-bump" spectral feature was detected, which is unequivocally linked to CR hadronic interactions in these SNRs (Ackermann et al. 2013, Cardillo et al. 2014). In this framework gamma-ray and radio data available in literature are simultaneously used in order to discuss hadronic vs. leptonic models. These studies pointed out a steepening of the primary particle spectrum at energies of ~ 10 GeV for W44 and ~ 100 GeV for IC443 that implies synchrotron spectral break at frequencies >10 GHz.

In recent models the possibility to explain the radio and the gamma-ray spectra of W44 in terms of re-acceleration and compression of Galctic CRs was also taken into account (Cardillo et al., 2016). These studies show that the hard radio spectrum can be explained in terms of low-energy secondary electrons with a maximum energy of ~1-2 GeV , which are produced in anelastic collisions between protons with a cut-off energy at ~ 10 GeV. In the same work a post-shock compressed field of ~1.4 mG was estimated. However, these results are obtained by considering the gamma-ray emission region of W44, which corresponds to the eastern bright radio shell where W44 interacts with a molecular cloud (MC) complex, while the radio data referred to integrated

flux density measurements.
Furthermore, as show in Fig.1.20, sensitive integrated fluxes are typically available in literature only up to 5−10 GHz. Sensitive radio continuum observations at high-radio frequencies (>10 GHz) and characterized by high-resolution are crucial in order to constrain the radio spectral break and to perform spatially-resolved spectral studies, which allow us to take into account the different primary and secondary electron populations that result from different shock conditions and/or undergoing different cooling processes. These measurements can be efficiently obtained by single-dish radio telescopes and this represents the aim of our research project based on the observation of galactic SNRs with the Sardinia Radio Telescope, which will be described in detail in the next Section.

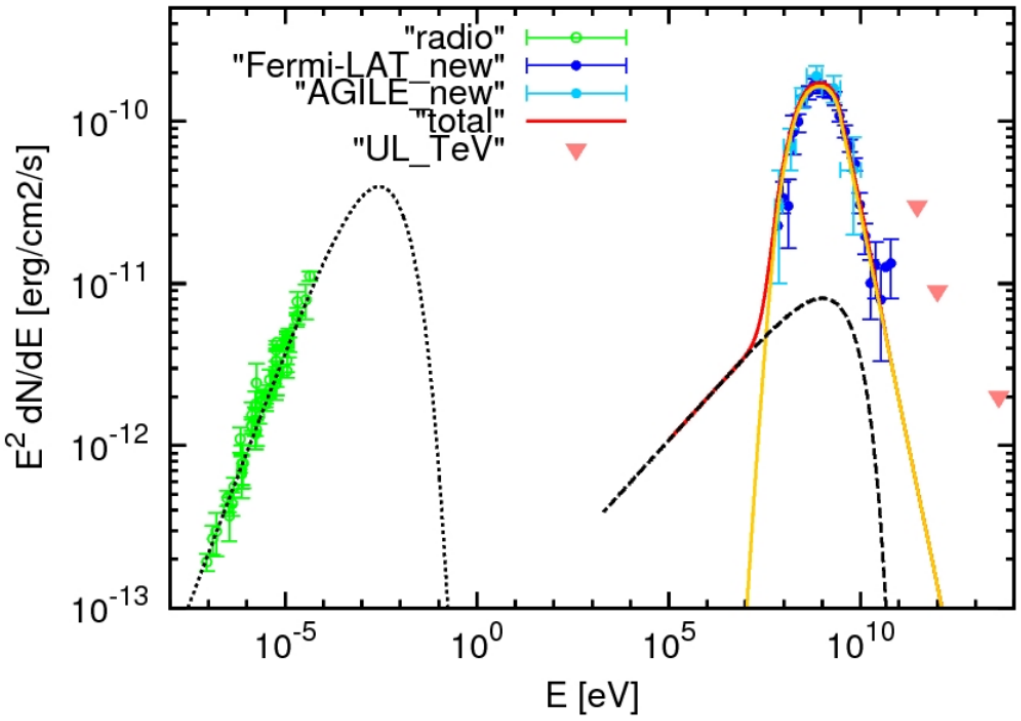

Figure 1.20: Broadband spectrum of the SNR W44 modeled by Cardillo et al. (2014). The radio data points are shown in green. The black curves show the electron contribution by synchrotron (dot) and bremsstrahlung (dashed) emissions, while the IC contribution was considered negligible. The red curve shows the total gamma-ray emission from the contribution of combined pion-decay and bremsstrahlung emissions.

CHAPTER 2

INVESTIGATING SPECTRAL FEATURES OF SNRS

Galactic SNRs are commonly identified as extended radio sources with steep spectra. For a fraction of them, multi-wavelength coverage ranging from radio to ultra-high energies (TeV) has been provided, although radio emission is the most common identifier of SNRs. In particular, about 20 SNRs have been firmly detected in gamma-rays mostly through the observations of Fermi-LAT (Acero et al., 2016) and AGILE satellites in the GeV range (Giuliani et al., 2011) and Cherenkov telescopes in the TeV range (H.E.S.S. Collaboration et al. 2011; Humensky & VERITAS Collaboration 2015). The gamma-ray emission of W44 and IC443 was detected with AGILE and Fermi-LAT (Giuliani et al. 2011, Abdo et al. 2010). These observations allowed to study the sub-GeV part of the gamma-ray spectrum in terms of acceleration of Galactic CRs (Ackermann et al. 2013, Cardillo et al. 2014, Cardillo et al. 2016). However, the identification of pion-decay gamma-rays, which are a direct signature of CRs accelerated in SNRs, has been difficult because the radio electrons also produce gamma-rays via Bremsstrahlung and IC processes. For this reason, the co-spatial study of the radio (in particular at high frequencies) and gamma-ray emissions coupled with a spatially-resolved analysis are required in order to test the hypothesis of hadron vs. electron emission.

SNR W44 and IC443 represent ideal targets for better test the models based on the radio and gamma-ray emissions, thanks to their interesting complex morphology and availability of extensive multi-wavelength data. Despite this promising perspective, the shape of the radio continuum spectra of Galactic SNRs at high frequencies is far from being fully understood due to a lack of accurate integrated flux densities. Indeed, sensitive radio continuum observations of large sources are not easy to perform, and only single-dish telescopes can do that at high frequencies.

We exploited the capabilities of the Italian radio telescopes (shown in Fig.2.1) to perform sensitive

single-dish radio observations of SNRs. In particular, SRT provides a good trade-off between sensitivity and resolution at frequencies up to 26.5 GHz. This thanks to the active surface that characterised its 64-m primary mirror, and corrects opto-mechanical deformations induced by gravity and temperature fluctuations (Prandoni et al., 2017). I participated in the observations of the SNRs W44 and IC443 that were performed with SRT in the framework of the ESP, between 2016 February and March, at three different central frequencies: L-band (1.55 GHz), C-band (7.0 GHz) and K-band (21.4 GHz). These observations required the implementation of a pipeline dedicated to the data analysis and calibration of single-dish continuum maps of extended sources. In this context, I contributed to the development of the SRT Single-Dish Imager (SDI), a state-of-the-art imaging data analysis software written in IDL and suitable for all SRT receivers/backends. The observations at 21.4 GHz were performed with the multi-feed K-band receiver in "Best Space Coverage configuration" (BSC; Bolli et al. 2015). This required a dedicated observational strategy and data analysis procedure, of which I took care first-hand. Tycho SNR was also included in our observations at 21.4 GHz because of its simple morphology and the availability of extensive flux density measurements at up to high radio frequencies (>100 GHz). These measurements were useful for cross-checking our calibration and data analysis procedure.

We provided, for the first time, single-dish deep imaging at 7 GHz and 21.4 GHz of W44 and IC443 and spatially-resolved spectral measurements in the 1.5−7.0 GHz frequency range. Our sensitive flux density measurements at high frequencies allowed us to characterise the integrated and spatially-resolved spectra of these SNRs, and to find significant frequency- and region-dependent spectral slope variations. Finally, I and my research group observed the very extended SNR Cygnus Loop at 8.3 GHz with the Medicina radio telescope in the framework of an observing project of which I am Principal Investigator. This allowed us to study the complex morphology and the integrated spectrum of Cygnus Loop at the highest frequency carried out so far with a single-dish telescope.

Figure 2.1: Representation of the Italian radio telescopes operated by the Italian National Institute for Astrophysics (INAF).

2.1 Observing SNRs with the Italian radio telescopes

2.1.1 Scientific background

SN explosions release a huge amount of energy (~10^{51} erg) that is transferred to the magnetic field and kinetic/thermal energy of the shocked interstellar gas and relativistic particles. For this reason SNRs are believed to be the main sources of Galactic CRs below $10^{15} - 10^{16}$ eV. Electrons and heavier particles are responsible for the non-thermal emission of SNRs, both in the radio and gamma-ray bands.

In the radio band, the SED of SNRs are characterised by synchrotron emission ($S_\nu \propto \nu^{-\alpha}$ with $\alpha \sim 0.5$) from relativistic electrons accelerated into the magnetic field by a diffusive shock mechanism. Assuming a magnetic field of the order of 10 μG, which typically arises by compression of the ISM in SNR shocks (Wielebinski & Beck, 2005), it is expected that 0.5−50 GeV electrons emit the observed synchrotron radiation in the 0.01−100 GHz frequency range. A steepening in the radio spectrum is associated with a decrease in the energy distribution of the emitting electrons.

The gamma-ray emission results from both leptonic (Bremsstrahlung and Inverse Compton, IC) and hadronic (π^0 mesons decay) processes. The latter shows the typical "pion-decay bump" spectral feature, which is characterised by a steepening below ~200 MeV and approximately

traces the energy distribution of parent protons. This spectral feature uniquely identifies π^0-decay gamma rays and hence the presence of high-energy proton populations in SNRs. A strong emission in gamma rays has been observed in the SNRs interacting with molecular clouds, like W44 and IC443. This reflects the fact that cosmic-ray protons accelerated by SNRs penetrate into high density clouds with a relative enhancement of p-p interactions and then of π^0-decay processes. However, also the leptonic processes show bumps in their gamma-ray spectra that are bound to the synchrotron spectral slope and cut-off in the radio domain. For this reason the identification of pion-decay gamma rays is not trivial. Recent works, which are based on gamma-ray observations, assume a combined emission contribution of hadronic π^0 and leptonic models in order to explain the SED of evolved SNRs from radio to the gamma ray band (Ackermann et al. 2013, Cardillo et al. 2014, Cardillo et al. 2016). Among nearby and large sources, SNRs W44 and IC443 are the best suited for multi-wavelength spectral studies ranging from radio to gamma-rays. These sources offer a rich region-dependent phenomenology including atomic/molecular clouds interactions, Pulsar Wind Nebulae (PWN) associations, thermal X-ray emission, halos and filamentary structures (Seta et al. 1998, Rho & Petre 1998).
A study of the gamma-ray emission spectra of the two SNRs W44 and IC443 as detected by the Fermi-LAT, was performed by Ackermann et al. (2013). In order to study the correlation between the gamma-ray spectral shape and the spectra of the accelerated protons, the data were fitted by using a π^0-decay spectral model. This was numerically calculated from a parametrised energy distribution of relativistic protons, which are characterised by a spectrum as a function of momentum well represented by a smooth power law:

$$\frac{dN_p}{dp} \propto p^{-s_1}\left[1+\left(\frac{p}{p_{br}}\right)^{\frac{s_2-s_1}{\beta}}\right]^{-\beta}$$

where s_1 and s_2 represent the spectral index values respectively below and above the break, and p_{br} is the high-momentum break. The break in the momentum spectrum (p_{br}) of the accelerated protons, which was derived from the χ^2-best fit to the flux points, is 239 ± 74 GeV c^{-1} for IC443 and 22 ± 8 GeV c^{-1} for W44 (Ackermann et al., 2013). As shown in Fig.2.2, this p_{br} value implies a high-energy break in the gamma-ray spectra at an energy of ~ 20 GeV and ~ 2 GeV for IC 443 and W44, respectively. The high energy cut-off in the proton spectrum, which was pointed out by the gamma-ray observations, is also expected for the leptonic particle spectrum. It depends on the SNRs age and other physical parameters like the magnetic field and the ambient density. Assuming the same value of the primary particle break (p_{br}) for both protons and electrons, an indirect estimation of the synchrotron spectral break in the radio band was obtained at frequencies above ~ 10 GHz for both sources.

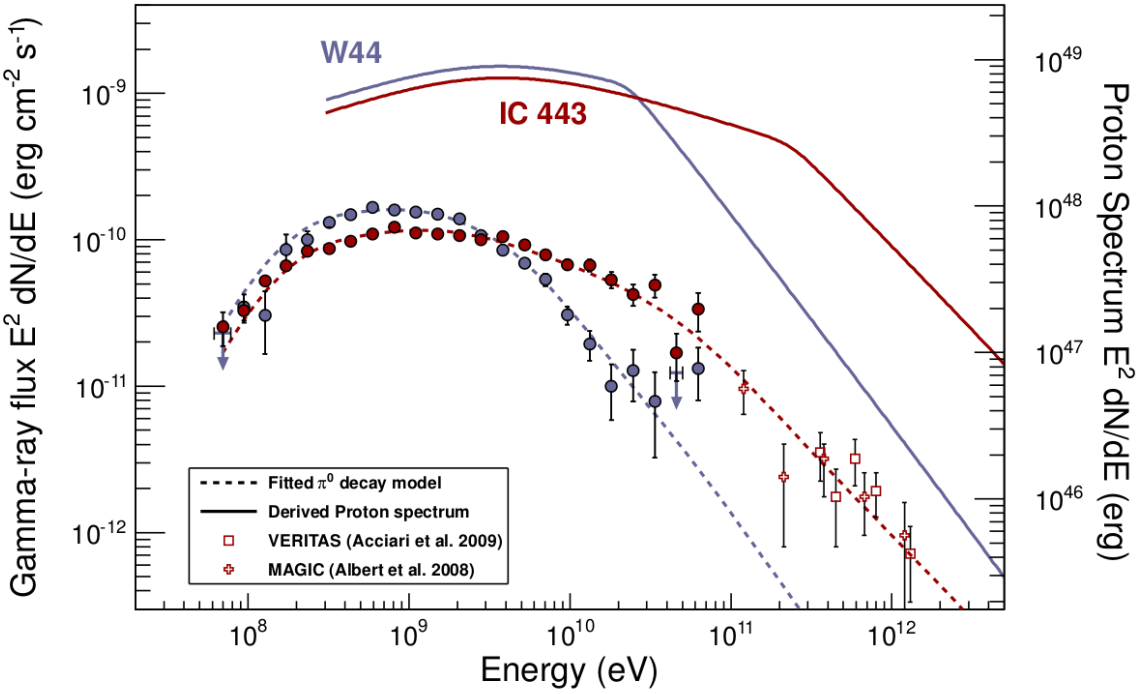

Figure 2.2: The gamma-ray spectra of IC443 and W44 obtained from the fit of the *Fermi*-LAT measurements with a π^0-decay spectral model. The solid lines represent the energy distributions of the high-energy protons derived from the gamma-ray fits (Ackermann et al., 2013).

The parameters of the magnetic field strength (B) and ambient gas density (n) were determined through the simultaneous fit of the synchrotron radio and the gamma-ray bremsstrahlung fluxes, obtaining $B = 50$ μG and 90 μG, $n = 300$ cm^{-3} and 650 cm^{-3} for IC443 and W44, respectively. The radio data related to the two SNRs strongly constrain the electron indices below the break (s_{IC443} = 1.72, s_{W44}=1.74), whereas the indices above the radio break (s_{IC443} = 3.2, s_{W44} = 3.7) and the location of the break are free parameters that can be determined through the fit of the gamma-ray spectra.

As shown in Fig.2.3, the energy range below ~ 200 MeV is crucial in order to constrain hadronic or leptonic contribution in the gamma-ray spectra. On the other hand the gamma-ray fluxes and spectra are strongly dependent on the IC photon target parameters and spectral breaks in the electron distribution, and in most cases there are no unambiguous model solutions without detailed measurements of the latter, since the former is intrinsically uncertain (Pellizzoni et al., 2017). Furthermore, the observed synchrotron radio emission still constrains the maximum energy of the electrons accelerated in the SNRs, but sensitive radio flux density measurements up to 20 GHz are required for this purpose (Fig.2.4 *right*). It is worth noting that in complex systems like the middle-aged SNRs, which show evidence of interactions with atomic and molecular

clouds, different populations of both electrons and protons could be present, including secondary electron populations produced in inelastic proton-proton collisions (Cardillo et al., 2016). Taking also into account a possible dominant secondary electron contribution in crushed clouds regions of the SNRs, a careful co-spatially verification of the radio high-frequency and gamma-ray emissions could provide a crucial test of the hypothesis of hadron vs. electron high-energy spectral contributions.

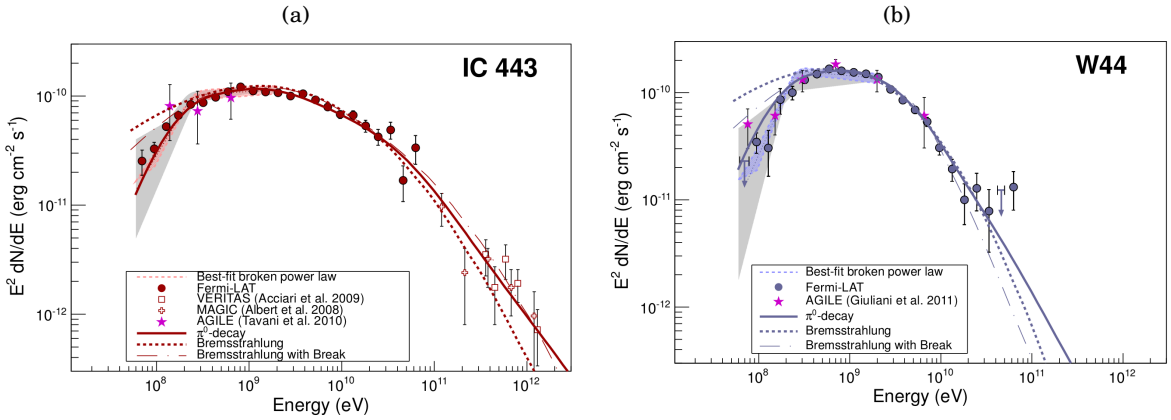

Figure 2.3: Gamma-ray spectra of IC 443 (a) and W44 (b) as observed with *Fermi*-LAT. Solid lines indicate the best-fit pion-decay spectra, dashed lines denote the best-fit bremsstrahlung spectra, and dash-dotted lines are associated with the best-fit bremsstrahlung spectra (Ackermann et al., 2013)

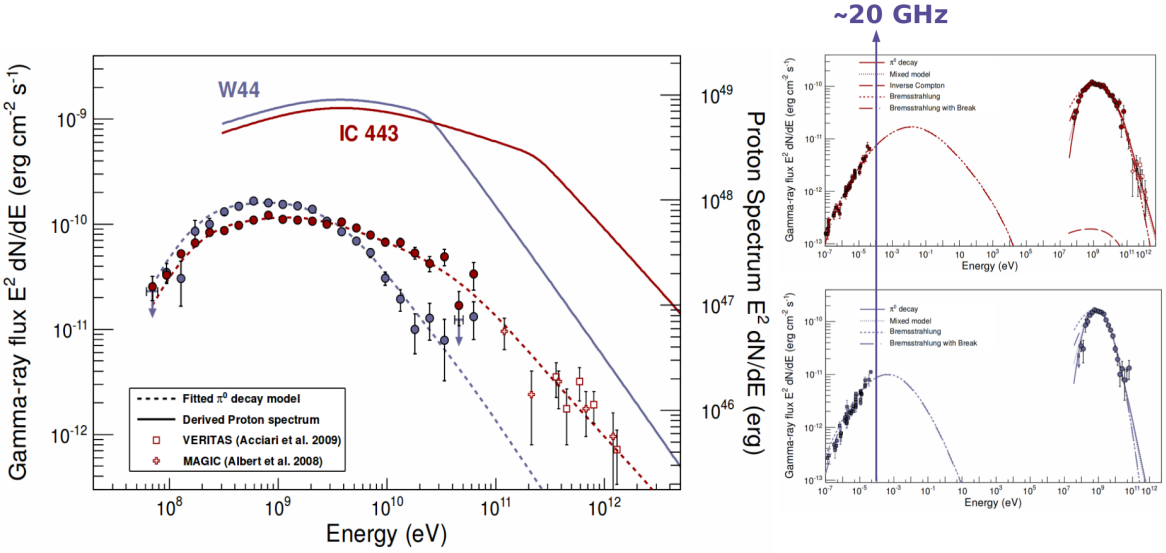

Figure 2.4: *Left*: Proton and gamma-ray spectra determined for IC 443 and W44. *Right*: the spectral energy distribution of IC443 (upper) and W44 (bottom) (Ackermann et al., 2013)

Observations of SNRs are then important not only for our understanding of the intrinsic phenomenology of stellar evolution but also to investigate global processes in our Galaxy such as the properties of the ambient interstellar medium and the origin of CRs (Egron et al., 2017). Despite the interesting morphology of W44 and IC443 encourages the local study of the peculiar SNR regions, recent constraints on CR emission from these SNRs and related models are based on integrated radio fluxes only (no spatially resolved spectra) implying the simplistic single-zone assumption of a single electron population for the whole SNR. Furthermore, multi-wavelength data on SNRs are still sparse and often puzzled also for the most interesting and bright objects at frequencies $> 5 - 10$ GHz. This is due to the difficulty of obtaining radio images with both a high resolution and the required sensitivity to carry out accurate continuum flux density measurements. Only single-dish telescopes can do that at high radio frequencies. Indeed, interferometric observations provide significant amount of information about the morphology of SNRs, but accurate flux estimation and imaging of large structures of $\sim$10$-$30 arcmin is infeasible above a few GHz.
Observations of Galactic SNRs at up to microwave frequencies have been carried out by the *Planck* and QUIJOTE instruments (Planck Collaboration et al. 2016, Génova-Santos et al. 2017) with a relatively low resolution, which makes it difficult to provide precise flux densities of sources located in crowded regions of the Galactic Plane. On the other hand, sensitive radio continuum observations can be performed with single-dish telescopes, offering in this way a good trade-off between sensitivity and resolution in the frequency range 5$-$50 GHz. In this context, the project to perform single-dish observations of SNRs with the Italian telescopes has started in 2012, with the aim to obtain sensitive high-resolution images up to high radio frequencies. We chose as main targets of our studies the evolved SNRs W44, IC443 and Cygnus Loop, which are characterized by both an interesting complex morphology and the availability of extensive multi-wavelength data from radio to gamma-rays. We have also included the young SNR Tycho which, thanks to its simple morphology and the availability of extensive flux density measurements up to high-radio frequency, represents an ideal target for testing our data analysis tool.

2.1.2 The project

The Astronomical Validation (AV) of SRT constituted a large project carried out from 2012 to 2015 with the aim to perform the implementation and/or fine-tuning of the advanced SRT subsystems such as the active surface, the derotator and new releases of the acquisition software. At the same time the AV included the development of the software tools to assist the preparation and the execution of typical scientific observations and related data analysis (Prandoni et al., 2017). In this framework the observations of the SNRs were devoted to test the radio-continuum imaging capabilities of SRT. Indeed the large-complex structure of the SNRs and their brightness up to high radio frequencies make these sources ideal targets to test the image fidelity, namely the

measure of the reliability of the image (in terms of surface brightness, size, and morphology) when mapping extended sources.
However, the importance of this work lies in the fact that single-dish observations of SNRs were never performed before with Italian telescopes. This required a broad project that included the feasibility studies of the observations and the development of the correct observational strategies associated with the implementation of a pipeline dedicated to the data analysis and calibration of single-dish continuum maps of extended sources. Furthermore these sources provide very challenging science, since a steepening in the radio spectrum is expected, but sensitive flux density measurements are missing above $\sim 5-10$ GHz and the observations at high radio frequencies are not easy to perform.
The Medicina telescope, already fully operational at the time, was exploited in order to plan in the most efficiently way the tests devoted to SRT. The Medicina antenna is a 32-m Cassegrain radiotelescope with parabolic primary mirror and hyperbolic secondary mirror. It was built in 1983, 30 km from Bologna, and can receive signals in the frequency range $1.4 - 26.5$ GHz. The main characteristics of this instrument are frequency agility (the observing frequency can be changed very quickly, with a maximum time lower than 4 minutes) and complete automation and remote control of the observing settings. Both W44 and IC443 were observed with Medicina in May 2012 at 5 GHz (C-band) and 8 GHz (X-band), with a corresponding beam size of $7.9'$ and $4.8'$, respectively. The observations was carried out with the Total Power (TP) back-end, an analog double polarisation device also available at SRT (see Section 2.4 for more details). The C-band observations were performed at the central frequency of 5.1 GHz, with a bandwidth of 150 MHz and by setting the Local Oscillator at 4.9 GHz, while for the X-band these parameters were set at 8.18 GHz, 250 MHz and 8.08 GHz, respectively. Mapping of W44 and IC443 was carried out through the On The Fly (OTF) scanning mode, which will be described in more detail in the following Sections. The resulting maps (shown in Fig.2.8(a) for W44 and Fig.2.8(b) for IC443) were obtained by merging the maps acquired in all the observational sessions. The results obtained in this phase allowed us to test the feasibility of single-dish mapping on extended sources and to improve the planning on the OTF mapping parameters with SRT.
In the context of our single-dish imaging studies of SNRs, we obtained the most important results from the observations carried out with SRT. This radio telescope (shown in Fig.2.5(a)) is a new general purpose fully steerable 64-m diameter radio telescope designed to operate with high efficiency across the 0.3-116 GHz frequency range (Prandoni et al., 2017). It is a challenging scientific project of the Italian National Institute for Astrophysics (INAF). The three research units of the INAF involved in the scientific and technical collaboration on the SRT project are: the Institute of Radio Astronomy (IRA), the Cagliari Astronomical Observatory (OAC), and the Arcetri Astrophysical Observatory (OAA). The project was funded by Italian Ministry of Education and Scientific Research (MIUR), the Sardinia Regional Government (RAS), the Italian Space Agency (ASI), and INAF itself. SRT is designed to be used for astronomy, geodesy, and space

(a) (b)

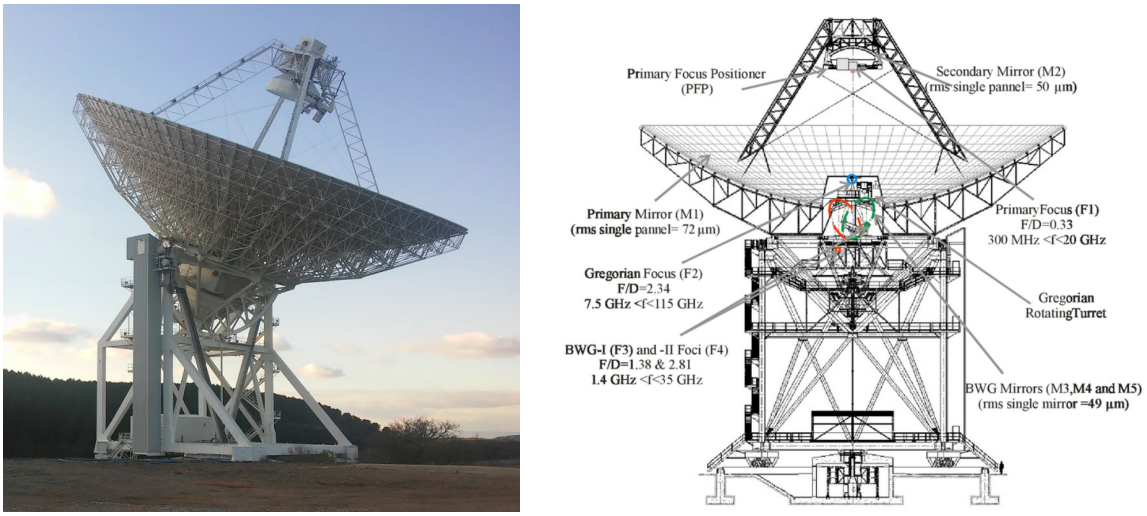

Figure 2.5: SRT (a) and the representation of its mechanical structure (b). The different focal positions are indicated.

science, both as a single dish and as part of European and international networks. The observing time of the telescope is distributed among the radio astronomy applications (on the order of 80% of the telescope time) and the activities of interest of ASI (the remaining 20%). The telescope is located 35 km North of Cagliari, Sardinia, Italy, at about 600 m above the sea level. The SRT optical design is based on a quasi-Gregorian configuration with shaped 64 m diameter primary and 7.9 m diameter secondary reflectors to minimize spillover and standing waves. The primary active surface consists of 1008 aluminium panels (with a panel manufacturing $rms < 70$ μm) and of 1116 electromechanical actuators under computer control that compensate the gravitational deformation of the backup structure (Orfei et al., 2004). SRT is presently equipped with three cryogenic dual-polarisation receivers placed at different focal positions (shown in Fig.2.5(b); Valente et al. 2010, Navarrini et al. 2016, Valente et al. 2016, Navarrini et al. 2017): a 7-beam K-band receiver (18−26.5 GHz, Gregorian focus), a mono-feed C-band receiver (5.7−7.7 GHz, Beam Wave Guide focal position), and a coaxial dual-feed L/P band receiver (0.305−0.41 GHz and 1.3−1.8 GHz, primary focus).

In the framework of the AV test activities, W44 and IC443 were observed for the first time with SRT in order to test the imaging capabilities and single-dish performances of the telescope for different receivers and backends configurations (Prandoni et al., 2017). At this time, I started my collaboration with the research group led by Alberto Pellizzoni that included my participation in the observing session at SRT and in the activities of implementation and test of the data analysis tool designed to perform continuum imaging of extended sources with the Medicina telescope and SRT. The observations were carried out from 2014 May 27 to December 10 (~12 hours of effective time on targets) with the Total Power backend at the central frequency of 7.24 GHz (C-band)

and a bandwidth of 680 MHz. In this phase we checked the effects of the RFI contamination on the single RA or Dec scans at this frequency. An example of the single scan quality is provided, in the case of IC443, in Fig.2.6. We also verified the improvement on the map quality obtained by merging the data carried out during the different observational sessions, in particular for what concerns the RFI rejection and the signal/noise (Egron et al., 2016). Finally, we observed the effects of a non optimal weather condition on the quality of the maps. As show in Fig.2.7, the clouds appear as a purple bow on the map, making it difficult to detect the source. A clear sky or at least an uniform coverage is then required in order to carried out good quality data.

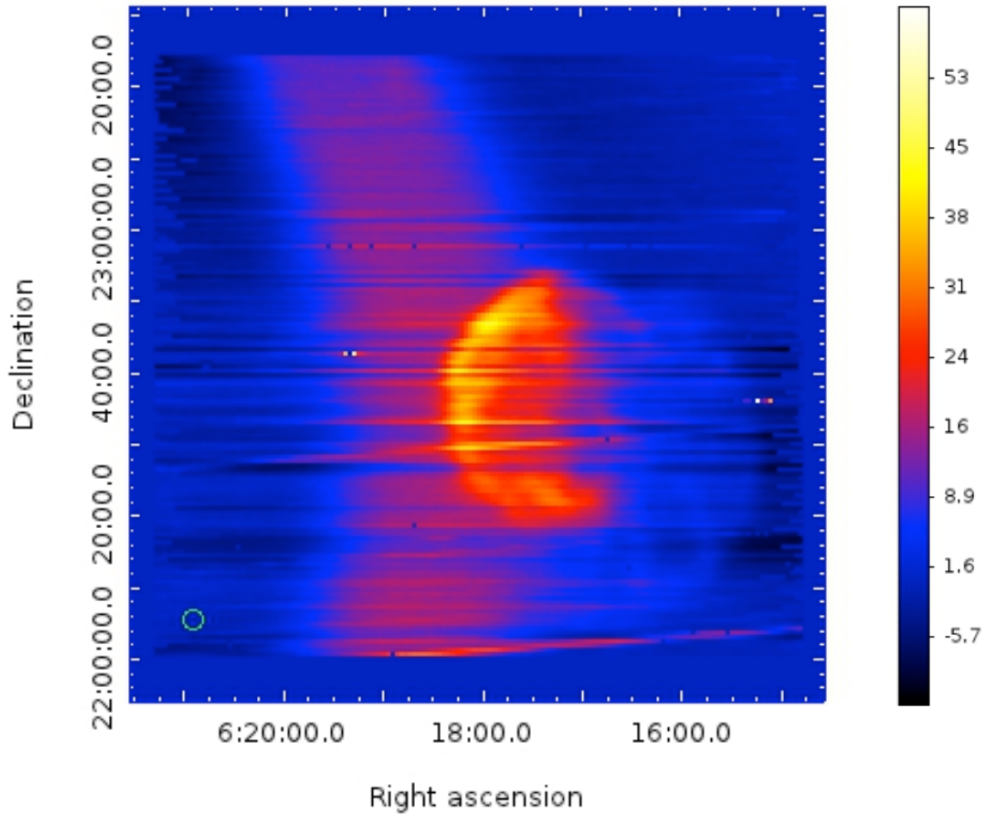

Figure 2.7: Not calibrated map of IC443 carried out with SRT at 7.24 GHz on 2014 April 14 under non-uniform cloudy sky conditions (Egron et al., 2016).

The maps of W44 and IC433 obtained with SRT at 7.24 GHz are shown in Fig.2.8, together with those carried out with the Medicina radio telescope at 5 GHz. For both sources the SRT images provide details of the remnant structure that are consistent with the main features observed in interferometric images. The related flux density measurements are in agreement with those available in the literature (Egron et al., 2017), as it is discussed in Subsection 2.5.1. These results enabled us to check the imaging capabilities of SRT in performing OTF observations of extended sources, and have also opened up promising possibilities to perform flux density

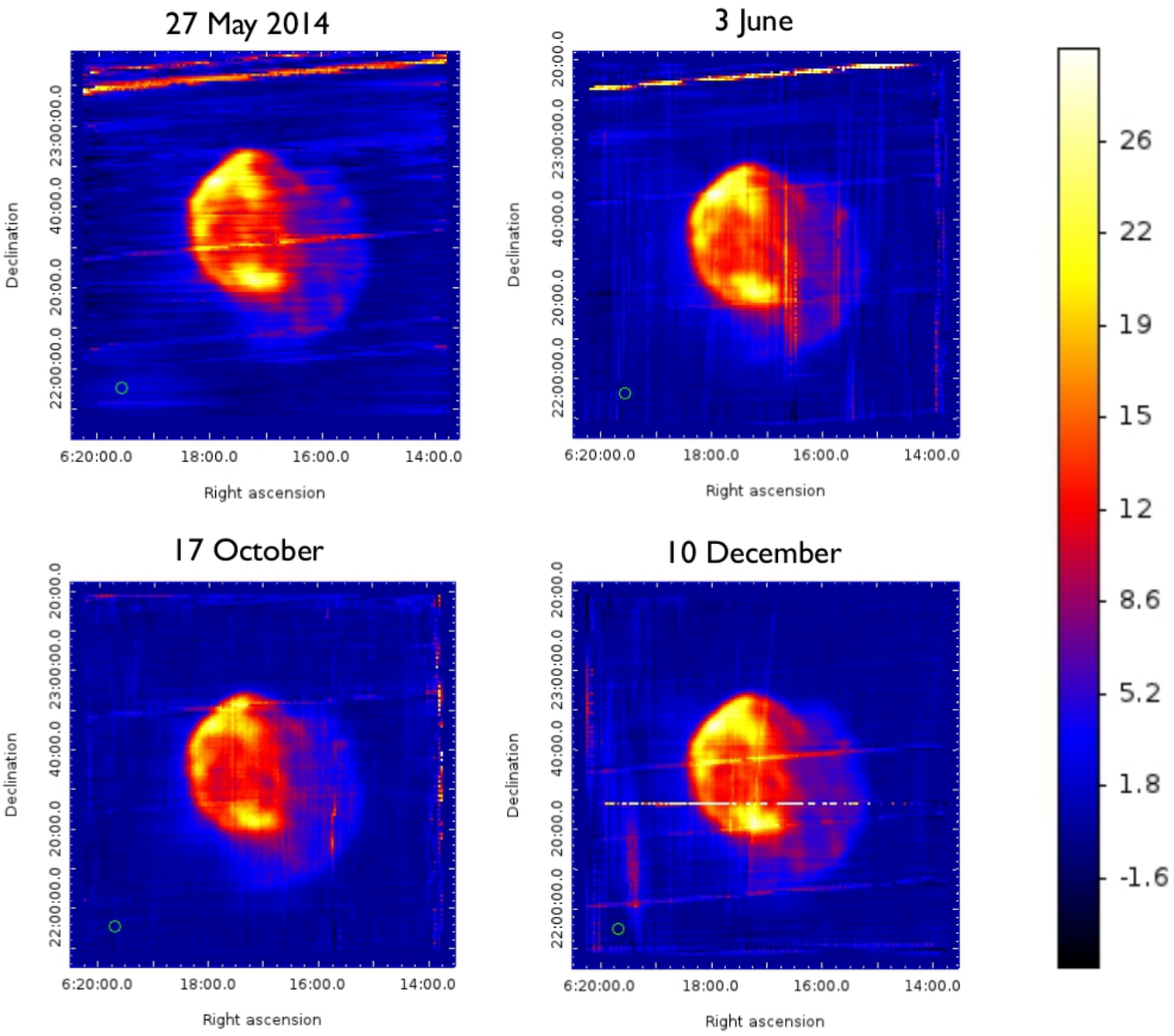

Figure 2.6: Not calibrated maps of IC443 at 7.24 GHz related to each observing session performed with SRT during the AV (Egron et al., 2016). The diagonal-bright lines are ascribed to RFI, while the horizontal line in the observation of the 2014 December 10 indicates a wrong baseline subtraction.

measurements in different resolved regions of the sources.
The obtained results encouraged us to propose a larger program entitled "Constraining Cosmic Rays Production in Supernova Remnants with SRT" dedicated to the observation of SNRs with SRT (S0009, PI A. Pellizzoni) in the framework of the ESP. The program was granted with 110 hours dedicated to the observations of the SNRs W44, IC443 and Tycho, which were performed between 2016 February and March at three different central frequencies: L-band (1.55 GHz), C-band (7.0 GHz) and K-band (21.4 GHz). This project has led to the publication on the scientific journal *Monthly Notices of the Royal Astronomical Society* (MNRAS) of the paper Egron et al. (2017) entitled "Imaging of SNR IC443 and W44 with the Sardinia Radio Telescope at 1.5 and 7 GHz", where we analysed the first images of W44 and IC443 at 7 GHz. In this work we also presented our flux density measurements obtained in the L- and C-band and their interesting implications on both the integrated and spatially-resolved spectral index studies. Subsequently, a second paper entitled "Investigating the high-frequency spectral features of SNRs Tycho, W44 and IC443 with the Sardinia Radio Telescope" was published in 2018 on MNRAS (Loru et al., 2019). In this work we presented, for the first time, the images of W44 and IC443 at 21.4 GHz and related sensitive flux density measurements, which have shed new light on the high radio frequency spectra of these evolved SNRs. These works are 2 among of the first 5 papers related to the early scientific production of SRT.
In view of the results obtained with Medicina and SRT both in the context of the AV and ESP (see Section 2.5 for more detail about these results), we decided to propose in 2017 an observing project entitled "Modelling spatially-resolved spectra of the Cygnus Loop Supernova Remnant" (project 14-17, PI: S. Loru) aimed to perform accurate OTF maps of Cygnus Loop with the Medicina Radio Telescope in the C-band (5 GHz) and X-band (8.3 GHz) in order to study its complex morphology at frequencies above those available so far. The proposal was accepted with 80 hours for the observations that were performed between 2017 June and August. More details about this project and related results are provided in Subsection 2.5.2.

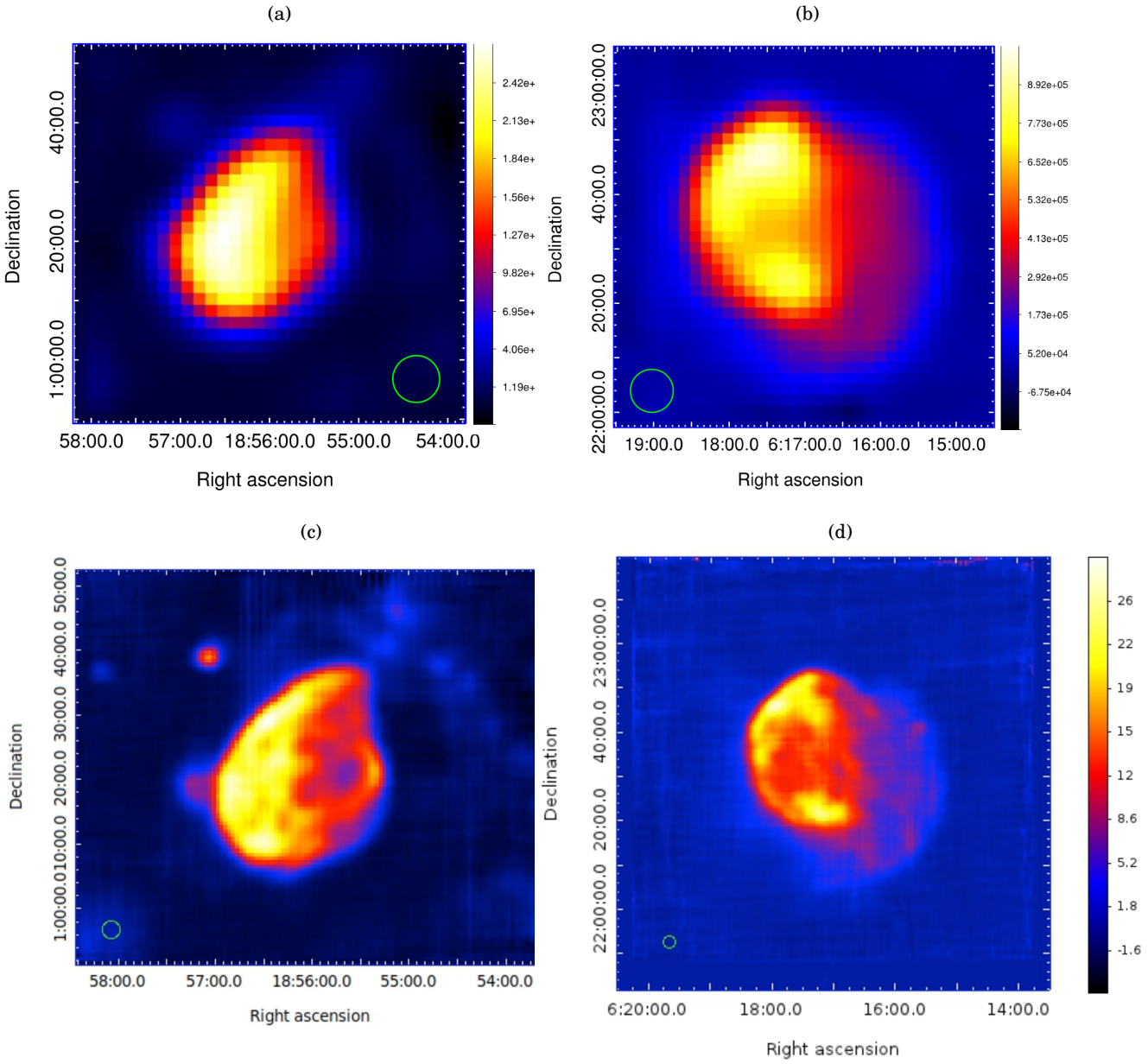

Figure 2.8: Maps of W44 (a) and IC443 (b) carried out with Medicina radio telescope at 5 GHz (resolution ~2′), and with SRT at 7 GHz (resolution ~0.6′), respectively (c) and (d). The green circles on the bottom left indicate the beam size at the observed frequencies equal to 7.9′ and 2.7′ for Medicina and SRT, respectively. The Medicina maps are calibrated and the colour bars are reported in units of Jy/sr. The SRT maps are not calibrated and the related colour bars are reported in units of counts/sr.

2.2 Observed targets

2.2.1 W44

W44 is a middle-aged SNR with an estimated age of ~20,000 yrs and an angular size of ~30′ (Wolszczan et al. 1991, Smith et al. 1985). This SNR is located in a crowded region of the Galactic plane, which is rich in both thermal and non-thermal sources, in the inner part of the W48 molecular cloud complex at a distance of ~ 3 kpc (Onić, 2015). It has been shown that W44 represents a typical case of a SNR-molecular cloud interacting system. Indeed, the W44 region is one of the brightest CO emission regions in the Milky Way (Seta et al., 1998).
In the radio band, this SNR is characterised by an asymmetric limb-brightened shell. A radio image of W44 at 324 MHz is shown in Fig.2.9(a) (Castelletti et al., 2007). The brightest emission is located along the eastern boundary (RA, Dec = $18^h56^m50^s$, 01°17′), where the SNR interacts with dense molecular clouds (Seta et al. 2004, Reach et al. 2005). A short bright arc is visible in the western region (RA, Dec = $18^h55^m20^s$, 01°22′), which is related to the interaction between the SNR shock and a molecular cloud. The bright filaments located in the eastern inner region are aligned in the south-east north-west direction (they are also visible in Fig.2.9(a)). They result from radiative shocks encountering the clouds or sheets of dense gas (Jones et al., 1993). A young-active pulsar PSR B1853+01 is associated to W44, and it is located nearly 9′ south of the centre of the SNR. A synchrotron nebula characterised by a cometary shape was also observed in W44. It is thought that this nebula is ionized by the spin-down energy of the pulsar, which is located at its southern apex (Frail et al., 1996).
A study performed by Seta et al. (1998) and based on the mapping of the molecular gas around W44, revealed the presence of six giant molecular clouds surrounding the SNR. Among these, the cloud GMC G34.8−0.6 shows evidence of interaction with W44. Indeed this cloud coincides in position with the SNR and its interaction is suggested from: the morphology and kinematics of the cloud; the detection of CO line wing emission with very high CO $J = 2-1$ to $J = 1-0$ ratios; the presence of near-infrared emission from vibrationally excited molecular hydrogen. A study performed by Seta et al. (2004), which is based on the CO $J = 1-0$ emission mapping carried out with the Nobeyama 45-m radio telescope, revealed several CO features possibly associated with the SNR. Among these there are: high-velocity line-wing emission, sharp-edged clouds at the CO/SNR interface, spatially extended moderately broad line emission (SEMBE) within the SNR, and CO emission morphologically associated with the radio continuum and/or X-ray emissions. These features are represented in the schematic picture of W44 provided by Seta et al. (2004) (see Fig.2.9(b)). The stronger interaction of W44 with the ISM, which principally occurs in the front side of the remnant, is provided in this picture. The giant molecular cloud G34.9−0.6 is detected in the CO map, and it shows a sharp edge that coincides with the eastern radio continuum rim of W44. This is interpreted by authors as the evidence that the SNR/cloud interaction is observed almost edge-on. Furthermore, the existence of the “edge” suggests that most of the molecular

mass resides in smaller clumps that evaporate rapidly after the passage of the supernova blast wave. In the southern part of the bright radio shell four spots of high-velocity CO emission were detected. One of them is associated with a filamentary structure, while the other three correspond to wing compact regions that unambiguously confirm the presence of compressed and accelerated gas resulting from the interaction between W44 and a giant molecular cloud. The SEMBE associated with the brighter radio continuum shell is interpreted as a layer of clumps formed in the shocked molecular gas and disturbed by the expanding shell of the SNR.

The giant molecular cloud associated with W44 was also investigated by Reach et al. (2005) by using the near-infrared and millimeter-wave observations. The CO maps show the giant molecular cloud associated to W44, most of which is located in front of the remnant. The velocity of this cloud is consistent with Galactic rotation at the longitude and distance of W44. This suggests that the molecular environment with which W44 is interacting could be the same environment from which the progenitor star formed. The morphology of the CO map of W44 at 45.4−52.0 km s^{-1} (see Fig.3e in Reach et al. 2005) shows the correlation between the north-eastern ridge of bright radio emission and the surface of the molecular cloud. On the other hand, the 38.9−42.8 km s^{-1} map (see Fig.3f in Reach et al. 2005) suggests the interaction of the cloud with the western part of W44 that probably explains the very bright western radio knot. This evidence of interaction is also highlighted by the images obtained from the near-infrared observations that revealed a bright-shocked H_2 emission in the north-eastern, southern, and western parts of W44. Furthermore, the H_2 images show some diagonal filamentary structures that match remarkably well the radio filaments observed across the western part of W44 (see Fig.10 in Reach et al. 2005). These features could likely be the result of a pre-shock medium that was highly structured with gaps between regions containing gas with density high enough to generate bright H_2 after being shocked.

A study of both integrated and spatially resolved radio spectrum of W44 was performed by Castelletti et al. (2007) in the framework of VLA observations at 74 and 324 MHz. They obtained an integrated spectral index of $\alpha = 0.37 \pm 0.02$ by using a simple power low ($S \propto \nu^{-\alpha}$) to model the SED of W44 in the 408−10700 MHz frequency range. This result rules out a possible turn over due to free-free absorption to well below 100 MHz, accordingly to previous studies (Kassim, 1989). The spatially-resolved spectral index study was performed using 74/342 GHz and 324/1442 MHz spectral index maps. This investigation revealed an unperturbed spectral index of $\alpha \sim 0.5$ between 74 and 1442 MHz, which is in agreement with a simple diffusive shock acceleration occurring in in the filamentary shell of W44. On the other hand, a spectral flattening is observed at the lowest frequency pair associated with the radio-bright westernmost arc. This feature could be attributed to strong post shock densities and enhanced magnetic field in this region where the SNR shock is colliding with a molecular cloud. The spectral index is instead inverted ($0.0 < \alpha < -0.4$) at low frequencies in the south-east border of the bright radio shell of W44. This effect is probably a consequence of two mechanisms: the free-free absorption from ionized

gas in the post shock region at the SNR/molecular cloud interface, and the thermal absorption associated with the HII region that here collides with the SNR edge, enhancing the density of thermal electrons. The same study included the comparison of the 324 MHz image with the 4.5 μm IR image. It was noted that there is a significant correspondence between the two emissions across the north and south-east parts of W44 with a perfect overlap of the filamentary structure. In order to investigate possible warm dust regions associated with star formation processes and interacting with W44, a further comparison was performed between the 324 MHz image and the *Spitzer* images at 8 μm and 24 μm. The resulting image, which is shown Fig.2.9(c), reveals the hot dust grain emission (indicated in red) related to the Strömgren sphere that is confined in its eastern side by an annular photo dissociation region (PDR) observable at 8 μm (indicated in green). The IRAS point source 18544+0112 was also observed in the region adjacent to the bright radio/spectra inverted filament, where a CO edge was detected (Seta et al., 2004). It is thought that this source is a young stellar object in a primitive evolutionary stage (Molinari et al., 1996). The complex nature and the rich phenomenology of this region could suggest that the cloud collapse that originated the young star could have been triggered by the wind from the progenitor star of W44.

Radio observations at higher frequencies were performed with low-resolution instruments like *Planck* (in the 30−70 GHz frequency range) and QUIJOTE (in the 10−20 GHz frequency range) (Planck Collaboration et al. 2016, Génova-Santos et al. 2017). The images carried out with $Planck$ (from 30 GHz to 857 GHz) and QUIJOTE at 17 GHz and 19 GHz are shown in Fig.2.10(a) and Fig.2.10(b), respectively. As shown in these images, W44 is located in a very crowed portion of the Galactic plane that makes the detection a challenge for these telescopes. A possible spectral break around 45 GHz was considered by $Planck$ collaboration (see Fig.3 in Planck Collaboration et al. 2016), but the discrepancy between the 30 GHz and 70 GHz flux density measurements, possibly due to confusion with unrelated large-scale emission from the Galactic plane, makes difficult to demonstrate its existence. The study carried out by Génova-Santos et al. 2017, showed instead a significant presence of anomalous microwave emission (AME) associated with W44. However, also in this case, more sensitive data are required to confirm the excess of emission associated with the AME in the frequency range $\sim$ 20−70 GHz.

W44 is an interesting source also from a high-energy point of view. Indeed it was the first SNR detected by the AGILE γ-ray satellite in the frequency range 50 MeV − 10 GeV (Giuliani et al., 2011). These observations allowed, for the first time, to investigate a SNR in the energy range (photon energy below 200 MeV) where it is possible to distinguish the leptonic or hadronic nature of the γ-ray emission. The data acquired with AGILE and, successively, with the Fermi-LAT satellite were largely used in order to test the theoretical models on the multiwavelength spectrum of W44 from the radio to the γ-rays (Ackermann et al. 2013, Cardillo et al. 2016). As shown in Fig.2.9(d), the γ-ray emission detected by AGILE indicates a quasi-elliptical morphology that corresponds to the interior part of the radio shell in its brightest parts along the north-west

and south-east regions. In addition, it was observed that the γ-ray morphology matches almost perfectly with the regions where the SNR interacts with the molecular cloud (Reach et al., 2005).

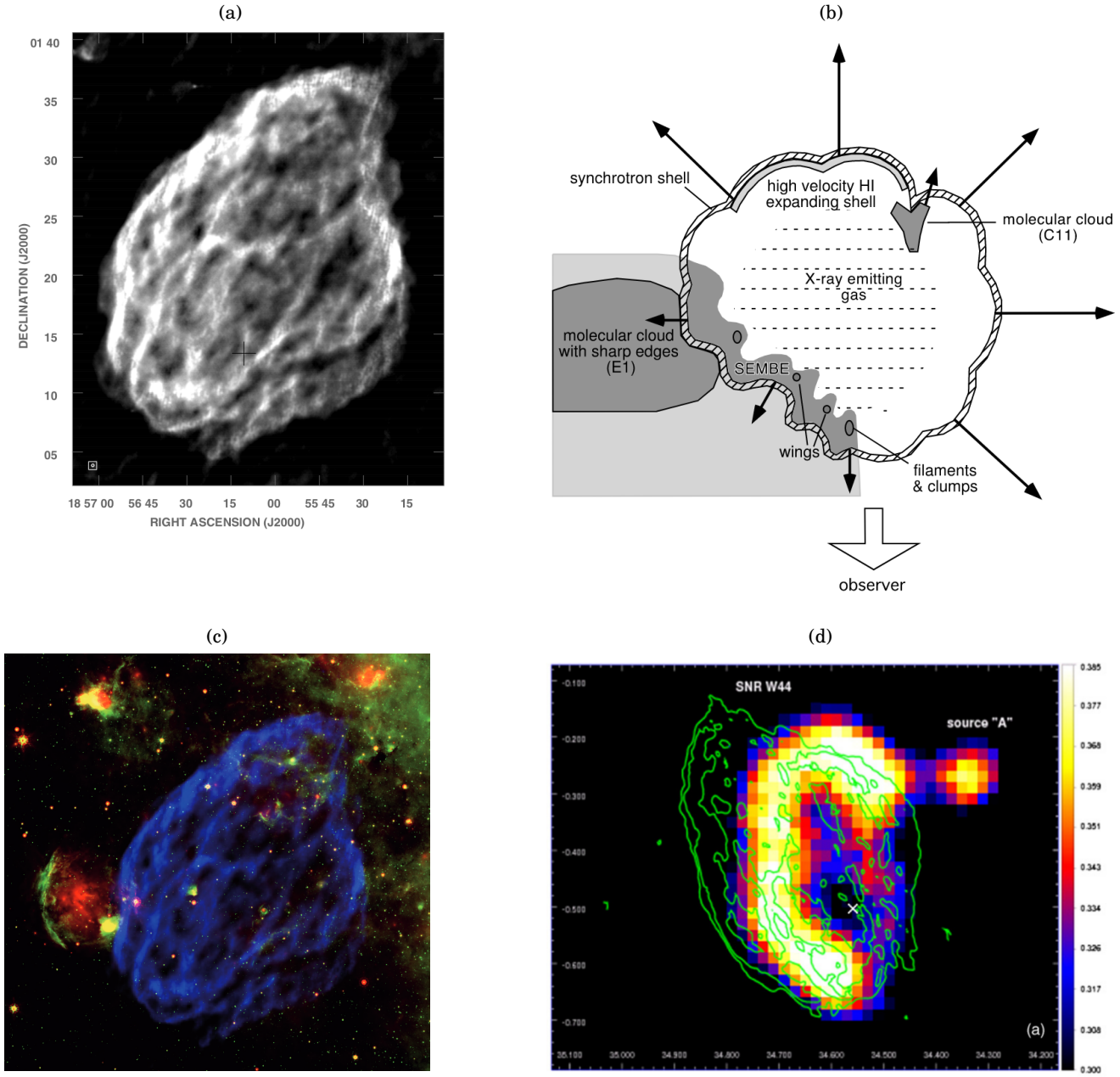

Figure 2.9: (a) Radio image of SNR W44 at 324 MHz carried out with the VLA with a resolution of 13′′. (b) Schematic representation of W44 and its interaction with the ISM that was provided by Seta et al. (2004) on the basis of their CO observations. (c) Multi-frequency image of W44 where the green and red images corresponds to the Spitzer 8 μm and 24 μm data, respectively, while the VLA 324 MHz image of the remnant is indicated in blue (Castelletti et al., 2007). (d) AGILE gamma-ray intensity map of W44 in the energy range 400 MeV−3 GeV as presented by Giuliani et al. (2011). The green contours indicate the 324 MHz radio emission.

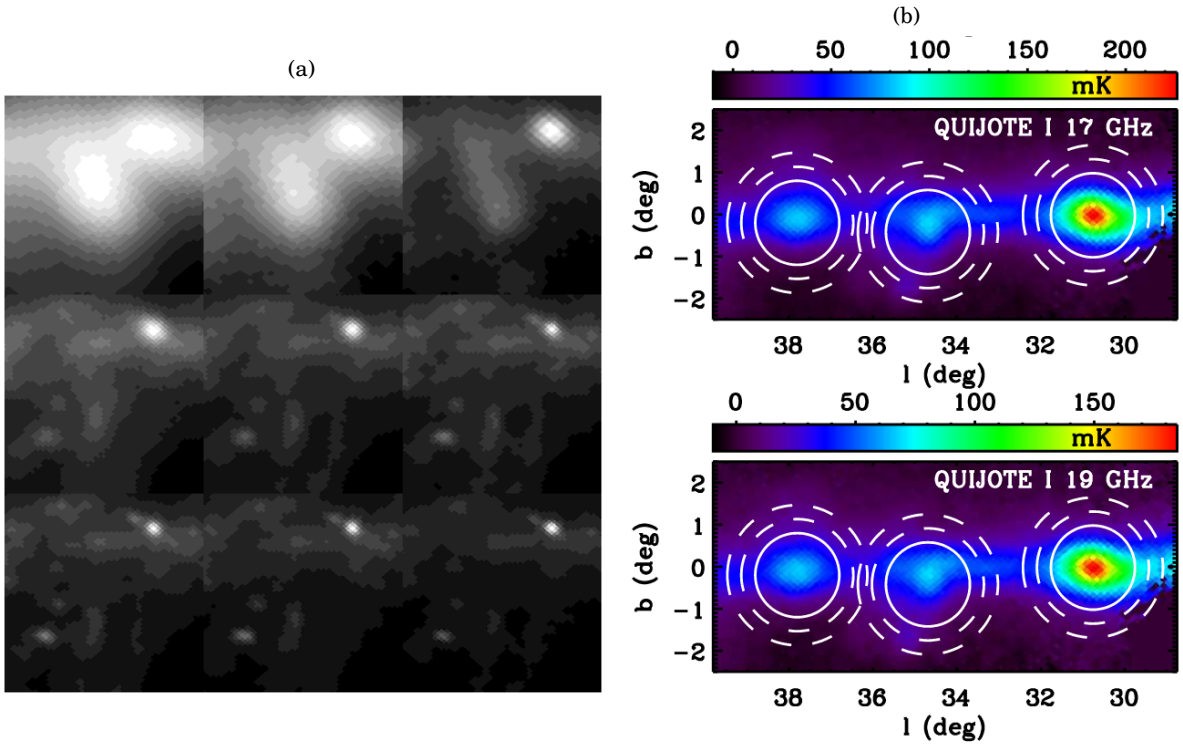

Figure 2.10: a) Images of W44 as observed by *Planck* at frequencies ranging from 30 GHz at top left to 857 GHz at bottom right. b) Images of the regions around W43, W44 (central source) and W47, derived from the QUIJOTE observations at 17 GHz and 19 GHz. The solid circles show the apertures that was used for flux integration, whereas the dashed contours limit the extent of the ring used for background subtraction.

2.2.2 IC443

IC443 is a large SNR of ~ 45′ in size. It was formed nearly 4,000 yrs ago (Troja et al., 2008), and it is located at a distance of ~1.5 kpc (Petre et al., 1988). The presence of both diluted and dense gaseous environments surrounding the SN blast wave and the interaction of the SN shock with several atomic and molecular clouds, make IC443 a very interesting system in order to assess the scenario of CRs acceleration in SNRs. Its location close to the Galactic anti-centre, which is relatively isolated from the confusing contamination by unrelated Galactic plane emission, also makes this SNR a suitable target for low resolution radio and gamma-ray observations (Planck Collaboration et al. 2016, Tavani et al. 2010).

In the radio domain, IC443 appears to be composed of two nearly concentric shells of synchrotron emission. The shell that is located in the eastern part of the SNR (shell A) includes the bulk of the radio emission, and it is connected in its western side to the weaker second shell (shell B), which is possibly related to a breakout portion of the SNR into a rarefied medium (Lee et al., 2008). A schematic representation of the radio morphology of IC443 is provided in Fig.2.11(a).

The bright-southern boundary of the shell A is associated with the interaction between the shock and a mostly molecular medium (Burton et al., 1988). Furthermore, the south-eastern part of the shell A is characterized by unusual features such as a halo and spurs, which are most likely originated from the interaction of IC443 with its environment. The latter are faint radial filaments from the bright shell that have a typical size of ~1′. The halo appears as a diffuse emission along the south-eastern boundary of the remnant, and it extends radially by ~5′ from the bright shell. In the same region, another SNR (G189.6+3.3) was observed, which is positionally coincident with the halo and filaments of IC443. Lee et al. (2008) suggested a possible physical interaction between the two SNRs, but this scenario has not yet been confirmed. The shell B is nearly completely circular with a diameter of about 50′. With the exception of some enhancement at the location of the optical filaments, the surface brightness is quite uniform and does not show noticeable limb-brightening, but it decreases near the edges. The 21 cm HI emission studies indicate several HI features mostly located in the southern boundary of the shell A (Lee et al., 2008). Their correspondence with the shocked molecular emission features could suggest an ongoing interaction between the SNR and a molecular cloud. The north-east region is also associated with the shocked HI emission, which consists of several well-defined filaments that are well correlated with the optical filaments, both in position and velocity. This correlation suggests the presence of recombined HI from an atomic shock in this region. Near infrared studies confirm this scenario. Indeed, as shown in Fig.2.11(c), the infrared morphology of IC443 is different if it is observed in the J (1.25 μm), H (1.65 μm), and K_s (2.17 μm) bands. The prominent broadband differences are attributed to both an atomic fine structure lines emission mechanism along the north-eastern rim and a molecular rovibrational lines emission along the southern ridge (Rho et al., 2001). A bright cometary-like PWN is located in the same region, and it is associated with the compact source CXOU J061705.3+222127. The PWN, ~2′×1.5′ in size, is characterised by synchrotron emission from relativistic particles generated by the pulsar that interact with the SNR shell (Swartz et al., 2015).

Castelletti et al. (2011) used the VLA high-resolution radio images of IC443 at 74 and 330 MHz in order to investigate both the integrated spectral properties and the spatially-resolved spectral features of this SNR. The integrated flux densities at 74 and 330 MHz were used with the measurements available in the literature in order to study the integrated spectrum of IC443 between 10 MHz and 1000 MHz. The SED of IC443 showed an inversion at low radio frequencies (below 10 MHz) that the authors ascribed to the free-free thermal optical absorption. In order to model the IC443 SED the authors adopted a power law with an exponential turn over, which provided a spectral index of α_{10MHz}^{10GHz}=0.36±0.02 and a significantly stronger absorption at 10 MHz (τ_{10}=1.07). Spatially-resolved spectral index studies were performed by coupling the images at 74 MHz and 330 MHz. The obtained spectral index maps showed a variation in the spectral index distribution from flat values, corresponding to the brighter synchrotron regions, and steeper values associated with the central region and the halo. In the eastern rim

of the shell A and related bright filaments, the flat spectrum ($0.05 < \alpha < 0.25$) was interpreted as consequence of a thermal absorption process. This assumption seems to be confirmed by the infrared observations (see Fig.2.11(c)) that show an impressive agreement in the H and J bands with the radio bright/flattest spectral features. As proposed by Rho & Petre (1998), the infrared emission in these bands comes from scattered dust produced by fast dissociating J-type shock. The passage of a dissociative shock through a molecular cloud dissociates molecules but could also ionize the atoms, producing the thermal absorbing electrons that lead to the peculiar flat radio spectrum in this region. A relativity flat spectrum was also observed in the southern bright region, but in this case the interpretation is related to the interaction with a molecular cloud. Indeed the impact of the SNR blast wave on denser ambient medium could provide stronger post compression shock densities and/or higher magnetic field, with a related enhancement of the Fermi shock acceleration mechanism that could be responsible for the spectral flattening. On the other hand, steeper spectral index values ($0.6 < \alpha < 0.85$) are observed in the central and western halo regions and could be explained by the linear diffusive shock acceleration model for weak shocks.

The outer Galaxy location of IC443 leaves it relatively well isolated from the confusing effects due to other radio sources, and make this SNR well suited for low-resolution radio studies at high frequencies. Indeed IC443 was detected with the *Planck* telescope in the 30−857 GHz frequency range (see Fig.2.12). The SED was analysed by Planck Collaboration et al. (2016) by using the $Planck$ data and the radio data available in the literature. The IC443 SED was described between 10 GHz and 143 GHz by a synchrotron emission model with a spectral break above $\sim$ 40 GHz, probably due to cooling losses by the energetic particles. Instead, at higher $Planck$ frequencies the dominant process is the thermal emission related to dust grains that survived the shock. However the contamination by unrelated Galactic plane emission is significant at these frequencies, and the uncertainty in background subtraction makes the flux density difficult to measure (Planck Collaboration et al., 2016).

A very high energy ($E > 100$ GeV) gamma-ray emission is also associated with IC443. The observations performed by MAGIC, VERITAS, and *Fermi* telescopes (Albert et al. 2007, Abdo et al. 2010, Acciari et al. 2011) revealed a correspondence between the γ-ray emission and the southern radio-bright boundary of the shell A. Furthermore, the ^{12}CO map (see Fig.6 reported in Zhang et al. 2010) showed a molecular gas distribution that is perfectly coincident with the TeV morphology of IC443 as observed by VERITAS (Acciari et al., 2011). This observed correlation between the SNR and the molecular cloud could explain the γ-ray emission in terms of hadronic CRs arising from enhanced pion decay processes. The centroid of the γ-ray emission is significantly displaced from the known PWN. This suggests that the PWN is not the major contributor in the energy band between 200 MeV and 50 GeV (Abdo et al., 2010), confirming the hypothesis of the CR emission from the regions where the SNR interacts with the molecular cloud.

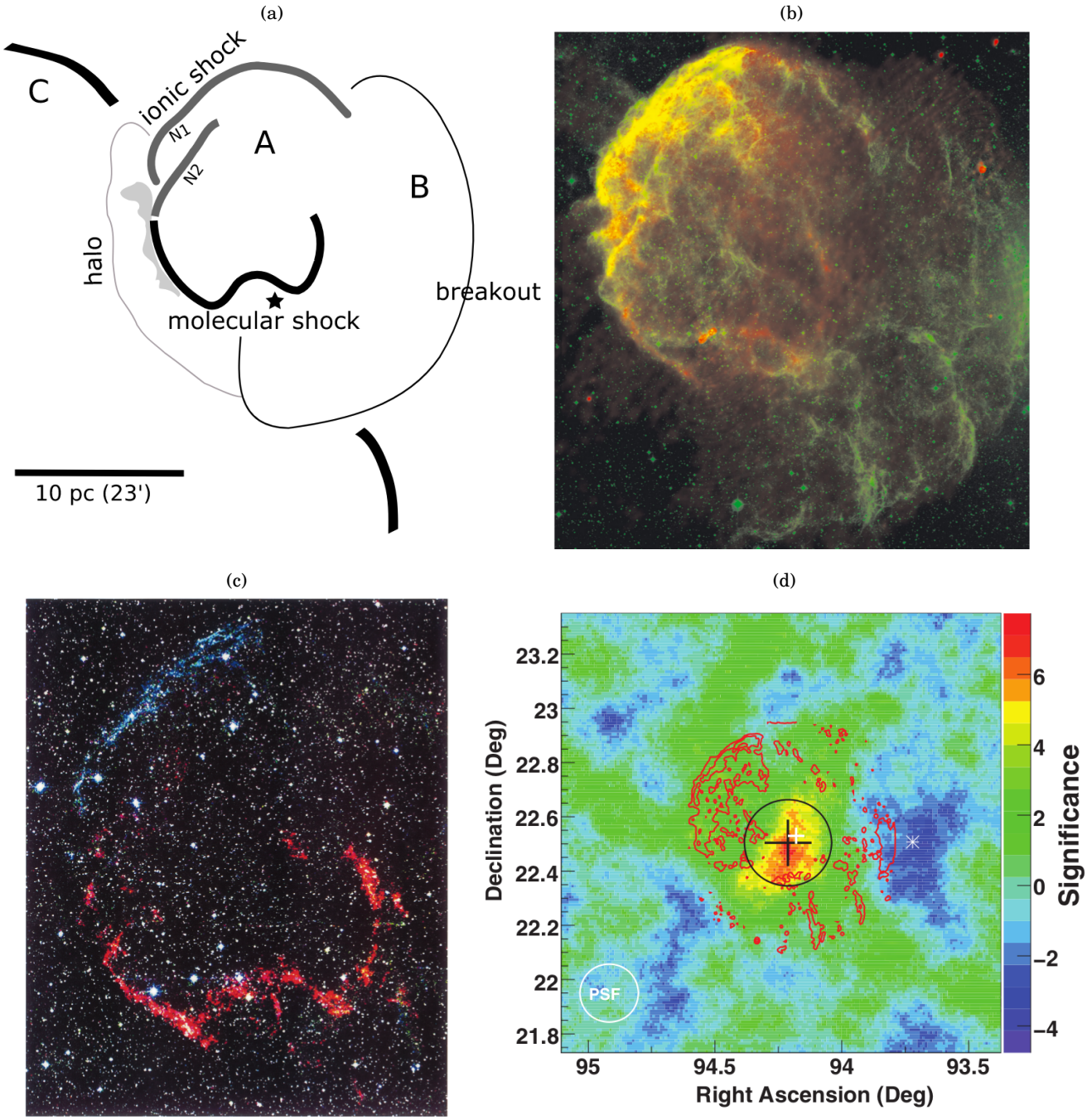

Figure 2.11: (a) Schematic representation of the IC443 morphology. The position of the pulsar is also indicated with the asterisk (Lee et al., 2008). (b) Multi-frequency image of IC443 provided by Castelletti et al. (2011). High-resolution comparison between radio and optical emission from IC 443 SNR. The optical emission is indicated in green, while the high-resolution radio emission at 330 MHz is showed in red. The yellow regions are areas where emission in both spectral bands overlap. (c) Near-infrared image of IC443 carried out with 2MASS in the J (blue), H (green), and K_s (red) bands (Castelletti et al., 2011). (d) Gamma-ray image of IC443 as observed with VERITAS. The black cross-hair indicates the centroid position and its uncertainty and red contours the optical intensity (for more details see Acciari et al. 2011).

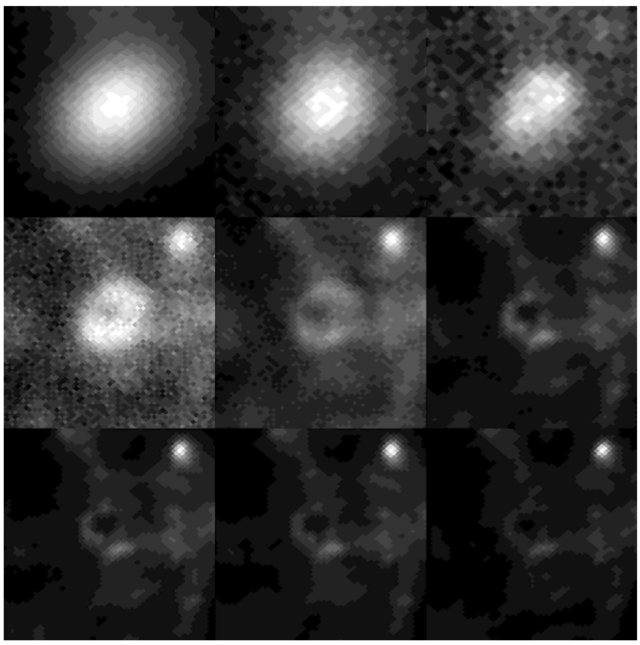

Figure 2.12: Images of IC443 at the nine Planck frequencies, which range from 30 GHz at top left to 857 GHz at bottom right (Planck Collaboration et al., 2016).

2.2.3 Tycho

Tycho SNR (also named 3C10) resulted from a Type Ia SN explosion, and it was discovered by Tycho Brahe in 1572. It is one of the youngest SNRs in the Galaxy, and it is expanding into the ISM without a strong radial density gradient. The average expansion rate is approximately 0.1% yr^{-1}, as expected for a SNR in transition from a rapid expansion to the Sedov adiabatic phase (Reynoso et al., 1997). Different techniques were used for the determination of the distance of this SNR. The value commonly assumed is 2.3 kpc as suggested by Chevalier et al. (1980), according to optical observations of non-radiative shocks and HI absorption (Albinson et al., 1986). Distances of over 4 kpc were also reported in the light of higher-resolution HI data (Swartz et al., 2015). Most recent studies, which are based on the comparisons of hydrodynamic simulations with the data, support a distance of Tycho of 3.5 kpc (Williams et al., 2013).
Tycho has been well investigate across the whole electromagnetic spectrum. The images of Tycho related to X-ray Chandra observations in the 3−8 keV range (Fig.2.13(a)), VLA radio observations at 1.4 GHz (Fig.2.13(b)) and the optical Hα observations (Fig.2.13(c)), are shown in Fig.2.13.
At radio wavelengths, Tycho exhibits a well defined loop structure with an angular diameter of $8'$ and a total continuum flux density of 56 Jy at 1 GHz (Green, 2017). The radio brightness distribution of this SNR indicates a thin outer rim where both shock compression and particle acceleration occur, and a thicker main shell in which instabilities and turbulent amplification of the magnetic field may be responsible for the emission. Three faint optical filaments appear

along the eastern rim of the radio shell, extending north in azimuth to the north-west rim. A thin bright rim located just outside the main shell is clearly distinguished in the radio images (Fig.2.13(b)). This rim is not continuous along the entire loop structure of Tycho. Where present it coincides perfectly with the outer X-ray boundary, while it is missing along the eastern edge, and coincides with some optical filaments. This overlap is associated with regions of strong compression where the expanding remnant has encountered a medium anomalously dense, which leads to an isothermal shock (Dickel et al., 1991). A good correlation between X-ray and radio emission has been detected also throughout the remnant. However, the emission from the main shell appears to be very clumpy both in radio and X-ray band, and not always their detailed features coincide. The X-ray emission is produced by the material heated by a reverse shock, which is characteristic of the double-shock stage that is reached by Tycho. In this phase, the interaction between the density irregularities/clumps in the circumstellar medium and the expanding shock can produce the Raleigh-Taylor instabilities. These provide energy for the magnetic field amplification and relativistic particle acceleration, which are accountable for the observed clumpier emission (Dickel et al., 1991).

Gamma-ray observations carried out by VERITAS were interpreted through leptonic and hadronic models by Acciari et al. (2011). Both models provide a reasonable fit to the data implying a magnetic field of ~80 μG, which is possibly interpreted as an evidence of magnetic field amplification. The integrated radio spectral index of Tycho in the 0.178−17.1 GHz frequency range is $\alpha = 0.58 \pm 0.02$ (Sun et al., 2011). A slightly concave up model (hardening to higher frequencies) was proposed to describe the integrated spectrum of Tycho (Reynolds & Ellison, 1992). Indeed, a spectral flattening, which arises from a thermal Bremsstrahlung component at high frequencies, and an integrated spectral index in the range 0.3−0.7 are considered to be typical characteristics of shell type remnants of which Tycho is thought to be a member (Hurley-Walker et al., 2009). Different spatially resolved spectral-slope studies of Tycho were performed in order to search for possible spectral steepening variations across the SNR. A study performed by Duin & Strom (1975) highlighted a spectral steepening close to the SNR centre that could be related to a high-energy electron distribution in the thinner shell, where the dense thermal material has been swept up from the interstellar medium. A following study of the spectral index distribution contradicted this result, and revealed no significant spatial variations (Klein et al., 1979). More recent sensitive low-frequency VLA observations (0.3−1.4 GHz, Katz-Stone et al. 2000) allowed to identify different radio structures within Tycho, providing a more detailed spatial study of the spectral index across the entire SNR. In the outer regions, the brighter filaments display flatter spectral indices than the fainter ones. This may be due to competing mechanisms such as the SNR blast wave-ambient medium interactions and the internal inhomogeneities of the magnetic field within the remnant (Katz-Stone et al., 2000).

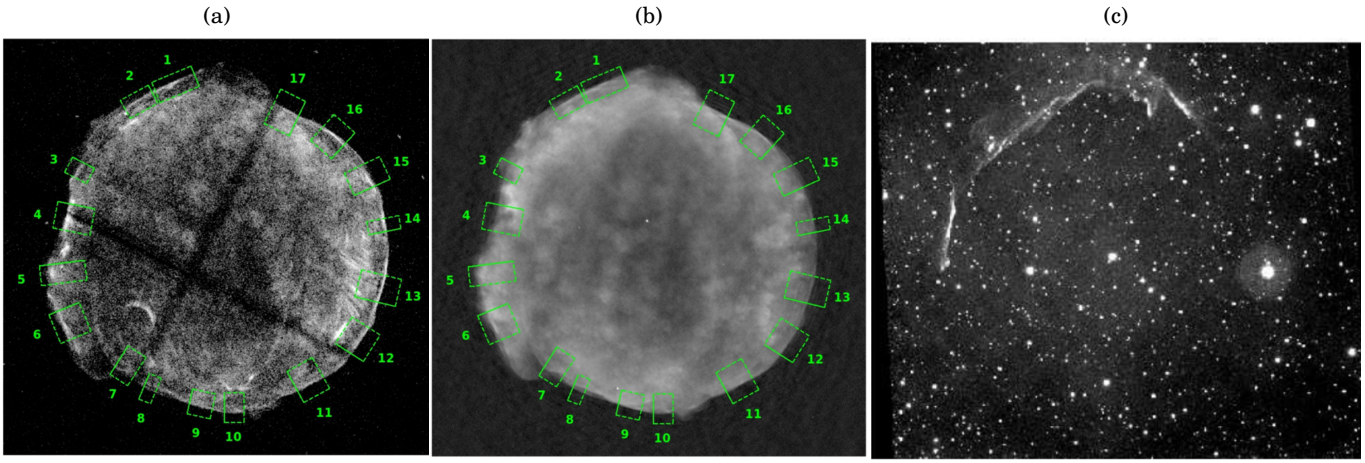

Figure 2.13: (a) Tycho's SNR as observed with *Chandra* in the 3−8 keV X-ray energy range (Williams et al., 2016). (b) VLA image of Tycho's SNR at 1.4 GHz with beam size of 1.91″ × 1.91″ (Williams et al., 2016). (c) High-resolution optical H_α image of Tycho's SNR as reported by Williams et al. (2013). Overlaid on both (a) and (b) images are the 17 regions used by Williams et al. (2016) to measure the proper motion of the shock.

2.2.4 Cygnus Loop

The Cygnus Loop (G74.0−8.5) is a bright SNR (its radio flux density is ∼ 210 Jy at 1 GHz) that was discovered by William Herschel in 1784. It is a middle-age remnant with an estimated age of $1–2\times10^4$ yr and characterized by an apparent size of $\sim 4° \times 3°$. From the *Hubble Space Telescope* data, the distance of this SNR was estimate by Blair et al. (2005) at 540 pc. More recent studies, which were based on the distance of two stars located within the remnant, established a distance to the Cygnus Loop of ∼ 1 kpc (Fesen et al., 2018). Thanks to its large size, its location well out of the Galactic plane, and its high brightness, Cygnus Loop is well suited for observations across the entire electromagnetic spectrum. Cygnus Loop has been classified as a typical middle-age shell-type SNR, however its complex morphology seems to deviate largely from a spherical shell (Uyanıker et al., 2004).

In the radio band this SNR presents a very characteristic morphology with a large northern circular shell and a bubble-like shell located in the southern part. The radio studies showed substantial differences in the total intensity between these two regions (Green, 1990). Indeed, the southern shell of the remnant appears incomplete in its western part (characterised by a crescent-like shape), which is related to a weak peripheral emission. This region is brighter than most of the northern portions of the Cygnus Loop, and a spectral index variation ($\Delta\alpha \sim 0.2$) was also observed between the two shells. These evidences suggest that the northern part of the remnant is governed by the compression of the magnetic field due to the SN explosion shock. Instead, the southern part results most likely from shock acceleration, which is thought to act in young remnants, rather than on the compression of the interstellar magnetic field (Green, 1984).

Recent observations carried out at 2695 MHz with the Effelsberg telescope (Uyanıker et al., 2004) support these evidences. As shown in Fig.2.14, the obtained radio image reveals a diffuse plateau surrounding the bright radio features of the remnant, in particular close to the north and north-eastern shell. This plateau appears as the counterpart of the X-ray and infrared emissions, a correlation that was not observed in the southern shell. The polarization data analysed in the same study revealed significant differences in the magnetic field configuration between south and north, which are attributable to different mechanisms acting in these regions. Furthermore, the authors highlighted that the upper part of the polarized southern shell overlaps with the northern shell, but it results from a shock originating in the south.

From a multi-wavelength study that combines the radio results with optical, X-ray and infrared data, Uyanıker et al. (2002) assumed an interaction between the two SNRs that compose Cygnus Loop. Indeed, as shown in Fig.2.15(b), the optical image shows that the H_α and OIII distributions are more extended in the northern shell. these emissions could be ascribed to a different interaction of the two shells with the surrounding medium. Furthermore, from the combination of the polarization radio results and the infrared (Fig.2.15(c)) and X-ray (Fig.2.15(d)) images, it was deducted that both SNR shells are not just seen in superposition, but are in physical interaction. Under this assumption, the enhanced soft X-rays might be related to the deceleration of the shock waves due to the collision of the two SNRs. A stellar remnant (probably a neutron star) was observed in the X-ray images (AX J2049.6+2939, detected by the ASCA satellite, Miyata & Tsunemi 2001) close to the centre of the southern shell, providing further proof that this part of Cygnus Loop is independent from the large northern shell. The two interacting SNRs that is thought constitute the Cygnus Loop on the basis of multi-wavelength studies, are centred at ~(RA, Dec)= (20^h 51.36^m, 31° $3'$) with an extension of $3^\circ \times 2.6^\circ$ for the northern shell (named G74.3−8.4), and ~(RA, Dec)= (20^h 49.56^m, 29° $33'$) with an extension of $1.4^\circ \times 1.8^\circ$ for the southern shell (named G72.9−9.0).

Tanks to its large size and its complex morphology, Cygnus Loop has been investigated in terms of spectral index studies. However, while the large extent of Cygnus Loop makes this source ideal to perform spectral index analysis, this same characteristic involves a series of observational limitations. In particular, a baseline stability of the receiving system is necessary in order to obtain a high signal-to-noise ratio and ensure that the large-scale background emission is correctly detected (Sun et al., 2011). If this condition is not fulfilled there is the risk to underestimate the integrated flux density, leading to an artificial steepening of the spectrum. In light of this, it is worth to note that a lot of studies available in the literature (Kundu & Becker 1972, Denoyer 1974 , Kovalenko et al. 1994) suggested an integrated spectral break at about 1 GHz that should be reconsidered taking advantage of new sensitive measurements.

In a more recent work, Uyanıker et al. (2004) performed both an integrated and spatially-resolved spectral analysis by using the high quality data carried out with Effelsberg telescope and DRAO Synthesis Telescope at 408 MHz, 863 MHz, 1420 MHz and 2675 MHz. The related maps at

the different radio frequencies are shown in Fig.2.16. The integrated flux densities associated with these maps are used together with those available in the literature in order to study the integrated spectrum of Cygnus Loop. Unlike previous results, no spectral break indications were observed and the spectrum resulted well fitted by a simple power law model with $\alpha = 0.42$. On the other hand, the spatially-resolved spectral index analysis revealed variations of the spectral indices across Cygnus Loop with an upper limit of $\Delta\alpha = 0.2$. In particular, a flat spectrum was detected in the three regions located respectively in the north-east, north-west and south of the SNR, corresponding to the bright radio filaments. The spectrum was observed to become steeper in the central regions towards the northern part ($\alpha = 0.4$) and the southern part ($\alpha = 0.6$), both confined by the flat spectrum filaments. The authors assumed that the flat spectra observed in correspondence to the brightest partial shells of G74.3−8.4 (NGC 6960 and NGC 6992, seen Fig.2.15(a)), could result from a compression of the magnetic field, similarly to that observed for the SNR S147 (Fuerst & Reich, 1986). However, the spectral variation of $\Delta\alpha = 0.2$ observed between flatter and steeper spectra regions of Cygnus Loop is too low to claim a spectral break around 1 GHz as in the case of S147 ($\Delta\alpha = 0.4$). This is probably due to the earlier evolutionary phase of Cygnus Loop with respect to S147, where the shock acceleration is still dominant. Therefore in this case, a spectral break could be expected at higher radio frequencies, and sensitive maps above ~5 GHz could be crucial to investigating on this respect.

A high frequency study was performed by Sun Sun et al. (2006) by using data carried out with the Urumqi telescope at 4.8 GHz. They used the related flux density measurements together with those carried out with Effelsberg and the DRAO synthesis telescope in the frequency range 408−2675 MHz (the related maps are shown in Fig.2.14), in order to study the integrated spectrum of Cygnus Loop. The resulting SED (shown in Fig.3.12) is well modelled by a simple power law with $\alpha = 0.40 \pm 0.06$, in agreement with the result of Uyanıker et al. (2004). It can be seen that the flux density measurement presented by Sun et al. (2006) is higher by ~20% than the only other measurement available at 4.8 GHz (Kundu & Becker 1972), and which suggests a spectral break. However, this indication of a spectral steepening could be due to the low sensitivity of the instrument with respect to the Urumqi telescope at this frequency, with a related loss of some diffuse emission from the source. Other sensitive flux density measurements at this frequency could be useful to better discuss a possible spectral index break. In the same study the integrated spectrum of Cygnus Loop was investigated taking into account all available flux density values from the literature. In this case, a spectral index of $\alpha = 0.50 \pm 0.06$ was obtained. A spatially-resolved spectral index study was also performed by using the Cygnus Loop maps at 863 MHz, 1420 MHz and 2675 MHz. The results obtained revealed a flattening of the spectral index, with respect to the average value, corresponding to the north-eastern and north-western region ($\alpha \sim 0.40$ for both) and the western edge of the south region ($\alpha \sim 0.34$). A spectral steepening was instead observed across the central region starting from the south edge of the bright filaments of the G74.3−8.4 SNR. The maximum spectral difference observed across Cygnus Loop was $\Delta\alpha \sim 0.3$.

These results are consistent with those obtained by Uyanıker et al. (2004). Cygnus Loop was well detected with *Planck Instruments* at 30 GHz and a similar structure was observed in the 44 and 70 GHz map, even if the total flux density could not be accurately estimated at these two frequencies due to uncertainty in the CMB subtraction (Planck Collaboration et al., 2016).

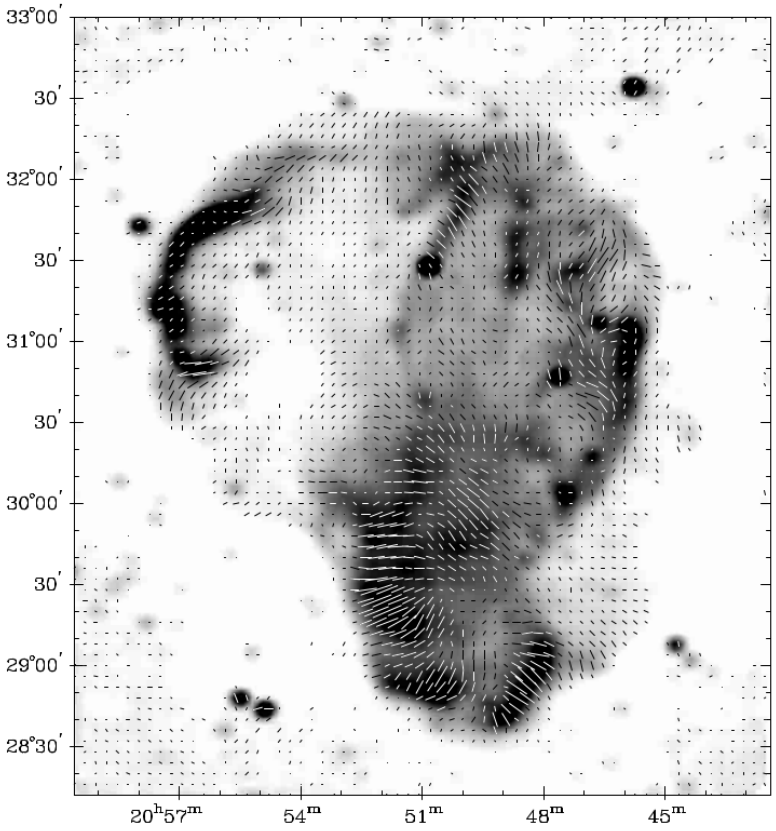

Figure 2.14: The total intensity map of the Cygnus Loop carried out by Effelsberg 100-m telescope at 2.695 GHz. The overlaid bars are the electric field vectors proportional to the polarized intensity (Uyanıker et al., 2002).

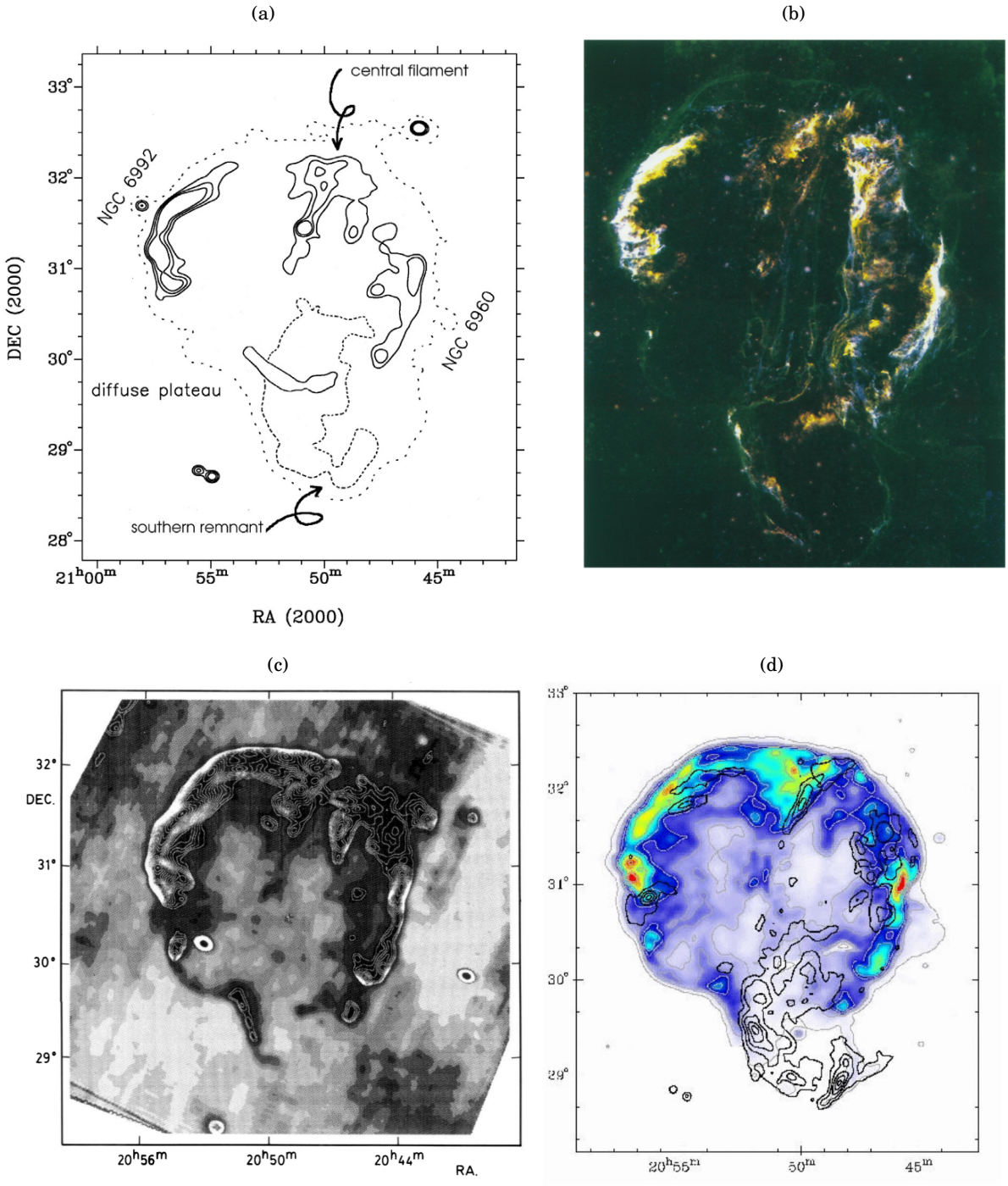

Figure 2.15: (a) Schematic representation of the major features of continuum emission of Cygnus Loop. The dotted line indicates the outer diffuse plateau, while the solid and dashed line are related to the northern and southern remnant, respectively (Uyanıker et al., 2004). (b) Map of Cygnus Loop in H_α, [SII] and [OIII], where H_α and [SII] are indicated in yellow when alone, [OIII] and [SII] together appear magenta, while H_α and [OIII] appear cyan (Levenson et al., 1998). (c) Background corrected warm dust emission from the Cygnus Loop in the IRAS 60 μm band (Braun & Storm 1986). (d) X-ray emission from the Cygnus Loop at 0.25 keV convolved with a 3′ beam (Uyanıker et al., 2002).

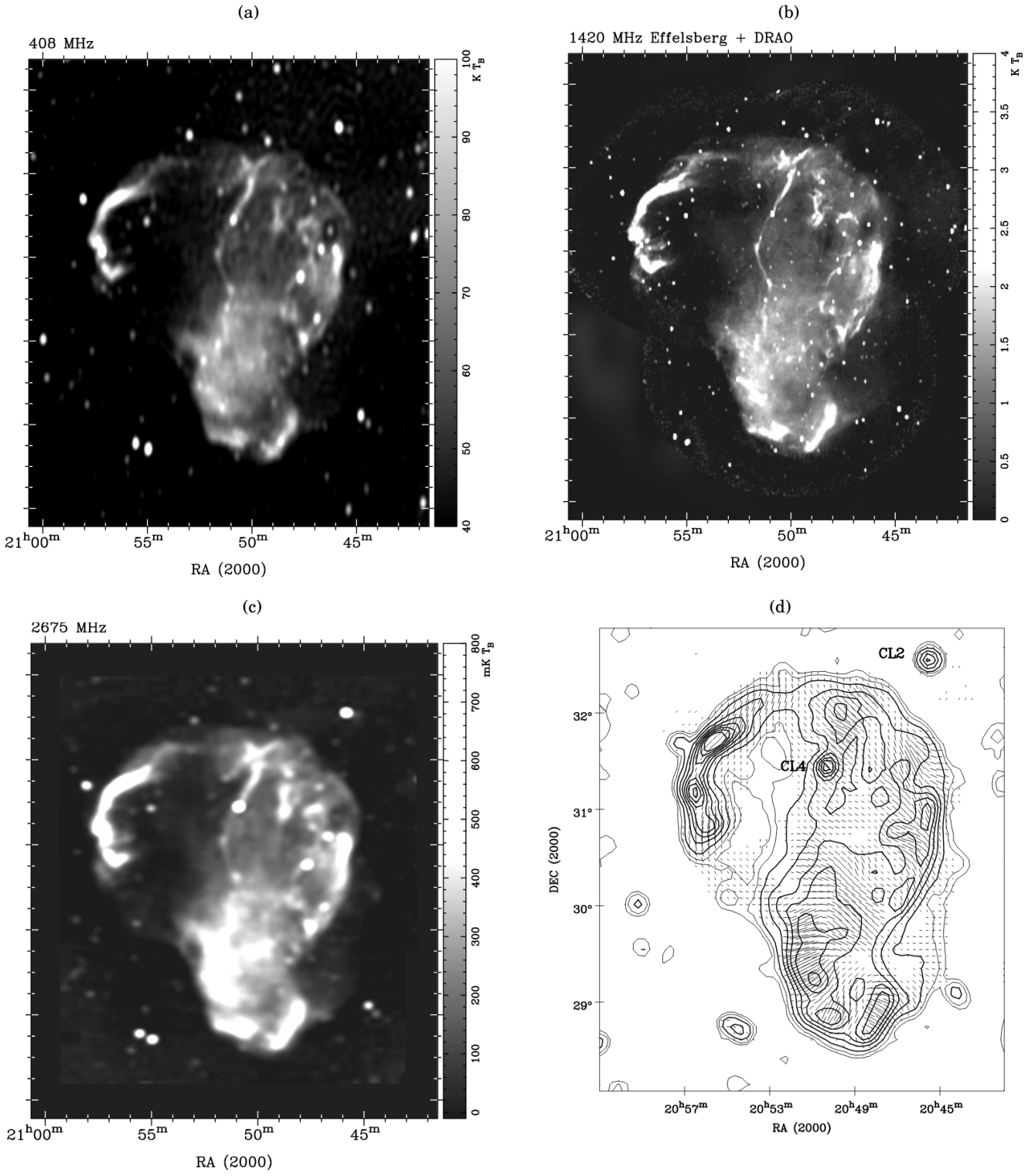

Figure 2.16: Total intensity maps of the Cygnus Loop obtained from the DRAO archive at (a) 408 MHz (HPBW = 3.4′×6.9 ′, Uyanıker et al. 2004), (b) 1420 MHz (HPBW = 1′×2′, Uyanıker et al. 2004), and carried out with Effelsberg at (c) 2675 MHz (HPBW = 4.3′, Uyanıker et al. 2004) and with Urumqi at (d) 5 GHz (HPBW = 10′) (Sun et al., 2006).

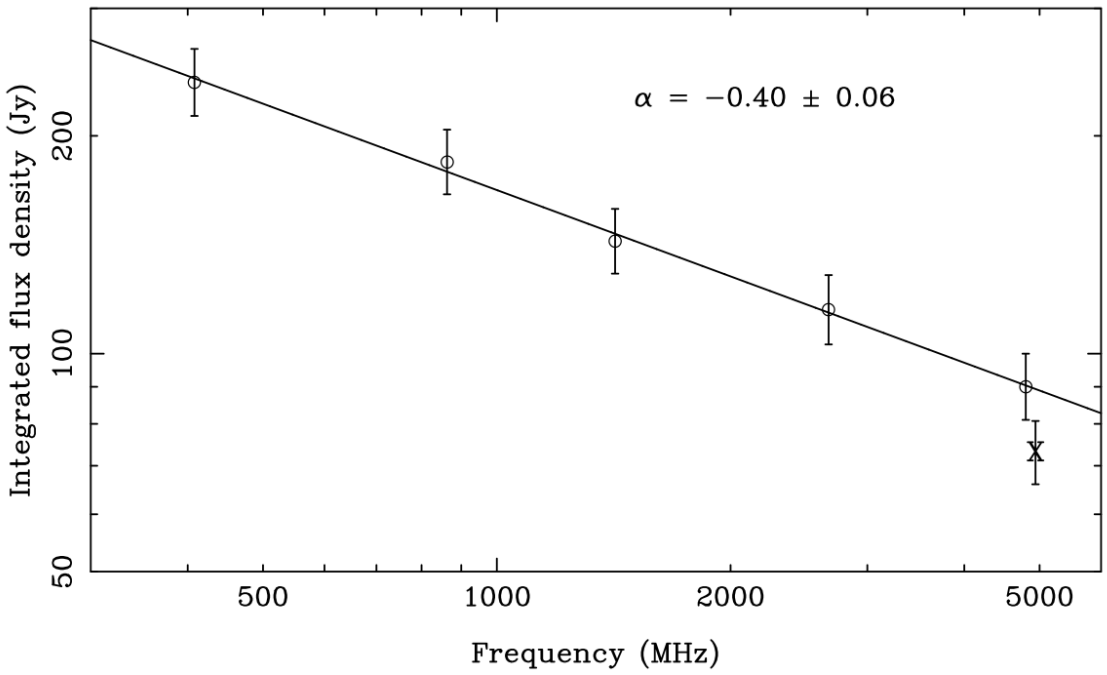

Figure 2.17: Spectrum of Cygnus Loop obtained from the maps at 408 MHz, 863 MHz, 1400 MHz presented by Uyanıker et al. (2004) and the map at 5 GHz presented by Sun et al. (2006). For comparison the flux density measurement obtained by Kundu & Becker (1972) is also reported and marked by "X".

2.3 SRT observations

In the context of the AV activities, we observed W44 and IC443 for the first time with SRT with the aim to test the imaging capabilities and single-dish performances of the telescope for different receivers and back-ends configurations (Prandoni et al., 2017). Taking advantage of their complementary visibility at the SRT site (transit at LST = 19h for W44 and LST = 06h for 3C157), W44 and IC443 were observed with SRT at 7.2 GHz (*C*-band) from 2014 May 27 to December 10 to reach a total effective time on targets of ~12 h. The beam size related to the *C*-band at this central frequency is of 2.66′ (half-power-beam-width; HPBW). The bandwidth was set at 680 MHz in order to cut the frequencies more affected by interferences, and the data were recorded with the Total Power (TP) back-end. This is an analog device provided with 14 input chains, each of which brings signal to a square-law-detector followed by a voltage-to-frequency converter to digitize the detected signals. Each of these chains generates an output that is proportional to the amplitude of the incoming signal. The TP contains a corresponding number of counters that count the impulses and integrate them (Egron et al., 2017).

The observations were performed using the On The Fly (OTF) scanning mode, of which a schematic representation is provided in Fig.2.18. During the OTF scanning, the antenna can scan the observed field along the axes of different reference frames at constant speed, which provides

continuous data acquisition (the sampling time can be in the $1-1000$ ms range). Each single set of OTF scans achieved along two orthogonal axes, typically Right Ascension (RA) and Declination (Dec), forms an elementary map of the source. Background emission and a system-related signal contribution form the so-called "baseline", which is related to the off-source OTF scan slope in its representation as signal-intensity vs. time plot. A precise subtraction of the baseline is very important in order to obtain an accurate flux density measurement of the observed source. From an observational point of view, this operation is guaranteed by requiring that at least $40-60\%$ of each scan be free from significant source contribution and radio-frequency interference (RFI) contamination (Egron et al., 2017).

Taking into account the size of the sources (that is of $\sim 30'$ for W44 and $\sim 45'$ for IC443), we set a subscan length to 1.2° in RA and 1° in Dec for W44 (accounting also for nearby sources contamination on the Galactic Plane), and to 1.5° in both RA and Dec for the IC443 maps. By choosing an OTF scan speed of 4 arcmin/sec, we obtained a duration for each scan of 18 sec (RA) and 15 sec (Dec) for W44 and of 22.5 sec (both RA and Dec) for IC443. This value of the scan speed, coupled with a sampling/integration time that was set to 40 ms, guarantees the oversampling of the beam w.r.t. Nyquist sampling, allowing an accurate evaluation of flux errors and an efficiently rejection of the outliers measurements ascribed to RFI. In order to guarantee a further oversampling, an offset of 0.01° was set between two consecutive subscans that, for the beam size of $2.7'$, implies 4.5 passages carried out per beam and about 17 samples per beam per scan. Apart from the observational parameters, the temporal duration of each subscan also depends on the additional dead time/slew time. This is typically up to $30-40\%$ of the overall duration and in the case of these observations it reached $10-16$ sec for each subscan. According to this, the total time required to carry out an observation, understood as a single RA+Dec map, was ~ 2 hours for W44 and ~ 3 hours for 3C157.

In the framework of the Early Science Program (ESP) W44 and IC443 were observed with SRT at three different frequencies. In this context, I contributed to planning the observations and on the choice of the observing strategy that is presented hereafter. The observations were performed in "shared-risk mode" at the central frequencies of 1.55 GHz (L-band, bandwidth = 460 MHz), 7.0 GHz (C-band, bandwidth = 1200 MHz) and 21.4 GHz (K-band, bandwidth = 1.2 GHz) between 2016 February 14 and March 24. During this period, I attended at the observing session of 24, 25 February 2016 and 22, 24 March 2016.

With regard to the observations in the L- and C-band, the data were recorded simultaneously with the TP and SARDARA (SArdinia Roach2-based Digital Architecture for Radio Astronomy; Melis et al. 2018) backends in the piggy-back mode. SARDARA is a new-generation and flexible ROACH2-based backend. A total bandwidth of 1500 MHz was available during ESP SARDARA operations, split into 1024×2 channels (left/right circular polarization) to carry out most of our observations. In the case of the L-band observations, it was also used in the configuration with 16384 channels. At the time of the ESP, the back-end SARDARA was available only in the

mono-feed configuration, and that made it impossible to use it to perform the K-band observations. In order to improve the image quality of the SNR maps at 21.4 GHz, we decided to carry out the observations by using the 7-beam K-band receiver coupled with the TP back-end, which was available for all observing modes including the multi-feed K-band configuration.
As shown in Fig.2.19, the K-band 7-feed receiver consists of a central feed and six lateral feeds arranged in a hexagonal configuration (the lateral/central feed separation in the focal plane is ~100 mm, resulting in an angular separation in the sky of ~2.3′). A mechanical rotator is used in the receiver to compensate for the Earth's rotation and maintain the parallactic angle, thus avoiding the astronomical field derotation caused by the SRT altitude-azimuth movement when tracking the sources in the sky. Furthermore, we adopted the "Best Space Coverage Configuration" (BSC; Bolli et al. 2015) that automatically rotates the dewar in order to best cover the scanned area, taking into account the reference frame of the observation (Equatorial, Galactic and Horizontal). For instance, if OTF scans are acquired in the Equatorial frame, the dewar is positioned so that the on-the-sky feed tracks are evenly-spaced in RA when scanning along Dec, and vice versa. This specific geometry over the whole acquisition allowed us to obtain, for each receiver scan, 7 simultaneous, equally-spaced (spacing ~0.86′) OTF scans for both polarization channels, which provide a full coverage of the scanned area (Fig.2.19). The seven-beam system increases the mapping speed of extended sources by a factor of seven when compared to a mono-feed. This fast mapping system is crucial to mitigating the effects of temporal atmospheric opacity variations on the image quality (Navarrini et al., 2016).

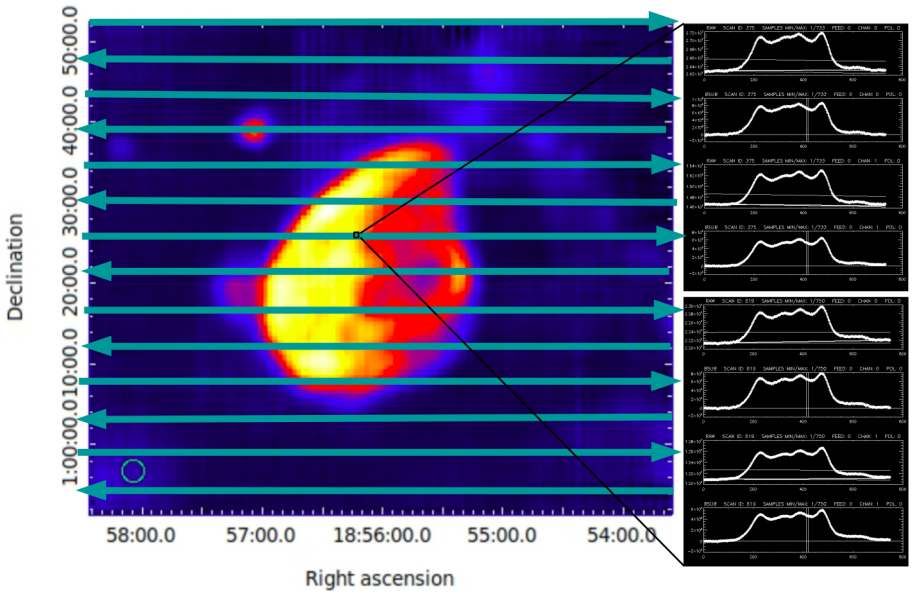

Figure 2.18: *Left*: schematic representation of an OTF map where each arrow indicates a subscan. *Right*: the OTF scansions along RA and Dec directions related to a pixel of the C-band map of W44 produced with the SDI tool.

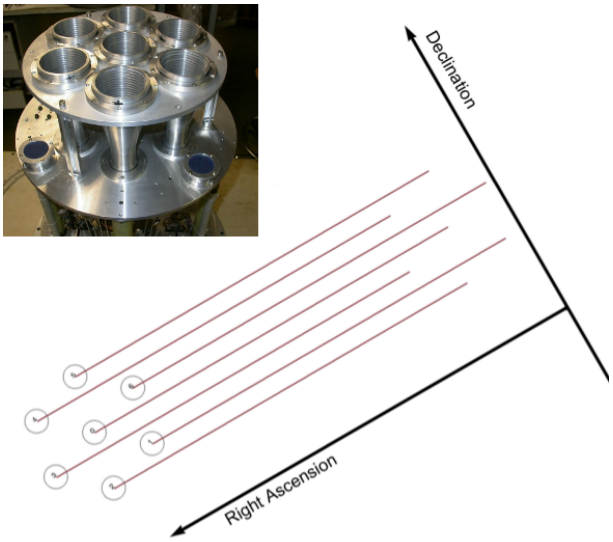

Figure 2.19: Schematic view of the "On-the-Fly" sky mapping using the SRT K-band 7-feed receiver (upper left) and adopting the "Best Space Coverage configuration" that maximizes the sky coverage (Credits: Development of the Italian Single-dish COntrol System, DISCOS; Orfei et al. 2010)

The L-band receiver is located in the primary focus (see Fig.2.5(b)), and the active surface was set with a parabolic profile in order to increase its efficiency. To observe with the C-band and K-band receivers, which are in the Beam Wave Guide focal position and Gregorian focus respectively, the active surface was set in a "shaped profile" in order to offer a better illumination of the Gregorian focus.

The observing parameters adopted for the ESP observations in the C-band are the same described above for the AV tests. Instead, to perform the L-band observations during the ESP, we chose for W44 a scan length of 1.6° in RA and 1.4° in Dec, which takes into account also the nearby sources contamination on the Galactic Plane. For IC443, which is a slightly more extended source, we used a scan length of 2° in both RA and Dec directions. For both sources, we have ensured that at least the 40−60 % of the scan length was free from significant source contribution (and RFI contamination) in order to properly identify and subtract the baseline component. This requirement is not trivially satisfied for targets located in crowded regions of the Galactic Plane, as in the case of W44. The OTF speed was maintained at 4 arcmin/s also for the L-band observations, implying a scan duration of 18 sec (RA) and 15 sec (Dec) for W44 and 22.5 sec for IC443. Two consecutive scans were separated by an offset of $3'$, which implies that 4 passages were carried out per beam on average, and about 17 samples beam^{-1} scan^{-1} (assuming a beam size of ~11 arcmin for the L-band) were taken. Thanks to the larger beam size, the total duration of a map carried out in the L-band was much faster compared to the C-band maps: ~40 min for IC443 and ~30 min in the case of W44. As we have already seen in the context of the AV observations, a stable weather characterized by a clear sky is required for the production of high-quality maps, even at frequencies as low as the C-band. Indeed, as shown in Fig.2.7, the baseline is heavily perturbed by the presence of an inhomogeneous cloud cover.

Our SNR observations at 21.4 GHz were the first ever carried out with the SRT 7-feed K-band receiver in the BSC configuration. For this reason, we decided to include the Tycho SNR in the

K-band observations. Thanks to the Tycho simple morphology and the availability of extensive flux density measurements at up to high radio frequencies, the K-band measurements of Tycho were useful for cross-checking our calibration and data analysis procedure. Also for the K-band observations, we set the scan length according to the angular size of the targets (see Table 2.1 for more details about the observing parameters). We adopted a scan speed of 4 arcmin/sec, which implies a duration for each map of 10.4 sec for Tycho, 18 sec (RA) and 15 sec (Dec) for W44, 22.5 sec for IC443. Taking account of the beam size ($\sim 0.86'$ in the K-band) and the sampling time of 20 ms, these observing parameters allowed us to obtain about 10 measurement samples for each beam and scan.
Considering the pioneering nature of our observations with the new SRT multi-feed system, we imposed conservative observing requirements in order to obtain a complete map of the target for each individual feed and fully verify its imaging performances. We scheduled an offset between two consecutive scans of the same scan of ~1/2 HPBW. Coupled with the 7 feed K-band receiver configuration (see Fig.2.19), this allowed us to obtain about 140 samples/beam and an exposure time of 5.3 sec/beam for a full RA or Dec map. This oversampling is fundamental to efficiently reject outlying measurements (due to RFI, individual feed anomalies, baseline subtraction issues), to perform an accurate evaluation of flux errors, and to optimise the final image accuracy. Including the additional dead/slew time, the total duration of an observation resulting from the combination (averaging) of two consecutive RA and Dec maps is ~ 2.5 h for W44, ~ 4.2 h for IC443, and ~ 1 h for Tycho. The K-band observations performed with SRT are strongly dependent on the atmospheric conditions, i.e. the opacity and water vapor content (Nasir et al. 2011, Buffa et al. 2017). The observations were carried out in "shared-risk mode" and ideal atmospheric opacity conditions (high-quality K-band conditions are intended for τ<0.1 Np) were not guaranteed. This had a negative impact on the quality of our preliminary SNR maps, resulting in an increase in the rejection of flagged data. Indeed, the presence of an inhomogeneous cloud cover makes it difficult to identify (i.e. to fit) both the baseline contribution and the weak signal of the source at this frequency, implying severe errors in a few data sets that were prudentially discarded. A summary of the observational parameters adopted for the AV and ESP observations is reported in Table 2.1.

2.3.1 Imaging data analysis and calibration of the L- and C-band images

The analysis of the OTF maps required the implementation of the SRT Single Dish Imager (SDI ; Egron et al. 2017; user manual, Pellizzoni et al. in prep), which is a tool designed to perform continuum (and in future, spectro-polarimetric) imaging starting from OTF scans, and suitable for all Medicina and SRT receivers/backends. SDI provides an automatic pipeline (quicklook analysis) and interactive tools for data inspection, baseline removal, RFI rejection and image calibration (standard analysis). In particular, I took part in the development and in the test

Table 2.1: Summary of the observing parameters for the imaging of IC443, W44 and Tycho performed with SRT during the AV and ESP. Freq, BW and HPBW indicate the central frequency, bandwidth and the half power beam width, respectively.

	source	MJD	Freq (MHz)	bw (GHz)	HPBW (arcmin)	Map Size (°,°)
AV	W44	56847, 56911, 56916	7.24	680	2.66±0.02	1.2×1.2
	IC443	56811, 56974, 57001	7.24	680	2.66±0.02	1.5×1.5
ESP	W44	57432, 57433, 57470	1.55	460	11.1±0.1	1.6×1.4
		57441, 57442	7.00	1200	2.71±0.02	1.2×1.2
		57443, 57471	21.4	1200	0.87±0.04	1.2×1.0
	IC443	57432, 57459	1.55	460	11.1±0.1	2.0×2.0
		57440	7.00	1200	2.71±0.02	1.5×1.5
		57442, 57468, 57470	21.4	1200	0.87±0.04	1.5×1.5
	Tycho	57442	21.4	1200	0.87±0.04	0.26×0.26

activities of our baseline subtraction and image calibration procedures. I also attended the analysis (following the steps that will be explained in detail in the aftermath of this subsection) of the L- and C-band data in order to obtain the images and the flux density measurements of W44 and IC443 presented in the paper Egron et al. (2017). SDI is written in IDL (porting in Python is undergoing), and it generates SAOImage DS9[1] output FITS images suitable for further analysis by standard astronomy tools. The core of the SDI features/performances is to fully exploit the availability of a significant number of measurements per beam (and then per pixel, typically chosen as about 1/3 of the beam FWHM), in order to have a direct evaluation of statistical errors (through standard deviation of the measurements in each pixel).
We developed our data analysis pipeline by introducing innovative techniques of RFI rejection and baseline subtraction, which include both automatic and manual/interactive more accurate procedures. In the following, I will describe the major steps/procedures of our data analysis pipeline.

1. ***RFI rejection***

   The dedicated campaigns, which were carried out during the AV both with the mobile laboratory and through the telescope, revealed that RFI environment was fairly quiet in the C-band (especially above 6400 MHz) and the K-band (almost everywhere in the band), while the P- and L- bands appeared more polluted (Bolli et al., 2015). Concerning the L- and C-band receiver, almost all the interfering signals were identified to be self-generated by the apparatus installed in the telescope, whereas for the K-band it has been shown that all the identified polluting signals came from external sources and are related to fixed links for mobile operators.

   It is possible to exclude part of the RFI by choosing the observing bandwidth in order to cut the most "polluted" frequency range, for instance excluding lower part of the C-band

[1] http://ds9.si.edu

receiver bandwidth (typically below the 6400 MHz). However, it is impossible to completely remove all the RFI in the pre-observational phase and for this reason it is crucial to providing a part of the data analysis software dedicated to the RFI detection and removal. Through our tool, we provided an automatic and interactive RFI flagging procedure. Since we performed the L- and C-band observations by using the TP and spectro-polarimetric SARDARA back-end in piggy-back mode, we were able to perform the automatic procedure by using two methods: a "spectral" and a "spatial" detection and rejection. The spectral RFI flagging applies to the SARDARA data analysis only. Indeed, in the case of SARDARA observations, each sample of each subscan is characterized by a frequency spectrum. This allowed us to detect the frequency range more affected by RFI, and we develop a code designed to cut it from our data. For the L-band, about 30 % of the channels were dynamically flagged and rejected for suspected RFI contamination. For the C-band, that percentage dropped to 5−10 %. In order to process the SARDARA data in the same way as the TP one, they were collapsed into a single continuum channel after RFI spectral filtering. The spatial RFI flagging procedure shall be instead applied successively and it is suitable for both TP and SARDARA backends. It consists in splitting the map into sub-regions, which correspond to adjacent solid angles in the sky. We chose the size of these areas in order to maintain a good trade-off between the need to avoid discarding actual fluctuations from the source and that to include a significant (typically >10) number of measurements. During the AV tests (Egron et al., 2016), we have empirically established that these areas have to be inferior to the beam size (typically 1/4−1/5 of HPBW). Then the automatic procedure identifies within each sub-region the "outlying" samples, which are specified as those with a count level above a standard deviation-based threshold that is typically 5σ level above average (also in this case the choice of the threshold value was empiric).

2. ***Baseline subtraction***

   The automated baseline subtraction was performed scan by scan, and it was based on a statistical method. The first step of our procedure involves the computation of the angular coefficient of the baseline slope (referred to a single subscan) taking only 80% of the samples with the lowest counts. This allow us to approximately discard the major RFI events and strong source contaminations. Thus the linear fit is normalized to the average of the 15% lowest counts samples. In order to perform a refinement of this "adjusted linear fit", we considered a baseline "fitness" parameter (BF) that is defined as the number/percentage of scan samples that are within a given rms of the baseline linear fit (i.e. 1σ level of the baseline fluctuation). The higher the BF value, the better the accuracy of the baseline model. Our tool then perform a trial loop on the angular coefficient and normalization of the linear fit in order to maximize the BF parameter. From a theoretical point of view, the linear fit trials performed on a scan on the empty sky converge to a maximum BF = 68 % (i.e. 68 % of the samples are within 1σ /rms from the best linear fit).

This baseline subtraction method provides both mathematically and physically exact results if at least 50 % of the scan samples are related to the baseline, or in other words if <50% of the samples are significantly contaminated by residual RFI and astrophysical sources. If this condition is satisfied, in principle a manual inspection/trimming of the baseline is not expected to provide more accurate (and rigorous) results. However, this requirement is not always trivially fulfilled, as in the case of scans performed along crowded regions of the Galactic Plane. For this reason, our procedure provides also an interactive final data inspection, which makes it possible to inspect each subscan in order to identify and adjust anomalies in the baseline subtraction and RFI rejection (e.g. discarding corrupted scans, further manual flagging/unflagging of RFI). An example of the subscans representation produced by SDI in order to perform the manual inspection is shown in Fig.2.18

3. ***Calibration***

In order to reconstruct the integrated flux density of the targets (Jy) and compare them with the literature values, it is necessary to convert the "counts maps" into brightness maps (expressed in Jy/sr). The calibration was performed using well known strong radio sources that exhibit constant flux density on long time scales and that appear as point-like at the frequency at which we were observing. This last characteristic allowed us to use simple OTF cross-scans in order to observe the calibrators. A cross-scan consists of four OTF scans (for our observations we set for each cross-scan an OTF subscan length of 0.5° and a speed of 1.25 arcmin/sec) centred on the source that are alternately performed along the RA and Dec directions.

The analysis of the calibrator data provides the automatic baseline subtraction of each OTF cross-scan, and then our pipeline applies a Gaussian fit to the data in order to measure the calibrator scan peak counts, and to check for pointing errors. For the L-band, pointing errors are negligible, while for the C-band they sporadically range up to $0.5'$. Bearing in mind that the SRT pointing requirement is HPBW/10, these pointing errors imply a calibrator counts correction up to ~10 %.

We used the flux density measurements and the polynomial expressions proposed by Perley & Butler (2013) in order to reconstruct/extrapolate the spectral flux density of the calibrators at the observed frequency. We noted that among our set of observed calibrators, 3C123, 3C286 and 3C295 showed flux variations of less than 5 % per century between 1 and 50 GHz. Taking into account the large bandwidth that characterized our observations, we wondered if the differences among calibrators and SNR spectra could affect the calibration results. Then we verified that bandpass corrections applied to SARDARA and TP data affect calibration results below ~0.3 %.

We calculated the conversion factor Jy/counts from the ratio between calibrator expected flux density and observed counts for both left and right circular polarization channels. This was done for each calibrator observation at different elevations by averaging the values

associated with consecutive cross-scans. The tests performed during the AV demonstrated that the gain curves are approximately flat both in L- and C-band thanks to optimized settings of the antenna's active surface (parabolic and shaped mode, respectively). The calibration factors are then expected to be roughly independent from the elevation (Bolli et al. 2015, Prandoni et al. 2017). However, we discarded the calibrators and target C-band observations obtained at elevations below 15° since pointing errors and beam shape instability effects are appreciable at low elevations. We established two main criteria in order to merge and average the calibration factors to apply to the raw data in the calibration phase:

a) calibration and target data must be observed with the same backend attenuation parameters

b) only calibration observations performed within 12 h (or less in case of changing weather) from each scan epoch are considered in order to guarantee the same conditions of target/calibrators observations and the highest stability of the conversion factor.

This procedure guaranteed the gain stability and implied errors, which are calculated as standard deviation on the calibration factors, of ~3 % for the L-band and up to ~5 % for the C-band. This difference mainly results from the impact of the actual weather conditions on the C-band observations. We verified that the antenna beam was very stable and equal to HPBW = 2.71 ± 0.02 arcmin at 7.0 GHz and HPBW = 11.1 ± 0.1 arcmin at 1.55 GHz, in the elevation range (~20−80°) at which we observed during the ESP. A Gaussian shape provides a very good fit to OTF scans on calibrators, thus we assumed a beam solid angle of $\pi(1.2\times\mathrm{HPBW}/2)^2$ sr for image calibration. The HPBW was weighted accordingly to target spectra in the observed band.

4. ***Image production***

The calibrated data were binned through ARC tangent projection by using pixel sizes ~1/4 of the HPBW, which corresponds to the effective resolution of the images. It is worth noting that bright and nearby point-like image features (e.g. having >0.1 Jy flux and a beam-size separation) associated with a Gaussian Point Spread Function (i.e. SRT beam shape) are not distinguishable when taking an image pixel size equal to the HPBW, while these are resolved when adopting a pixel size equal to the effective resolution (~1/4 HPBW). This arises from Gaussian beam oversampling in our mapping procedures. Our DS9 FITS images were produced in units of Jy beam^{-1} and Jy/sr by incorporating the WCS reference system, and using the cubehelix colour scheme (Green, 2011).

2.3.2 *K*-band multi-feed data reduction

The observations of the SNRs W44, IC443 and Tycho, which was performed at 21.4 GHz during the ESP, were the first carried out by using the multi-feed receiver in the BSC configuration. This required the study of the the gain curve and the beam shape in order to tests the receiver performances that characterized our observations, of which I dealt personally with. Furthermore, we imposed conservative observational requirements in order to obtain a complete map of the target for each individual feed and fully verify its imaging performances. For this reason, even though the *K*-band data reduction procedure is similar in many respects to those already described for the lower frequencies, we had to implement dedicated data analysis tools, in particular regarding the calibration and the final image production. In this respect, I took care of the analysis of the data acquired at 21.4 GHz as principal investigator. In this subsection, I will describe the specific peculiarities of the multi-feed *K*-band analysis.
We performed the data analysis by using the SDI software tool, which was tested during the SRT AV, and which has already been described in the previous subsection. The first step of our data analysis procedure was the generation of the 14 individual feed images (separating left/right polarisation channels) related to the same target map. This was obtained through three subsequent steps:

- scan-by-scan baseline subtraction
- RFI rejection
- production of the preliminary calibrated images

Throughout this procedure, we could assess the individual feed map quality in order to check the single-feed performance and discard outlying samples as compared with the feed-averaged pixel value, before proceeding to the final merge (averaging) of all feed images. The operations of baseline subtraction and RFI rejection were performed through an automatic process, and they were refined by a manual/interactive procedure, in the same way described in subsection 2.3.1. At the end of these filtering procedures related to the comparison of feed measurements, a significant fraction of "outliers" were identified and carefully discarded. Most rejected events were related to baseline subtraction anomalies due to atmospheric fluctuations, since the SRT *K*-band is relatively free from strong RFI contaminations.
For the calibration of the multi-feed data, we assumed that each feed (and polarisation channel) was characterised by a specific efficiency that is mostly due to the different noise temperatures of the individual electronic chains (Orfei et al., 2010). We first evaluated the gain curves (as a function of the elevation) for the two polarisation channels of the central feed through the analysis of the OTF cross-scans that were performed on known flux density calibrators (3C286, 3C295, 3C147, 3C48 and NGC7027). We adopted the Perley & Butler (2013) flux density scale. We performed the baseline subtraction and the Gaussian fit of each scans in order to measure

the peak counts associated with each calibrator. We used this values to calculate the conversion factors, which is defined as the ratio between the observed counts from the calibrators and their expected flux density (counts/Jy).
We used the conversion factors to check the stability of the SRT K-band gain as a function of elevation, and to test its consistency with that obtained during the SRT AV (Prandoni et al., 2017). This study was necessary because our gain curves implicitly include the attenuation effects due to the atmospheric opacity (in the range 0.04−0.12 Np during the observations; Buffa et al. 2016, Buffa et al. 2017), which also affected the target observations.
While the calibration measurements were taken temporally close to the target observations, the opacity conditions could in principle have been slightly different when we observed the calibrators and targets. For this reason, we thought necessary to verify that the gain curve fluctuations due to a variable opacity during the observations were within the errors of the gain curve fit. To prevent this effect, calibration cross-scan observations were performed for different elevations just before and after SNR mapping for each observing session, in order to account for atmospheric opacity fluctuations as a function of time.
The antenna gain varied according to the elevation, and it reached a maximum at 45°. A good interpolation was obtained with a parabolic curve, such as: $G(el) = p_2 el^2 + p_1 el + p_0$. We used such a function to fit the conversion factors as a function of the elevation. In this way, we studied the gain curve associated with the left and right polarization channels, independently for each calibrator observed on 2016 February and March.
As shown in Fig.2.20, all gain curves obtained are consistent, within the statistical fluctuations, with those obtained during the AV (Prandoni et al. 2016, Fig.2.21) and show a decrease in efficiency below 45° of elevation. This feature indicates a not perfectly optimized modelling of the gravity deformations of the telescope at low elevations. We also noted that the gain curves related to the observations performed in March (see Fig.2.20(c) and Fig.2.20(d)) slightly deviated from the expected trend compared to those carried out in February (see Fig.2.20(a) and Fig.2.20(b)). We attributed this effect to the different atmospheric conditions encountered during the observations that were characterized in March by inhomogeneous cloud cover and high humidity levels.
We used the coefficients of the gain curve (shown in Fig.2.20) associated with the different observational sections and polarization channels in order to obtain a correct renormalization (which was referred to 90° in our data analysis procedure) of the conversion factor to be applied respectively to the data obtained with different polarization channel, in February or March. As a further refinement, each target data sample was calibrated using the value obtained by averaging the calibration factors obtained within 6 hrs (or less in case of changing weather conditions) from the measurement, in order to guarantee comparable conditions for the target/calibrators observations.

Table 2.2: Summary of the OTF maps of the calibrators carried out with SRT during the ESP. The flux densities at 21.4 GHz are extrapolated from Perley & Butler (2013).

calibrator name	MJD	N. maps (RA+Dec)	Elevation (°)	Flux density (Jy)
3C147	57553	1	18.5–22.2	1.8
	57471	1	17.9–19.9	
3C286	57553	1	79.6–80.8	2.6
	57471	1	80.1–81.0	
3C295	57553	1	74.8–76.3	1.0
	57471	1	75.2–76.6	
NGC7027	57553	1	14.0–15.3	5.4

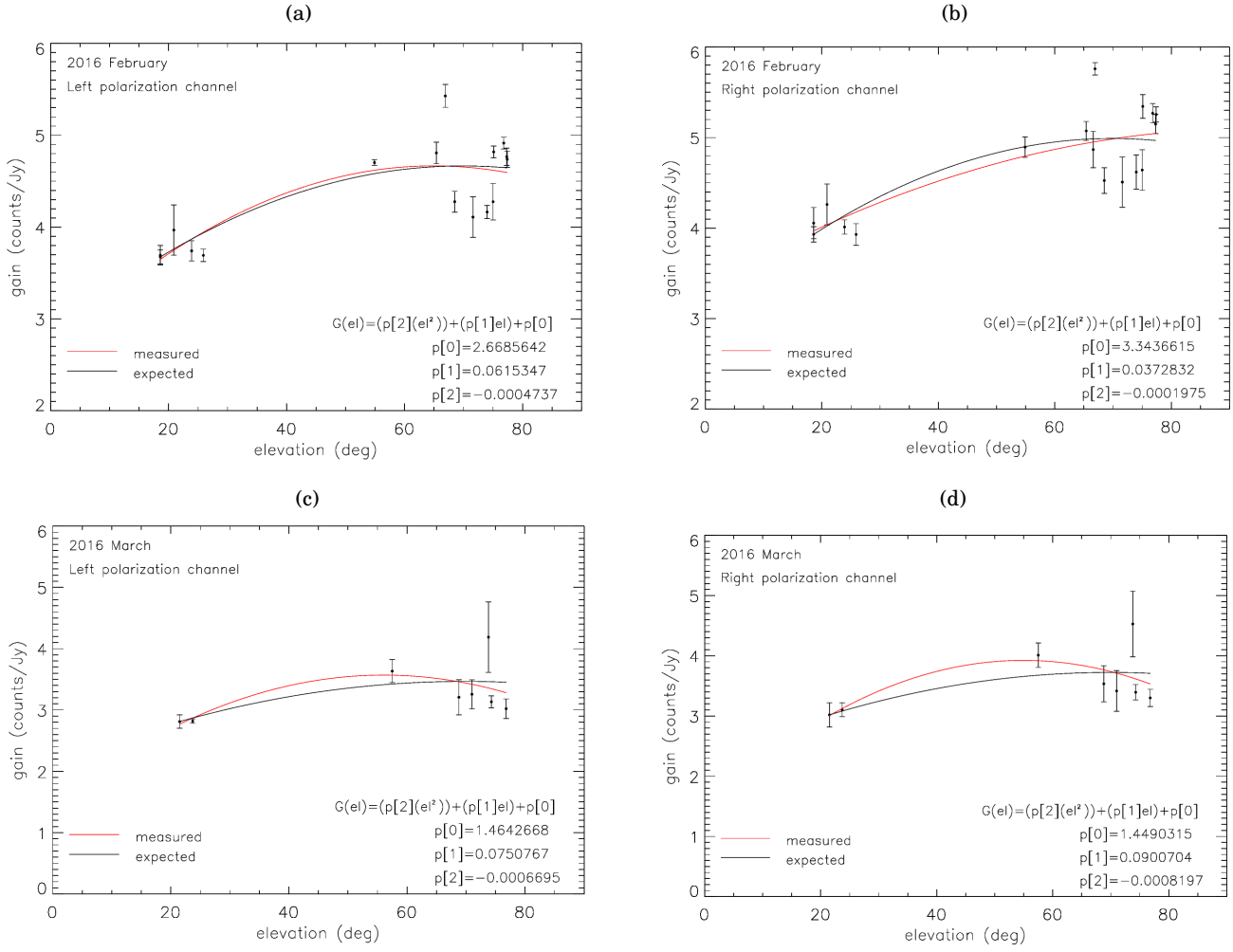

Figure 2.20: Gain curves in counts/Jy at 21.4 GHz carried out with the central feed of the SRT *K*-band receiver through OTF scans on calibrators. For both the February and March sessions we calculated individually the gain curves associated to the left (panel (a) and (c), respectively) and right (panel (b) and (d), respectively) polarization channels. The error bars are associated with the uncertainties on the Gaussian fit and on the calibrator flux density extrapolation.

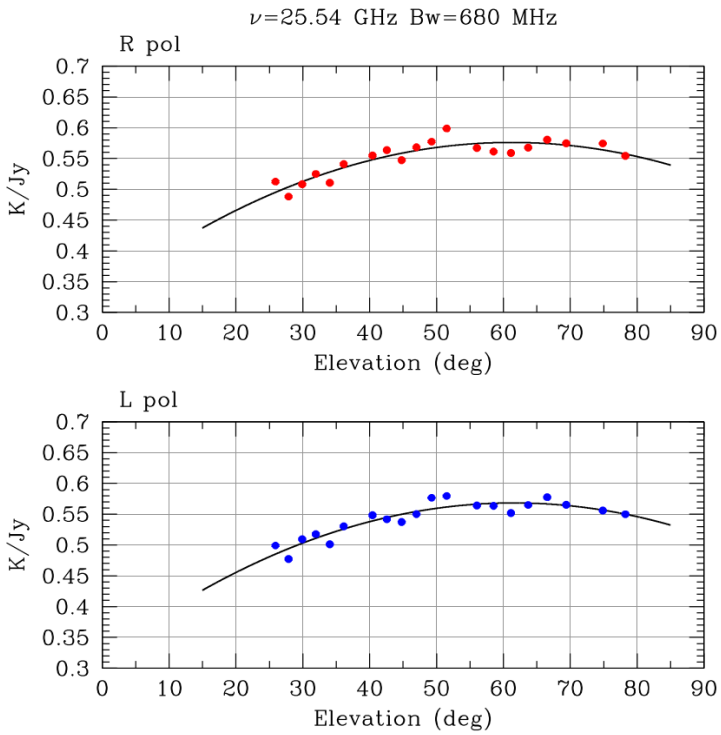

Figure 2.21: Gain (in K/Jy) as a function of elevation measured through OTF scans carried out at 25.54 GHz by the central feed of the SRT *K*-band receiver, with a bandwidth of 680 MHz. The right in left polarizations are shown in the top and bottom panels, respectively (Prandoni et al., 2017).

Furthermore it was necessary to verify that gain curves of the lateral feeds only differ from that of the central feed by a normalisation factor. In order to calculate this scaling factor for each feed/polarisation, we compared calibrator counts as seen by different feeds with the central feed counts. However, this could not be done by using the OTF cross-scan described above. Indeed, in the multi-feed configuration, the cross-scan observations can be set up to observe the point-like sources with one of the seven feed (typically the central feed), and in this way the conversion factor can be obtained only for these feed maps. Another observational strategy on the calibrators is therefore necessary in order to correctly calibrate also the lateral feed maps. In this respect, we performed mapping of the calibrators in order to determine the rate between the gain of each lateral feed and the central feed and to assess the beam size that strongly affects calibration results. With this aim, we carried out OTF maps on the calibrators, paying attention to choose their size so that the point source was visible in each single-feed map. This technique based on imaging was also used during the AV (Prandoni et al., 2017), and it is very efficient for multi-feed receivers, since it allows us to obtain the gain curves for all beams simultaneously.
We carried out the maps of the calibrators 3C147, 3C286, 3C295 and NGC7027 (adopting a map size of $0.2° \times 0.2°$) during two sessions (2016 February 25 and March 24), by using the same central frequency, bandwidth, attenuation levels and OTF scan parameters that were adopted for the target observations. The time required to perform a complete map of a calibrator along both RA and Dec direction (including slew and dead time) is about 20 minutes. In Table 2.2, I report a summary of the observations carried out on the calibrators.

Through 2D Gaussian fits of the calibrator images for each feed, we calculated the peak count ratio between each lateral feed and the central feed. We performed an accurate study of the peak count ratio related to each feed and polarization channel by analysing each map (RA+Dec) of each calibrator individually. We calculated the final peak count ratios to be applied to the lateral feed maps in order to perform their correct calibration, by averaging all ratio values associated with each feed an each polarization channel. The values obtained are shown in Fig.2.22 along with their standard deviations. We could note that not all the ratio measurements were consistent with 1. For this reason, we ascribed the observed gain fluctuations to a trend related to the characteristics of each feed.
These scaling factors and the gain curves of the central feed allowed us to properly calibrate the lateral feed maps. We expected that the gain differences between the feeds do not change from an observation to another, and then this test performed during the ESP is not necessary for each observational session. Finally, we noted that the errors on the flux density related to the gain variations between the feeds, which are ascribed to the rms of the rate measurements (see Fig.2.22), result in an uncertainty on the flux density measurements of <5%.

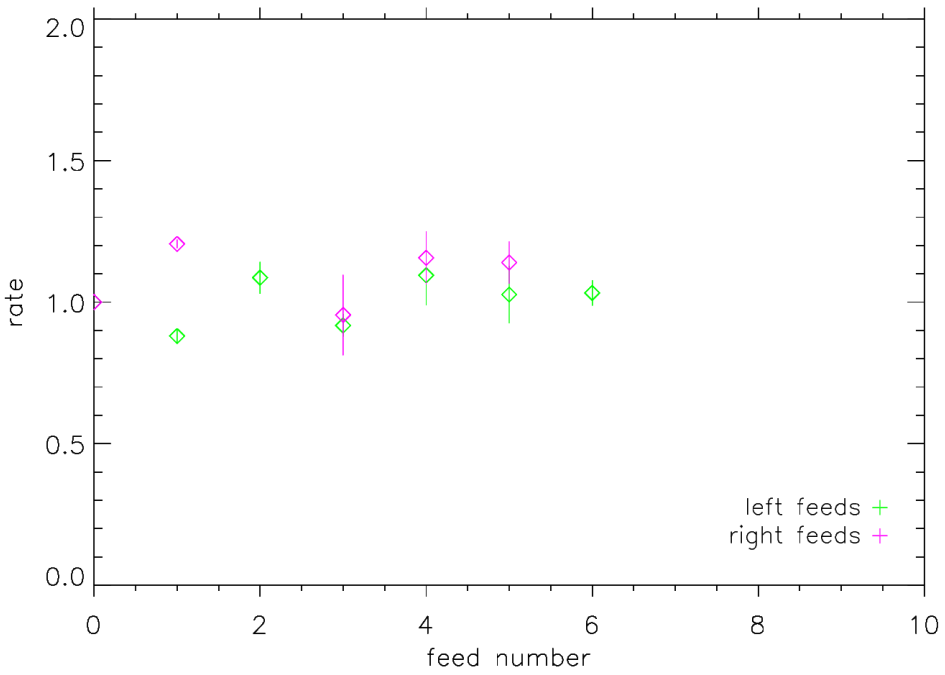

Figure 2.22: Peak count ratio between each lateral feed and the central feed obtained by averaging, for each feed, the values related to each RA+Dec map of calibrators.

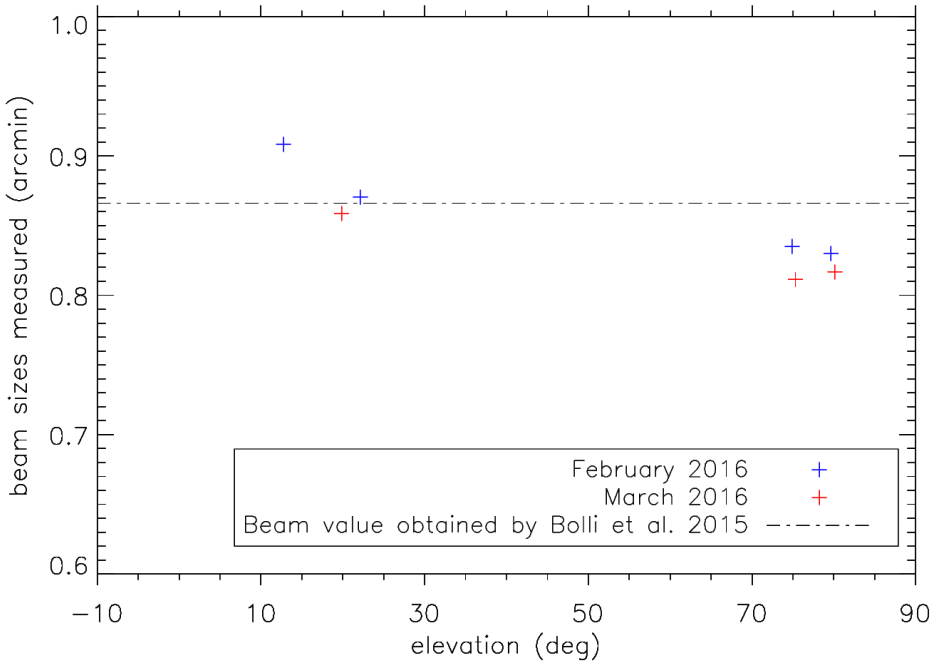

Figure 2.23: Beam size as a function of the elevation. Each point was calculated through 2D Gaussian fits on a calibrator map. The dotted line indicates the ideal beam size value obtained by Bolli et al. (2015) for the central frequency of 21.4 GHz.

The 14 data sets related to each feed/polarisation were individually mapped using the ARC tangent projection (pixels size equal to 1/2 HPBW) with respect to the world coordinate system, taking into account the actual feed positions. All feed images were merged (averaged) together. However, those strongly affected by high noise were removed, since they contributed to the overall image with a low signal-to-noise ratio. A final filtering step removed measurements that were significant "outliers" with respect to the average (due to local gain fluctuation and/or badly removed baseline and/or residual RFI) for each pixel feed. Considering all the SNR images, we discarded about 23% of the data with a sensitive improvement of the final image quality. Despite that, we still maintained about 100 good measurements per pixel.
We also used the calibrator maps in order to study the size of the beam associated with our central frequency. Indeed, in order to obtain brightness images (in units of Jy/sr), a precise evaluation of the beam solid angle is needed. We achieved this through 2D Gaussian fits on each calibrator map listed in Table 2.2. We estimated the beam size values from the average of the beam size in the RA and Dec directions, and they are shown as a function of the elevation in Fig.2.23. We reported a good agreement between the measurements related to the observations carried out in February and March at the same elevations, and a decrease of the beam size at elevations above ~80°. This later effect could be related to mechanical deformations that affect the system at high and low elevations. Indeed, the same argument may be used to explain the highest value obtained at ~10° of elevation. We obtained an averaged HPBW of $0.86' \pm 0.02'$ at 21.4 GHz, which

is only sightly dependent from the elevation in the observing target range ($10°-80°$). Our result is consistent with the values obtained during both the technical commissioning and the AV of SRT (Bolli et al. 2015, Prandoni et al. 2017). Indeed, the beam size at 21.4 GHz extrapolated from Bolli et al. (2015) is $0.87'$, as shown in Fig.2.23. We noted that the variations observed on the beam size with respect to the elevation have a squared impact on the flux densities, and then represent one of main source of uncertainties for our flux density measurements. The error on the estimate of the effective beam solid angle (and then on the brightness and integrated fluxes of the diffuse SNR targets) is ~5%, which includes slight fluctuations of the HPBW for different elevations and weather conditions.

2.4 Medicina radio telescope observation

The Cygnus Loop SNR is an intense nearby non-thermal radio source, which has been frequently studied since the early years of radio astronomy. As described in subsection 2.2.4, different spectral index studies were performed in order to characterise both the integrated and spatially-resolved spectrum of this source. However, the highest frequency at which the Cygnus Loop was observed so far is 5 GHz, and a possible spectral steepening above 2.7 GHz is still debated (Sun et al., 2006). Despite this scientific interest, sensitive flux density measurements are missing at higher frequencies, due to the technical difficulties in performing radio continuum observations of large sources like Cygnus Loop. It is worth noting that only single-dish telescopes can perform this kind of observations at high frequencies, but a high sensitivity and baseline stability of the receiving system are required (Sun et al., 2006). These arguments make Cygnus Loop a challenging and very interesting target to observe with the Italian radio telescopes.
With this aim, we performed some observational tests on this extended source during the ESP in the framework of the project "Constraining Cosmic Rays Production in Supernova Remnants with SRT" (described in subsection 2.1.2). These observations were performed between 2016 February and March at the lowest frequency available (1.5 GHz, L-band). Indeed, the time required to map a region of that size at higher frequencies could be too long in the context of a test, and the effects of temporal atmospheric variations could have a strong impact on the image quality. In Fig.2.24, I show the raw map (not calibrated) of Cygnus Loop obtained with SRT. We can see that the map quality is not as expected; we attributed this effect to the adverse weather conditions experienced during the observations. However, the source is well detected. On the basis of this result, I decided to apply as Principal Investigator for observations at the 2017 call with the Medicina radio telescope with the proposal entitled "Modelling spatially-resolved spectra of the Cygnus Loop Supernova Remnant".
We proposed to perform accurate OTF maps of Cygnus Loop with the continuum back-end in the C-band (5 GHz) and X band (8.3 GHz) in order to study its complex morphology with detailed maps at frequencies above those available so far. Our aim was also to use these maps with those

available in the literature in order to study its integrated spectrum, and to investigate for the possible spectral steepening that was suggested by earlier studies (Kundu & Becker, 1972).
We used the Single-Dish Exposure Time Calculator [2] to plan the observations by setting a bandwidth of 150 MHz and 680 MHz for the C-band and X-band, respectively. For the C-band observations, we proposed to perform OTF maps along RA and Dec directions with a speed of 4 arcmin/s, a sampling time of 20 ms and a single scans per HPBW. The latter value is lower than the one that was used during the ESP observations, which was set to 4 scans per HPBW. This choice was made in order to guarantee, for each single map, a higher number of measurements per beam, which allowed us to have a direct evaluation of statistical errors. The case of Cygnus Loop is more complex since the mapping with 4 scans per HPBW of a source with such a large size requires a long time, which could hamper to guarantee the stability of the weather conditions during the observation. Therefore, our strategy was to carried out, for each observing session, 4 maps with 1 scans per HPBW, which once merged are equivalent to a map performed wit 4 scan per HPBW.
We set a map size of $5^\circ \times 6^\circ$ in order to obtain scans with about 50% of their length/duration free from significant source contribution and, in this way, to properly identify and subtract the baseline component. The adopted observing parameters imply a beam oversampling that allowed us to perform an accurate evaluation of flux errors and efficient rejection of outliers measurements ascribed to RFI. We planned a total duration of a C-band target observation (single map RA+Dec) of about 6 hours (taking into account also the additional dead time/slew time) with a target image rms of ~5 mJy/beam. We considered the same observing parameters for the X-band OTF maps achieving a total duration for a single map of about 7 hours with a target image rms of ~ 10 mJy/beam. We scheduled the observations of the point-like flux density calibrators (3C286, 3C295, 3C147, 3C48, 3C123 and NGC7027) through repeated OTF cross-scans at the beginning and at the end of each observing session.
Our goal was to perform 3 repeated OTF maps (RA+DEC map with 4 scans per HPBW) for each band, requesting 6 observing intervals (one for each map) and implying theoretical net exposure of about 45 hours. It was very important to perform at least 3 repeated OTF maps for each band, since the quality of a map is highly improved by adding the data performed during different observing sessions, in particular for what concerns the RFI rejection and the improvement of the signal-to-noise ratio. This point becomes crucial to performing accurate spatially-resolved spectral index studies for which high-quality radio maps are required. Instrument configuration operations, pointing, calibrations (cross-scans on standard flux calibrators) and weather uncertainties imply significant overheads, although we can manage/shift different receivers accordingly to weather conditions. For these reasons, we estimated a total operation time of about 50 hours. The described project was approved, and all the 50 observing hours requested were scheduled in June 2017. In order to try to rule out the interferences observed in the X-band, 30 additional

[2] http://www.ira.inaf.it/expotime/all_ETC.html

backup hours were granted to the project in August 2017 by using a bandwidth of 250 MHz, narrower than that used in previous X-band observations.
During the first observing sessions, we realized that the C-band was affected by strong RFI and we decided to spend more time on the X-band observations. A detailed summary of the observations is reported in Table 2.3. I performed all the 10 observing session with the Medicina radio telescope through a VNC remote connection to a machine located at the site.

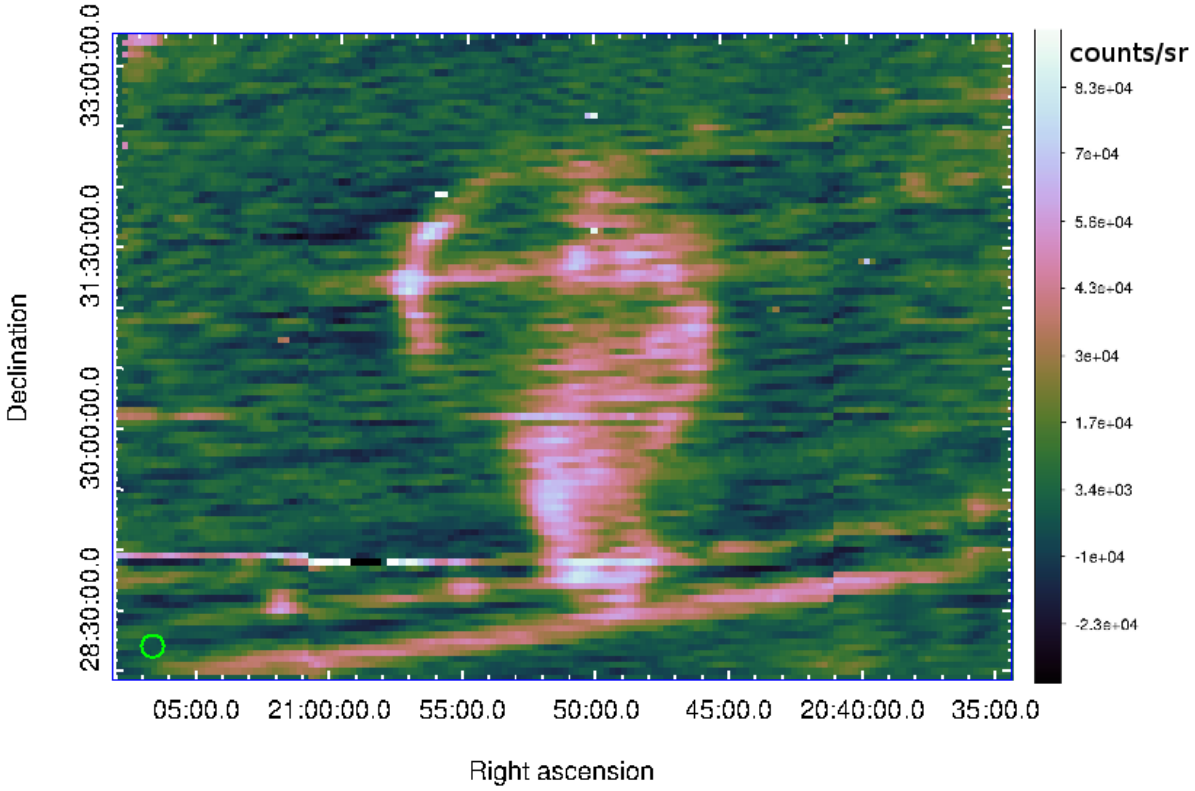

Figure 2.24: Not calibrated map of SNR Cygnus Loop carried out with SRT at 1.5 GHz during the ESP.

Table 2.3: Summary of the observations of Cygnus that we carried out with the Medicina radio telescope. Freq, BW and HPBW indicate the central frequency, bandwidth and the half power beam width, respectively.

MJD	Freq (GHz)	HPBW (arcmin)	BW (MHz)	N. maps (RA+Dec)	Eff. time (h:min)	Elevation min-max (deg)
57923/57924	8.5	4.77	680	2	6:25.1	31.4–79.2
57925/57926	8.5	4.77	680	2	6:25.1	32.9–79.2
57927/57928	5.1	7.3	150	2	5:3.6	43.2–79.2
57929/57930	8.5	4.77	680	2	6:25.1	41.7–79.2
57930/57931	8.5	4.77	680	2	6:25.1	41.7–58.9
57933/57934	5.1	7.3	150	2	5:3.6	38.0–79.1
57993	8.5	4.77	250	2	6:23.8	35.3–79.2
57994	8.5	4.77	250	2	6:23.8	29.1–76.7
57995	8.5	4.77	250	2	6:23.8	29.4–77.3
57996	8.5	4.77	250	2	6:23.8	30.0–77.2

2.5 Flux density and spectral index measurements

2.5.1 SRT results

In order to measure the flux densities of our targets, we considered an extraction area with a radius of 0.32° in the case of W44 (centroid coordinate: RA = $18^h\ 56^m\ 05^s$, Dec = 01° 21.6′), of 0.5° for IC443 (centroid coordinate: RA = $06^h\ 16^m\ 58^s$, Dec = 22° 31.6′), and finally for Tycho, we took a region with a radius of 0.09° (centroid coordinate: RA = $0^h25^m19.4^s$, Dec = 64°0.8′). It is worth noting that the choice of the extraction region does not significantly affect flux measurements when it include the whole SNR and exclude external sources, since our data analysis procedure ensures that the background in the baseline-subtracted images is zero in average in regions that are free from unrelated source contamination. We averaged the maps related to each observational session in order to improve the final map quality, in particular as regard to the RFI rejection and the optimal signal/noise.

The data sets selected to obtain the final images of W44, IC443 and Tycho and related imaging parameters are reported in Table 2.4, together with the image rms and the integrated flux density measurements. Thanks to the observations performed in the piggy-back mode with TP and SARDARA back-ends at 7.0 GHz during the ESP, we verified the fully consistency between the flux density measurements carried out with the different back-ends. We also noted that these measurements are compatible within 1σ with the AV measurements performed at 7.24 GHz more than 1 yr earlier.

The integrated fluxes measured with SARDARA at 1.55 GHz are 214.4 ± 6.4 Jy for W44 and 133.7 ± 4.0 Jy in the case of IC443, while from the average of TP and SARDARA measurements

Table 2.4: Flux densities of the SNRs W44, IC443 and Tycho for averaged maps and related image parameters obtained with SRT during the AV (May-December 2014) and ESP (February-March 2016). ESP observations at 7.0 GHz were simultaneously performed by TP and SARDARA back-ends in piggy-back mode. The effective exposure refers to the observation time for each target map, without including overheads. A single map is intended as the combination of complete scans along RA and Dec directions.

Target	Program	Freq (GHz)	N. Maps (RA+Dec)	Eff. time (h:min)	Flux TP (Jy)	RMS TP (mJy Beam^{-1})	Flux SARDARA (Jy)	RMS SARDARA (mJy Beam^{-1})
W44	AV	7.24	5	4:45	91.4±4.6	13	–	–
	ESP	1.55	14	4:11	–	–	214.4±6.4	81
		7.0	7	6:50	92.9±4.6	11	95.7±4.8	7
		21.4	2	2:59	25±3	48	–	–
IC443	AV	7.24	3.5	6:26	63.6±3.1	6	–	–
	ESP	1.55	13.5	7:13	–	–	133.7±4.0	76
		7.0	3	5:32	66.9±3.3	25	69.0±3.5	20
		21.4	2	5:38	66±7	75	–	–
Tycho	ESP	21.4	2	0:39	8.8±0.9	23	–	–

at 7.0 GHz we obtain a continuum flux of 93.7 ± 4.0 Jy for W44 and 66.8 ± 2.9 Jy for IC443.
We noted that the map rms is slightly better in the case of SARDARA with respect to the TP when we observed with similar weather conditions, as expected from a new-generation spectroscopic back-end that allows us to perform a better RFI rejection.
With regard to the 21.4 GHz observations, we obtained flux density measurements of 25 ± 3 Jy, 66 ± 7 Jy and 8.8 ± 0.9 Jy respectively for W44, IC443 and Tycho. The total averaged maps of W44 and IC443 obtained at 1.55, 7.0 GHz (Egron et al., 2017) are presented in Fig.2.25 and Fig.2.26, respectively, while the maps of W44, IC443 and Tycho carried out at 21.4 GHz (Loru et al., 2019) are shown in Fig.2.27.

We studied the differences in the mean surface brightness of W44 and IC443 at 7.0 GHz between the brightest rims and the fainter central regions or halos. For W44, the brightest rims have a mean brightness of ~1.8 Jy beam^{-1}. In the case of IC443, we estimated a mean surface brightness associated with the brightest rims of ~0.6 Jy beam^{-1} , which is about five times larger than that corresponding to the western halo. We also estimated the flux densities

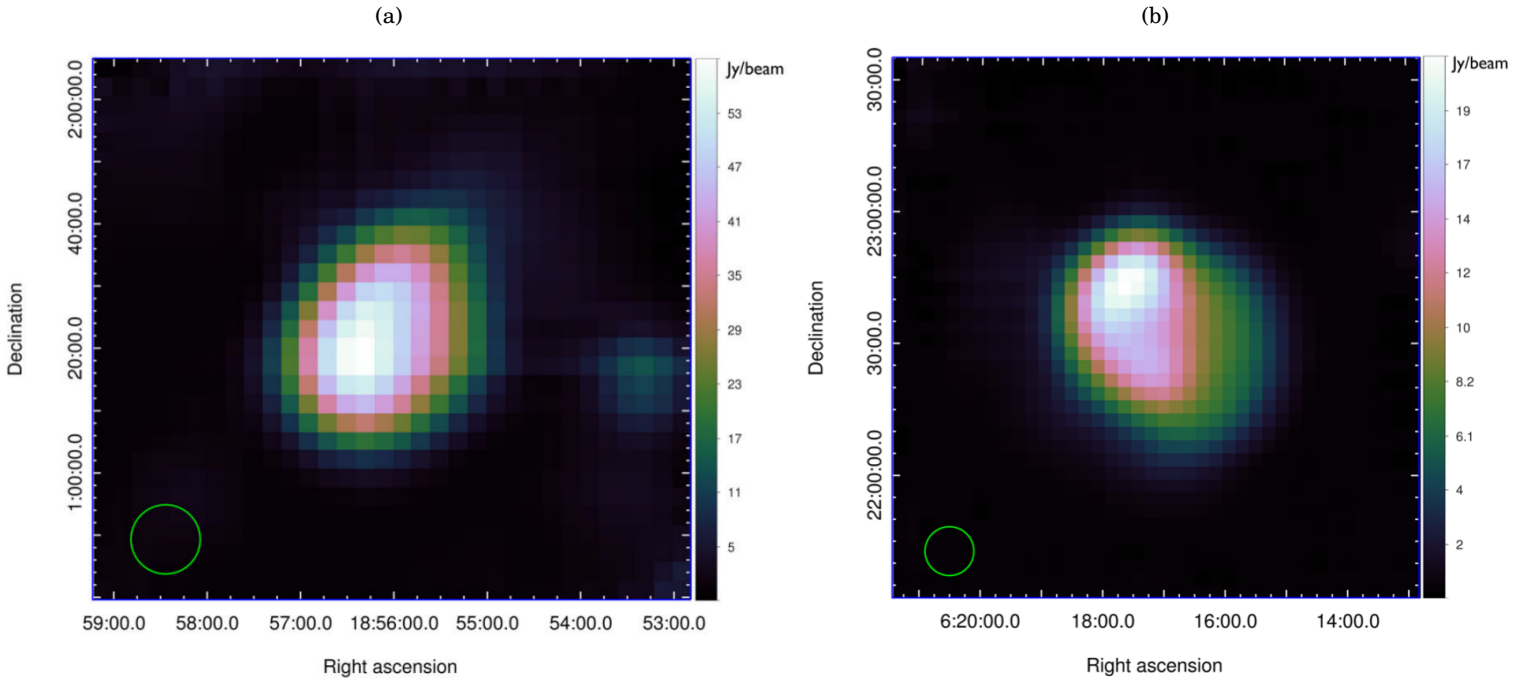

Figure 2.25: Continuum maps of the SNRs W44 (a) and IC443 (b) carried out with SRT at 1.55 GHz with the SARDARA back-end during the ESP. The pixel size is 3.0′ and the beam size is of 11.1′, and it is indicated by the green circles on the bottom left.

at 21.4 GHz related to the bulk of the radio emission that is located in the eastern boundary of W44 (the largest blue region in Fig.2.28(a)) and in the north-eastern region of IC443 (indicated by green contours in Fig.3.10). We obtained 13 ± 1 Jy and 14 ± 1 Jy, respectively. As can be seen in Fig.2.26(a) and 2.27(a), in the C and K-band maps of W44, the Galactic plane is also clearly detected as well as the non-identified source at (RA, Dec) = (18^h 57^m 04^s, 1° 38′ 45″), which appears point-like in C-band and spatially-resolved in K-band. This source is also visible in the VLA images at low frequencies and other wavelengths (e.g IR with Spitzer). It could be associated with a classified HII region G035.040−00.510, as listed, e.g. in the WISE Catalog of Galactic H_{II} regions[3]. The corresponding flux density is 0.94 ± 0.05 Jy at 7.2 GHz and 1.2 ± 0.1 Jy at 21.4 GHz. We used the C-band and L-band point-like flux densities in order to estimate the spectral index associated with this region, and we obtained a value of α = -1.1 ± 0.1 (with $S \propto \nu^{-\alpha}$), which is compatible with an optically-thick thermal emission. We considered a section of the Galactic plane that contribute with an integrated flux density of 8.4 ± 0.8 Jy at 21.4 GHz, which is calculated on a box centred at (RA, Dec)=($18^h54^m20.618^s$, +1°26′28.23″) and an area of 1° × 0.3° (as highlighted in magenta in Fig.3.3).

Our maps at 21.4 GHz showed that the K-band observations performed with SRT are strongly dependent on the atmospheric conditions, i.e. the opacity and water vapor content (Nasir et al.

[3]astro.phys.wvu.edu/wise/

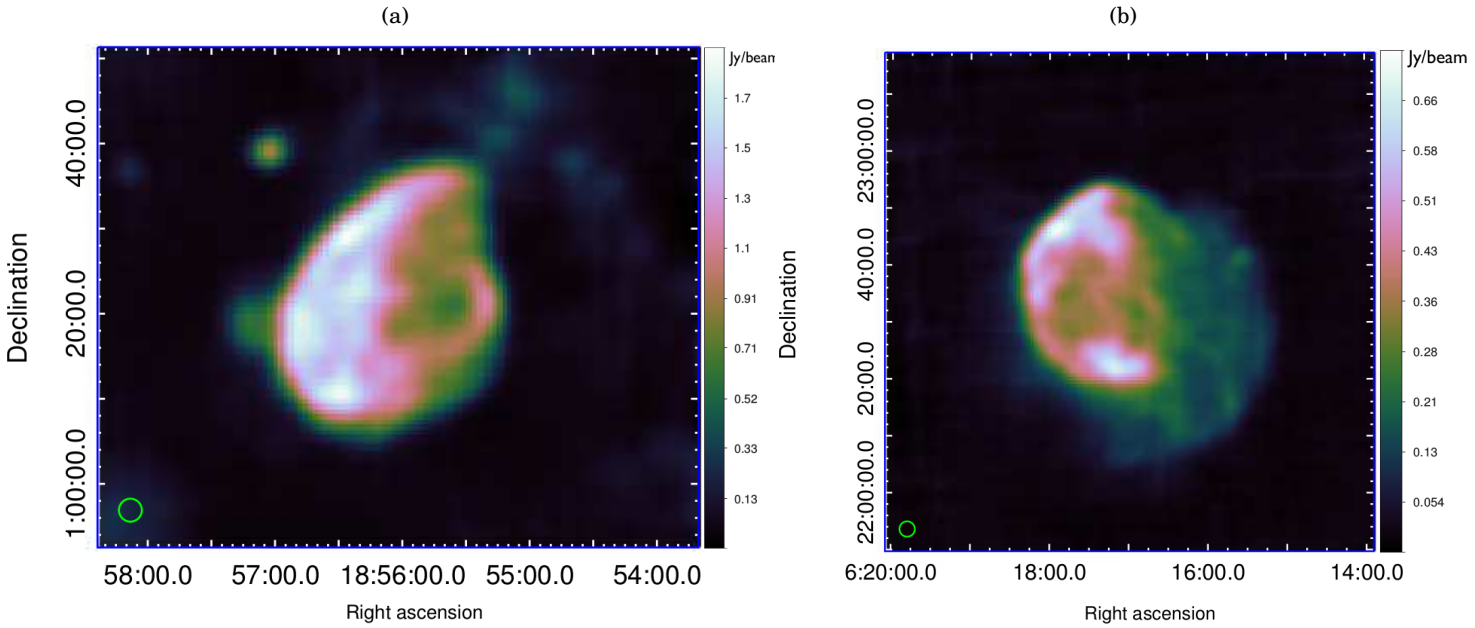

Figure 2.26: SRT continuum maps of SNRs W44 (a) and IC443 (b) carried out with SRT at 7.0 GHz with the TP back-end during the AV tests. The pixel size is 0.6′ and the beam size is of 2.66′, which is indicated by the green circles on the bottom left.

2011, Buffa et al. 2017). Indeed, the observation of Tycho, which was carried out on 24 February 2016 (MJD 57442) in optimal opacity conditions and in the absence of a cloud cover, provides a high signal-to-noise ratio map that allowed us to perform an efficient baseline subtraction, which leads to a low rms value (see Table 2.4). The high-quality map of Tycho (Fig.2.27(c)) clearly shows the bright shell with its main filamentary structures, and the faint inner emission.

In the case of W44 and IC443, the cloudy sky conditions and high humidity level attenuated the astronomical signal. This introduced noise in the measurements with a significant amount of rejected data and higher image rms. Despite these weather conditions, the SRT map of W44 (Fig.2.27(a)) shows the highly filamentary structure of the eastern region. The brightest emission is visible along its boundary, and the short bright arc is detected in the western region where the SNR shock collides with a molecular cloud (Mavromatakis et al. 2003, Giacani et al. 1997). In the SRT map of IC443, we detected the main structures of the complex SNR morphology (Fig.3.7(d)): the bright region corresponding to signatures of atomic/ionic shock in the north-eastern part of the shell, the southern bright structure that includes the PWN region, and the main structures of the western halo region related to a breakout portion of the SNR into a rarefied medium (Lee et al., 2008).

The SNR edges are clearly identified in our images when compared with other high-frequency data with lower resolution (e.g. Planck Collaboration et al. 2016 and Génova-Santos et al. 2017). Although, as already mentioned, the baseline-subtracted off-source pixels have zero mean flux in

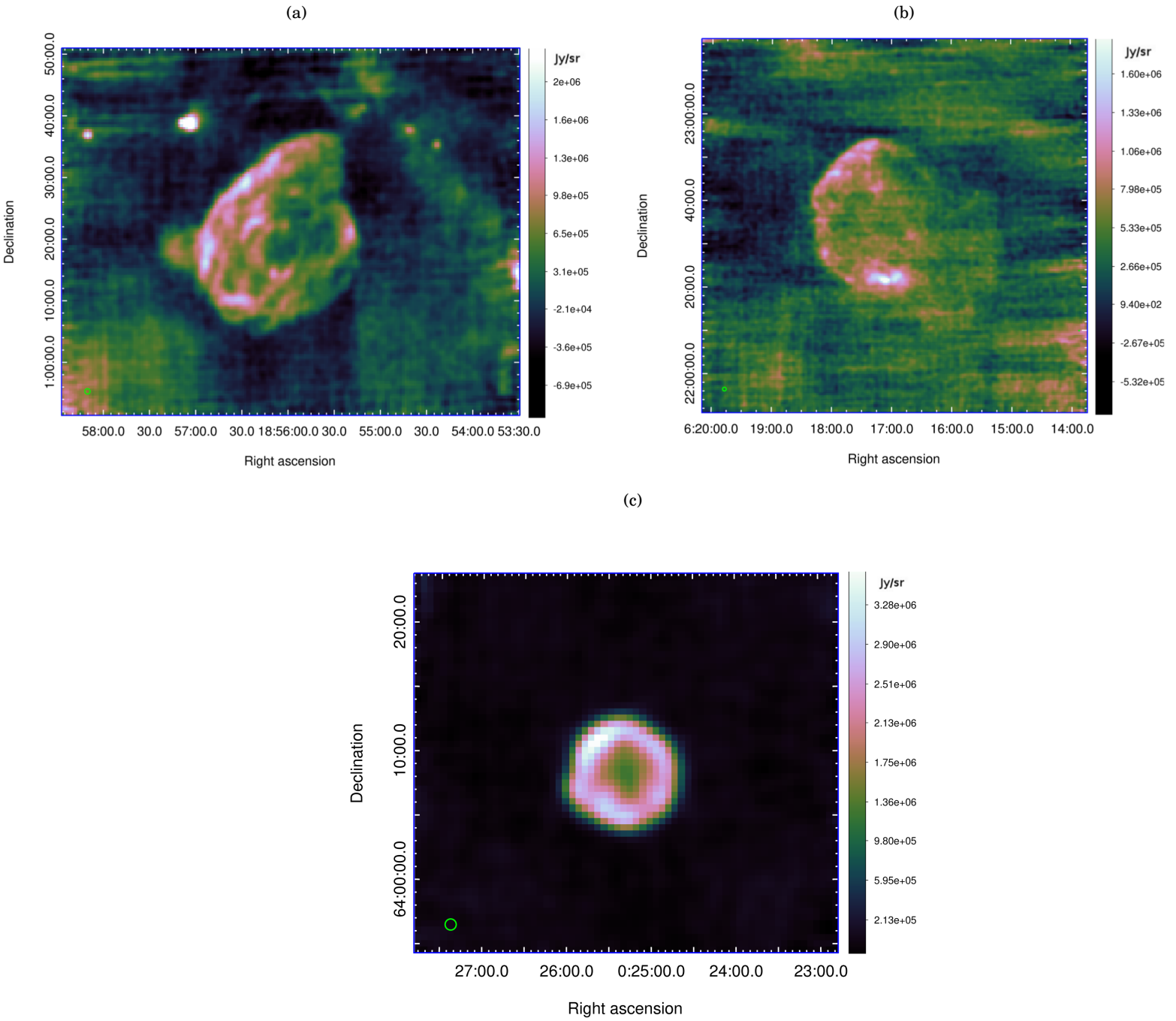

Figure 2.27: Map of SNRs W44 (a), IC443 (b) and Tycho (c) obtained with SRT at 21.4 GHz. The pixel size is 0.4′. The beam size is indicated by the green circle on the bottom left corner of the maps. Sky opacity-related artefacts, particularly evident in the IC443 image, minimally affect the flux density estimates. A portion of the Galactic Plane is visible in the top-right corner of the W44 image (see also Fig.3.3 left). The bright shell structure of Tycho with its main filamentary structures, and the faint inner emission are well detected in our high-quality maps of Tycho SNR.

our maps, in this case, our choice of the source extraction region allowed us to properly calculate the integrated flux densities, by excluding the other image content (e.g. the Galactic plane and the unidentified source unrelated to W44).
In order to study the spatially-resolved spectra of W44 and IC443, we coupled our L-band and C-band maps with the same parameters and topology (same projection centre and pixel size). In particular, the spectral index maps were obtained by convolving data at low resolution (accordingly to L-band resolution). I was directly involved in the development of the SDI tool devoted to the generation of the spectral index maps, and I contributed to the physical interpretation of these. In our spectral index maps, the estimate of the spectral index related to each pixel was obtained fitting the two corresponding L-band and C-band measurements. This was possible since OTF single-dish imaging techniques allow us precise measurements of the flux density for each direction in the sky (i.e. for each pixel map). Relative errors among adjacent pixels are <1 per cent.
When we compared our spectral index maps with those obtained in previous studies from interferometric images (Castelletti et al. 2007, Castelletti et al. 2011), we could note that the available angular resolution for low-frequency single-dish imaging is much worse than that from interferometric images, and this is reflected in the accuracy of the related spectral index maps. On the other hand, single-dish flux density measurements are straightforward than those obtained from the more complex interferometric data processing, and the related errors are typically lower. Indeed, it is worth noting that the conservative uncertainties associated with our flux density measurements are about 3% in L Band (1.55 GHz), while the typical continuum flux errors for W44 and IC443 reported in the literature to approximately the same frequency are of the order of $\sim$10$-$15 % (see Table 2 in Castelletti et al. 2007 and Castelletti et al. 2011 for W44 and IC443, respectively).
Our spectral index maps of W44 and IC443 give us an estimate of region-dependent spectral indices, and they are shown in Fig.2.28 together with the related surface brightness C-band maps in order to highlight the correlation between the radio emission structures and the spectral index values. From this comparison, our low-resolution results for single-dish spectral mapping of SNRs indicate a direct correlation with the corresponding brightness of the largest sub-regions targets; indeed small structures are missing in our spectral index maps. As shown in Fig.2.28, our data highlighted a correlation between the brightest flux density regions and flat spectral indices for both W44 and IC443. These regions are mostly located on the edge and on the brightest filaments of the SNRs, where the SNR shock is stronger and it collides with atomic or molecular clouds.
For W44, we also noted that these regions match with the bulk of the gamma-ray emission. The approximate location of the gamma-ray emission detected with AGILE (Giuliani et al., 2011) and Fermi-LAT (Abdo et al., 2010) for W44, and with VERITAS and Fermi-LAT in the case of IC443 (Humensky & VERITAS Collaboration, 2015), is indicated in blue in Fig.2.28(a) and Fig.2.28(c).

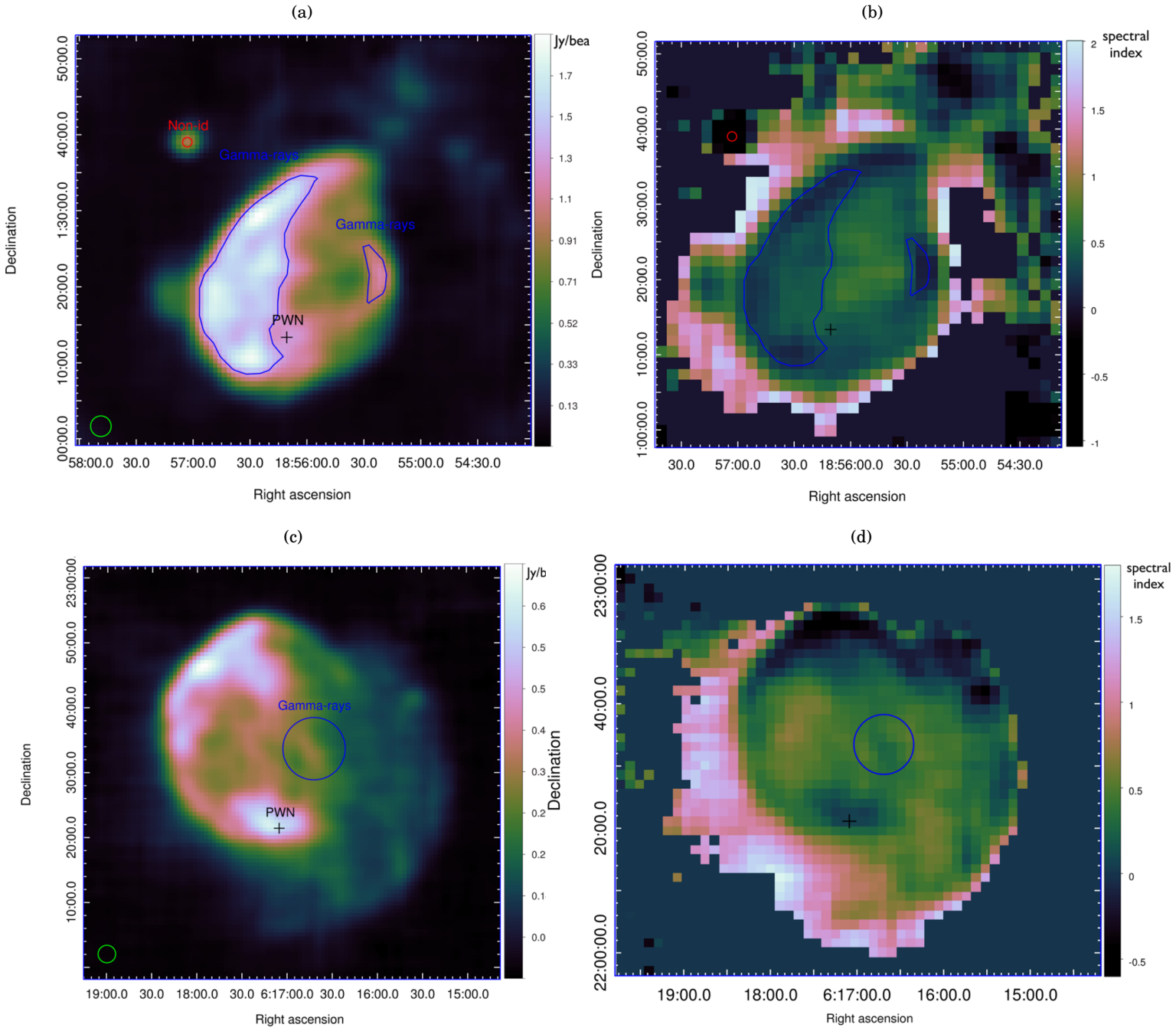

Figure 2.28: Continuum map of SNR W44 at 7 GHz (a) and spectral index map obtained by using 1.55 GHz and 7 GHz data (b). The black cross and the red circle indicate the position of the PWN and the non-identified source, respectively. The blue areas correspond to the gamma-ray emissions as detected with AGILE and Fermi-LAT (Abdo et al. 2010; Giuliani et al. 2011). Continuum map of SNR IC443 at 7 GHz (c) and spectral index map obtained by using 1.55 and 7 GHz data (d). The black plus symbol indicates the position of the PWN, whereas the blue circle indicates the bulk of the gamma-ray emission seen with VERITAS and Fermi-LAT (Humensky & the VERITAS Collaboration 2015).

More accurate images, in terms of higher angular resolution, could be provided through combination of C-band and K-band (21.4 GHz) images, the latter having an HPBW of about 40 arcsec. However, we decided not to use our maps of W44 and IC443 at 21.4 GHz for such a study because of the problems related to the low signal-to-noise ratio. Our aim is to obtain higher quality maps for this purpose in the context of other observing project with SRT dedicate to the observation of SNRs, such as that approved at the 2018 call for observations and currently in progress (for details about this project see Chapter 4). Our spectral index studies are anyway the first carried out at frequencies up to 7 GHz. For both the sources, they revealed a significant spread in the distribution of the spatially resolved spectra that range from a flat (for W44) or slightly inverted (up to -0.5 for IC443) spectral indices to a relatively steep spectrum ($\alpha > 0.7$) compared to a mean value of ~0.5.

2.5.2 Medicina radio telescope results

I performed first-hand the analysis of data acquired with the Medicina radio telescope at 5.1 GHz and 8.5 GHz. We separately analysed each map (RA and Dec) of the Cygnus Loop observations reported in Table 2.3, in order to assess the individual map quality and to efficiently remove the outlying measurements due to non-ideal weather conditions or to RFI contaminations. We used the SDI tool to analyse the data acquired with the Medicina radio telescope, and we followed the same procedure of RFI rejection, baseline subtraction and image calibration that have been already described in detail in subsection 2.3.1.

We analysed separately the C-band data related to the two observational sessions performed on 23-24 and 29-30 August 2017 to assess the individual map quality. Furthermore, we created individual images for the left and right polarization channels in order to check for possible RFI contaminations and/or mechanical problems related to a particular polarization of the signal. As shown in Fig.2.29, all the obtained maps present a strong and similar RFI contamination, which makes it impossible to detect the source. Therefore we considered the data carried out at 5.1 GHz unusable to perform flux density measurements. Further C-band high-resolution measurements can be carried out through future observational proposal with SRT (5.7−7.7 GHz, see Chapter 4 for more details about our observing project including Cygnus Loop at these frequencies) or the Noto telescope, which provide a cleaner C-band.

The presence of persistent RFI that affected the 8.5 GHz band at the Medicina site and the cloudy sky conditions encountered in some observational sessions introduced noise in the measurements, which required an accurate manual procedure of RFI rejection and baseline subtraction. All images were merged (averaged) together in order to obtain the final image that is shown in Fig.2.30. This is the highest-frequency map of Cygnus Loop obtained so far with a single-dish telescope. As can be seen in this image, Cygnus Loop is well detected in our map at 8.5 GHz, in which we can distinguish the two prominent shells (NGC6960 and NGC6992) and the central filament, which constitutes the northern remnant, as well as the southern remnant.

In the merging phase, a filtering process was executed in order to remove residual "outliers" measurements with respect to the average (due to local gain fluctuation and/or badly removed baseline and/or residual RFI) for each pixel feed. This procedure leads to discard about 21% of the data with a sensitive improvement of the final image quality.
As in the case of the images carried out with SRT, the statistical errors on the integrated flux density associated with the final Medicina map of Cygnus Loop are negligible (<2%) compared to the systematic errors. In this case, the main source of uncertainties on the flux density measurements is related to the fluctuations that affected the conversion factors (Jy/counts) obtained from the ratio between the calibrator expected flux densities and the observed counts at different elevations. We estimated an error on the flux density measurements related to the gain stability of $\sim 7\%$.

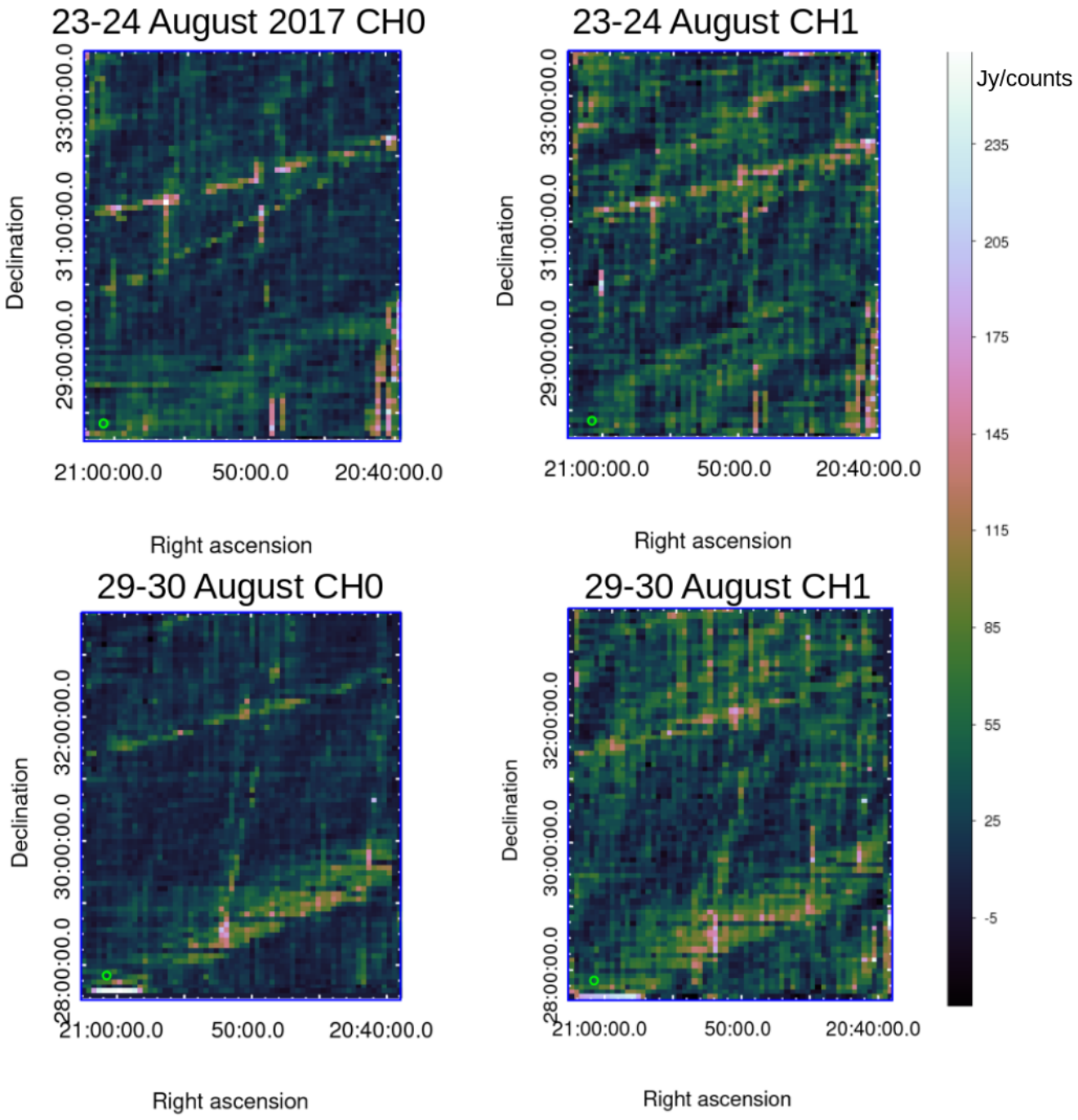

Figure 2.29: Maps of Cygnus Loop SNR carried out with Medicina radio telescope at 5.1 GHz. The pixel size is of 5′, which corresponds to about the beam size, and it is indicated by the green circle on the bottom left corner of each map. We analysed individually the maps related to the left and right polarization channel of each observational session (2017 23-23 Agust and 29-30 August)

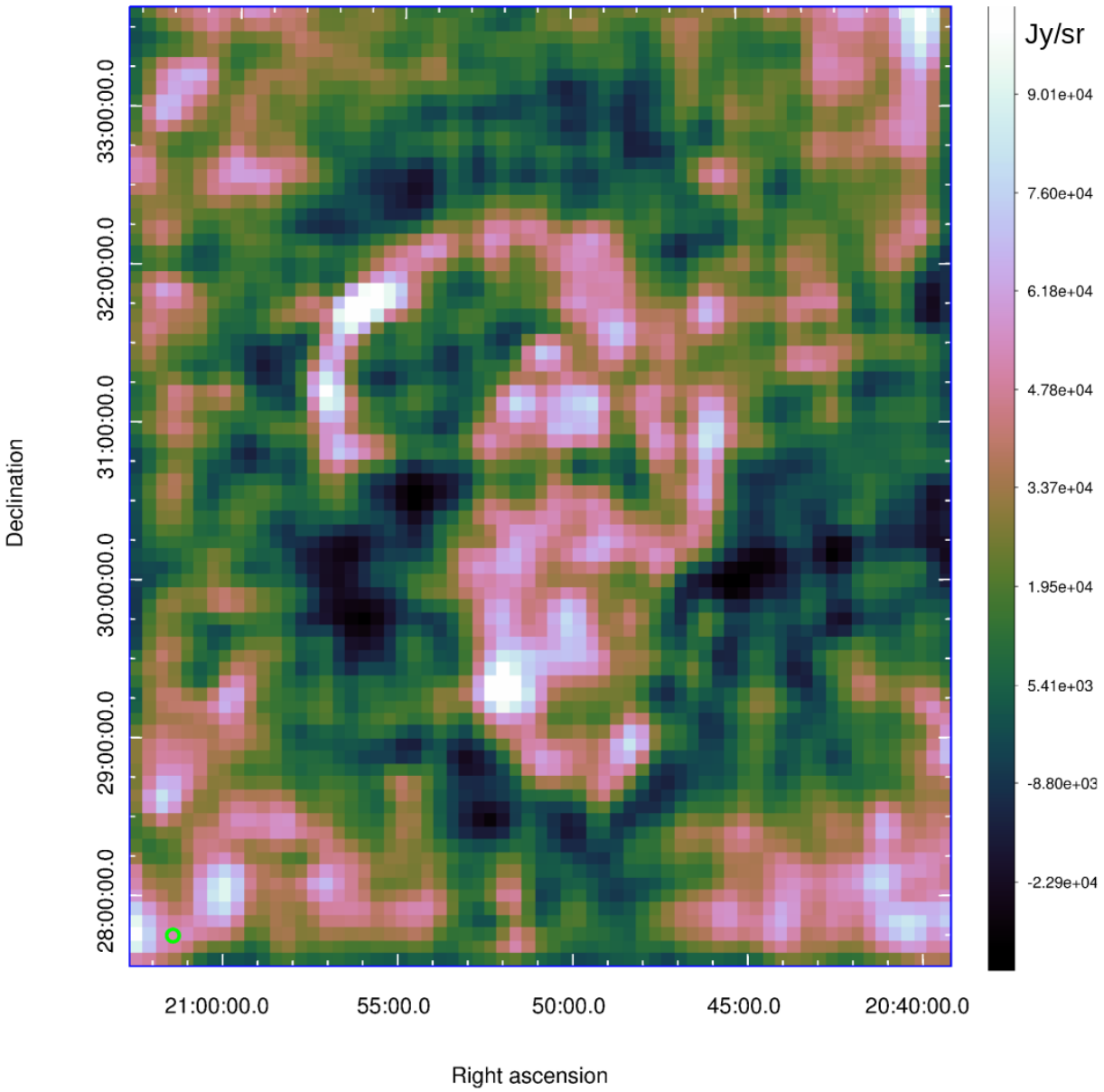

Figure 2.30: Map of Cygnus Loop SNR obtained with Medicina radio telescope at 8.5 GHz. The pixel size is of 4.8′ that corresponds to about the beam size, which is indicated by the green circle on the bottom left corner.

CHAPTER 3

DISCUSSION

The accurate SNR images obtained at 1.5, 7 and 21.4 GHz with SRT in the framework of the AV and the ESP represent a scientific milestone for SRT, because they enabled us to attest its capabilities and performances in single-dish imaging. Indeed, these observations have shown the reliable performances of the instrumentation over 2 years (gain stability <5 %) and provided self-consistency checks in measurements performed by simultaneous piggy-back observations with two different back-ends. On the other hand, the obtained results are of great scientific interest, since they provided the first images of W44 and IC443 at 7.0 GHz and 21.4 GHz, and allowed us to perform accurate spatially-resolved spectral studies in the 1.5−7 GHz range. We compared our maps with those available in the literature that were carried out with both VLA at low frequencies and single-dish in the 0.8−5 GHz frequency range. We noted that the resolution of our maps at 7.0 GHz allowed us to assess the actual SNR edges in a very accurate way compared to the other single-dish maps. This is crucial to obtaining sensitive flux density measurements that are not affected by the contamination of radio emission from nearby sources in the crowded regions of the Galactic Plane, as in the case of W44. As described in subsection 2.5.1, we coupled our images at these two frequencies in order to obtain spectral index maps (Fig.2.28), which highlighted a spread in the spectral slope distribution of both sources. We discussed the physical implications of the observed region-dependent spectral indices for W44 and IC443 and we compared them with both the radio and gamma-ray intensity maps in order to show possible correlations.

In view of our results in terms of both high quality maps and sensitivity of the flux density measurements, we believe that the single-dish techniques represent the most complete way to perform radio imaging of large structures (~1° or more) at high frequencies. Indeed the interferometry is certainly unbeatable in terms of image resolution, but synthesis imaging

becomes difficult in the context of extended sources at high frequencies. On the other hand, we have seen that the most prominent features highlighted in the SRT maps at 7 GHz and 21.4 GHz are coherent with the high-resolution, low-frequency interferometric images of W44 and IC443. These results allow us to assert that good mapping quality of large structures can be maintained with SRT in the single-dish configuration even at high frequencies if deep and oversampled OTF single-dish mapping is provided.
Sensitive high-resolution radio observations at up to ~18 GHz are reported in the literature only for Tycho, while for SNRs W44 and IC443, the highest reported radio frequencies are at up to 5−10 GHz. *Planck* observations of W44 and IC443 were performed at up to 70 GHz and 857 GHz, respectively, with an angular resolution in the $5' - 31'$ range (Planck Collaboration et al., 2016). SRT *K*-band observations of W44 and IC443 provided the first images ever obtained above 10 GHz with sub-arcmin resolution, which is enough to obtain accurate continuum flux density measurements and spectra. I managed to use these measurements with radio data available in the literature in order to characterise the integrated and spatially-resolved spectra of these SNRs, and to find significant frequency- and region-dependent spectral slope variations. I performed the weighted least-square fit of Tycho, W44 and IC443 radio spectra using the MPFIT[1] (Markwardt, 2009) package.

3.1 W44

As discussed in subsection 2.5, our SRT maps of W44 at 7.0 and 21.4 GHz (see Fig.2.26(a) and 2.27(a)) show a detailed structure of the remnant. However, concerning the map obtained at 1.55 GHz, we could use it only to carry out the sensitive integrated flux density measurement, since the beam of SRT at this frequency (HPBW = 11.1′) makes it impossible to get an adequate resolution in order to resolve the SNR and to perform a spatially-resolved study. Then, we compared our maps at 7.0 GHz and 21.4 GHz with those carried out with both other single-dish telescopes and VLA observations performed at lower frequencies.
In order to perform a direct comparison between the SRT performances and those of other single-dish telescopes, we considered the images carried out with Effelsberg at 4.9 GHz and Urumqi at 4.8 GHz, and we compared them with our 7.0 GHz maps (the most similar in terms of frequency). The Effelsberg map of W44 was acquired during a survey of the Galactic Plane performed at 4.875 GHz (Altenhoff et al., 1979), which was characterized by an HPBW of 2.6′, and it is comparable with the SRT resolution of 2.7′ at 7.0 GHz. Scans were taken in Galactic latitudes over b = ±2° with a rate of 80 arcmin min^{-1}, and spaced every 1 arcmin in Galactic longitude. This map is compared with that obtained with SRT in Fig.3.1, and we could note that both images show very similar details in the W44 morphology. A more recent observation of W44 was performed during a polarization survey carried out with Urumqi at 4.8 GHz (Sun et al.,

[1] http://purl.com/net/mpfit

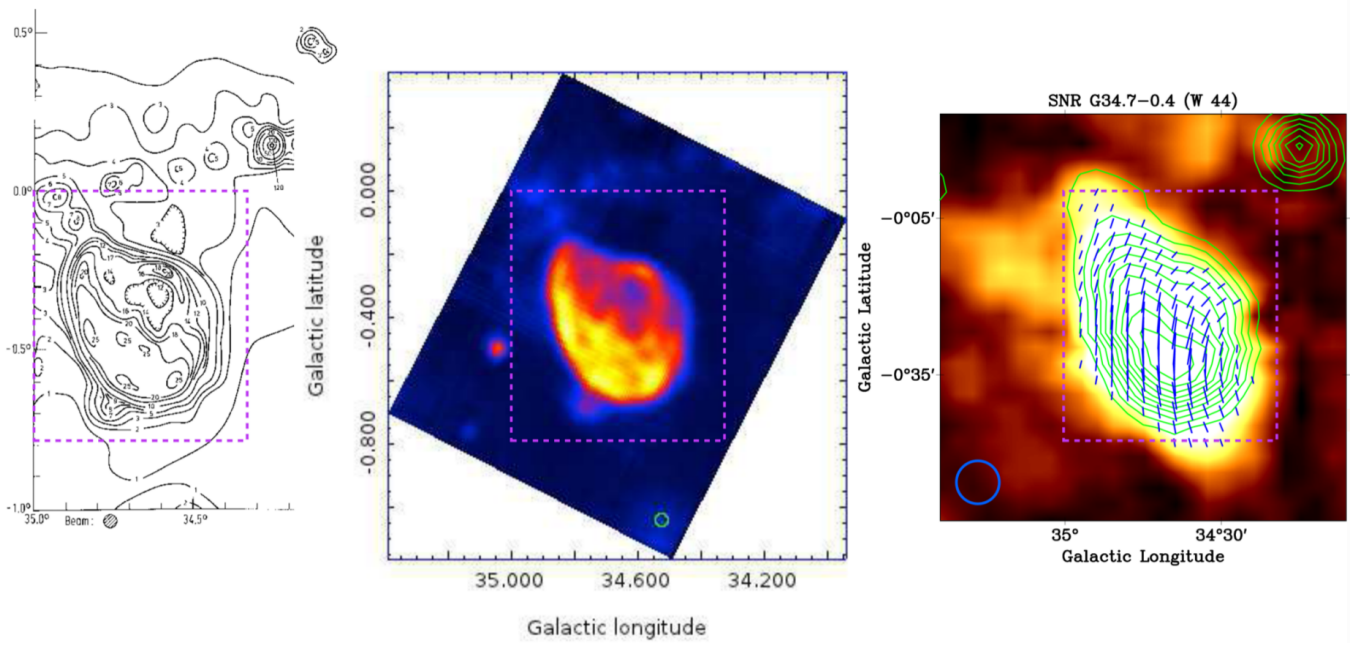

Figure 3.1: $Left$: contour map obtained with Effelsberg at 4.9 GHz (Credit: Altenhoff et al. 1979, reproduced with permission ©ESO). $Middle$: SRT image at 7.0 GHz. $Right$: intensity contours (indicated in green) obtained with Urumqi at 4.8 GHz (Credit: Sun et al. 2011, reproduced with permission ©ESO). The dotted rectangles indicate the same sky region. The blue and green circles in the bottom corner of the maps show the beam size (Egron et al., 2017).

2011). The related map is also shown in Fig.3.1. By comparing the three images, it can be noted that the maps carried out with Effelsberg and SRT show the strong intensity regions that are located mainly in the south (Galactic latitude) of the remnant and the details of its morphology. The Galactic Plane and sources nearby W44 are also clearly observable with SRT. Instead, W44 appears more confused in the case of the Urumqi map, since the sources in the vicinity of the SNR and part of the Galactic Plane are not resolved from the remnant (see Fig.3.1), such as in the case of the unidentified source detected at ~1 Jy by SRT in the north-east direction. This is related to the beam width associated with Urumqi at 4.8 GHz, which is about 3.5 times larger than that of SRT at 7 GHz (9.5 arcmin for Urumqi against 2.7 arcmin for SRT).

We then compared the W44 maps carried out with SRT at 7.0 GHz and 21.4 GHz with the high-resolution VLA images of the remnant at 1465 MHz (Jones et al., 1993) and 324 MHz (Castelletti et al., 2007), which were obtained using interferometric multiple-configurations. The comparison of the four maps is provided in Fig.3.2. The radio emission of W44 is characterised by an asymmetric limb-brightened shell, which is well detected in all images. It occurs along the eastern boundary at ~(RA, Dec) = (18^h 56^m 50^s, 01°17′), and it results from the interaction between W44 and dense molecular clouds observed in this region (Seta et al. 2004; Reach et al. 2005). The VLA images revealed the numerous bright knots and filaments of radio emission

related with shocked and compressed clouds or sheets of dense gas of size ~ 0.4 to 8 pc. The main features of this emission, like the bulk of the radio emission and the western bright arc, are detected in our C-band map. The brightest filaments are also detected, although not well resolved as in the VLA images. On the other hand, the resolution of the SRT map at 21.4 GHz is high enough to detect the filamentary structures of the eastern-bright shell, which are in good agreement with those revealed in the interferometric images. A radio synchrotron nebula associated with the pulsar PSR 1853+01 was also detected within the SNR both in the VLA and K-band SRT images. Its position is slightly offset w.r.t. the pulsar, which is consistent with a motion of the pulsar away from the SNR centre (Jones et al. 1993, Castelletti et al. 2007).

As shown in Fig.2.9(c), the mid-IR study presented by Castelletti et al. (2007) revealed a region of size ~10′ located just outside the south-east limb of W44 (centred at RA = 18^h 56^m 47.9^s, Dec = 01° 17′ 54″, and indicated by the red nebula in Fig.2.9(c)) that was previously identified as the H_{II} region G034.7−00.6 by Paladini et al. (2003). In the same region, the combination of the Spitzer observations at 24 μm and 8 μm showed the Strömgren sphere, limited to the east by an annular photo dissociation region (PDR) emitting near 8 μm (green) and to the west side by the IRAS point source 18544+0112, probably associated with a young stellar object (YSO) in a primitive evolutionary stage (Molinari et al., 1996) and located in the concave shape of the brightest radio filament. This interesting infrared region is also visible in our images at 7.0 GHz and 21.4 GHz as a bright spot centred at (RA, Dec) = (18^h 57^m 10^s, 01° 18′). In particular, in the K-band map, this region seems more structured and we note a correspondence between its brightest part and the 8 μm infrared emission related with a photo dissociation region (PDR) dominated by polycyclic aromatic hydrocarbon (PAH) (Castelletti et al., 2007). We calculated a brightness associated with this region of about 0.7 Jy beam^{-1} in C-band and a flux density of 1.1±0.1 Jy in K-band.

The short bright arc, which is located in the western side of the remnant at (RA, Dec) = (18^h 55^m 20^s, 01° 22′), is also revealed both in the 7.0−21.4 GHz SRT and VLA images. It corresponds to the SNR shock colliding with a molecular cloud located in this region, which is consistent with bright optical filaments (Giacani et al. 1997; Mavromatakis et al. 2003) and IR observations.

After the qualitative analysis of the images, we studied the integrated flux densities obtained with SRT at 1.55 and 7 GHz in comparison with those presented in the literature. We considered the the continuum flux results presented in the literature, which were corrected by Castelletti et al. (2007) to Baars et al. (1977) flux density scales, between 0.408 GHz and 10.7 GHz. They are shown together with our measurements in Table 3.1. We wanted to stress that the Altenhoff et al. (1970) flux density measurements at 1.414 GHz, 2.695 GHz and 5.0 GHz reported in Table 3.1 included the actual errors of 10 %, contrary to what reported by Castelletti et al. (2007) that erroneously reported 0.4 Jy as error for all these flux values.

First of all, we noted that no recent observations above 2 GHz were performed since the late 1970s for W44. Furthermore, the continuum flux results presented in the literature provide a

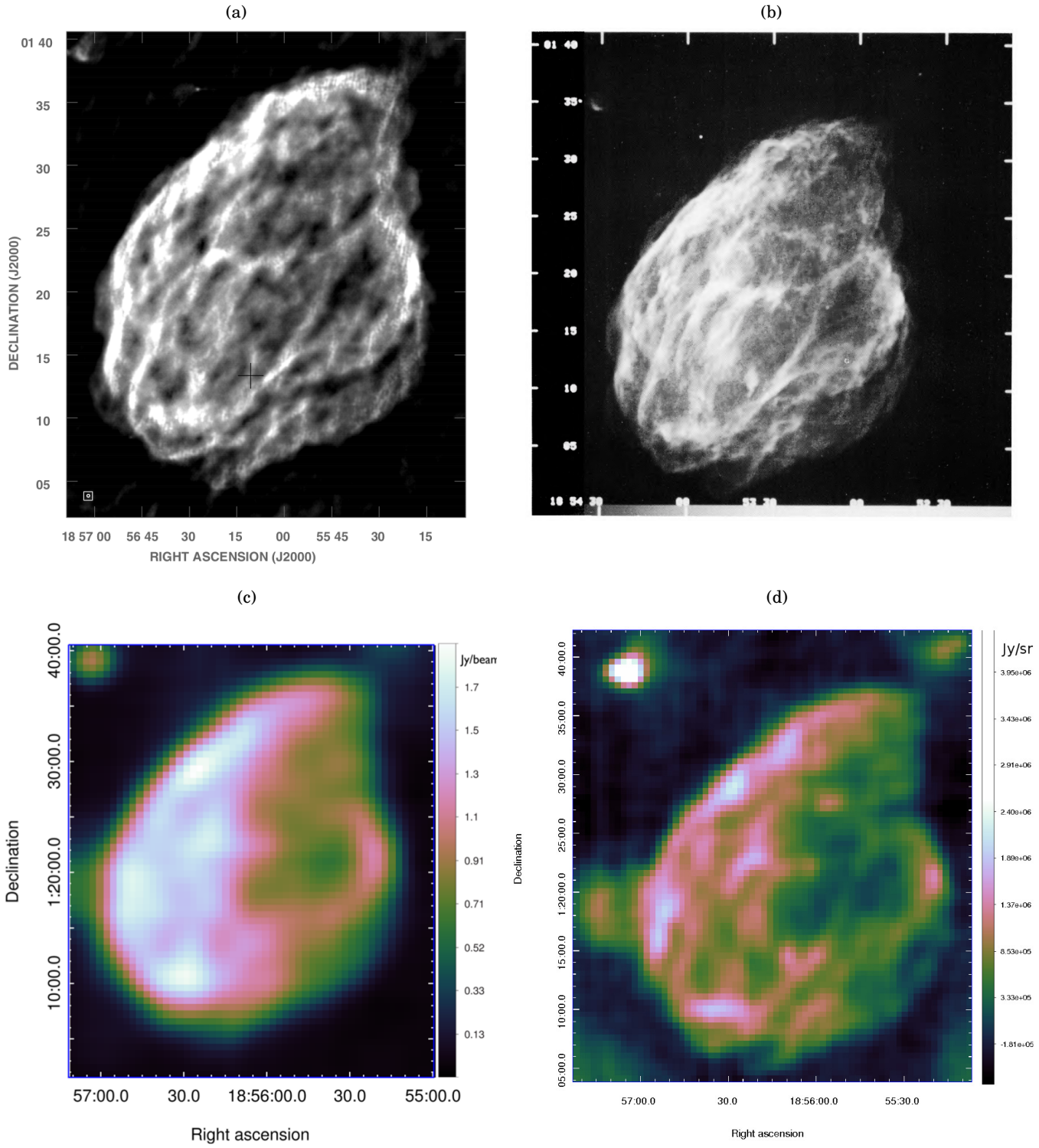

Figure 3.2: Comparison of the continuum maps of SNR W44 obtained with the VLA at a) 324 MHz (Castelletti et al., 2007) and b) 1465 MHz (Jones et al., 1993) with that carried out with SRT at c) 7.0 GHz (Egron et al., 2017) and 21.4 GHz (Loru et al., 2019). The beam size in the C-band SRT map is represented by the point-like source in the top left corner.

wide scatter. In particular, the measurements at 1.4 GHz by Giacani et al. (1997) ($S_{1.4GHz}$ = 210 ± 20 Jy) and Castelletti et al. (2007) ($S_{1.4GHz}$ = 300 ± 7 Jy) are inconsistent. On the other hand, our result at 1.55 GHz ($S_{1.55GHz}$ = 214.4 ± 6.4 Jy) is comparable within 1σ with the Giacani et al. (1997) value and most other L-band flux measurements obtained in the 1960s (Leslie 1960; Scheuer 1963; Pauliny-Toth et al. 1966a, Pauliny-Toth et al. 1966b; Beard & Kerr 1969). Our measurement at 7.0 GHz ($S_{7.0GHz}$ = 93.7 ± 4.0 Jy) shows an agreement with the previous measurements of 95 ± 23 Jy obtained at the near frequency of 8.3 GHz by Hollinger & Hobbs (1966).

Taking into account the SRT flux density measurements at 1.55 and 7.2 GHz, we achieved an estimate of the high-frequency spectral index of α= 0.55 ± 0.03. We observed that the flux density measurements reported in Table 3.1 at lower frequencies suggest a softer spectral index than our 1.55−7.0 GHz estimate. In Fig.3.1, I show the SED of W44 in the 0.408−10.7 GHz frequency range obtained from the data reported in the literature and SRT measurements at 1.55 and 7.0 GHz (all values are reported in Table 3.1). In the same figure, I also show the linear fit provided by previous studies (blue dashed line; $\alpha_{0.22-10.7GHz}$=0.37 ± 0.02, Castelletti et al. 2007) and that obtained considering the SRT measurements (red dashed line). This comparison confirms the possibility of a spectral steepening up to ∼1 GHz. In light of this, we decided to perform a weighted fit to the data in the 0.02−1.0 GHz, obtaining a spectral index of α = 0.36 ± 0.02 associated with a very significant goodness-of-fit (χ^2/dof = 1.06). This confirms the possible spectral steepening at high frequencies for W44.

This kind of spectral behaviour could be related to the approach to a possible break in electron energy distribution (as averaged for the whole SNR extent). Indeed, a steepening in the high-frequency spectra of evolved SNR is expected, and it could depend on the SNR age and other physical parameters such as the ambient density and the magnetic field. An indication of the frequency at which this break could take place arises from gamma-ray observations. Recent gamma-ray studies pointed out a steepening of the primary particle spectrum at energies of ∼ 10 GeV for W44 (Giuliani et al. 2011; Ackermann et al. 2013; Cardillo et al. 2014) that implies synchrotron break/cut-off at frequencies >10 GHz. On the other hand, it is important to bear in mind that in complex sources like SNRs secondary electron populations produced by hadronic interactions could represent a major fraction of the whole leptonic plasma present in the remnant (Lee et al. 2015; Cardillo et al. 2016). These secondary hadronic electrons are expected to take ∼10 % of the primary particle energy. Thus, a corresponding synchrotron spectrum change due to this particle population could be expected in the GHz range, in addition to the primary particle spectrum change at higher frequencies. However, more observations are required in the 1−10 GHz range in order to confirm these spectral turnovers and better constrain the precise break frequencies. With this aim we performed a detailed high-frequency study using our SRT measurements at 21.4 GHz.

The K-band flux density measured for W44 is far below the extrapolation of the spectrum

Table 3.1: Integrated flux density on the SNR W44. The measurements used to perform the high-frequency spectral study are indicated in grey.

Freq. (GHz)	Flux density density (Jy)	Reference	Freq. (GHz)	Flux density density (Jy)	Reference
0.408	291±58	Large et al. (1961)	1.442	300±7	Castelletti et al. (2007)
0.408	440±88	Kesteven (1968)	**1.55**	**214.4±6.4**	**Egron et al. (2017)**
0.408	290±58	Clark et al. (1975)	2.65	167±17	Beard & Kerr (1969)
0.43	291±59	Kundu & Velusamy (1967a)	2.695	170.3±17	Altenhoff et al. (1970)
0.43	567±178	Dickel et al. (1991)	2.7	107±10	Altenhoff et al. (1970)
0.61	314±32	Moran (1965)	2.7	169±18	Willis (1973)
0.75	242±24	Kellermann et al. (1969)	2.7	179±10	Velusamy & Kundu (1974)
0.75	270±27	Pauliny-Toth et al. (1966a)	2.7	124±19	Milne & Dickel (1974)
0.96	208±8	Harris (1962)	3.0	146±29	Scheuer (1963)
0.96	266±40	Wilson (1963)	3.125	135±14	Kuz'min et al. (1960)
1.39	173±35	Westerhout (1958)	4.875	123±12	Downes et al. (1980)
1.4	188±23	Pauliny-Toth et al. (1966a)	5.0	117.55±6	Sun et al. (2011)
1.4	173±26	Kellermann et al. (1969)	5.0	155±23	Milne & Hill (1969)
1.41	236±47	Scheuer (1963)	5.0	126.7±13	Altenhoff et al. (1970)
1.41	236±35	Beard & Kerr (1969)	**7.0**	**95.7± 4.6**	**Egron et al. (2017)**
1.414	274±30	Altenhoff et al. (1970)	10.7	104±7	Kundu & Velusamy (1972)
1.442	210±20	Giacani et al. (1997)	**21.4**	**25.3±3**	**Loru et al. (2019)**

obtained through low-frequency SRT measurements (Egron et al., 2017). We estimated a spectral index of $\alpha = 1.26 \pm 0.09$ using the integrated flux density measurements carried out with SRT at 7.0 GHz and 21.4 GHz. The comparison between this result and the spectral index of $\alpha = 0.55 \pm 0.03$ (1.55−7.2 GHz) obtained by Egron et al. (2017) suggests a significant spectral index steepening at high frequencies.

In Fig.3.1, I show a comprehensive picture of the SED of W44 in the 610−21.4 GHz frequency range , which was obtained by using the flux density measurements from Table 2 by Castelletti et al. (2011)[2], the integrated flux density at 5 GHz provided by Sun et al. (2011) and those that we obtained with SRT at 1.5 GHz, 7.0 GHz (Egron et al., 2017) and 21.4 GHz (Loru et al. 2018). All integrated flux density estimates that we used to perform this spectral index study are highlighted in grey in Table 3.1. We did not consider the flux density measurements available in the literature under 610 MHz (these too reported in Table 3.1), since they do not affect the study of the high-frequency spectrum of W44. We decided to exclude from our analysis the Altenhoff et al. (1970) measurements at 1.414 GHz, 2.695 GHz and 5 GHz on view of the already mentioned controversies on the flux errors and the availability of other integrated flux density estimates at the same frequencies. Further high-frequency measurements between 30 GHz and 70 GHz were carried out by *Planck* with an angular resolution from $31'$ to $5'$ (Planck Collab-

[2]Only data corrected to the scale of Baars et al. (1977) are taken into account

oration et al., 2016). Since the resolution of *Planck's Low Frequency Instrument* (LFI) makes it difficult to obtain sensitive flux density measurements of a source located in a very crowded portion of the Galactic plane, we decided to exclude *Planck* data from our study. Similar arguments may apply to the low-resolution QUIJOTE data at 10−20 GHz (Génova-Santos et al., 2017).

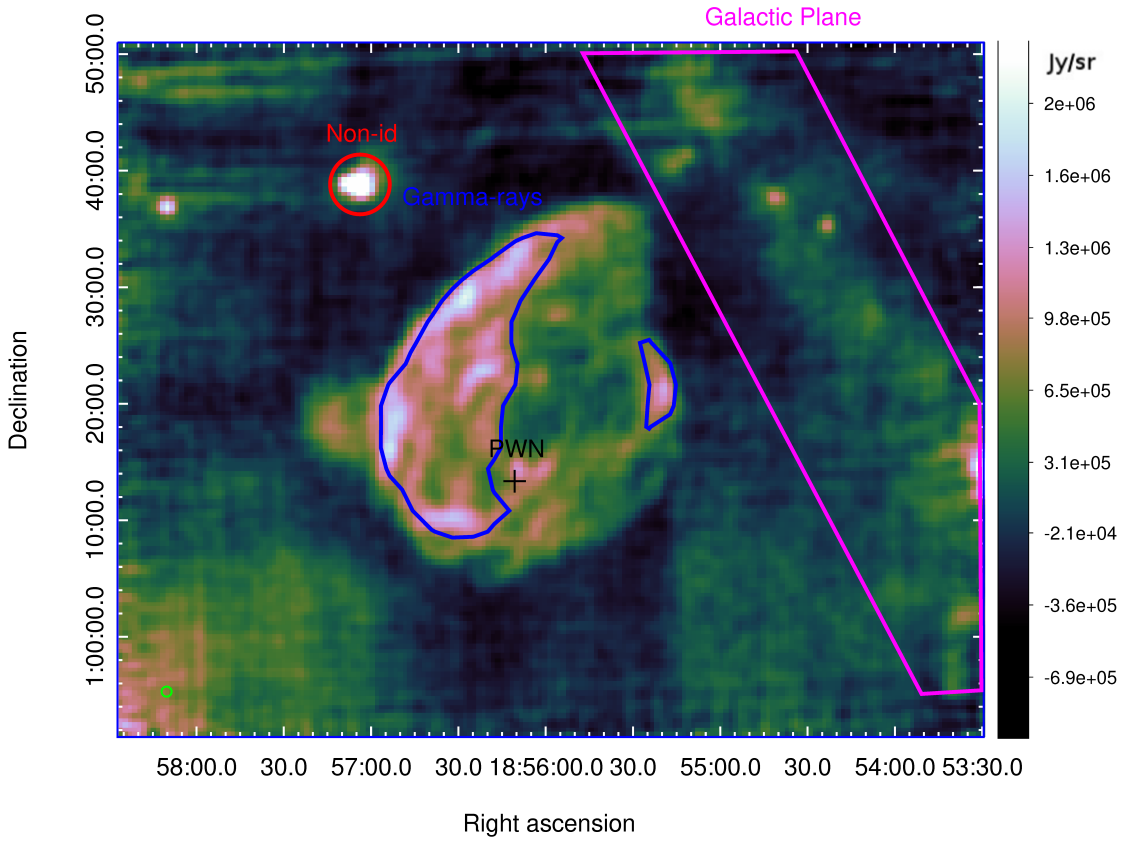

Figure 3.3: Continuum map of SNR W44 at 21.4 GHz (Loru et al., 2019). The blue regions indicate the gamma-ray emission seen by AGILE and Fermi-LAT (Giuliani et al. 2011, Abdo et al. 2010). The red circle refers to the bright non-identified source described in the text. The black cross shows the position of the PWN. The magenta region indicates the Galactic plane.

Taking into account the significant scatter of flux density measurements and the low availability of high-frequency measurements, we modeled the integrated spectrum of W44 using a simple synchrotron model with an exponential cutoff expressed by $S(\nu) = K\left(\frac{\nu}{\nu_0}\right)^{-\alpha} e^{-\frac{\nu}{\nu_0}}$, where K is a normalisation constant and ν_0 is the cut-off frequency. The weighted least-squared fit (shown in Fig.3.1) gives a spectral index of $\alpha = 0.24 \pm 0.04$, a cut-off frequency of $\nu_0 = 15 \pm 2$ GHz and $K = 267 \pm 5$ Jy. This result is consistent with the synchrotron break at frequencies $\gtrsim$10 GHz predicted by the models based on gamma-ray observations (Ackermann et al., 2013).
An electron of energy E accelerated in a magnetic field B radiates its peak power at a frequency ν so that $E = 14.7(\nu_{GHz}/B_{\mu G})^{\frac{1}{2}} GeV$ (Reynolds, 2008). Assuming a magnetic field in the range 18−90

μG (Castelletti et al. 2011, Ackermann et al. 2013) and our derived cut-off frequency of 15 GHz, we obtained a maximum energy of the electron distribution in the ∼6−13 GeV range. This result is in agreement with the particle maximum energy of ∼10 GeV estimated from the gamma-ray data (Uchiyama et al. 2012, Ackermann et al. 2013). The magnetic field interval reported above is typically in agreement with leptonic-dominated emission scenarios and could also be simply explained by the compression theory of the ISM magnetic field (about 5 μG, Wielebinski & Beck 2005) by a factor of 3 to 4.

In order to properly investigate the co-spatial radio-gamma emitting regions, we restricted our analysis to the regions shown with blue contours in Fig.3.3 that correspond to the gamma-ray emissions detected with AGILE and Fermi-LAT (Giuliani et al. 2011, Abdo et al. 2010). The eastern gamma-ray region was considered by Cardillo et al. (2016) to study the radio and gamma-ray spectra from W44 in terms of re-acceleration and compression of Galactic CRs. Using the flux density measurements obtained for this region from the SRT maps in the L, C (Egron et al., 2017) and K-band (Loru et al., 2019), we found a cutoff frequency of 16 ± 1 GHz, which is consistent and slightly higher than the corresponding value obtained from the total integrated flux for W44. Coupling this result with the locally enhanced magnetic field of 1.4 mG deduced by Cardillo et al. (2016) for this region, we obtained a maximum electron energy of 1.6 GeV. This lower energy cutoff with respect to the ∼10 GeV limit obtained from standard magnetic field values, could suggest the presence of a spectrum dominated by secondary electrons produced from pion decay following proton-proton scattering. Indeed, as reported by Cardillo et al. (2016), electrons with a maximum energy ∼1−2 GeV could result in crushed clouds regions from protons with a cutoff energy at ∼ 10 GeV.

We studied the spectral indices associated with all the different peculiar regions of W44, which are shown in Fig.3.3, by using the flux density measurements carried out with SRT at 7.0 GHz (Egron et al., 2017) and 21.4 GHz (Loru et al., 2019). In our analysis, we also included a region centred in (RA, Dec) = ($18^h55^m49.9^s$, $1^\circ20'00.8''$) with radius of $4.5'$, which is representative of the fainter central emission. We obtained $\alpha = 1.0 \pm 0.1$ for the eastern boundary, α = 0.9 ± 0.1 for the western arc, and α = 1.4 ± 0.1 for the central region. The comparison of these spectral indices with those calculated by Egron et al. (2017) in the 1.55−7.0 GHz range confirms the steepening observed in the integrated spectrum of W44 for all the considered SNR sub-regions. On the other hand, this result suggests a spectral index spread ranging from relatively flatter spectra, which are associated with bright radio limbs and filaments, to steeper spectra in fainter radio regions. The same region-dependent scatter in the spectral slope distribution was highlighted by spatially-resolved spectral measurements in the 1.5−7.0 GHz frequency range (Egron et al., 2017), and might suggest the existence of distinct electron populations subject to different shock conditions and/or undergoing different cooling processes. Furthermore, we observed a correspondence between bright-flat spectrum regions and gamma-ray emission that could represent a signature of secondary electron populations produced by hadronic interactions in regions where

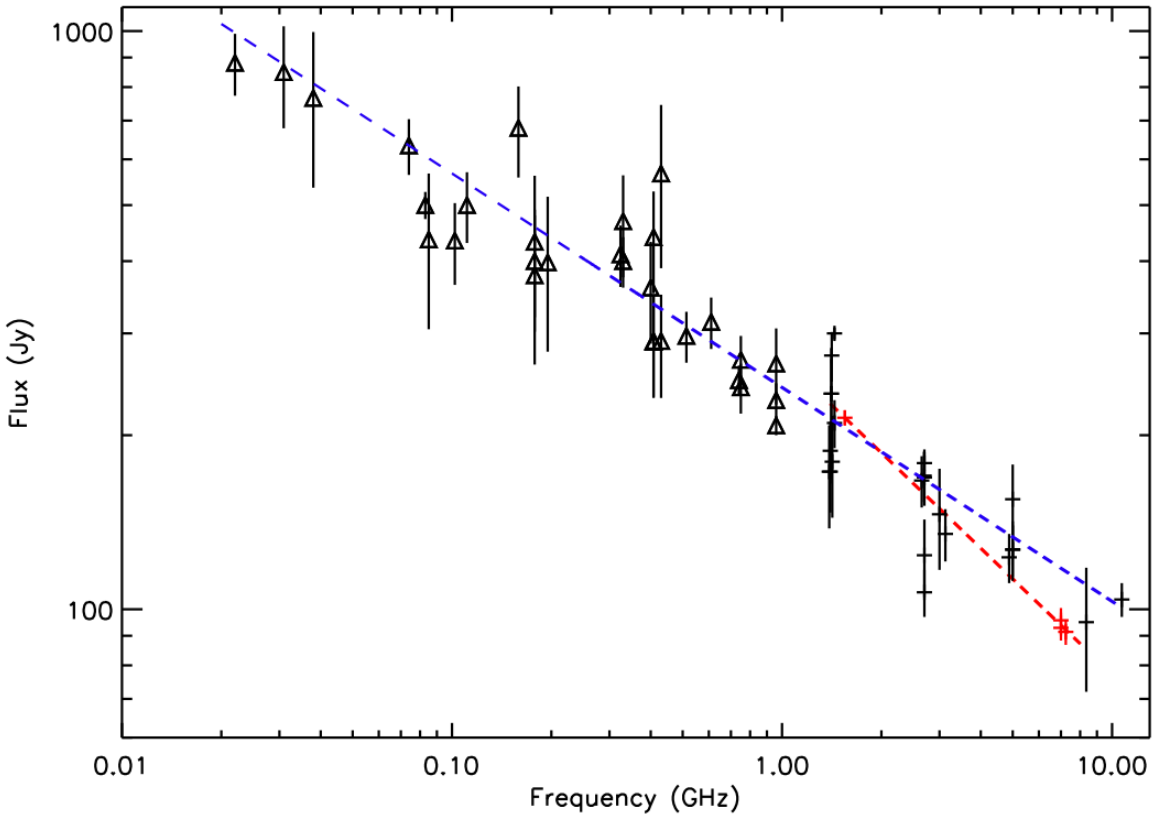

Figure 3.4: Integrated radio continuum spectra of W44 obtained from the flux density values available in the literature (Table 3.1; black points) in the frequency range 0.02−10.7 GHz together with the fit provided by Castelletti et al. 2007 on the same data (blue dashed line). The spectral slopes derived from SRT data (Table 3.1; red points and dashed line) at high frequencies (1.5−7.2 GHz) suggest a possible spectral steepening with respect to the lower frequency measurements (0.02−1 GHz; triangles).

the SNR shock collides with dense molecular clouds (Cardillo et al., 2016).

An unidentified source is spatially resolved by SRT at 21.4 GHz in the north-east direction, with an associated flux density of 1.2 ± 0.1 Jy. Very Large Array (VLA) radio images at 74 and 324 MHz (Castelletti et al., 2007) and *Spitzer Space Telescope* infrared observations at 24 μm and 8 μm (Reach et al., 2006) detected this source that could be associated with the G035.040-00.510 HII region. We also detected this source as a point-like with SRT at 7.0 GHz (Egron et al., 2017) with a flux density of 0.94 ± 0.05 Jy. The associated spectral index obtained combining the SRT flux density measurements at 7.0 GHz and 21.4 GHz is $\alpha = -0.2 \pm 0.1$ (implicitly assuming non-variability of the source flux).

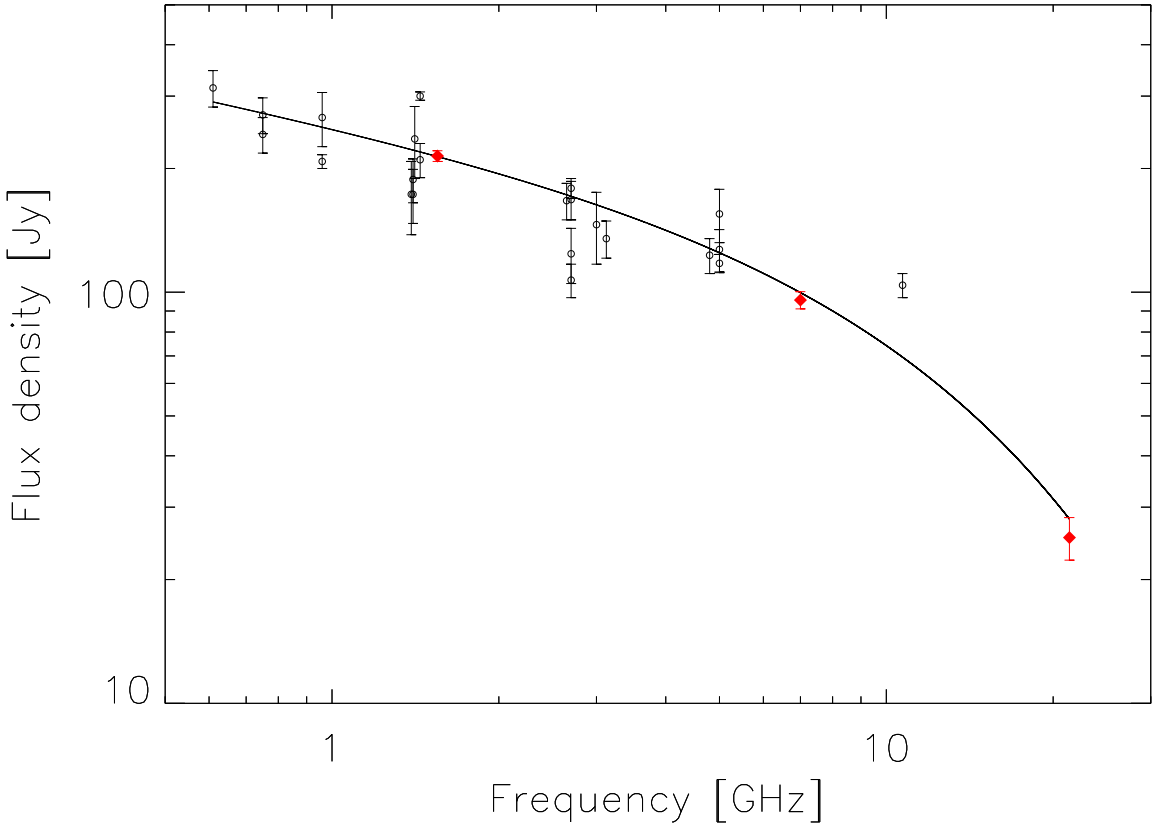

Figure 3.5: Weighted least-squares fit applied to the W44 SED for a synchrotron power-law with an exponential cut-off model. The red diamonds correspond to the SRT flux density measurements at 1.55, 7.0 and 21.4 GHz.

3.2 IC443

As described in Section 3.1 for W44, also for IC443, we compared the maps obtained with SRT at 7.0 and 21.4 GHz with those available in the literature that are carried out both with single-dish and interferometric telescopes. Single-dish observations of IC443 were performed with Effelsberg at 868 MHz in 1999−2000 (Reich et al., 2003), and with Urumqi in the frame of a 5 GHz polarization survey of the Galactic Plane between 2004 and 2009 (Gao et al., 2011). The related maps are shown in Fig. 3.6 together with our image at 7.0 GHz for a direct comparison between images at about the same frequency.

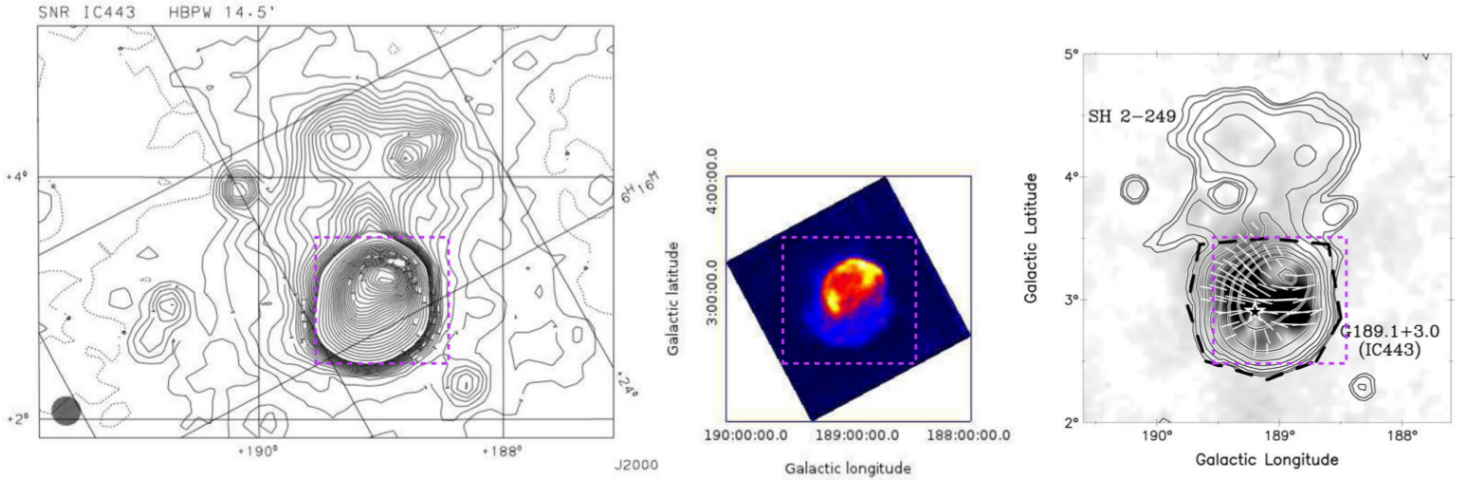

Figure 3.6: Radio continuum images of the SNR IC443 carried out with single dish telescopes (Egron et al., 2017). *Left* Contour plot observed at 868 MHz with Effelsberg (Credit: Reich et al. 2003, reproduced with permission ©ESO). *Middle*: SRT observation at 7.2 GHz in Galactic coordinates. *Right*: Radio continuum and polarization image of IC443 obtained with Urumqi at 5 GHz (Credit: (Gao et al., 2011), reproduced with permission ©ESO). The dotted rectangles indicate the same sky region.

In the three images, the regions within the remnant with different strong emission can be distinguished. We noted that the images obtained with Effelsberg and Urumqi show in detail the northern (Galactic latitude) region where IC443 interacts with an HII region (S249). These features are not appreciable in the SRT map, where more details on the morphology of the remnant are showed. This arises from the better SRT angular resolution (HPBW = 2.7′) with respect to Urumqi (HPBW = 9.5′) and Effelsberg (HPBW = 14.5′) at the observed frequencies. Therefore, we compared the SRT images of IC443 carried out at 7.0 GHz and 21.4 GHz with the high-resolution images, which were obtained coupling interferometric and large-area single-dish observations, in order to evaluate the morphological details of the remnant that are appreciable with the two observational techniques and instruments. We considered the interferometric image obtained by Lee et al. (2008) by coupling VLA and Arecibo low-frequency data at 1.4 GHz in order to achieve an extremely good sensitivity and angular resolution of about 40″, and that obtained by Castelletti et al. (2011) at 330 MHz from multiple-configuration VLA observations. These images are shown together with SRT maps at 7.0 and 21.4 GHz in Fig.3.7. IC443 consists of two nearly concentric shells, which present a complex structure with the presence of filaments and a clear difference in the radio continuum intensity. The main features of the morphology of IC443 are detected in all the images, although not resolved in our maps. The eastern shell is open on the western side towards a weaker second shell (halo), which is possibly related to a breakout portion of the SNR into a rarefied medium (Lee et al., 2008). In our image at 7.0 GHz the filamentary structure of the halo is detected, and it is resolved with VLA at 1.4 GHz. This region is also visible

in our 21.4 GHz map, although not well detected. Indeed, despite the SRT high-resolution at this frequency, the adverse weather conditions that characterised the ESP observations of IC443 have lead to a negative impact on the quality of the image. The bulk of the emission comes from the north-eastern part of this shell, corresponding to signatures of atomic/ionic shock (Duin & Strom, 1975). The bright emission from the south-western part of the ridge has a more complex origin. Various signs of H_2 molecular shocks were highlighted by Burton et al. (1988). The pulsar and its PWN are located in this region. They very likely correspond to the remnant of the explosion which later formed IC443. No pulsations were detected from the neutron star, but all evidence points to the nature of a rotation-powered pulsar (Swartz et al. 2015, and references therein). We noted that the PWN is well detected in our K-band map, and it is presented like a brightest spot in the southern region. Two bright extragalactic point-like sources unrelated to the remnant (Braun & Strom 1986) are also present near (RA, Dec) = (06^h 17^m 30^s , 22° $25'$), although these are not resolved in the SRT maps.

In order to study the integrated spectrum of IC443, we considered the flux density measurements available in the literature that are reported in Table 2 by Castelletti et al. (2011). From the comparison with these data, we observed that our measurement at 1.55 GHz ($S_{1.55GHz}$ = 133.7 ± 4.0 Jy) is consistent with the values at ~ 1.4 GHz reported by Wanner (1961), Milne & Hill (1969), Green (1986) and Hill (1972). In the same way, our measurement at 7.0 GHz (S_{7GHz}= 66.8 ± 2.9 Jy) is consistent within 1σ with the measurement at 6.6 GHz reported by Dickel (1971) and equal to $S_{6.6GHz}$ = 70 ± 15 Jy.

We pointed out that typical continuum flux errors in the literature for IC443 are of the order of ~10−15 %, while we provided more accurate measurements, in particular for L-band flux densities. This is mostly due to our oversampled maps, in which tens of OTF baseline-subtracted scans are available for each pixel, providing straightforward error measurements through standard deviation estimates. We observed that previous spectral index studies performed on IC443 showed a turnover at the lowest radio frequencies (below ~ 30 MHz) that was attributed to thermal absorption processes at the SNR site (Castelletti et al., 2011).

We executed a fit of our SRT measurements in the interval 1.55−7.2 GHz, obtaining a spectral index estimate of α= 0.46 ± 0.03. This result is in perfect agreement with a spectral index estimate of α = 0.47 ± 0.06 that we obtained through a weighted fit of all previous radio data available in the literature in the 1.39−8.0 GHz frequency range. We noticed that SRT measurements halve the spectral index error previously obtained for the high-frequency range.

In order to investigate a possible spectral index steepening, we performed the same analysis on the literature data at low frequencies (0.02−1.0 GHz). We decided to exclude the very low-frequency data at 10 MHz, which is possibly affected by a turnover due to thermal absorption as suggested by Castelletti et al. (2011). The obtained spectral index is α= 0.33 ± 0.01, which suggests a flattening of the spectrum a low frequencies. Therefore, a slight steepening of the IC443 spectrum ($\Delta\alpha$ ~ 0.1) around ~1 GHz could be speculated considering previous data in

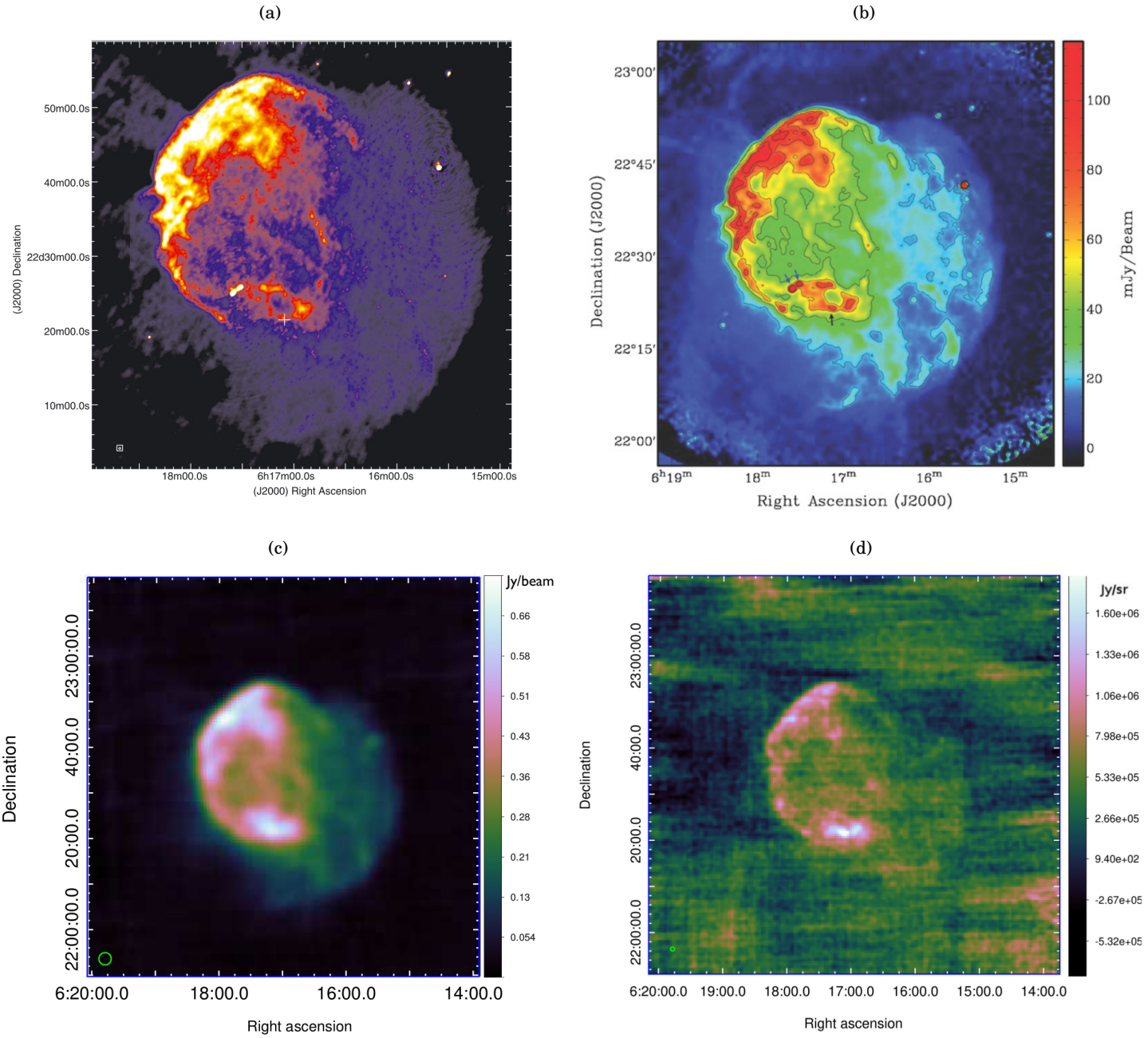

Figure 3.7: Comparison of the continuum maps of IC443 obtained with: (a) VLA at 330 MHz carried out with the multiple-configuration; (b) the combination of VLA and Arecibo at 1.4 GHz; (c) SRT at 7 GHz and (d) 21.4 GHz.

Table 3.2: Integrated flux densities on the SNR IC443.

Freq. (GHz)	Flux density (Jy)	Reference	Freq. (GHz)	Flux density (Jy)	Reference
0.01	400±100	Bridle & Purton (1968)	0.408	289±28	Colla et al. (1971)
0.02	600±144	Braude et al. (1969)	0.635	179±18	Milne & Hill (1969)
0.022	615±75	Roger et al. (1986)	0.863	160±5	Reich et al. (2003)
0.02225	535±65	Roger et al. (1969)	0.960	196±24	Harris & Roberts (1960)
0.0223	529±36	Guidice (1969)	1.39	177±15	Westerhout (1958)
0.025	630±132	Braude et al. (1969)	1.4	146±18	Wanner (1961)
0.0263	600±48	Viner & Erickson (1975)	1.41	131±13	Milne (1971)
0.0267	561±33	Guidice (1969)	1.419	130±13	Green (1986)
0.0335	582±37	Guidice (1969)	1.42	138±15	Hill (1972)
0.0345	440±88	Dwarakanath et al. (1982)	**1.55**	**133.7±4**	**Egron et al. (2017)**
0.038	650±95	Baldwin (1954)	2.65	86±9	Milne & Hill (1969)
0.038	730±100	Blythe (1957)	2.7	104±15	Milne (1971)
0.38	460±46	Williams et al. (1966)	5.0	79±11	Milne (1971)
0.0386	547±40	Guidice (1969)	5.0	84.6±9.4	Gao et al. (2011)
0.074	470±51	Castelletti et al. (2011)	**7.0**	**69.0±3.5**	**Egron et al. (2017)**
0.0815	420±63	Baldwin (1954)	8.0	90±18	Howard & Dickel (1963)
0.0815	470±70	Shakeshaft et al. (1955)	**21.4**	**66±7**	**Loru et al. (2019)**
0.083	470±80	Kovalenko et al. (1994)	30.0	56±3	Planck Collaboration et al. (2016)
0.102	480±80	Kovalenko et al. (1994)	44.0	39±3	Planck Collaboration et al. (2016)
0.111	440±80	Kovalenko et al. (1994)	70.0	20.5±1.2	Planck Collaboration et al. (2016)
0.151	280±35	Green (1986)	100.0	17.3±0.9	Planck Collaboration et al. (2016)
0.159	270±40	Edge et al. (1959)	143.0	11.1±0.8	Planck Collaboration et al. (2016)
0.178	210±42	Bennett (1962)	217.0	56±10	Planck Collaboration et al. (2016)
0.195	290±45	Kundu & Velusamy (1968)	353.0	229±30	Planck Collaboration et al. (2016)
0.330	248±15	Castelletti et al. (2011)	545.0	720±100	Planck Collaboration et al. (2016)
0.4	230±34	Davis et al. (1965)	857.0	2004±300	Planck Collaboration et al. (2016)
0.4	210±31	Seeger et al. (1965)	2300	2200±300	Planck Collaboration et al. (2016)
0.4	251±8	Kellermann (1964)			

the literature (without including SRT measurements), though not statistically significant (~2σ level). The SED of IC443 related to the data reported in the literature and SRT measurements is shown in Fig.3.8, which includes both the fit obtained from the literature in the frequency range 0.02−10.7 GHz (blue dashed line) and that resulting from SRT data at high frequencies (red dashed line). A possible spectral steepening at frequencies above ~ 1 GHz seems to be supported at >4σ confidence level using SRT observations alone, thanks to the smaller error on the high-frequency spectral index.

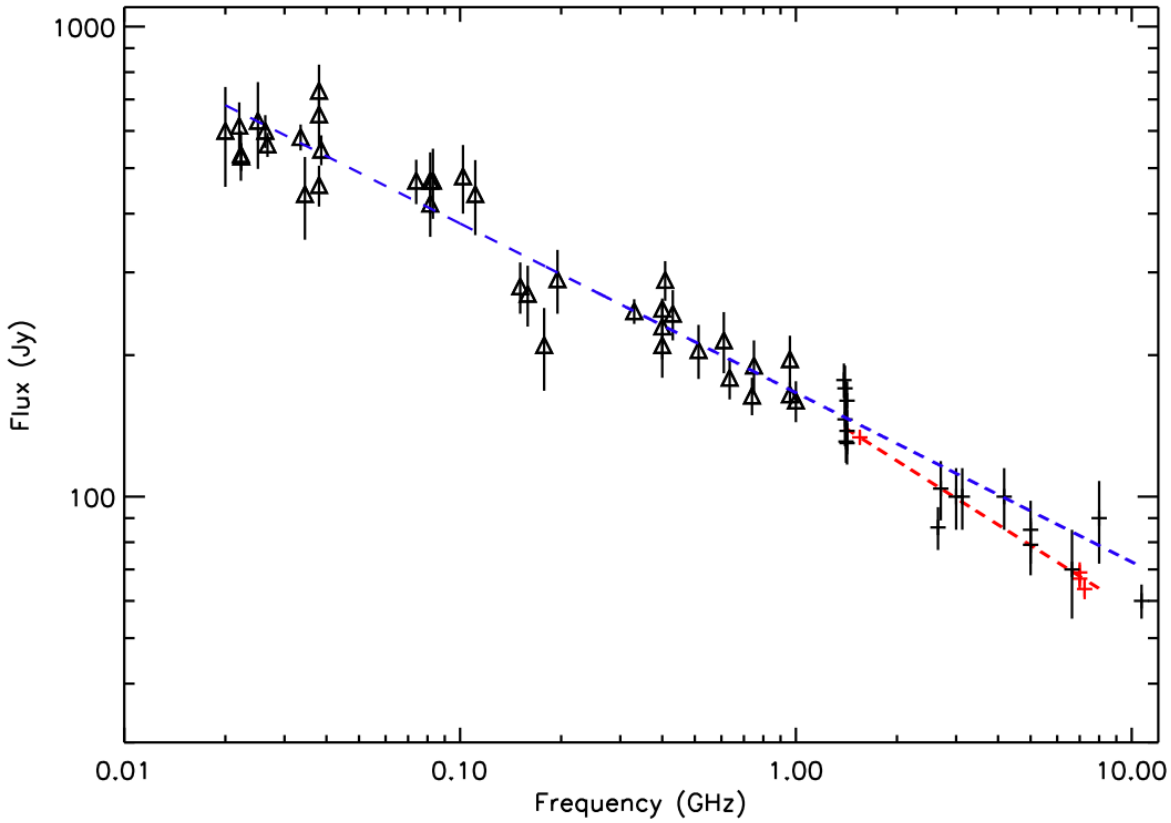

Figure 3.8: Integrated radio continuum spectrum of IC443 obtained from the flux density values available in the literature (Table 2 of Castelletti et al. 2011; black points) in the frequency range 0.02−10.7 GHz. The fit provided by (Castelletti et al., 2007) on the same data (blue dashed line) is also reported. As in the case of W44, although less significant, the spectral slopes derived from SRT data (red points and dashed line) at high frequencies (1.5−7.2 GHz) suggest a possible spectral steepening with respect to the lower frequency measurements (0.02−1 GHz; triangles).

The possibility of a significant production of thermal Bremsstrahlung radiation at radio continuum frequencies was proposed by Onić et al. (2012) to describe the IC443 spectrum at high radio frequencies (at up to ∼ 10 GHz) with a "concave up" model. On the other hand, a radio-microwave study performed by the Planck Collaboration et al. (2016) showed no indication of thermal Bremsstrahlung emission. They suggested a combination of synchrotron and dust emission to explain the integrated spectrum of IC443 in the 1−857 GHz frequency range. Furthermore, *Planck* data suggested the presence of a spectral bump in the 20−70 GHz range in contrast with the hypothesis of a concave-up spectrum. In order to disentangle these possible emission scenarios, we studied the integrated spectrum of IC443 up to high radio frequencies by including our sensitive measurement at 21.4 GHz.

We performed a weighted fit of the SRT data at 1.5 GHz, 7.0 GHz (Egron et al., 2017) and 21.4 GHz (Loru et al., 2019) with a simple power-law model, and we obtained a spectral index of α =

0.38 ± 0.03. This result is 1.3σ from the integrated spectral index of α = 0.46 ± 0.03 obtained in the 1.55−7.0 GHz interval. Coupling this result with the slight steepening ($\Delta\alpha$~0.1) around ~1 GHz pointed out previously, we could support the concave-up curvature of the radio spectrum firstly suggested by Onić et al. (2012).

A recent work (Onić et al., 2017), which coupled *Planck* data with microwave observations from space telescopes such as the *Wilkinson Microwave Anisotropy Probe* (WMAP), again showed a synchrotron component at up to ~70 GHz, with an additional contribution of Anomalous Microwave Emission (AME) due to the spinning dust process that leads to the observed bump. The spinning dust emission is based on a mechanism whereby the dust asymmetric grains with a non-zero electric dipole moment may be spinning due to the interaction with the ISM and radiation field, and thus radiate electromagnetic waves due to the rotation of their electric dipole moment (Ali-Haïmoud et al., 2009). The study of Galactic clouds performed by the Planck Collaboration et al. (2014) suggested that the AME could come from molecular clouds dust or photo-dissociation regions (PDR). The observed higher-frequency emission in IC443 above ~150 GHz could instead be attributed to thermal dust emission form the dust grains that survived the shock (Planck Collaboration et al., 2016).

In order to test the model proposed by Onić et al. (2017), we considered the flux densities available in the literature that are corrected accordingly to Baars et al. (1977) flux density scale in the frequency range 0.02−10.7 GHz. These values are reported together with the SRT measurements in Table 3.2. In Fig.3.9, I present the spectral model of IC443 proposed by Onić et al. (2017), based on least-squares fits (χ^2/dof = 2.3) of integrated flux density measurements from Table 3.2. Both the model that includes the spinning dust emission contribute and the one that only includes the synchrotron and dust emission contributions were considered. The resulting SED was modelled by a synchrotron emission with an exponential cut-off at 148 ± 23 GHz and a normalisation constant of 161 ± 3 Jy, spinning dust emission (peaked at the frequency 28 ± 3 GHz) represented by the expression shown in Equation (5) by Onić et al. (2017) and a high-frequency (> 140 GHz) thermal dust emission component.

SRT data at 1.5 GHz, 7.0 GHz and 21.4 GHz are consistent with the model that includes the spinning dust emission. In particular, our flux density measurement at 21.4 GHz independently supports the observed spectral bump, and confirms the trend suggested by the low-resolution *Planck* measurements at 30 GHz.

The possibility of a significant spinning dust emission from a SNR was introduced for the first time by Scaife et al. (2007) in a study of the SNR 3C96, which was not later confirmed. Later on, there was a possible detection of spinning dust emission from W44 (Génova-Santos et al., 2017). However, this result is strongly affected by unresolved emission contributions from the Galactic Plane. Within this context, our result on IC443 would be the first confirmation of spinning dust emission in a SNR.

Spatially-resolved spectral index studies on IC443 highlighted a correspondence between the

radio bright/flattest spectrum eastern region and the near-infrared ionic lines (Castelletti et al., 2011). Considering the cut-off observed at lowest radio frequencies, the thermal absorption of electrons would be the main mechanism responsible for the spectral flattening in this region (Rho et al., 2001). Our study performed on spectral index maps (Fig.2.28) showed a spread in the spectral index distribution of IC443 that instead could be due to an intrinsic variety in primary and secondary electron populations (spectral slopes and breaks) produced in shocks that are located in different SNR/PWN environments.

We coupled our map of IC443 at 21.4 GHz with that obtained with SRT at 7.0 GHz (Egron et al., 2017) in order to study the spectral indices associated with different peculiar regions across the SNR. As shown in Fig. 3.10, we analysed the north-eastern shell region related to the bulk of the radio emission, the region associated with the PWN, and those coincident with the gamma-ray emission as seen with MAGIC (Albert et al., 2007). The spectral index associated with the brightest part of the eastern shell is steeper ($\alpha = 0.35 \pm 0.1$) than the averaged value obtained in the same frequency range ($\alpha = 0.04 \pm 0.1$). This result indicates that the spectral bump related to the spinning dust emission is not evident in the eastern region.

A spectral flattening related to the brightest SNR regions is evident when we consider the southern region with an extraction radius of $1.4'$, which includes the associated PWN described at lower radio frequencies by Castelletti et al. (2011). We obtained a flux density of 0.53 ± 0.05 Jy and a flat spectral index of $\alpha = -0.05 \pm 0.09$ (7.0−21.4 GHz), in agreement with that reported in previous studies (Castelletti et al., 2011), and probably associated with optically thin PWN emission. In the bright southern region that includes the PWN and where the SNR interacts with a molecular cloud, the spinning dust emission could further contribute to the observed spectral flattening.

The VHE γ-ray source associated with IC443, such as seen by MAGIC (Albert et al., 2007), is located at (RA, Dec)=($06^h16^m43^s$, $+22°31'48''$) and occupies approximately a circular region with radius $\sim 0.05°$. Previous studies highlighted the morphological coincidence between the TeV emission and a molecular gas distribution (Castelletti et al., 2011). As shown in Fig.3.10, our 21.4 GHz image reveals a bright radio structure corresponding to the TeV source, with a flat spectral index of $\alpha = 0.03 \pm 0.09$ (7.0−21.4 GHz). The correlation between the TeV emission and bright radio/flat spectral regions could be related to an increase in hadron emission associated with a significant secondary electrons injection (Lee et al. 2015, Cardillo et al. 2016, Egron et al. 2017). The co-spatial presence of a molecular cloud interacting with the SNR could imply CR acceleration in a region characterised by strong post-shock densities and an enhanced magnetic field. This results from the fast decrease of the shock speed in a dense medium and an increasing role of the radiative losses (Petruk et al., 2016).

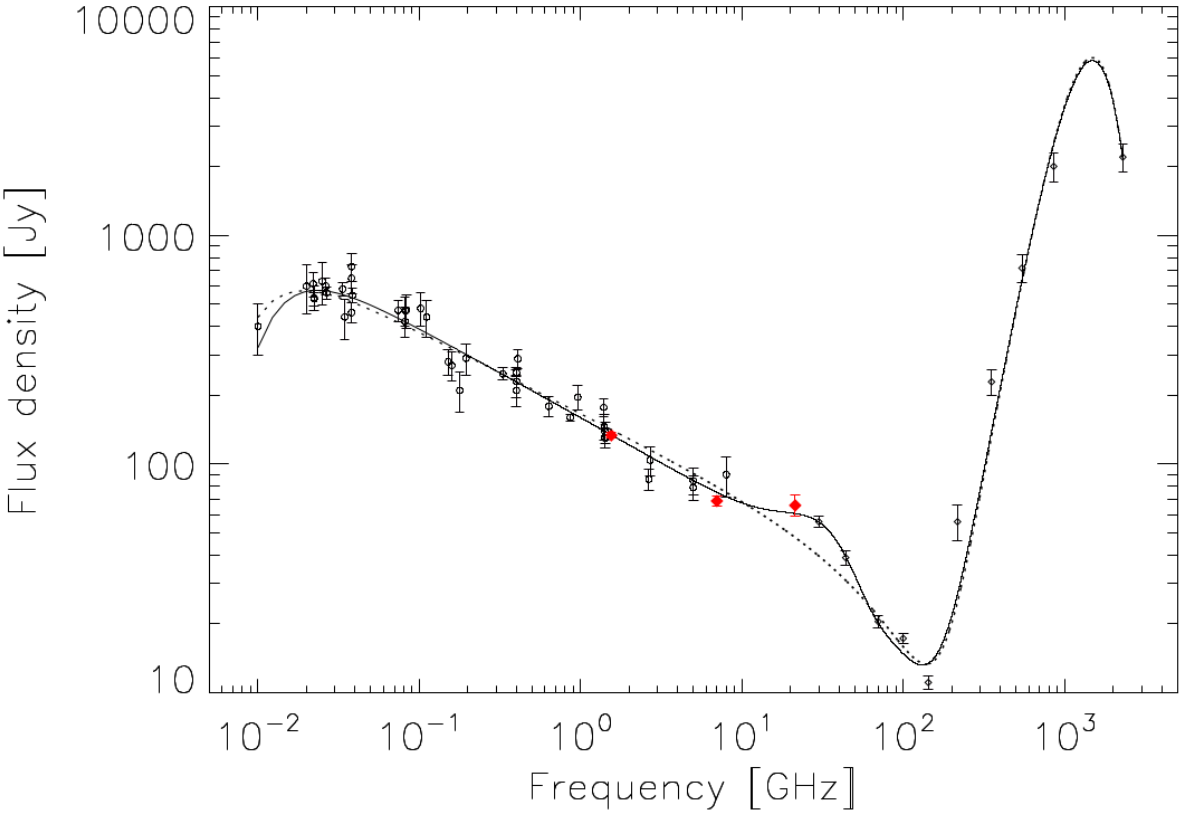

Figure 3.9: SED of IC443 from 0.408 to 857 GHz. Open circles and diamonds represent radio data from the literature at up to 8 GHz and the *Planck* data, respectively. SRT measurements are indicated with filled red diamonds. The solid and dashed lines represent the weighted least-square fit considering the spinning dust emission and without it, respectively.

3.3 Spatially-resolved studies of W44 and IC443

Our spatially-resolved spectral index studies, based on spectral index maps (Fig.2.28) in the frequency range 1.55−7.0 GHz, showed a significant spectral scatter along different SNR regions in our data. We considered this result as the demonstration that several electron populations are present in SNRs, including secondary electrons, which result from different shock conditions and/or undergoing different cooling processes. Despite this evidence, the investigation on the different phenomenological regions is made difficult by the fact that until now the SNRs was often studied under the simplistic assumption of a single-electron population (by performing integrated spectral analysis only).

Our results and those obtained by Castelletti et al. (2007) and Castelletti et al. (2011) on W44 and IC443 from the analysis of VLA data at lower frequencies (74−330 MHz), highlighted a correlation between the flat spectra and the brightest SNR regions near the limbs or filaments, while the fainter central regions and haloes exhibited steeper spectra.

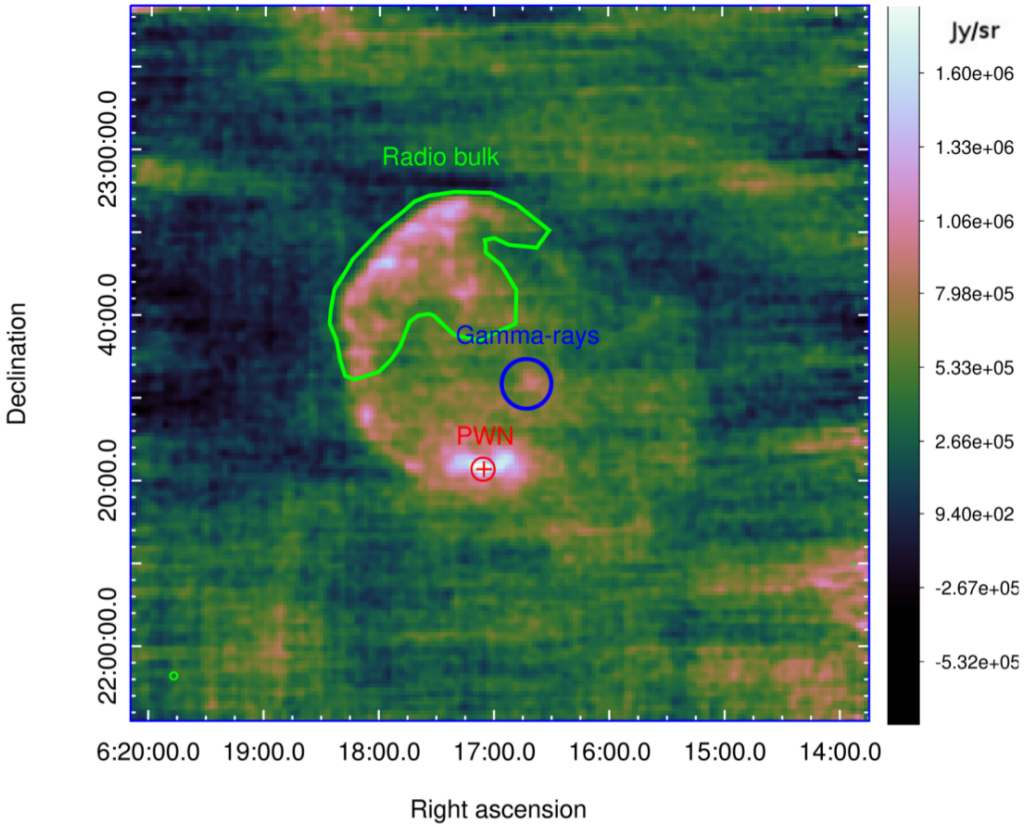

Figure 3.10: Continuum map of SNR IC443 at 21.4 GHz. The red cross and circle indicate the position of the compact source CXOU J061705.3+222127 and the associated PWN, respectively. The blue circle indicates the gamma-ray emission seen with MAGIC (Albert et al. 2007). The green region shows the bulk of the radio emission.

The VLA studies performed at low-radio frequencies (74−330 MHz, Castelletti et al. 2011) on IC443 attributed the correspondence between the spectral flattening and the brightest regions to the effect of the thermal absorption. Indeed this process could explain both the low-frequency cut-off (at frequencies <50 MHz) observed in the integrated SNR spectrum of IC443 and the apparent spread in spectral index distributions seen by the VLA at <1 GHz, which is possibly correlated with the non-uniform optical depth along the SNR. Thus, in our investigation we first considered the possibility of a thermal absorption (free-free) contribute. However, we noted that the average free-free continuum optical depth, which is equal to τ_{74MHz}=~0.3 according to the derivation made by Castelletti et al. (2011), is negligible for frequencies > 50 MHz. Indeed for frequencies above 1 GHz we obtained an absorption coefficient of $\exp\left(-\tau_{74}(\frac{\nu}{74_{MHz}})^{-2.1}\right) \sim 1$, which suggests that free-free thermal absorption could not be responsible for the observed spectral index region-dependent scatter at high frequencies.
Thus, we considered the possibility that the spectral steepening could be related to a strongly enhanced, region-dependent cooling. However, this hypothesis is disfavoured by the evidence

for a correlation among bright/flat-spectrum radio regions and gamma-ray emission (i.e. the electron cooling to gamma-ray energies does not significantly affect radio spectra). Furthermore, this hypothesis is disfavoured by the temporal evolution models of non-thermal particle and photon spectra at different stages of shell-type SNR lifetime. These theories provide a significant steepening of the spectral index due to synchrotron cooling from a particle gas drifting away from the shock region on a time-scale of 10^4-10^5 yr (Sturner et al., 1997), exclusively in the case of a significant local enhancement of the magnetic field. However, we noted that both primary and secondary electron distribution cut-offs could approach the synchrotron radio-emitting range on these time-scales, thus providing a change in the synchrotron spectral index at high frequencies. An evidence of this could be found in the slight steepening of the integrated spectra of both W44 and IC443 at frequencies > 1 GHz.

Excluding this possibility, we proposed that the significant spread in the spectral index distributions within different SNR regions observed by SRT could in principle be related to several and possibly concurring processes. This seems to be confirmed by the fact that the naive shock acceleration theory fails to describe flat or inverted spectra as seen in bright SNR selected regions. That theory predicts a single particle spectrum that is a power law in momentum with spectral index ~2, with little fluctuation, depending on the actual shock parameters (e.g. Sturner et al. 1997, and reference therein). This particle spectrum results in a synchrotron spectral slope that is expected to be ~0.5, which is compatible with our integrated spectra above ~1 GHz. Even in the ultra-relativistic regime and assuming a high shock compression factor (~4), electron spectra slopes are expected to be above ~1.5 (Ellison et al., 1995), thus implying a synchrotron spectral index >0.2 that is incompatible with our results. This "apparent" inconsistency could be resolved taking into account the contribute of secondary hadronic electrons in addition to the primary electron canonical distribution (Cardillo et al., 2016). This secondary electron population could indeed explain the spectral flattening effects, and their presence is supported by the correlation among bright flat-spectrum SNR regions and the gamma-ray emission. Indeed, this represents a possible signature of enhanced hadronic emission and then of a significant secondary hadronic electrons injection. In the case of W44, as shown in Fig.2.28(b), we observed a correlation between the gamma-ray emission and the bright radio rims and filaments of the SNR (Abdo et al. 2010; Giuliani et al. 2011; Cardillo et al. 2014). However, a typical particle spectrum of both primary and secondary electrons is expected to have a high energy cut-off which depends on the SNR age and other physical parameters (i.e. ambient density and magnetic field). We cannot rule out the possibility of a spectral shape related to an efficient CR acceleration due to a significant local enhancement of the magnetic field, according to peculiar shock conditions arising from different interacting structures in the ISM. For these reasons, as future perspective, our qualitative assumption based on the radio and gamma-ray emission correlation could be reinforced by accurate model of evolution of secondary electrons form acceleration and emission sites. We obtained a different result for IC443, for which the gamma-ray emission seems to be anti-correlated with the

SNR limbs (see Fig.2.28(d)), although it is still associated with a relatively bright radio filament (with a flatter spectrum w.r.t. average central region spectra) close to a molecular cloud enhancing IC/bremsstrahlung emission (Humensky & VERITAS Collaboration, 2015).
In light of this, we concluded that the observed spread in spectral slopes could in principle reflect a region-dependent amount of secondary electron production, but this hypothesis can't be clearly proven by present multi-wavelength data (Pellizzoni et al., 2017).

3.4 Tycho

At radio wavelengths, Tycho exhibits a well defined loop structure with an angular diameter of $8'$ and a total continuum flux density of 56 Jy at 1 GHz. The radio brightness distribution indicates a thin outer rim where both shock compression and particle acceleration occur, and a thicker main shell in which instabilities and turbulent amplification may be responsible for the emission (Dickel et al., 1991).
We observed Tycho SNR with SRT in the framework of the ESP at the frequency of 21.4 GHz in order to test our data analysis tools on SRT K-band data. The excellent opacity and weather observing conditions allowed us to produce a very good quality image (Fig.2.27(c)). We appreciated both the brightness enhancements along the northern and eastern rims and some filaments of enhanced brightness in the interior of the remnant, consistently with what observed in the interferometric images (Katz-Stone et al., 2000). From our image, we achieved an integrated flux density of 8.8 ± 0.9 Jy, which is consistent with the predicted value at 21.4 GHz equal to 9 ± 0.4 Jy that results from the weighted least square fit performed on flux density measurements in the literature (Sun et al., 2011). These results assured us the reliability of the SRT K-band multi-feed system and of our data analysis tools. On the other hand, they allowed us to take a step forward on the study of the integrated spectrum of this SNR. Furthermore, our results laid the foundations to investigate for possible spatial variations of the continuum radio spectral index within this remnant by using SRT maps at different frequencies.
A slightly concave up model (hardening to higher frequencies) was proposed to describe the integrated spectrum of Tycho (Reynolds & Ellison, 1992). Indeed, a spectral flattening (thermal Bremsstrahlung component) at high frequencies combined with an integrated spectral index in the range $0.3-0.7$, are considered to be typical characteristics of "shell" type remnants of which Tycho is thought to be a member (Hurley-Walker et al., 2009). However, this hypothesis was not confirmed by a recent study performed by Sun et al. (2011). The flux density measurement of Tycho obtained at 5 GHz in the framework of the Sino-German $\lambda 6$ cm polarization survey of the Galactic plane was exploited together with the previous measurements available in the literature in order to study the spectral proprieties of this SNR. The obtained SED in the $0.178-17.1$ GHz frequency range did not show any spectral curvature, and it was perfectly fitted by a simple

Table 3.3: Integrated flux density measurements towards Tycho SNR.

Freq. (GHz)	Flux density density (Jy)	Reference	Freq. (GHz)	Flux density density (Jy)	Reference
0.178	161±16	Bennett (1963)	15.0	11±1	Klein et al. (1979)
0.408	100±10	Fanti et al. (1974)	15.0	12±0.5	Green et al. (1975)
0.408	86±5	Kothes et al. (2006)	15.0	11.2±0.6	Hurley-Walker et al. (2009)
0.612	73±3.7	Conway et al. (1965)	15.7	11±0.6	Hurley-Walker et al. (2009)
0.750	62.9±2.1	Kellermann et al. (1969)	16.4	10.4±0.5	Hurley-Walker et al. (2009)
1.4	43.1±2.1	Kellermann et al. (1969)	17.1	10.4±0.5	Hurley-Walker et al. (2009)
2.695	29.2±0.5	Kellermann et al. (1969)	**21.4**	**8.8±0.9**	**Loru et al. (2019)**
2.695	28.5±2	Horton et al. (1969)	30.0	8.1±0.4	Planck Collaboration et al. (2016)
4.995	19.2±1	Horton et al. (1969)	44.0	5.2±0.3	Planck Collaboration et al. (2016)
5.0	21.2±0.4	Kellermann et al. (1969)	70.0	4.4±0.3	Planck Collaboration et al. (2016)
5.0	20.03±2	Sun et al. (2011)	100.0	4±0.2	Planck Collaboration et al. (2016)
10.7	13.1±0.8	Klein et al. (1979)	143.0	3.5±0.2	Planck Collaboration et al. (2016)

power law function at which corresponds an integrated spectral index of α = 0.58 ± 0.02 (Sun et al., 2011).

Spatially resolved spectral-slope studies of Tycho (Duin & Strom, 1975) showed evidence for a significant spectral steepening close to the SNR centre. This result suggested a high-energy electron distribution in the thinner shell, where the dense thermal material has been swept up from the ISM. A following study of the spectral index distribution performed by Klein et al. (1979) contradicted this result, revealing no significant spatial variations. Then the issue is still debated. More recent sensitive low-frequency VLA observations (0.3−1.4 GHz, Katz-Stone et al. 2000) identified different radio structures within Tycho, allowing for a spatial study of the spectral index across the entire SNR. Brighter filaments located in the outer regions display flatter spectral indices than the fainter ones. This may be due to competing mechanisms of SNR blast wave-ambient medium interactions and internal inhomogeneities of the magnetic field within the remnant (Katz-Stone et al., 2000).

We analysed the radio spectrum of the SNR Tycho by considering the flux density measurements available in the literature for the 0.038−143 GHz frequency range. Flux density values at up to 17 GHz were taken from Tables 1 of Klein et al. (1979) and from Sun et al. (2011). For the high radio frequencies, we used the measurements obtained between 15 and 17.1 GHz with the *Arcminute Microkelvin Imager Small Array* (AMI SA) given in Table 4 by Hurley-Walker et al. (2009), our measurements obtained at 21.4 GHz with SRT, and the *Planck* measurements carried out at up to 140 GHz, which are reported in Table 3 of Planck Collaboration et al. (2016). These flux density measurements and related references are listed in Table 3.3.

The overall radio SED for Tycho is displayed in Fig.3.11. The SRT value at 21.4 GHz (represented with a filled red diamond) perfectly matches the trend suggested by the other data without any

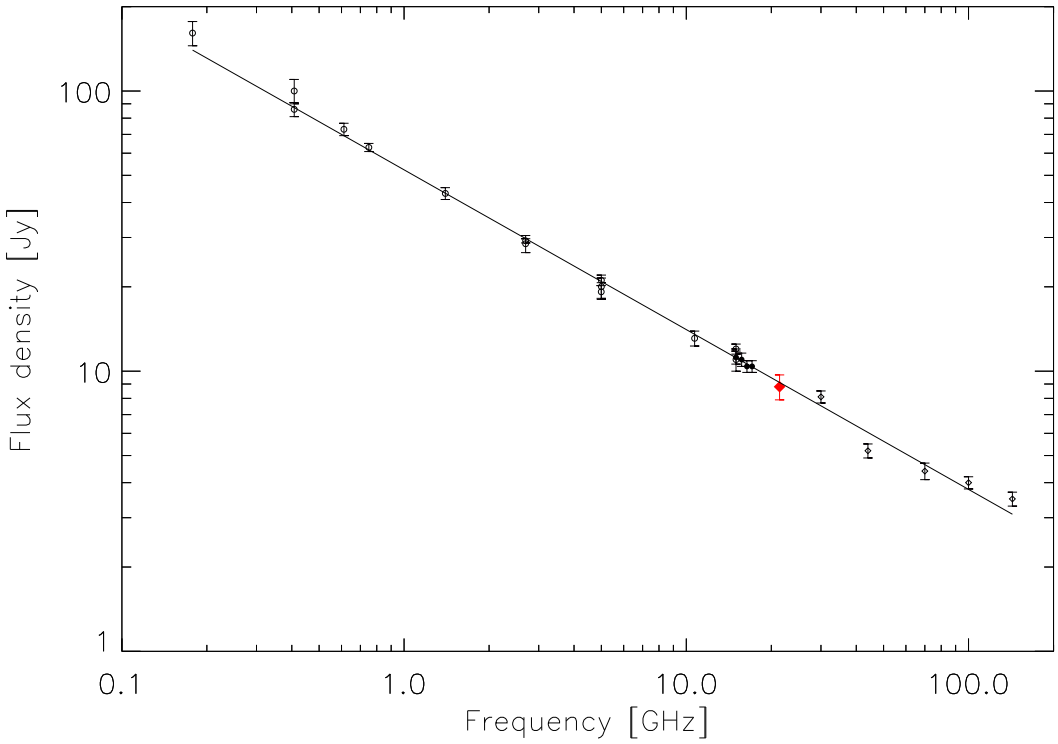

Figure 3.11: Weighted least-squares fit applied to the Tycho SED for the synchrotron power-law model. The circles represent the flux density measurements available in the literature in the 0.178−15 GHz frequency range, while the black filled circles are associate with the Hurley-Walker et al. (2009) measurements from 15 GHz to 17.5 GHz. The red-filled and the black diamonds correspond respectively to the SRT point at 21.4 GHz and the *Planck* data Planck Collaboration et al. (2016).

apparent spectral variation. The data are fitted ($\chi^2/dof = 1.3$) by a synchrotron emission model represented by a simple power law function (with a normalisation constant of 52.3 ± 0.7 Jy that represents the flux density at 1 GHz), which rules out spectral flattening models. The resulting spectral index $\alpha = 0.58 \pm 0.01$ is consistent with the value obtained by Sun et al. (2011).

A spectral steepening is also unsupported by our points, confirming the trend suggested by *Planck* data. This is consistent with the predictions based on gamma-ray observations of Tycho carried out with VERITAS, and interpreted by Acciari et al. (2011) through leptonic and hadronic models, which suggest a steepening of the radio spectrum at much higher frequencies (above $\sim 10^{14}$ Hz). Both these models provide a reasonable fit to the gamma-ray data and imply a magnetic field of ~80 μG, which is possibly interpreted as evidence for magnetic field amplification (Morlino & Caprioli, 2012).

Our study of the integrated spectrum of Tycho provides a useful verification of the performance of

SRT in the K-band multi-feed configuration and at the same time confirms (through the highest frequency single-dish observations performed so far) non-thermal synchrotron as the dominant emission process for Tycho at up to high radio frequencies.
Exploiting the high quality of our 21.4 GHz map of Tycho, we tried to use it in order to disentangle a possible variation in the radio emission from the central region to the outer limbs. Taking into account the brightest and faintest regions located at (RA, Dec)=($00^h25^m38.041^s$, +64°11′09.26″) and (RA, Dec)=($00^h25^m15.384^s$, +64°08′06.40″) respectively, we obtained a flux density ratio of ~4. A ratio of ~7 can instead be obtained by considering the highest and lowest flux density measurements carried out by Katz-Stone et al. (2000), in the context of a study of the flux density of Tycho at 1.4 GHz as function of distance from the remnant center (see Fig. 4 in Katz-Stone et al. 2000). This could suggest a flatter spectral index in the faint central region with respect to the north-eastern bright region. However, taking into account the early age of Tycho and its expansion rate, more recent high-resolution radio images are required in order to discuss spatial variations of the spectrum within the SNR.

3.5 Cygnus Loop

In order to measure the integrated flux density of Cygnus Loop, we considered an elliptic extraction region centered in (RA, Dec)=($20^h51^m39.058^s$, +30°34′45.40″) and with semi-major and semi-minor axis of $\sim 2.2°$ and $\sim 1.8°$, respectively. We obtained a continuum flux density of 54 ± 4 Jy and a rms of 24 ± 2 mJy/beam at 8.5 GHz.
We analysed the radio spectrum of the SNR Cygnus Loop by considering our measurement coupled with all of the flux density measurements available in the literature, including the $Planck$ measurement carried out at 30 GHz, the only one at which the flux density of Cygnus Loop could be accurately estimated with this instrument (Planck Collaboration et al., 2016).
All values and related references are reported in Table 3.4. It is worth noting that our measurement is the more sensitive flux density at the highest frequency where the Cygnus Loop SNR was observed so far with high-resolution.
The overall radio SED for Cygnus Loop is displayed in Fig.3.12. The Medicina value at 8.5 GHz is represented with a filled red circle and we can see that it perfectly matches the trend suggested by the other data without any apparent spectral variation. We modelled the integrated spectrum of Cygnus Loop using a simple synchrotron power-law function. From the weighted least-squared fit ($\chi^2/dof = 1.15$), we obtained a spectral index of $\alpha = 0.53 \pm 0.01$ and a normalisation at 1 GHz of 164 ± 5. This result is consistent within 1σ with the spectral index of $\alpha = 0.5 \pm 0.06$ estimated by Uyanıker et al. (2004) by considering all flux density measurements available in literature in the frequency range 0.022−4.94, and within 2σ with the spectral index of $\alpha = 0.40 \pm 0.06$ that was estimated by Sun et al. (2006) by considering the flux density measurements carried out with the Urumqi telescope at 0.408 GHz, 0.863 GHz, 1.420 GHz, 2.675 GHz and 4.8 GHz. Furthermore,

our measurement rules out any spectral steepening up to high radio frequencies, and it confirms the trend suggested by the *Planck* data at 30 GHz.

Table 3.4: Integrated flux density measurements towards Cygnus Loop SNR.

Freq. (GHz)	Flux density density (Jy)	Reference	Freq. (GHz)	Flux density density (Jy)	Reference
0.022	1378±400	Roger et al. (1999)	0.863	184±18	Uyanıker et al. (2004)
0.0345	1245±195	Sastry et al. (1981)	0.960	190±50	Kenderdine (1963)
0.038	956±150	Kenderdine (1963)	1.420	143±14	Uyanıker et al. (2004)
0.041	770±140	Kundu & Velusamy (1967b)	2.675	115±12	Uyanıker et al. (2004)
0.158	350±70	Mathewson et al. (1960)	2.695	125±16	Green (1990)
0.195	382±60	Kundu & Velusamy (1967b)	2.7	88±6	Kundu (1969)
0.408	230±50	Kenderdine (1963)	4.940	73±7	Kundu & Becker (1972)
0.408	260±50	Mathewson et al. (1960)	4.8	90±9	Sun et al. (2006)
0.408	237±24	Uyanıker et al. (2004)	**8.5**	**54±4**	**this work**
0.430	297±50	Kundu & Velusamy (1967b)	30	24.9±1.7	Planck Collaboration et al. (2016)

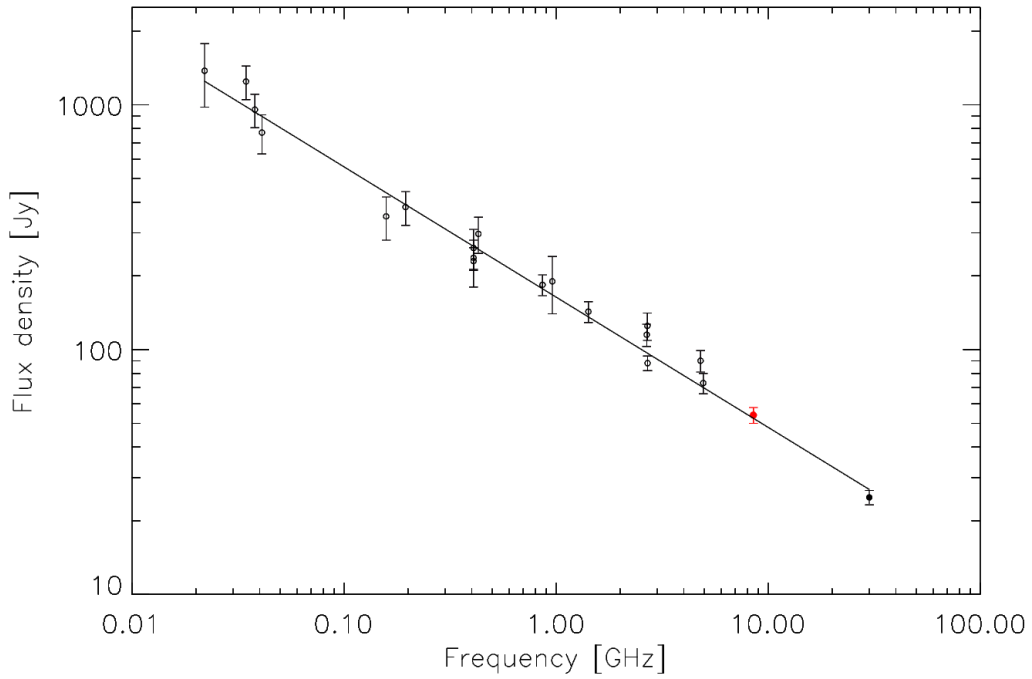

Figure 3.12: Weighted least-squares fit applied to the Cygnus Loop SED for the synchrotron power-law model. The red and the black filled diamonds correspond respectively to the SRT point at 21.4 GHz and the *Planck* data.

CHAPTER 4

SUMMARY AND FUTURE PERSPECTIVES

The aim of my PhD project was to characterise the integrated radio spectra of SNRs that present an interesting complex morphology, like W44 and IC443, and to investigate possible significant region-dependent spectral slope variations through spatially-resolved spectral studies of these SNRs. For this purpose, we exploited the capabilities of the Italian radio telescopes to perform sensitive single-dish radio observations, which represent a good trade-off between sensitivity and spatial resolution in the frequency range 5−50 GHz. In particular, SRT provides an improvement of typical single-dish spatial resolution at high frequencies thanks to the active surface that characterises its primary mirror. The seven-beam system available for the *K*-band receiver (18−26.5 GHz) allowed us to perform a fast mapping of large sources, which is crucial to mitigating the effects of atmospheric opacity variations on image quality (Navarrini et al., 2016).

We observed W44 and IC443 at the three different frequencies (1.55 GHz, 7.0 GHz and 21.4 GHz) during the SRT astronomical validation and the early science program, obtaining high-resolution maps at the highest frequencies where these sources were observed so far (Egron et al. 2017, Loru et al. 2019). The maps at 7.0 GHz and 21.4 GHz reveal features of the SNR morphology that are consistent with those highlighted in the interferometric observations, and provide accurate continuum flux density measurements.

We performed spatially-resolved spectral studies by coupling the SRT maps at 1.5 GHz and 7.0 GHz. The obtained spectral measurements suggest a spread in spectral slope distribution, ranging from flat or slightly inverted spectra (up to $\alpha \sim -0.5$ for IC443) corresponding to bright radio structures, to relatively steep spectra ($\alpha \sim 0.7$) in fainter radio regions of these SNRs (Egron et al., 2017). We also observed a correspondence between bright-flat spectrum regions and gamma-ray emission that could represent a signature of secondary electron populations

produced by hadronic interactions in regions where the SNR shock collides with dense molecular clouds (Cardillo et al., 2016). For these reasons, we attributed the observed region-dependent wide spread in spectral slope distribution to distinct electron populations in the SNRs, including secondary hadronic electrons, and resulting from different shocks conditions and/or undergoing different cooling processes.

Thanks to our high-resolution imaging data at 21.4 GHz, we investigated the shape of the radio continuum spectra of W44, IC443 and Tycho at high frequencies, where different electron acceleration mechanisms could contribute to the shape of the spectra (Loru et al. 2018). Our flux density measurement on Tycho obtained at 21.4 GHz confirms the non-thermal synchrotron as the dominant emission process, ruling out any spectral curvature up to high radio frequencies. This is a result expected from the DSA theory under which young SNRs in their early phase generally do not show a spectral break in the radio band due to very efficient acceleration conditions (Urošević, 2014). On the other hand, a spectral index steepening is expected at radio frequencies in evolved SNRs wherein the particle acceleration mechanisms are not efficient (Ackermann et al. 2013, Urošević 2014). Although comparable in age, our observations surprisingly show that W44 and IC443 present different cut-off energies in their synchrotron spectra.

For the first time, we observed a synchrotron spectral break in W44 at a frequency of 15 ± 2 GHz. This result provides a direct estimate for the maximum energy of accelerated CR electrons in the 6−13 GeV range, which is consistent with indirect evidence from gamma-ray observations (Ackermann et al. 2013, Cardillo et al. 2014, Cardillo et al. 2016). In the case of IC443, our flux density measurement at 21.4 GHz confirmed the significant dust emission bump observed by Onić et al. (2017) in the frequency range 20−70 GHz. In the same work Onić et al. (2017) estimated a synchrotron cut-off frequency (148 ± 23 GHz) of an order of magnitude higher than what we found for W44. We do not rule out the possibility that a dust emission component could also be present in the W44 SED (Génova-Santos et al., 2017). This hypothesis could be confirmed by further high-resolution measurements in the crowded field of W44 in the 10−100 GHz range.

Finally, in this work, we presented the high-resolution image of the Cygnus Loop SNR carried out with the Medicina radio telescope at 8.5 GHz, which is the highest frequency at which this source was observed so far with a single-dish telescope. The only flux density measurement at higher frequency is that carried out with *Planck* instruments at 30 GHz with a relatively low resolution. We estimate a flux density at 8.5 GHz of 54 ± 4 Jy, which we used in conjunction with all measurements available in the literature in order to investigate the integrated spectrum of Cygnus Loop. By modelling the Cygnus Loop SED with a simple synchrotron emission model, we obtained a spectral index of $\alpha = 0.53 \pm 0.01$, which is consistent with the previous values reported in the literature (Uyanıker et al. 2004, Sun et al. 2006). Our measurement rules out any global spectral steepening up to 8.5 GHz and confirms the trend suggested by the *Planck* data.

Our single-dish imaging of evolved SNRs sheds new light on the characteristics of their radio continuum spectra in the ∼10−20 GHz frequency range. Different electron populations and

acceleration mechanisms could modify the SNR spectral shape compared to that resulting from a simple shock-driven synchrotron emission, especially at high radio frequencies. These mechanisms can be related to the age of the SNRs and/or the properties of the ambient interstellar medium with which they interact.

Our studies on the spectra of the three middle-aged SNRs W44, IC443 and Cygnus Loop highlighted extremely different spectral features at high radio frequencies, although they are approximately at the same evolutionary phase. This suggests that the differences on the peculiar conditions of the ISM interacting with the SNRs could lead to an enhancement of the secondary electron populations produced by hadronic interactions in regions where the SNR shock collides with dense molecular clouds. On the other hand, the different spectral shapes could be related to a magnetic field amplification at SNR shocks, which results in an efficient CR acceleration. Egron et al. (2017) attributed the synchrotron cut-off differences between W44 and IC443 to different primary and secondary electron energy distributions and/or magnetic fields, according to local shock conditions arising from different interacting structures in the ISM.

An interesting way to disentangle among different theoretical possibilities for explaining the findings above could be provided by spectro-polarimetric observations of W44 and IC443. Indeed, differences in magnetic field configuration between peculiar regions across the SNRs indicate the action of different particle acceleration mechanisms. Furthermore, the co-spatial study of the magnetic field orientation and the continuum radio emission could provide a crucial test for the processes of magnetic field amplification. Observations of SNRs at different radio frequencies performed with SRT through the recently implemented spectro-polarimetric back-end SARDARA (Melis et al., 2018) would enable us to investigate the effects of the magnetic field amplification at SNRs shock fronts and its implications on the CR acceleration in SNRs. Indeed, the establishment of the magnetic field geometry of SNRs at high radio frequencies and its correlation with the geometry of the CR electron distribution would allow us to test the theoretical models on the synchrotron emission in the framework of quasi-perpendicular and quasi-parallel shocks (West et al., 2016).

Furthermore, at the light of the results obtained in the study of the SNR Cygnus Loop spectrum, we believe it would be interesting to independently investigate the emission of the two shells through a detailed study of related spectra up to high radio frequencies. This would be executed by exploiting different receivers and back-ends available at SRT. Indeed, as described in this work, SRT provides very good performances in single-dish imaging of extended sources at 1.5 GHz, 7.0 GHz and 21.4 GHz. Furthermore, in near the future, deeper images can be provided by SRT in the frequency range 3−4.5 GHz with the S-band receiver and at up to 50 GHz with the Q-band multi-feed receiver (a Q-band receiver, in the frequency range of 33−50 GHz, is currently being implemented for SRT, Navarrini et al. 2016). Observations at such high radio frequencies could be crucial to fully constraining synchrotron spectral breaks in SNR SEDs that are tightly related to Galactic CR acceleration.

Finally, the synchrotron cut-off differences between W44 and IC443 observed at high radio frequencies are evidence of the way through which the shock wave of the SNRs interacts with the ISM of the environment, heavily affecting the physical conditions in the compression regions and then the emission mechanisms. This aspect introduces the scientific interest in improving the population sample of the SNRs observed in the radio continuum, in order to understand the morphological and evolutionary similarities related to the peculiar emission processes.
In light of these interesting perspectives we participated at the 2018 call for observations with the Sardinia Radio Telescope with the proposal entitled "Challenging electron populations and acceleration models in Supernova Remnants shocks through high-frequency continuum and polarization observations" (PI: Alberto Pellizzoni). The proposal was approved and I participated in the first observing sessions that were performed on 19 and 28 December 2018. The aim of the observing project was to perform high-frequency and polarimetric investigations on a wider population sample of young and middle-aged SNRs in order to clarify the origin of the observed spectral differences among targets. We proposed to perform the observations with the SARDARA back-end in the C-band and K-band in order to perform polarimetric imaging of a carefully selected SNRs sample. We chose to observe the SNRs W44, Cygnus Loop, G85.4+0.7 and Kes 73 according to their complex and/or controversial region-dependent spectra with the aim to perform:

- a precise modelling of the region-dependent continuum spectral indices, features and breaks, in order to obtain CR acceleration maps (electron maximum energy and spectra) for each target.
- a study of the spatially-resolved correlation between polarimetric information, flux density and spectral slopes, in order to disentangle possible magnetic enhancement processes from spectral variation contributions due to different primary and secondary electron populations.
- an assessment of the flux densities and spectra associated to gamma-ray emitting regions in order to disentangle hadronic versus leptonic contributions to the SEDs.

We decided to further investigate the SNR W44 on which our previous studies provided evidence, for the first time, of a spectral break in K-band in a middle-aged SNR, though detected in poor opacity conditions with the Total Power back-end. A further characterisation of the integrated spectra of this source is needed in order to confirm the observed cut-off and to investigate for other spectral features related to specific emission mechanisms at these frequencies (e.g spinning dust emission). Furthermore, the spectro-polarimetric studies on this source would allow us to perform a more precise characterization of the spatially-resolved spectral shape (through multi-frequency observations in the $18-26$ GHz range) and to derive polarimetric information so far unknown at these frequencies. The correlation between these information could provide an useful test for magnetic enhancement shock models (Morlino, 2017).

Previous observations of the bright and very large SNR Cygnus Loop ($\sim 4^\circ \times 3^\circ$) revealed region-dependent variations on spectral indices and polarisation properties up to ~ 5 GHz Sun et al. (2006). These differences are attributable to different acceleration mechanisms acting in these regions: the northern part of the remnant is governed by the compression of the magnetic field due to the SN explosion shock, while the southern part results most likely from shock acceleration, which is thought to act in young remnants, rather than on the compression of the interstellar magnetic field Green (1984). From these evidence, Uyanıker et al. (2002) suggested that Cygnus Loop is composed of the two interacting SNRs. A spectral flattening was observed in the bright filaments both in the northern large circular shell and in the southern bubble-like part (Uyanıker et al., 2002). It could be related to a strong shock acceleration process (south, Cygnus Loop A) and a compression of the magnetic field (north, Cygnus Loop B), similarly to that observed for the SNR S147 (Uyanıker et al., 2004). These interesting regions are showed in Fig. 4.1. However, in the case of SNR S147, the spectral index variations are associated with a spectral break in its integrated spectrum above 1 GHz, which is not observed for Cygnus Loop. This is probably due to the earlier evolutionary phase of Cygnus Loop with respect to S147, where the shock acceleration is still dominant. Therefore in this case, a spectral break could be expected at higher radio frequencies, and sensitive maps above ~5 GHz could be crucial to investigating on this respect. Furthermore could be interesting to separately study the magnetic field configuration of the north and south shells with the highest-frequency map of Cygnus Loop obtained so far with a single-dish telescope.

G85.4+0.7 is a recently discovered SNR (Kothes et al., 2001) with a incomplete radio shell surrounding a weak, extended X-ray source. The particular aspect of this object is its double shell composition. From the calculation of the spectral index profile, Kothes et al. (2001) concluded that the external shell has a thermal origin, while the inner one is non-thermal. This noticeable and intriguing SNR structure is still debated and not yet confirmed: strong polarisation of both shells would testify for synchrotron radiation. High-frequency polarimetric and spectral measurements would be useful to better understand the thermal/non-thermal nature of the external shell and its detailed SED.

Kes 73 (G027.4+00.0) is a young (with an age < 2.2 kyr, Gotthelf & Vasisht 1997) and small ($4'$ diameter) shell-type radio SNR. It is located along the Galactic plane at a distance of about 7.5 kpc. X-ray observations revealed a clumpy emission and a compact central source (1E 1841−045) associated with this SNR (Tian & Leahy, 2008). A recent study based on VLA observations of Kes 73 at 1.4 GHz and 5 GHz (in combination with the GBT map at this frequency) revealed a striking differentiation in its spectral index, with a classical synchrotron spectrum in the eastern part and a flatter spectrum in the opposite side (Ingallinera et al., 2014). The authors attributed this spatial variation of the radio spectral index to two possible causes: the flatter spectral index characterising the western region might be due to inhomogeneities of the strong magnetic field from the central object, causing a superposition of different "regular" synchrotron

contributions with different turnover frequencies that results in a global flatter spectrum; the spectrum flattening could be ascribed to the impact of the SN shock on dense molecular clouds. Yet no radio data at frequency higher than 5 GHz have been collected so far, resulting in a hampering lack of information. In particular K-band observations are crucial to determine if this spectral dichotomy persists at higher frequency and/or if a spectrum cut-off occurs. This information would allow us to better constrain the physical properties of the electrons in this remnant and link the radio emission to the recent gamma-ray observations (Yeung et al., 2017). Our observing strategy was to adopt the well-established OTF mapping strategy as described in the Section 2.3. We require bolometric target sensitivities of about 20−30 mJy/beam for K-band (enough to detect SNR weak emission regions) that could be achieved through OTF imaging with exposures of ~0.5 minutes/beam (the precise value depending on actual observing conditions: opacity, elevation etc.). For C-band observations, the back-end SARDARA demonstrated to achieve 10−20 mJy/beam sensitivities for exposures of ~0.5 minutes/beam. In order to perform polarimetric observations and optimise RFI spectral rejection, we propose to observe with the SARDARA backend in full-stokes mode with 1024 spectral channels and the maximum bandwidth available in the shared risk mode in order to maximise the signal-to-noise ratio (1.2 GHz both for C and K-band); the relatively wide band of the receivers allow us to exploit different central frequencies in order to optimise SED coverage of targets (see Table 4.1). For K-band observations, the OTF "Best Space Coverage configuration" (BSC) automatically rotates the dewar in order to best cover the scanned area (subscan spacing ~$0.87'$ comparable to the HPBW). All observing parameters that we required for each target observation, including calibrations and ancillary operations, are summarised in Table 4.1.

Always within SRT observations, a future project could be based on the exploitation of the high-resolution and the frequency agility of the SRT receivers in order to perform a radio survey of Galactic SNRs, in particular those already well studied at higher wavelengths (Green, 2017), looking for high-frequencies spectral breaks and features. Such a study would allow us to precisely classify these objects in order to investigate how the different environmental conditions can influence the emission processes and the CR acceleration mechanisms.

Finally, a comprehensive understanding of the different radiation mechanisms that take place in SNRs can be achieved through a detailed study of the global spectral index, of the curvature of the spectrum and of the local variations of the spectral index within the remnant. These kinds of investigations require sensitive, high-resolution images of the SNRs across a wide frequency range (0.01−100 GHz). On this regard, we need to exploit the complementary capabilities of both single-dish telescopes and radio interferometers. Indeed, interferometric observations can resolve out a source when this is more extended than the interferometer largest angular scale, resulting in an underestimate of the total flux density and in imaging artefacts. On the other hand, single-dish observations do produce accurate total flux density measurements but often confuse SNRs with nearby objects, especially on the Galactic plane (Dubner & Giacani, 2015). To

overcome this problem it is possible to combine interferometric and single-dish data. The result is an image with a resolution similar to the original interferometric image but with an precise recovery of the extended emission and an accurate flux density restoration. In this way we can obtain highly detailed maps, and so information on the morphology and small-scale structure of the SNRs, and quantitatively reliable flux density measurements. In this scenario SRT can have a crucial role. Its diameter is much greater than the shortest baseline of many current interferometers, like the VLA (in C and D configurations). This is a necessary requirement, since the combination process is based on the possibility to overlap the interferometric and single-dish data on the uv-plane. Smaller single-dish telescopes cannot serve this purpose. Having a look at the next future, mid-frequency SKA precursors, ASKAP and MeerKAT (both in the early-science phase), are going to require also the single-dish aid. Though these instruments are located on the southern hemisphere, they are planned to observe at least up to $\delta = +30^\circ$ and therefore SRT data can be used as short-spacing complement. In this way we can use synergically all these instruments to achieve an unprecedented sensitivity (5 to 1 μJy/beam per 1h) and resolution (from $20''$ to $0.05''$) over a frequency range spanning from 50 MHz to 14 GHz, without being hampered in the quantitative analysis. This will allow us to have remarkable insights on radio SNRs, and in particular on their morphology, the local emission processes occurring in different remnant regions and the properties of the magnetic field in SNRs.

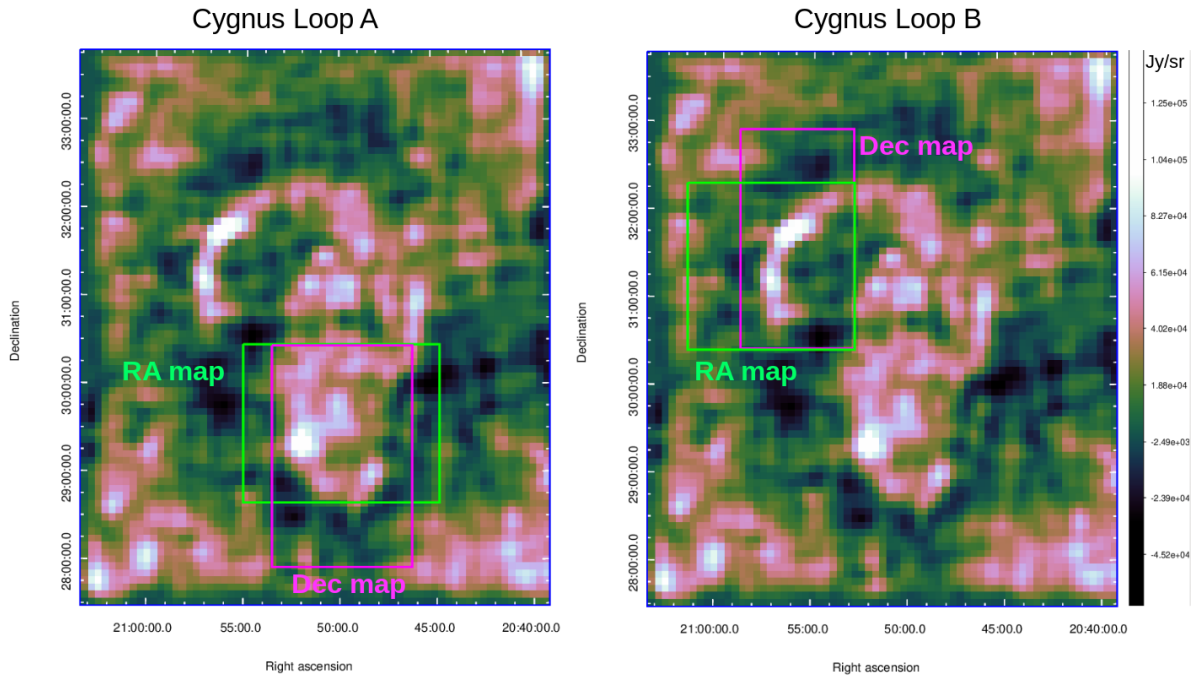

Figure 4.1: Representation of the two regions of Cygnus Loop that we decided to observe in the 2018 December-March observing session with SRT. As shown by green and magenta boxes, we decided to perform not overlapping RA and Dec maps in order to ensure that about 50% of the subscans length/duration is free from significant source contribution and, at the same time, to minimise the observing time.

Table 4.1: **Observation parameters and scan summary.** Targets are observed at different frequencies in order to search for possible spectral features/breaks/curvature. Before each target map (and also after target observation for longer maps), we plan to perform OTF cross-scans on standard flux density and polarimetric calibrators ("Flux cal." time requirements in the table below). The well known CAS A SNR could be observed as a "cross calibrator" in order to verify the quality of "shared-risk" multi-feed SARDARA polarimetric observations in K-band. A typical observing session should include basic standard calibrations ("Standard Cal."): attenuation level set-up, pointing and focus calibrations, and skydips for K-band operations. A short K-band multi-feed imaging session ("Imaging Cal.") on flux calibrators should be also daily required in order to check for lateral feed status and relative gain (w.r.t. central feed). We require target visibility at elevations >20°. Accounting for the resulting LST range, an observing program of ~86 hours could be split - e.g. - in 6−8 observing sessions, each of them requiring the above Standard/Imaging Cal. session. This observation splitting strategy could reasonably increase the chance of good opacity conditions (τ <0.1 Np), necessary to guarantee at least part of K-band observations.

Target	Freq. (GHz)	Map size (°;°)	N. maps (RA+Dec)	Target obs time hours	Flux Cal. hours	Total time hours	LST range
Standard Cal.	-	-	-	-	-	0.5 (× 7 sess.)	14-04
Imaging Cal.	-	$0.5° \times 0.5°$	2	-	-	0.8 (× 7 sess.)	14-04
W44	18.6	$1.2° \times 1.0°$	2	4	1	5	14-00
W44	22.0	$1.2° \times 1.0°$	2	4	1	5	14-00
W44	25.4	$1.2° \times 1.0°$	2	4	1	5	14-00
W44	7.1	$1.2° \times 1.0°$	2	2	1	3	14-00
Cygnus Loop A	22	$RA = 2.2° \times 1.8°$ $Dec = 1.6° \times 2.5°$	2	16.8	1.5	18.3	15-03
Cygnus Loop B	22	$RA = 1.9° \times 1.9°$ $Dec = 1.3° \times 2.5°$	2	6.7	1.5	8.2	15-03
Cygnus Loop A	7.1	$RA = 2.2° \times 1.8°$ $Dec = 1.6° \times 2.5°$	2	8.4	1.5	9.9	15-03
Cygnus Loop B	7.1	$RA = 1.9° \times 1.9°$ $Dec = 1.3° \times 2.5°$	2	3.3	1.5	4.8	15-03
G85.4+0.7	18.6	$0.7° \times 0.7°$	2	1.7	1	2.7	14-04
G85.4+0.7	22	$0.7° \times 0.7°$	2	1.7	1	2.7	14-04
G85.4+0.7	25.4	$0.7° \times 0.7°$	2	1.7	1	2.7	14-04
G85.4+0.7	7.1	$0.7° \times 0.7°$	2	0.8	0.5	1.3	14-04
Kes 73	18.6	$0.5° \times 0.5°$	2	0.8	0.5	1.3	14-23
Kes 73	22	$0.5° \times 0.5°$	2	0.8	0.5	1.3	14-23
Kes 73	25.4	$0.5° \times 0.5°$	2	0.8	0.5	1.3	14-23
Kes 73	7.1	$0.5° \times 0.5°$	2	0.4	0.5	0.9	14-23
CAS A	18.6	$0.5° \times 0.5°$	2	0.8	0.5	1.3	(15-08)
CAS A	22	$0.5° \times 0.5°$	2	0.8	0.5	1.3	(15-08)
CAS A	25.4	$0.5° \times 0.5°$	2	0.8	0.5	1.3	(15-08)
TOTAL	-	-	40	60.3	17	**86.4**	**14-04**

Papers in refereed journals

- "Investigating the high-frequency spectral features of SNRs Tycho, W44 and IC443 with the Sardinia Radio Telescope"
  S. Loru, A. Pellizzoni, E. Egron, S. Righini, M. N. Iacolina, S. Mulas, M. Cardillo, M. Marongiu, R. Ricci, M. Bachetti, M. Pilia, A. Trois, A. Ingallinera, O. Petruk, G. Murtas, G. Serra,R. Concu, F. Gaudiomonte, A. Melis, A. Navarrini, D. Perrodin, and G. Valente
  Monthly Notices of the Royal Astronomical Society, March 2018

- "The SArdinia Roach2-based Digital Architecture for Radio Astronomy (SARDARA)"
  A. Melis, R. Concu, A. Trois, A. Possenti, A. Bocchinu, P. Bolli, M. Burgay, E. Carretti, P. Castangia, S. Casu, C. Cecchi Pestellini, A. Corongiu, N. D'Amico, E. Egron, F. Govoni, M. N. Iacolina, M. Murgia, A. Pellizzoni, D. Perrodin, M. Pilia, T. Pisanu, A. Poddighe, S. Poppi, I Porceddu, A. Tarchi, V. Vacca, G. Aresu, M. Bachetti, M. Barbaro, A. Casula, A Ladu, S. Leurini, F. Loi, **S. Loru**, M. Marongiu, P. Maxia, G. Mazzarella, C Migoni, G. Montisci, G. Valente, G. Vargiu
  Journal of Astronomical Instrumentation, 2018 March

- "Multi-messenger Observations of a Binary Neutron Star Merger"
  Abbott, B. P. et al.
  The Astrophysical Journal Letter, 2017

- "Single-dish and VLBI observations of Cygnus X-3 during the 2016 giant flare episode"
  E. Egron, A. Pellizzoni, M. Giroletti, S. Righini, M. Stagni, A. Orlati, C. Migoni, A. Melis, R. Concu, L. Barbas, S. Buttaccio, P. Cassaro, P. De Vicente, M. P. Gawroński, M. Lindqvist, G. Maccaferri, C. Stanghellini, P. Wolak, J. Yang, A. Navarrini, **S. Loru**, M. Pilia, M. Bachetti, M. N. Iacolina, M. Buttu, S. Corbel, J. Rodriguez, S. Markoff, J. Wilms, K. Pottschmidt, M. Cadolle Bel, E. Kalemci, T. Belloni, V. Grinberg, M. Marongiu, G. P. Vargiu, A. Trois
  Monthly Notices of the Royal Astronomical Society, 2017

- "Imaging of SNR IC443 and W44 with the Sardinia Radio Telescope at 1.5 GHz and 7 GHz"
  E. Egron, A. Pellizzoni, M. N. Iacolina, **S. Loru**, M. Marongiu, S. Righini, M. Cardillo, A. Giuliani, S. Mulas, G. Murtas, D. Simeone, R. Concu, A. Melis, A. Trois, M. Pilia, A.

Navarrini, V. Vacca, R. Ricci, G. Serra, M. Bachetti, M. Buttu, D. Perrodin, F. Buffa, G. L. Deiana, F. Gaudiomonte, A. Fara, A. Ladu, F. Loi, P. Marongiu, C. Migoni, T. Pisanu, S. Poppi, A. Saba, E. Urru, G. Valente, G. P. Vargiu
Monthly Notices of the Royal Astronomical Society, 2017

- "The Sardinia Radio Telescope: From a Technological Project to a Radio Observatory "
  I. Prandoni , M. Murgia, A. Tarchi, M. Burgay, P. Castangia, E. Egron, F. Govoni, A. Pellizzoni, R. Ricci, S. Righini, M. Bartolini, S. Casu, A. Corongiu, M. N. Iacolina, A. Melis, F. T. Nasir, A. Orlati, D. Perrodin, S. Poppi, A. Trois, V. Vacca, A. Zanichelli, M. Bachetti, M. Buttu, G. Comoretto, R. Concu, A. Fara, F. Gaudiomonte, F. Loi, C. Migoni, A. Orfei, M. Pilia, P. Bolli, E. Carretti, N. D'Amico, D. Guidetti, **S. Loru**, F. Massi, T. Pisanu, I. Porceddu, A. Ridolfi, G. Serra, C. Stanghellini, C. Tiburzi, S. Tingay, G. Valente
  Astronomy & Astrophysics, 2017

Astronomer's Telegrams

- "Medicina ToO of the non-identified gamma-ray source AGL J1412-0522"
  Egron,E. et al.
  No. 10718, September 2017

- "Monitoring of Cyg X-3 giant flare with Medicina and the Sardinia Radio Telescope"
  Egron,E. et al.
  No. 9508, September 2016

- "Detection of a bright radio flare of Cygnus X-1 at 7.2 GHz with the Sardinia Radio Telescope"
  Egron,E. et al.
  No. 9087, June 2016

- "Detection of GRS 1915+105 and SS 433 at 7.2 GHz and 21.4 GHz with the Sardinia Radio Telescope"
  Egron,E. et al.
  No. 8921, April 2016

- "Observations of H1743-322 with the Sardinia Radio Telescope: upper limits"
  Egron,E. et al.
  No. 8849, March 2016

- "Sardinia Radio Telescope observations of IGR J17091-3624 – upper limit"
  Egron,E. et al.
  No. 8821, March 2016

Proceedings

Peer-reviewed proceeding papers

- "High-Resolution Imaging of the Solar Chromosphere in the Millimetre Band through Single-Dish Observations"
  Pellizzoni et al.
  Proceeding of 2nd URSI AT-RASC, 2018

- "High-resolution spectral imaging of SNR W44 and IC443 at 22 GHz with the Sardinia Radio Telescope"
  Loru et al.
  Proceedings of the International Astronomical Union, IAU Symposium 331, 2017

- "Evidence for a wide electron spectra scatter among different SNR regions from high radio-frequency observations"
  Pellizzoni et al.
  Proceedings of the International Astronomical Union, IAU Symposium 331, 2017

- "High-resolution imaging of SNR IC443 and W44 with the Sardinia Radio Telescope"
  Egron et al.
  Proceedings of the International Astronomical Union, IAU Symposium 331, 2017

Proceeding papers

- "A multi-wavelength pipeline for pulsar observations"
  Pilia et al.
  Proceedings IAU Symposium 337, 2017

- "SETI activities in Sardinia: status and ongoing development"
  Melis et al.
  68th International Astronautical Congress (IAC), 2017

- "The Sardinia Radio Telescope (SRT): A large modern radio telescope for observations from meter to mm wavelengths"
  Carretti et al.
  Electromagnetics in Advanced Applications (ICEAA), 2017

- "Modelling high-resolution spatially-resolved Supernova Remnant spectra with the Sardinia Radio Telescope"
  Loru et al.
  Proceednigs della conferenza Supernova Remnants: An Odyssey in Space after Stellar Death, 2016

Observing proposal

Sardinia Radio Telescope

- "Constraining Cosmic Rays Production in Supernova Remnants with the Sardinia Radio telescope"
  PI: Alberto Pellizzoni, project S0009, 110 observing hours.
  2016 February-August.

- "Monitoring of neutron star and black hole X-ray binaries with the Sardinia Radio telescope"
  PI: Elise Egron, project S0013, 120 observing hours.
  2016 February-August

- "Searching for pulsar at high frequency in the Galactic Center region"
  PI: M. Noemi Iacolina, project S0008, 256 observing hours.
  2016 February-August

Medicina radio telescope

- "Modelling spatially-resolved spectra of the Cygnus Loop Supernova Remnant"
  PI: **Sara Loru**, project 14-17, 89 observing hours.
  2017 June-August

- "Single-Dish Imaging of the Solar Chromosphere I: Testing Continuum Observations at 24 GHz"
  PI: Alberto Pellizzoni, project 37-18, 15 observing hours in DDT mode (Director Discretionary Time)
  2018 January.

- "Catching the radio variability of X-ray binaries during outbursts"
  PI: Elise Egron, project 18-17 and 28-17, 126 ore observing hours in ToO mode (Target of Opportunity).
  June 2017-May 2018

- "Observations of PSR J2032+4127/MT91 213 near periastron"
  PI: Maura Pilia, project 01-17, 24 observing hours in ToO mode.
  2017 June-November

- "Observations of the possible Pulsar Wind Nebula around PSR B0355+54"
  PI: Maura Pilia, project 33-17, 36 observing hours.
  November 2017.

VLBI

- "Catching the microquasar CygX-3 during a giant flare"
  PI: Elise Egron, project ToO-CygX3, 50 observing hours in ToO mode with SRT, Medicina, Noto, Torun and Yebes telescopes.

BIBLIOGRAPHY

Abdo A. A., et al., 2010, Science, 327, 1103

Acciari V. A., et al., 2011, ApJL, 730, L20

Acero F., et al., 2016, apjs, 224, 8

Ackermann M., et al., 2013, Science, 339, 807

Aharonian F. A., Atoyan A. M., 1996, A&A, 309, 917

Albert J., et al., 2007, ApJL, 664, L87

Albinson J. S., Tuffs R. J., Swinbank E., Gull S. F., 1986, MNRAS, 219, 427

Ali-Haïmoud Y., Hirata C. M., Dickinson C., 2009, MNRAS, 395, 1055

Allen G. E., Houck J. C., Sturner S. J., 2008, ApJ, 683, 773

Altenhoff W. J., Downes D., Goad L., Maxwell A., Rinehart R., 1970, aaps, 1, 319

Altenhoff W. J., Downes D., Pauls T., Schraml J., 1979, aaps, 35, 23

Baars J. W. M., Genzel R., Pauliny-Toth I. I. K., Witzel A., 1977, A&A, 61, 99

Baldwin J. E., 1954, Nature, 173, 164

Beard M., Kerr F. J., 1969, Australian Journal of Physics, 22, 121

Bell A. R., 1978a, MNRAS, 182, 147

Bell A. R., 1978b, MNRAS, 182, 443

Bell A. R., 2004, MNRAS, 353, 550

Bell A. R., 2005, MNRAS, 358, 181

Bell A. R., Schure K. M., Reville B., 2011, MNRAS, 418, 1208

Bennett A. S., 1962, MmRAS, 68, 163

Bennett A. S., 1963, MNRAS, 127, 3

Blair W. P., Sankrit R., Raymond J. C., 2005, AJ, 129, 2268

Blandford R., Eichler D., 1987, Physics Reports, 154, 1

Blythe J. H., 1957, MNRAS, 117, 652

Bolli P., et al., 2015, Journal of Astronomical Instrumentation, 4, 1550008

Braude S. Y., Lebedeva O. M., Megn A. V., Ryabov B. P., Zhouck I. N., 1969, MNRAS, 143, 289

Bridle A. H., Purton C. R., 1968, AJ, 73, 717

Buffa F., Serra G., Bolli P., Fara A., Deiana G., Nasir F., Castiglia C., Delitala A., 2016, INAF - Osservatorio Astronomico di Cagliari. Internal Report N.54,

Buffa F., Bolli P., Sanna G., Serra G., 2017, Measurement Science and Technology, 28, 014004

Burton M. G., Geballe T. R., Brand P. W. J. L., Webster A. S., 1988, MNRAS, 231, 617

Cardillo M., et al., 2014, A&A, 565, A74

Cardillo M., Amato E., Blasi P., 2016, A&A, 595, A58

Castelletti G., Dubner G., Brogan C., Kassim N. E., 2007, A&A, 471, 537

Castelletti G., Dubner G., Clarke T., Kassim N. E., 2011, A&A, 534, A21

Chevalier R. A., Kirshner R. P., Raymond J. C., 1980, ApJ, 235, 186

Clark D. H., Caswell J. L., Green A. J., 1975, Australian Journal of Physics Astrophysical Supplement, 37, 1

Colla G., et al., 1971, AJ, 76, 953

Conway R. G., Daintree E. J., Long R. J., 1965, MNRAS, 131, 159

Davis M. M., Gelato-Volders L., Westerhout G., 1965, bain, 18, 42

Denoyer L. K., 1974, AJ, 79, 1253

Dickel J. R., van Breugel W. J. M., Strom R. G., 1991, AJ, 101, 2151

Downes D., Wilson T. L., Bieging J., Wink J., 1980, aaps, 40, 379

Dubner G., Giacani E., 2015, A&ARv, 23, 3

Duin R. M., Strom R. G., 1975, A&A, 39, 33

Dwarakanath K. S., Shevgaonkar R. K., Sastry C. V., 1982, Journal of Astrophysics and Astronomy, 3, 207

Edge D. O., Shakeshaft J. R., McAdam W. B., Baldwin J. E., Archer S., 1959, MmRAS, 68, 37

Egron E., Pellizzoni A., Iacolina M. N., Loru S., Righini S., Trois A., SRT Astrophysical Validation Team 2016, INAF - Osservatorio Astronomico di Cagliari. Internal Report N.59,

Egron E., et al., 2017, MNRAS, 470, 1329

Ellison D. C., Baring M. G., Jones F. C., 1995, ApJ, 453, 873

Fanti C., Felli M., Ficarra A., Salter C. J., Tofani G., Tomasi P., 1974, A&A, 16, 43

Ferrand G., Decourchelle A., Ballet J., Teyssier R., Fraschetti F., 2010, A&A, 509, L10

Fesen R. A., Neustadt J. M. M., Black C. S., Milisavljevic D., 2018, MNRAS, 475, 3996

Frail D. A., Giacani E. B., Goss W. M., Dubner G., 1996, ApJL, 464, L165

Fuerst E., Reich W., 1986, A&A, 163, 185

Gao X. Y., Han J. L., Reich W., Reich P., Sun X. H., Xiao L., 2011, A&A, 529, A159

Génova-Santos R., et al., 2017, Mon. Not. Roy. Astron. Soc., 464, 4107

Ghavamian P., Schwartz S. J., Mitchell J., Masters A., Laming J. M., 2013, Space Science Reviews, 178, 633

Giacani E. B., Dubner G. M., Kassim N. E., Frail D. A., Goss W. M., Winkler P. F., Williams B. F., 1997, AJ, 113, 1379

Giacani E., Smith M. J. S., Dubner G., Loiseau N., Castelletti G., Paron S., 2009, A&A, 507, 841

Giordano F., et al., 2012, ApJL, 744, L2

Giuliani A., et al., 2011, ApJL, 742, L30

Gotthelf E. V., Vasisht G., 1997, ApJL, 486, L133

Green D. A., 1984, MNRAS, 211, 433

Green D. A., 1986, MNRAS, 221, 473

Green D. A., 1990, AJ, 100, 1927

Green D. A., 2011, Bulletin of the Astronomical Society of India, 39, 289

Green D. A., 2014, Bulletin of the Astronomical Society of India, 42, 47

Green D. A., 2017, VizieR Online Data Catalog, 7278

Green A. J., Baker J. R., Landecker T. L., 1975, A&A, 44, 187

Guidice D. A., 1969, PhD thesis, THE OHIO STATE UNIVERSITY.

H.E.S.S. Collaboration et al., 2011, A&A, 531, A81

Harris D. E., 1962, ApJ, 135, 661

Harris D. E., Roberts J. A., 1960, PASP, 72, 237

Hill L. E., 1972, MNRAS, 157, 419

Horton P. W., Conway R. G., Daintree E. J., 1969, MNRAS, 143, 245

Howard III W. E., Dickel H. R., 1963, PASP, 75, 149

Humensky B., VERITAS Collaboration 2015, in 34th International Cosmic Ray Conference (ICRC2015). p. 875 (arXiv:1512.01911)

Hurley-Walker N., et al., 2009, MNRAS, 396, 365

Ingallinera A., Trigilio C., Umana G., Leto P., Agliozzo C., Buemi C., 2014, MNRAS, 445, 4507

Inoue T., Yamazaki R., Inutsuka S.-i., Fukui Y., 2012, ApJ, 744, 71

Jones L. R., Smith A., Angelini L., 1993, MNRAS, 265, 631

Kassim N. E., 1989, ApJ, 347, 915

Katz-Stone D. M., Kassim N. E., Lazio T. J. W., O'Donnell R., 2000, ApJ, 529, 453

Kellermann K. I., 1964, ApJ, 140, 969

Kellermann K. I., Pauliny-Toth I. I. K., Williams P. J. S., 1969, ApJ, 157, 1

Kenderdine S., 1963, MNRAS, 126, 55

Kesteven M. J. L., 1968, Australian Journal of Physics, 21, 369

Klein U., Emerson D. T., Haslam C. G. T., Salter C. J., 1979, A&A, 76, 120

Kothes R., Landecker T. L., Foster T., Leahy D. A., 2001, A&A, 376, 641

Kothes R., Fedotov K., Foster T. J., Uyanıker B., 2006, A&A, 457, 1081

Kovalenko A. V., Pynzar' A. V., Udal'Tsov V. A., 1994, Astronomy Reports, 38, 78

Kundu M. R., 1969, ApJL, 158, L103

Kundu M. R., Becker R. H., 1972, AJ, 77, 459

Kundu M. R., Velusamy T., 1967a, Annales d'Astrophysique, 30, 59

Kundu M. R., Velusamy T., 1967b, Annales d'Astrophysique, 30, 723

Kundu M. R., Velusamy T., 1968, MNRAS, 140, 173

Kundu M. R., Velusamy T., 1972, A&A, 20, 237

Kuz'min A. D., Levchenko M. T., Noskova R. I., Salomonovich A. E., 1960, AZh, 37, 975

Large M. I., Mathewson D. S., Haslam C. G. T., 1961, MNRAS, 123, 113

Lee J.-J., Koo B.-C., Raymond J., Ghavamian P., Pyo T.-S., Tajitsu A., Hayashi M., 2007, ApJL, 659, L133

Lee J.-J., Koo B.-C., Yun M. S., Stanimirović S., Heiles C., Heyer M., 2008, AJ, 135, 796

Lee J.-J., Raymond J. C., Park S., Blair W. P., Ghavamian P., Winkler P. F., Korreck K., 2010, ApJL, 715, L146

Lee S.-H., Patnaude D. J., Raymond J. C., Nagataki S., Slane P. O., Ellison D. C., 2015, ApJ, 806, 71

Leslie P. R. R., 1960, The Observatory, 80, 23

Levenson N. A., Graham J. R., Keller L. D., Richter M. J., 1998, apjs, 118, 541

Longair M. S., 2011, High Energy Astrophysics

Loru S., et al., 2019, Monthly Notices of the Royal Astronomical Society, 482, 3857

Markwardt C. B., 2009, in Bohlender D. A., Durand D., Dowler P., eds, Astronomical Society of the Pacific Conference Series Vol. 411, Astronomical Data Analysis Software and Systems XVIII. p. 251 (arXiv:0902.2850)

Mathewson D. S., Large M. I., Haslam C. G. T., 1960, MNRAS, 121, 543

Mavromatakis F., Boumis P., Goudis C. D., 2003, A&A, 405, 591

Mayer C. H., McCullough T. P., Sloanaker R. M., 1957, ApJ, 126, 468

Melis A., Concu R., Trois A., 2018, Journal of Astronomical Instrumentation

Milne D. K., 1971, Australian Journal of Physics, 24, 429

Milne D. K., Dickel J. R., 1974, Australian Journal of Physics, 27, 549

Milne D. K., Hill E. R., 1969, Australian Journal of Physics, 22, 211

Miyata E., Tsunemi H., 2001, ApJ, 552, 624

Molinari S., Brand J., Cesaroni R., Palla F., 1996, A&A, 308, 573

Moran M., 1965, MNRAS, 129, 447

Morlino G., 2017, High-Energy Cosmic Rays from Supernovae. p. 1711, doi:10.1007/978-3-319-21846-5_11

Morlino G., Caprioli D., 2012, A&A, 538, A81

Nasir F. T., Buffa F., Deiana G. L., 2011, Experimental Astronomy, 29, 207

Navarrini A., et al., 2016, in 27th international symposium on space therahertz technology.

Navarrini A., et al., 2017.

Onić D., 2013, Ap&SS, 346, 3

Onić D., 2015, Serbian Astronomical Journal, 191, 29

Onić D., Urošević D., Arbutina B., Leahy D., 2012, ApJ, 756, 61

Onić D., Urošević D., Leahy D., 2017, AJ, 153, 32

Orfei A., Morsiani M., Zacchiroli G., Maccaferri G., Roda J., Fiocchi F., 2004, in Antebi J., Lemke D., eds, Proceedings of the SPIEVol. 5495, Astronomical Structures and Mechanisms Technology. pp 116–125, doi:10.1117/12.548944

Orfei A., et al., 2010, IEEE Antennas and Propagation Magazine, 52, 62

Ostrowski M., 1999, A&A, 345, 256

Paladini R., Burigana C., Davies R. D., Maino D., Bersanelli M., Cappellini B., Platania P., Smoot G., 2003, A&A, 397, 213

Pauliny-Toth I. I. K., Wade C. M., Heeschen D. S., 1966a, apjs, 13, 65

Pauliny-Toth I. I. K., Wade C. M., Heeschen D. S., 1966b, apjs, 13, 65

Pellizzoni A., et al., 2017, in Marcowith A., Renaud M., Dubner G., Ray A., Bykov A., eds, IAU Symposium Vol. 331, Supernova 1987A:30 years later - Cosmic Rays and Nuclei from Supernovae and their Aftermaths. pp 194–200, doi:10.1017/S1743921317004811

Perley R. A., Butler B. J., 2013, ApJ, 204, 19

Petre R., Szymkowiak A. E., Seward F. D., Willingale R., 1988, ApJ, 335, 215

Petruk O., Kuzyo T., Beshley V., 2016, MNRAS, 456, 2343

Planck Collaboration et al., 2014, A&A, 565, A103

Planck Collaboration et al., 2016, A&A, 586, A133

Prandoni I., et al., 2017, A&A, 608, A40

Reach W. T., Rho J., Jarrett T. H., 2005, ApJ, 618, 297

Reach W. T., et al., 2006, AJ, 131, 1479

Reich W., Zhang X., Fürst E., 2003, A&A, 408, 961

Reynolds S. P., 2008, araa, 46, 89

Reynolds S. P., 2011, Ap&SS, 336, 257

Reynolds S. P., 2017, Dynamical Evolution and Radiative Processes of Supernova Remnants. p. 1981, doi:10.1007/978-3-319-21846-5_89

Reynolds S. P., Ellison D. C., 1992, ApJL, 399, L75

Reynoso E. M., Moffett D. A., Goss W. M., Dubner G. M., Dickel J. R., Reynolds S. P., Giacani E. B., 1997, ApJ, 491, 816

Reynoso E. M., Hughes J. P., Moffett D. A., 2013, AJ, 145, 104

Rho J., Petre R., 1998, ApJL, 503, L167

Rho J., Jarrett T. H., Cutri R. M., Reach W. T., 2001, ApJ, 547, 885

Roger R. S., Costain C. H., Lacey J. D., 1969, AJ, 74, 366

Roger R. S., Costain C. H., Stewart D. I., 1986, aaps, 65, 485

Roger R. S., Costain C. H., Landecker T. L., Swerdlyk C. M., 1999, aaps, 137, 7

Safi-Harb S., 2012, in Aharonian F. A., Hofmann W., Rieger F. M., eds, American Institute of Physics Conference Series Vol. 1505, American Institute of Physics Conference Series. pp 13–20 (arXiv:1210.5406), doi:10.1063/1.4772215

Sastry C. V., Dwarakanath K. S., Shevgaonkar R. K., 1981, Journal of Astrophysics and Astronomy, 2, 339

Scaife A., et al., 2007, MNRAS, 377, L69

Scheuer P. A. G., 1963, The Observatory, 83, 56

Schlickeiser R., Fuerst E., 1989, A&A, 219, 192

Seeger C. L., Westerhout G., Conway R. G., Hoekema T., 1965, bain, 18, 11

Seta M., et al., 1998. pp 286–298, doi:10.1086/306141

Seta M., Hasegawa T., Sakamoto S., Oka T., Sawada T., Inutsuka S.-i., Koyama H., Hayashi M., 2004, AJ, 127, 1098

Shakeshaft J. R., Ryle M., Baldwin J. E., Elsmore B., Thomson J. H., 1955, MmRAS, 67, 106

Shklovskii I. S., 1960, Soviet Astronomy, 4, 355

Smith A., Jones L. R., Watson M. G., Willingale R., Wood N., Seward F. D., 1985, MNRAS, 217, 99

Sturner S. J., Skibo J. G., Dermer C. D., Mattox J. R., 1997, ApJ, 490, 619

Sun X. H., Reich W., Han J. L., Reich P., Wielebinski R., 2006, A&A, 447, 937

Sun X. H., Reich W., Han J. L., Reich P., Wielebinski R., Wang C., Müller P., 2011, A&A, 527, A74

Swartz D. A., et al., 2015, ApJ, 808, 84

Tavani M., et al., 2010, ApJL, 710, L151

Temim T., Slane P., Kolb C., Blondin J., Hughes J. P., Bucciantini N., 2015, ApJ, 808, 100

Tian W. W., Leahy D. A., 2008, ApJ, 677, 292

Troja E., Bocchino F., Miceli M., Reale F., 2008, A&A, 485, 777

Uchiyama Y., Funk S., Katagiri H., Katsuta J., Lemoine-Goumard M., Tajima H., Tanaka T., Torres D. F., 2012, ApJL, 749, L35

Urošević D., 2014, Ap&SS, 354, 541

Uyanıker B., Reich W., Yar A., Kothes R., Fürst E., 2002, A&A, 389, L61

Uyanıker B., Reich W., Yar A., Fürst E., 2004, A&A, 426, 909

Valente G., et al., 2010, in Millimeter, Submillimeter, and Far-Infrared Detectors and Instrumentation for Astronomy V. p. 774126, doi:10.1117/12.857306

Valente G., et al., 2016, in Millimeter, Submillimeter, and Far-Infrared Detectors and Instrumentation for Astronomy VIII. p. 991422, doi:10.1117/12.2232625

Velusamy T., Kundu M. R., 1974, A&A, 32, 375

Viner M. R., Erickson W. C., 1975, AJ, 80, 931

Vink J., 2012, A&ARv, 20, 49

Wanner J. F., 1961, PASP, 73, 143

West J. L., Safi-Harb S., Jaffe T., Kothes R., Landecker T. L., Foster T., 2016, A&A, 587, A148

Westerhout G., 1958, bain, 14, 215

Wielebinski R., Beck R., eds, 2005, Cosmic Magnetic Fields Lecture Notes in Physics, Berlin Springer Verlag Vol. 664, doi:10.1007/b104621.

Williams P. J. S., Kenderdine S., Baldwin J. E., 1966, MmRAS, 70, 53

Williams B. J., Borkowski K. J., Ghavamian P., Hewitt J. W., Mao S. A., Petre R., Reynolds S. P., Blondin J. M., 2013, ApJ, 770, 129

Williams B. J., Chomiuk L., Hewitt J. W., Blondin J. M., Borkowski K. J., Ghavamian P., Petre R., Reynolds S. P., 2016, ApJL, 823, L32

Willis A. G., 1973, A&A, 26, 237

Wilson R. W., 1963, AJ, 68, 181

Wolszczan A., Cordes J. M., Dewey R. J., 1991, ApJL, 372, L99

Woltjer L., 1972, araa, 10, 129

Xiao L., Fürst E., Reich W., Han J. L., 2008, A&A, 482, 783

Yeung P. K. H., Kong A. K. H., Tam P. H. T., Hui C. Y., Takata J., Cheng K. S., 2017, ApJ, 837, 69

Zhang Z., Gao Y., Wang J., 2010, Science China Physics, Mechanics, and Astronomy, 53, 1357